Identification and Mitigation of Degradation Mechanisms Induced by Heat and Light in NiOx-based Perovskite Solar Cells

Marion Solange Madeleine DUSSOUILLEZ

"Nothing in life is to be feared, it is only to be understood. Now is the time to understand more, so that we may fear less."

Marie Curie

Acknowledgments

This manuscript is the result of over four years of work and research at CSEM and EPFL-PV-Lab. It would not have been possible without all the people around me who supported me, both professionally and personally.

First of all, I would like to express my gratitude to my thesis director, Prof. Christophe Ballif, for allowing me to conduct my thesis in his laboratory and under his guidance. I thank him for his advice, feedback throughout my work, and for sharing his passion and knowledge with all of us (both in PV and juggling). I would also like to extend special thanks to Dr. Adriana Paracchino, my co-director, who supported me on a daily basis throughout my work. I thank her for her availability, her patience, her kindness, and her insightful ideas along this challenging journey. She helped me to gain self-confidence, never judging me for the things I didn't know, and for that, I am truly grateful. Thank you for taking the time to review my papers in a way that I can learn from. I would also like to thank Dr. Sylvain Nicolay and Dr. Quentin Jeangros, my team leaders, for their guidance and proofreading of my writings. I would like to particularly thank Sylvain, who taught me how to develop my critical thinking regarding literature and my results, which is essential for a scientist. I would like to express my deepest gratitude to Aïcha, the mom of the PV Lab, for her unwavering support during the times when I needed it most. I would also like to thank Christian for the corrections he made to my first article and for his scientific input throughout my thesis. I appreciated being welcomed at pvlab-Pk meetings.

I would like also to express my gratitude to the members of my thesis committee who agreed to evaluate my thesis, Prof. Roland Logé, Prof. Stefaan De Wolf, Dr. Solenn Berson, and Dr. Yaroslav Romanyuk.

I would like to thank the "PK dream team" at CSEM from my early days, especially Brett, Soo-Jin, Arnaud, and Laura, who supported me during a time when I was still the baby on the team. Special thanks to Florent (who finally joined the "dark side" after his thesis) for his support, and friendship over the past years. He has always been there when I needed him. Thanks for the hours you spent listening to me talk! Thanks to those who joined us during my thesis, including Daniel (thanks for your help during my Candidacy exam), Jean-David (sorry for asking the old-CsFA difficult to prepare…), Ludo, Felipe, Lisa, Xin Yu, Adrien, and also the PK team at PV-Lab, including Kerem, Deniz, Peter, Quentin G., Ricardo, Mostafa, Hilal, Mohammadreza, for their scientific input and the enjoyable times we spent together. I would also like to express my gratitude to Michele, who joined our team when I was about to finish my Ph.D. and coached me during the preparation of my oral presentation. I'm truly thankful for the time you spent teaching me. Thanks also to Franz, who helped me during my Candidacy.

A huge thank you to the technicians, both at CSEM and PV-Lab, including Cédric, Aymeric, Lionel, Dzevad, Nicolas, Nathanaël, Joël. Without you, nothing would have been possible. Thank you for always responding to my requests for help, often immediately after I asked! A special thanks to Aymeric, the Police Apéro, without whom life at Microcity would be much less fun. Thanks for all the events you organized for us to enjoy together, such as the apéro saumon, thesis defense celebrations, and more… And especially for managing the beer club!!

Neuchâtel, October 24, 2023

Abstract

Perovskite solar cells (PSCs) offer an attractive solution to increase the efficiency of PV panels via perovskite/silicon tandems thanks to their potential cost-effectiveness and high efficiency. In inverted PSC architecture (p-i-n), commonly used hole contact materials include NiO_X, self-assembled monolayers (SAMs), and semiconducting polymers. With the aim of bringing tandem solar cells to the commercial market, NiO_X stands out as the preferred choice due to the ease of scalability and uniform coverage achievable by sputtering on both flat and textured substrates. Additionally, NiO_X exhibits advantageous optoelectronic characteristics, thanks to its wide bandgap, charge carrier selectivity and minimal parasitic absorption losses.

The commercialization of tandem solar cells demands rigorous testing, including damp heat and light soaking tests. However, PSCs are susceptible to various degradation mechanisms when exposed to elevated temperatures, light, or humidity. This thesis aims to investigate these degradation mechanisms and propose some mitigation strategies.

NiO_X-based PSCs stability under damp heat testing was first investigated. It was found that the presence of NiO_X was responsible for the degradation at elevated temperatures in absence of oxygen. Thicker NiO_X layers exacerbate the problem, leading to S-shaped *J-V* curves. Mitigation strategies, such as NiO_X thickness reduction and the use of SAM interlayers, successfully limit degradation, with encapsulated devices retaining 94% of their initial efficiency after 1000 hours of damp-heat testing.

Alternatively, we show that a modified sputtering process in an argon-oxygen atmosphere and the introduction of cesium into NiO_X resulted in a reduction of Ni^{3+} species, a smoother surface and denser NiO_X layer, ensuring less than a 5% relative efficiency change in PSCs after more than 5000 h of test, complying with IEC 61215 damp-heat test requirements.

Moreover, the thesis investigated the light-soaking stability, the most challenging test for PSCs, especially at elevated temperatures. It identifies that perovskite composition plays a key role in device degradation. Excess PbI_2 accelerates perovskite decomposition, ionic movements can cause halide segregation, structural damage (amorphization), and formation of non-photoactive phases. Besides, light and heat can accelerate the loss of volatile perovskite components, even in the presence of a SnO_2 ALD barrier layer and an ITO electrode. Inhomogeneous electric field can lead to perovskite degradation, particularly at the device boundaries. Redox reactions at the NiO_X/perovskite interface pose a significant problem and metal electrodes are vulnerable to chemically react with the I_2 vapor. Finally, the study also revealed that the incorporation of an additive used for perovskite/C_{60} interface defects passivation, as well as the use of a hydrophilic SiO_X nanoparticles layer on the SAM/perovskite interface (used as wetting agent), can result in significant degradation.

In conclusion, achieving long-term operational stability in PSCs necessitates meticulous material control, effective interface engineering, and protective layers implementation. The thesis provides some valuable insights into these aspects.

Key words: NiO_x, perovskite degradation, stability, damp heat, light-soaking.

Résumé

Les cellules solaires à base de pérovskite (CSP) offrent une solution attrayante pour accroître l'efficacité des panneaux solaires photovoltaïques grâce à la technologie des tandems pérovskite/silicium, en raison de leur rentabilité et de leur haute efficacité. Dans l'architecture des CSP inversées (p-i-n), les matériaux de contact couramment utilisés pour les trous comprennent le NiO_X, les *self-assembled monolayers* (SAM) et les polymères semiconducteurs. Dans le but de commercialiser les cellules solaires tandem, le NiO_X se distingue comme le choix préférable, grâce à sa technique de dépôt, la pulvérisation cathodique, qui permet de déposer ce matériau sur de grandes surfaces et ce, de manière uniforme, sur des substrats plats et texturés. De plus, le NiO_X présente des caractéristiques optoélectroniques avantageuses, notamment grâce à sa large bande interdite, à sa sélectivité des porteurs de charge et à ses faibles pertes d'absorption parasite.

La commercialisation des CSP exige des tests rigoureux, notamment des tests de résistance à l'humidité et d'exposition à la lumière. Cependant, les CSP souffrent de multiples mécanismes de dégradation lorsqu'ils sont exposés à des températures élevées, à la lumière ou à l'humidité. Cette thèse vise à étudier ces mécanismes de dégradation et à proposer des stratégies d'atténuation.

La stabilité des CSP à base de NiO_X a d'abord été étudiée lors des tests de résistance à la chaleur et à l'humidité. Il a été constaté que la présence de NiO_X était responsable de la dégradation à des températures élevées en l'absence d'oxygène. Des couches plus épaisses de NiO_X aggravent le problème, conduisant à des courbes courant-tension en forme de S. Des stratégies d'atténuation, telles que la réduction de l'épaisseur du NiO_X et l'utilisation de couches intermédiaires SAM, limitent avec succès la dégradation : les cellules encapsulées conservent 94 % de leur efficacité initiale après 1000 heures de test de résistance à l'humidité.

Alternativement, la modification du processus de pulvérisation, dans une atmosphère d'argon-oxygène et avec l'introduction de césium dans le NiO_X, ont permis de réduire la quantité des espèces de Ni^{3+}, d'obtenir une surface plus lisse et une couche de NiO_X plus dense, garantissant une variation d'efficacité relative de moins de 5 % dans les CSP après plus de 5000 heures de test, ce qui est conforme aux exigences du test de résistance à l'humidité IEC 61215.

De plus, la stabilité lors de l'exposition à la lumière a été étudiée dans cette thèse. Ce test est le plus exigeant pour les CSP, en particulier à des températures élevées. Il a été identifié que la composition de la pérovskite joue un rôle clé dans la dégradation des dispositifs. Un excès de PbI_2 accélère la décomposition de la pérovskite, les mouvements ioniques peuvent entraîner la ségrégation des halogénures, des dommages structuraux (amorphisation) et la formation de phases non photoactives. De plus, la lumière et la chaleur peuvent accélérer la perte de composants volatils de la pérovskite, même en présence d'une couche barrière de SnO_2 ALD et d'une électrode d'ITO. Un champ électrique inhomogène peut conduire à la dégradation de la pérovskite, en particulier aux bords de la cellule. Les réactions rédox à l'interface NiO_X/pérovskite posent un problème significatif et les électrodes métalliques sont vulnérables aux réactions chimiques avec les vapeurs d'I_2. Enfin, l'étude a également révélé que l'incorporation d'un additif utilisé pour la passivation des défauts d'interface pérovskite/C_{60}, ainsi que l'utilisation d'une couche de

nanoparticules de SiO_X hydrophile sur l'interface SAM/pérovskite (utilisée comme agent mouillant), peut entraîner une dégradation significative.

En conclusion, l'obtention d'une stabilité opérationnelle à long terme dans les CSP nécessite un contrôle minutieux des matériaux et interfaces, et la mise en place de couches de protection. Cette thèse apporte des éclairages précieux sur ces aspects.

Mots-clés : NiO_X, dégradation de la pérovskite, stabilité, test de résistance à la chaleur et à l'humidité, exposition à la lumière.

Contents

1. Introduction and State of the Art

1.1 Energy transition

1.1.1 Global Warming and Energy Crisis

Meeting the challenge of global climate change must be the world's top priority. The burning of fossil fuels, uneven and unsustainable use of energy and land, lifestyles, and patterns of consumption and production have led to global warming of 1.1 degrees Celsius above pre-industrial levels (Figure 1.1a). It is now urgent to limit global warming to 1.5° to 2°C, as stipulated in the Paris Agreement. However, rising energy demand and ever-increasing greenhouse gas emissions make this challenge even more difficult to meet (Figure 1.1b). According to the Intergovernmental Panel on Climate Change (IPCC), the best estimate for reaching +1.5°C is in the early 2030s,[1] the limit underscored at COP27 in 2022. Actions need to be adopted to meet the growing demand for energy while reducing greenhouse gas emissions and guaranteeing a livable future for all. Among these measures, the widespread deployment of renewable energy sources emerges as a crucial action to simultaneously meet escalating energy demands while slowing drastically down carbon emissions from electricity generation. Being both faster and more cost-effective to implement than alternative renewable energy options, photovoltaics (PV) stands out as one of the most promising solutions to overcome this challenge and comply with the Paris Agreement.

In addition, the rapid post-Covid global economic recovery and the geopolitical crises, such as Russian invasion of Ukraine, have led to significant increases in natural gas and coal prices in Europe. In this context, the accelerated deployment of PV technologies has been favorable, thanks to their cost-efficiency and rapid installation, ideal for meeting the growing demand for energy and promptly addressing the current energy crisis.
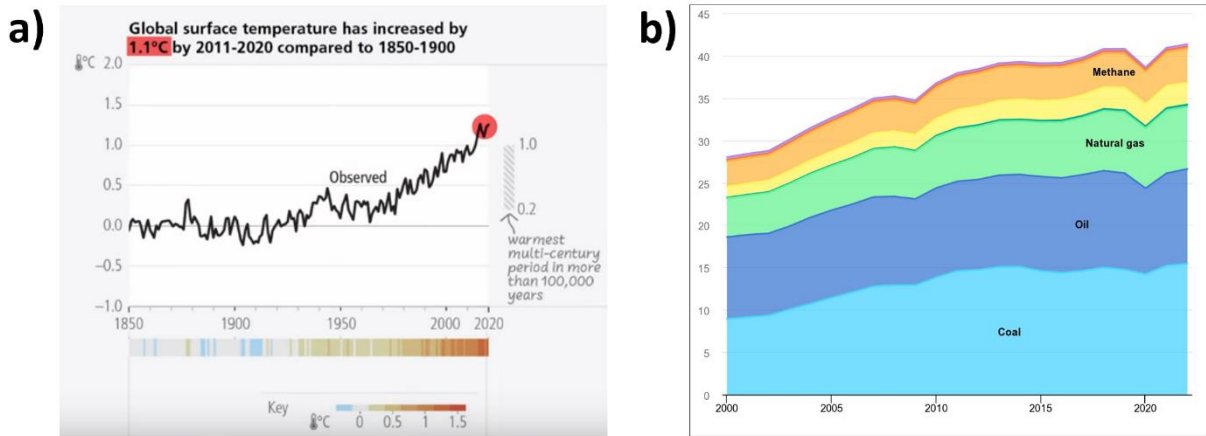
Figure 1.1: Global Climate Data Trends: Temperature and Greenhouse Gas Emissions *a) global surface temperature recorded from 1850 to 2020,[1] and b) global-energy-related-greenhouse-gas-emissions-2000-2022[2]*

1.1.2 Introducing Photovoltaics to the Energy Market

In 2022, with the addition of 239 GW, the global installation of solar energy capacity reached a significant milestone, surpassing a total installed photovoltaic capacity of 1 TW$_{DC}$. This achievement underscores the remarkable growth of the PV industry over the last five decades, characterized by a consistent doubling of production and capacity every three years. Forecasts indicate the possibility of reaching the next terawatt of installed capacity by 2024,[3] which would be adequate to fulfill the annual demand outlined in the IEA's Net Zero Emissions by 2050 Scenario. Furthermore, there is the potential for the PV industry to achieve a production rate of 1 TW per year by 2028. In addition, from 2021 to 2023, average wholesale electricity prices fell by 3% in 2021, 8% in 2022 and expected to fall by 15% in 2023, thanks to renewable energy deployment. These developments translate into substantial savings of around 100 billion euros on electricity supply costs for the entire European Union (Figure 1.2).[3]
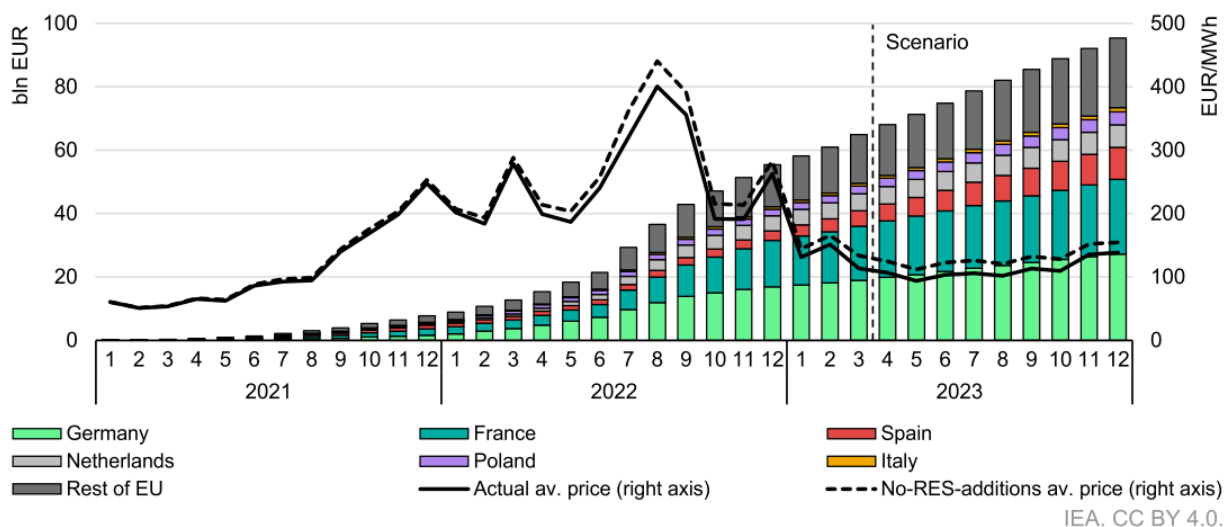
Figure 1.2: Electricity Cost Trends and Average EU Wholesale Spot Prices (2021-2023). *Actual price (black line) and in no-renewable energy source-additions (dashed line) scenario. Electricity cost increased due to post-Covid economy rebound (2021-2022) and then decrease thanks to PV and wind additions (2022-2023).*[3]

Despite these impressive advancements, PV currently accounts only for 4-5% of the global electricity production (2022) and remains the third most important renewable electricity technology, behind hydroelectricity and wind power.[3] Nevertheless, in contrast to other renewable technologies, PV stands out as a more cost-effective and rapidly deployable option, as evidenced by its levelized cost of electricity (LCOE). This key metric evaluates the relationship between the total energy generated by the energy system over its lifetime and the average total cost of the system over that same period. As a matter of fact, the global weighted average generated by recently commissioned large-scale solar PV installations has fallen by a remarkable 89% decrease between 2010 and 2022.[4]

1.1.3 PV as a Competitive Technology

The global weighted-average LCOE of PV technology was USD 0.445/kWh in 2010, 710% more expensive than the cheapest fossil fuel-based option. However, by 2022, a remarkable reduction in costs has brought solar PV global weighted-average LCOE down to USD 0.049/kWh, 29% less than the cheapest fossil fuel option.[4] This transformation underscores photovoltaics' key role in accelerating the energy transition, as a **"no-regrets option"**[5] essential for long-term energy security, price stability and national resilience. Furthermore, its appeal continues to grow for residential and commercial installations. To further its growth in the energy market, PV must maintain a competitive LCOE. Achieving a lower LCOE involves altering materials, enhancing efficiency, employing cost-effective manufacturing processes, and scaling up production.

Notably, the cost of crystalline solar PV modules sold in Europe saw a remarkable 91% decrease between December 2009 and December 2022.[4] Equipment and processes standardization of has been a key driver in reducing costs along the entire supply chain. Over the past decade, the cost of establishing new silicon

15

photovoltaic (Si PV) production facilities has consistently decreased by 50% every three years.[6] Additionally, both Si wafer size and average efficiency significantly increased during the last 20 years, rising from 2.5 to 10 watts of power output per cell and from 150 to 400 watts for residential modules power outputs while large utility panels can reach up to 700 watts.[5] Efforts to further reduce costs involve the use of less expensive materials, such as exploring alternatives to silver like copper or aluminium. Moreover, addressing the scarcity of materials like indium is essential before scaling up production capacities.[5]

As Haegel emphasized, "Waiting is not an option". [5] To contribute to achieving the goals of the Paris Agreement and reduce the ecological footprint, improving efficiency, minimizing cell-to-module losses, reducing production time, and enhancing reliability are critical factors. Although silicon has demonstrated its reliability and long-term stability in PV applications with high efficiency over large area devices, it is approaching its theoretical efficiency limit of 29.4%.[7] In September of this year, Fujian GS Solar Co., Ltd. In collaboration with the National Engineering Research Center for High-efficiency Solar Cell Equipment and Technology achieved a groundbreaking milestone in solar efficiency. They set a new world record for efficiency using a Hybrid Back Contact Heterojunction (HBC) module. The HBC module achieved an impressive full area conversion efficiency of 24.88%,[8] with the use of remarkable HBC solar cells, achieving a record-breaking 27.42% conversion efficiency in September of the same year.[9] Earlier, at of the end of 2022, LONGI certified HJT silicon solar cells on full-size silicon wafers at 26.81%[10] and Trina Solar achieved a certified a module efficiency at 24.24% using large-area industrial n-type i-TOPCon modules based on high-efficiency n-type i-TOPCon cells measuring 210 mm x 210 mm.[11]To surpass Si theoretical efficiency limit,[12,13] multi-junction cells are required, where each layer absorbs a different part of the solar spectrum. These multi-junction modules have the potential to significantly reduce solar energy costs. A promising technology is the perovskite/silicon tandem cell,[14,] which combines a perovskite single junction cell on top of a silicon cell to broaden the spectrum of light absorption.
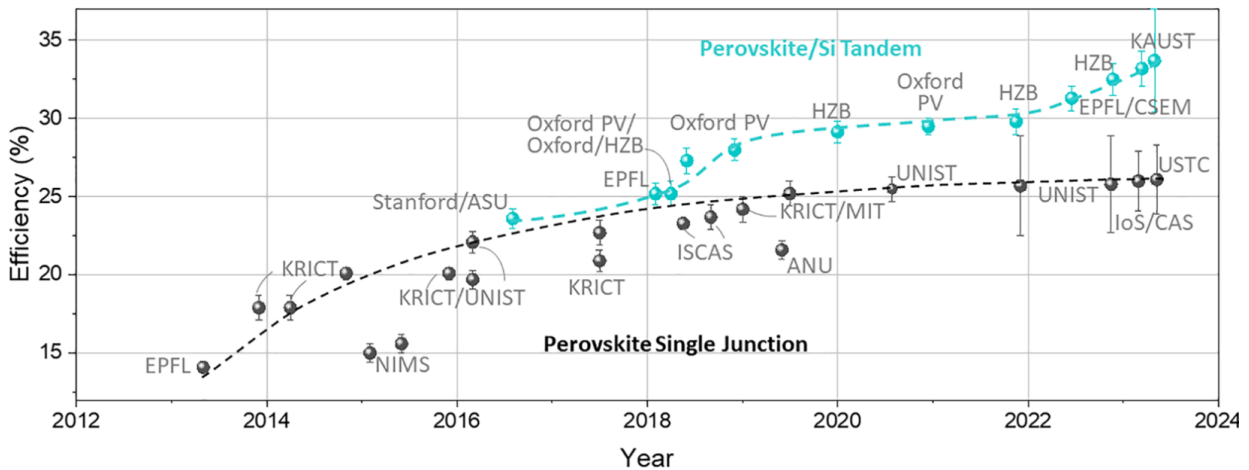
Figure 1.3: Photovoltaic efficiency of single-junction perovskite solar cells and monolithic two-terminal perovskite–silicon tandem solar cells for the period 2013–2023.[13]

Perovskite is an ideal material to complement silicon since it absorbs light in the blue part of the spectrum, while silicon absorbs in the red part.[15] Perovskite single junction solar cells have already achieved efficiencies rivaling those of silicon, albeit with a smaller active area (Figure 1.3).[10] Laboratory-scale perovskite/silicon tandems have for the first broken the 30% efficiency barrier in 2022 (EPFL and CSEM

team)[16] and now reached record efficiencies of 33.7%, indicating their potential to enter the PV market as the next generation of PV modules. However, a significant challenge hindering large-scale production of these perovskite/silicon tandems could be the degradation of the perovskite top cell over time due to various stressors. Current PV systems are expected to operate for 25 years or more with minimal performance degradation. Meeting this operational standard is essential before perovskite/silicon tandems can replace the current generation of PV systems.[17]

The importance of module efficiency should be stressed here. With limited potential to decrease the installation cost per m^2, which makes now for the largest share in.

1.2 Perovskite, an attractive material to enhance solar cells efficiency: its strengths and weaknesses

Emerged in 2009 from dye-sensitized solar cells (DSSCs) research, solar cells incorporating hybrid perovskite semiconductors as their light-absorbing materials have now reached 26.1% efficiency[10], coming close to silicon technology (even though with mm^2 size devices, compared to quasi-industrial solar cells). Perovskites refers to a group of compounds sharing the $CaTiO_3$ crystal structure (ABX_3). In the context of hybrid organic-inorganic perovskites, the A cation component is organic, typically involving methylammonium (MA) and/or formamidinium (FA), sometimes in combination with cesium (Cs). The B element is usually lead (Pb), occasionally mixed with tin (Sn), and X represents a halide anion, which can be chlorine (Cl), bromine (Br), iodine (I), or mixtures thereof.

Perovskite materials have garnered attention due to their exceptional photophysical and electrical properties, which include a high absorption coefficient, tunable band gap ranging from 1.2 to over 2 eV,[18-19] and long charge carrier diffusion lengths.

Since perovskite was initially used in dye-sensitized solar cell (DSSC), many groups started to work on mesoscopic solar cells, i.e. N-I-P cells with the perovskite incorporated inside a TiO_2 or Al_2O_3 mesoscopic scaffold. However, because perovskite can have long diffusion lengths (even >1um), the carriers can easily reach the electrodes without any scaffold. Today, most of the research group are working on planar N-I-P or P-I-N structures. Additionally to the high efficiency and negligible *J-V* hysteresis, the P-I-N structure[20] has the advantage to be processable at low temperature, and more importantly can be made transparent for IR light, making it very useful for tandem application (both PK/c-Si and PK/PK tandems). In addition, low production cost makes perovskites an ideal candidate for the next generation of solar panels. For the reasons detailed above, my thesis focuses only on P-I-N devices.

In order to become a commercially viable product, perovskite solar cells (PSCs) must also prove to be stable. In the context of tandem applications, they would be required to match Si and pass at least the IEC-61265 standard degradation tests required by the silicon PV industry, such as damp heat, UV-light soaking and thermal cycling. To successfully pass these tests, the perovskite absorber, the charge carrier-selective

layers as well as the electrodes should be stable. Noticeably such standard tests, usually designed for technologies which can stabilise in efficiency after a certain time under e.g. light soaking, might still not be sufficient to grant a field lifetime over 20 years. New standard will at some point likely be required for perovskite based solar cells and modules.

Despite the promise of high-efficiency, perovskite-based solar cells struggle to pass even standard degradation tests. Indeed, thanks to their ionic nature, perovskites have low formation energy and are easy to make. However, their strength is also their weakness, as they are also easy to break (or degrade),[21] especially under environmental stressor such as moisture, heat or light. The degradation of PSCs stems from various intrinsic instability factors, such as halide diffusion leading to phase segregations, the outgassing of volatile organic cations, reactions of accumulated charge carriers with the perovskite itself and reaction between halides and metal electrodes. Additionally, extraction barriers develop at the perovskite interfaces due to aging or thermal stress, and extrinsic factors like temperature, moisture, and UV-induced degradation can further contribute to the overall degradation process.

1.2.1 Moisture and oxygen-induced degradation

The primary environmental factors that significantly impact the stability of solar cells are oxygen (O_2) and water (H_2O).[22,23] Moisture ability to easily penetrate the perovskite structure and establish hydrogen bonds with cations weakens its interactions with metal cations and halide anions, thus compromising the structural stability of the crystal. The formation of a hydrated perovskite phase is a reversible process. However, when the moisture penetration is extensive, perovskite can decompose irreversibly, resulting in the release of byproducts such as lead iodide (PbI_2), methylamine (CH_3NH_2), hydroiodic acid (HI) and iodine (I_2).[24,25,26] To address this challenge, it is crucial to prevent the ingress of both oxygen and water. At a device level, the use of hydrophobic layers or blocking layer could help to delay oxygen and moisture ingress. According to Raiford et al., having a dense atomic layer deposited (ALD) in the device is the key to achieve stability. For this purpose, they introduced a thin layer of polyethylenimine ethoxylated (PEIE) to enhance the nucleation of ALD-SnOx,[27] resulting in the formation of a highly dense SnO_2 layer. Devices incorporating PEIE exhibited no visible degradation even when annealed at 200°C in air for 120 minutes. In contrast, devices without PEIE began to exhibit a yellow discoloration after only 15 minutes of annealing, and severe degradation was evident by the end of the test (Figure 1.4a). Similarly, a rapid degradation of the perovskite occurred in control devices when exposed to water droplets. Yellow regions became visible immediately after the droplet impact. In contrast, the PEIE-based devices did not show any color variation throughout the test duration. This enhanced performance can be attributed to the improved nucleation of ALD-SnO_2 facilitated by PEIE. As a result, SnO_2 acted as a robust protective barrier against moisture even under elevated temperatures of 200°C. Furthermore, devices fabricated with inorganic ALD transport layers for both electrons and holes demonstrated high PCE and stability at 85°C.[28] Nevertheless, despite the dense and impermeable nature of these transport layers, external encapsulation remains necessary to enhance the long-term stability of the PSCs.
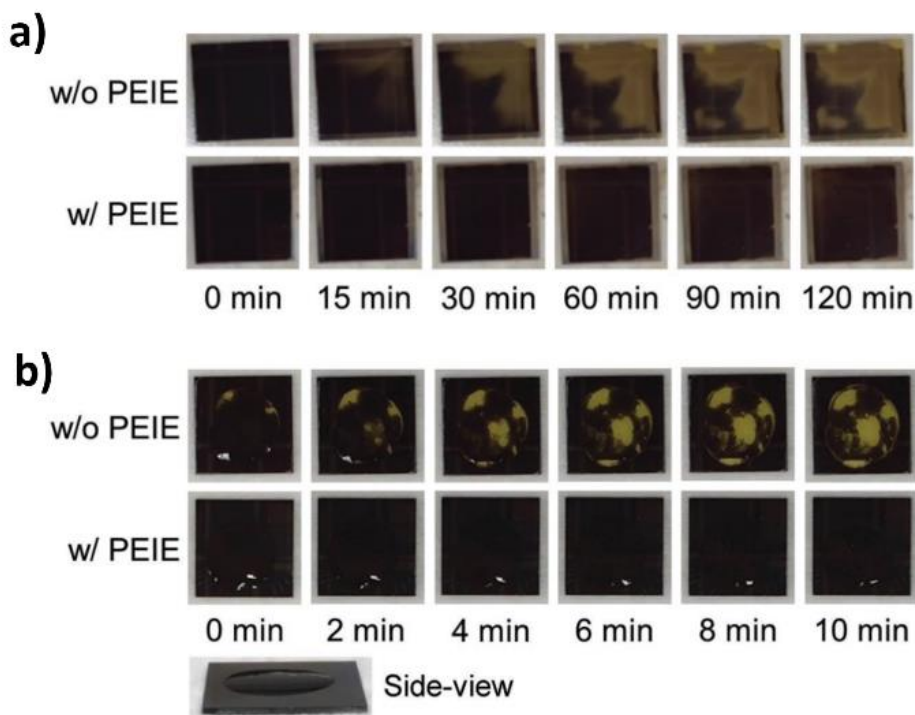
Figure 1.4: Evolution of CsFA/C$_{60}$/ALD SnO$_2$ Films with and without PEIE Nucleation Layer.[27] *a) during annealed at 200 °C in air for 120 min, or b) after a water droplet on the SnO$_2$ surface for 10 min. For a better understanding, a side-view of the water droplet is also presented.*

1.2.2 Heat induced-degradation

When subjected to heat, the structural integrity and stability of the perovskite phase can be compromised. For instance, the A-site cation, situated in the center of a cube formed by metal cations and halide anions, exhibits significant volatility, with MA$^+$ being particularly prone to escaping, consequently leading to excess PbI$_2$.[29] Even below 70°C, in MAPI perovskite devices, A Kumar et al. reported the accumulation of ions and charge carriers at the perovskite interfaces, leading to an increase in charge carrier recombination and a subsequent reduction in PSC performance. [21] The FAPbI$_3$ perovskite undergoes easily phase changes even at room temperature, a process that accelerates under elevated temperatures.[30,31,32] The black photo-active perovskite phase (alpha phase) changes into a yellow one (delta phase), which is not photoactive. The insertion of larger cations, such as Cs and MA, has shown enhanced crystal stability thanks to a better tuning of the tolerance factor.[33,34] Despite the superior optoelectronic properties of the triple cation CsFAMA perovskite, Yang et al. observed a decreased charge mobility and an increase in charge recombination sites near the interface, attributed to the formation of traps and PbI$_2$ regions at temperatures as high as 85°C.[35] To address these challenges and enhance thermal stability, the implementation of surface passivation techniques becomes imperative.

In this context, Azmi et al. developed a room-temperature post-treatment of three-dimensional (3D) perovskite using oleylammonium iodide (OLAI) to create two-dimensional Ruddlesden-Popper–phase layers, effectively passivating the defect at the C$_{60}$ interface, reducing ion migration and barring moisture

and oxygen ingress. They show that this passivation also suppresses the ion migration and blocks moisture and oxygen ingress. This advancement enabled highly efficient devices to endure a damp heat test, losing less than 5% efficiency after over 1200 hours, maintaining a PCE of over 19%.[36] Similarly, Yao et al. introduced n-propylammonium iodide (PAI) into CsFAMA perovskite and demonstrated that PAI additive reacts with PbI_2 to form a 2D perovskite. This hydrophobic material minimized oxygen and moisture penetration, upshifting the perovskite's conduction band, enhancing device performance and stability in air. [37] While various molecules aimed to enhance the perovskite/C_{60} interfaces,[38–41] Isikgor et al. highlighted that common passivation methods with larger organic molecules couldn't effectively interact with the lead-rich surface due to repulsion by Pb^{2+} ions. They proposed Phenformin Hydrochloride (PhenHCl), a multi-functional molecule,[42] capable of passivating grain boundaries and mitigating surface defects. This enhanced passivation led PhenHCl-treated single-junction PSCs to achieve over 20% efficiency, showcasing an average 100 mV V_{OC} increase compared to control devices, reaching V_{OC} values up to 1.22 V.
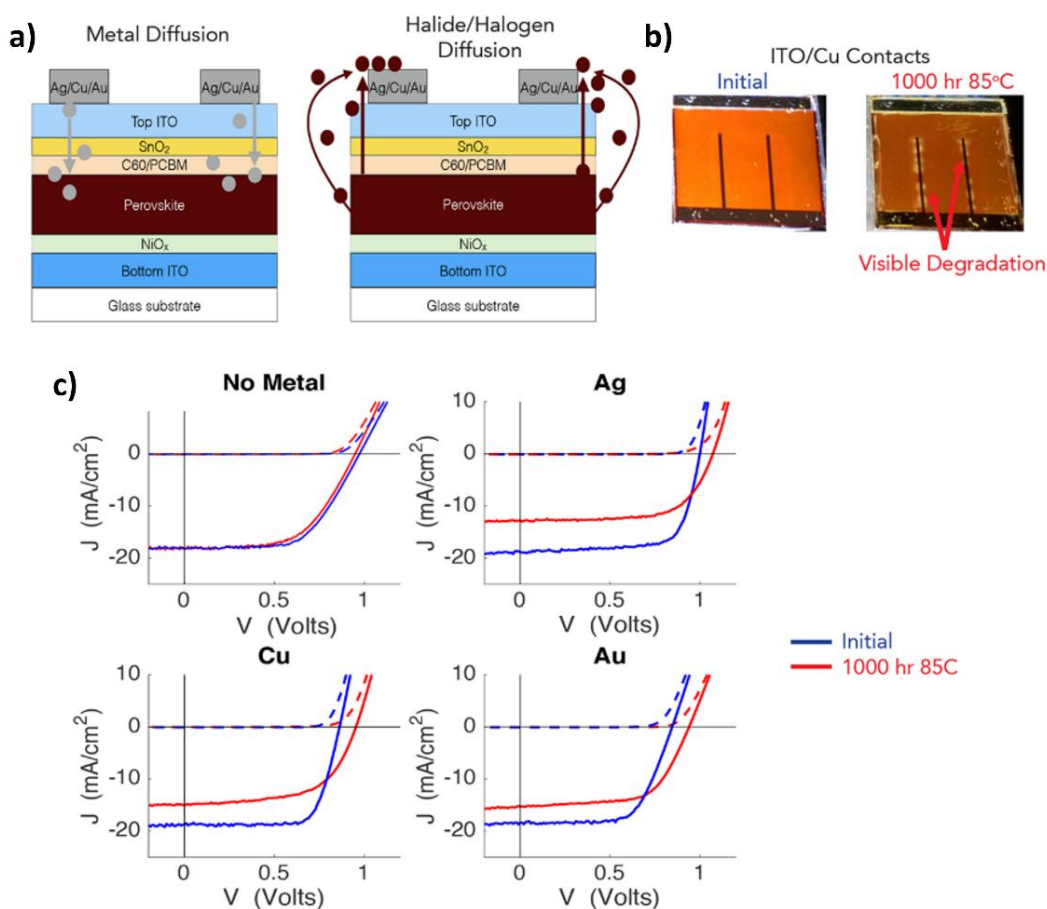
Figure 1.5: Metal Electrodes-Induce PSCs Degradation Under Thermal Stress.[43] *(a) Sketch of the p-i-n device structure showing possible degradation mechanisms of metal and iodide diffusion through C_{60}/PCBM, SnO_2, and ITO layers. (b) Picture of a CsFA-based cell with Cu as metallic contact before and after aging at 85 °C, in N_2 and a dark environment for 1000 h. Yellow regions around the metallic fingers are a sign of the perovskite degradation. (c) J-V curves of CsFA-based devices for different electrodes, before (blue) and after (red) thermal testing at 85 °C for 1000 h in N_2.*

Moreover, when subjected to elevated temperatures exceeding 80°C, the degradation of PSCs can be initiated by the metal electrodes.[21,43] Regardless of the type of metal used, a noticeable change in the visual color of the perovskite, shifting from brown to yellow, is observed around the metal fingers (Figure 1.5b).[43] After 1000 hours at 85°C, devices based on Cu, Ag or Au exhibit similar degradation patterns, characterized by a decrease in J_{SC} and an increase in V_{OC}. Conversely, in absence of metal contact, the initial and final J-V curves closely overlap. Consequently, it is proposed that Ag diffuse through defects or grain boundaries in the ITO layer into the perovskite, resulting in the formation of an insulating layer. Additionally, volatile halide species may escape from the perovskite by diffusing into the device or reaching the top metal contact in vapor phase,[44] and form for instance AgI, which weakens carrier extraction. [43,45] These results highlight the need of identifying more suitable charge transport layers and blocking layers to improve the thermal stability of PSCs. In this context, Boyd et al. have proposed to replace the evaporated fullerene with a spin coated one, to planarize the surface and promote the growth of a dense and uniform ITO layer on top, thus blocking species migration.[43]

1.2.3 Light-induced degradation

As previously discussed, the ionic nature of perovskite materials allow for the easy movement of halide ionic vacancies within the perovskite structure, resulting from their low formation energies,[46] which ultimately compromise the stability of perovskites. This feature is exacerbated under light exposure.[47–51]

Moreover, under illumination, organic cations may undergo deprotonation and escape the structure, while the byproduct PbI_2 photo-decomposes into metallic Pb and I_2 gas.[45,52–54] Second, the byproducts can speed up the degradation of perovskite material, particularly in devices exposed to light at elevated temperatures.

For instance, Fu et al. showed that after 1000 hours of light soaking at 60°C in N_2 atmosphere, $FAPbI_3$-based cells exhibited no visible signs of degradation (Figure 1.6a) while after only 320 hours under 1 sun at 80°C, nearly the entire active area turned yellow due to the emergence of porous PbI_2.[45] Cross-section scanning electron microscopy (SEM) images of the cell revealed significant differences in perovskite morphology between pristine and heavily degraded areas (Figure 1.6b). The degraded region displayed a porous morphology with cracks and voids, indicative of material loss, while the non-degraded zone exhibited a compact and uniform film. These observations highlight a preference for degradation within the bulk of the perovskite rather than at its interfaces. Additionally, cracks and bending of the TCO were evident. The authors proposed that the loss of A-site cation results in the release of I_2 vapor and the formation of PbI_2-rich regions. I_2 acts as a catalyst for degradation near the fresh perovskite, leading to an increased production of PbI_2 and, consequently, more I_2 due to photodecomposition. As a result of vapor pressure build-up, the top TCO layer eventually breaks. Therefore, although excess PbI_2 has been shown to enhance the initial efficiency of the cell by passivating the perovskite defects,[55–57] it is detrimental for photostability.[58–60] Consequently, stoichiometric perovskite compositions are necessary to withstand stability tests, particularly extended light soaking tests.
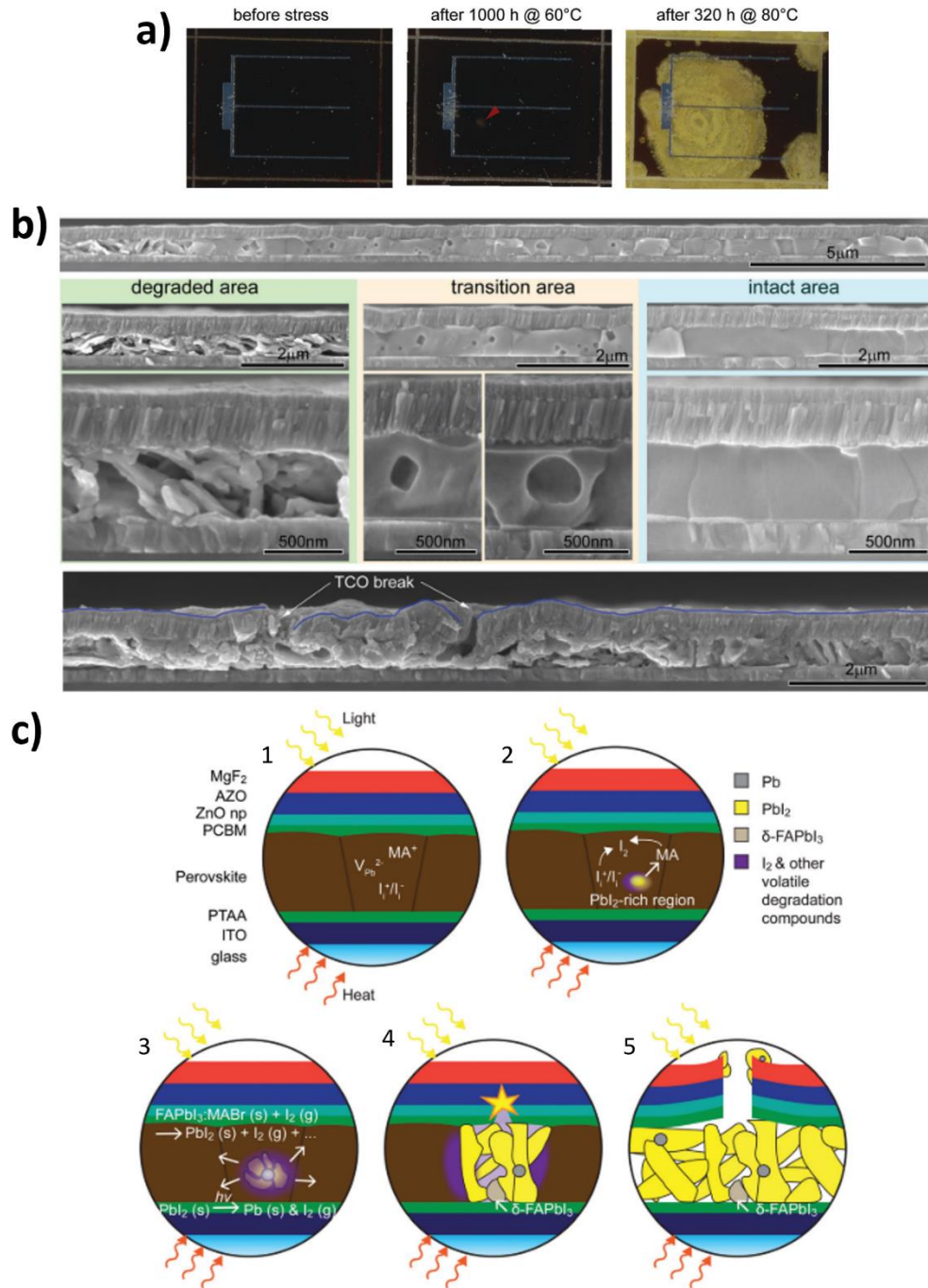
Figure 1.6: *Operational* **Stability under Light Soaking at Elevated Temperatures**.[45] *(a) Pictures of the PSCs before the test, after 1000h of MPPT at 60°C or after 320h at 80°C. Cells were not encapsulated and illuminated without shadow-mask, under 1 sun intensity in a N_2 atmosphere. (b) SEM cross section of a PSCs after MPPT 320 hours at 80°C, scanned from the degraded (yellow region) to the pristine (brown regions) areas. (c) Sketch of the I_2 vapor-assisted degradation mechanism under light and heat, step by step.*

The aforementioned results of Fu et al. show clearly that degradation in perovskite devices is rarely uniform across the active area. Non-uniform degradation is frequently the result of particle contamination, a problem which is exacerbated by the self-catalyzing nature of degradation reactions, which cause the degradation at localized weak spots to spread.

Jacobs et al. have shown that in addition to particle contamination, inhomogeneous degradation rates can occur as a result of device boundaries such as the edge of the top metal electrode, as the difference in electric field is maximum in this region. This effect is especially pronounced in small laboratory-scale devices. By matching the spatial distribution and voltage dependence of observed degradation patterns with drift-diffusion simulations, the authors show that degradation around device boundaries can be understood as resulting from ion migration in the plane of the substrate (i.e. "lateral migration").

Previously, it was observed that ions can move in response to the electric fields generated by localized light exposure.[61] The occupation of traps during light exposure perturbs the system,[62] creating electric fields that induce ion migration[62] either within the crystal or along the film grain boundaries. Instead of traps, the edge effects observed by Jacobs et al. are driven by the electric fields associated with the built-in voltage of devices, plus the additional potentials associated with applied bias and photovoltage in illuminated areas (V_{OC}). It was shown that even in the absence of any applied voltage or illumination, the built-in field of typical perovskite solar cells will drive lateral ion migration across its electrode boundaries (Figure 1.7a). Since applied voltage in the forward direction (forward bias) acts against the built-in field, lateral migration was predicted to decrease when moving from short-circuit conditions (0V, Figure 1.7b) towards open-circuit (V_{OC}, Figure 1.7c). Indeed, it was experimentally verified that this is the case: devices held at 0V under illumination were observed to undergo severe degradation around their device boundaries (Figure 1.7d), particularly in the dead-space adjoining the ITO boundary, whereas devices held at forward voltages of 0.9V and 1.2V suffered less. Top-view SEM images of the perovskite layer after peeling off the top electrode confirmed the degradation visible optically in Figure 1.7d, with the observed presence of voids primarily in the inactive region. (Figure 1.7e). At the same time, the presence of voids within the active area was found to increase at 1.2V (Figure 1.7e), which is the expected trend for carrier-induced degradation.

Although edge effects caused by lateral ion migration are expected to be more pronounced in small-scale laboratory devices with large amounts of dead space, it was also observed that the characteristic of such degradation strongly resembles the processes occurring around contaminant particles within the active area, suggesting a connection to the observations of Fu et al. This may be explained by the fact that particles located in the active area will generically induce lateral electric fields (Figure 1.7f), such that the same ion-induced degradation processes will be triggered around particles as at the electrode edges.
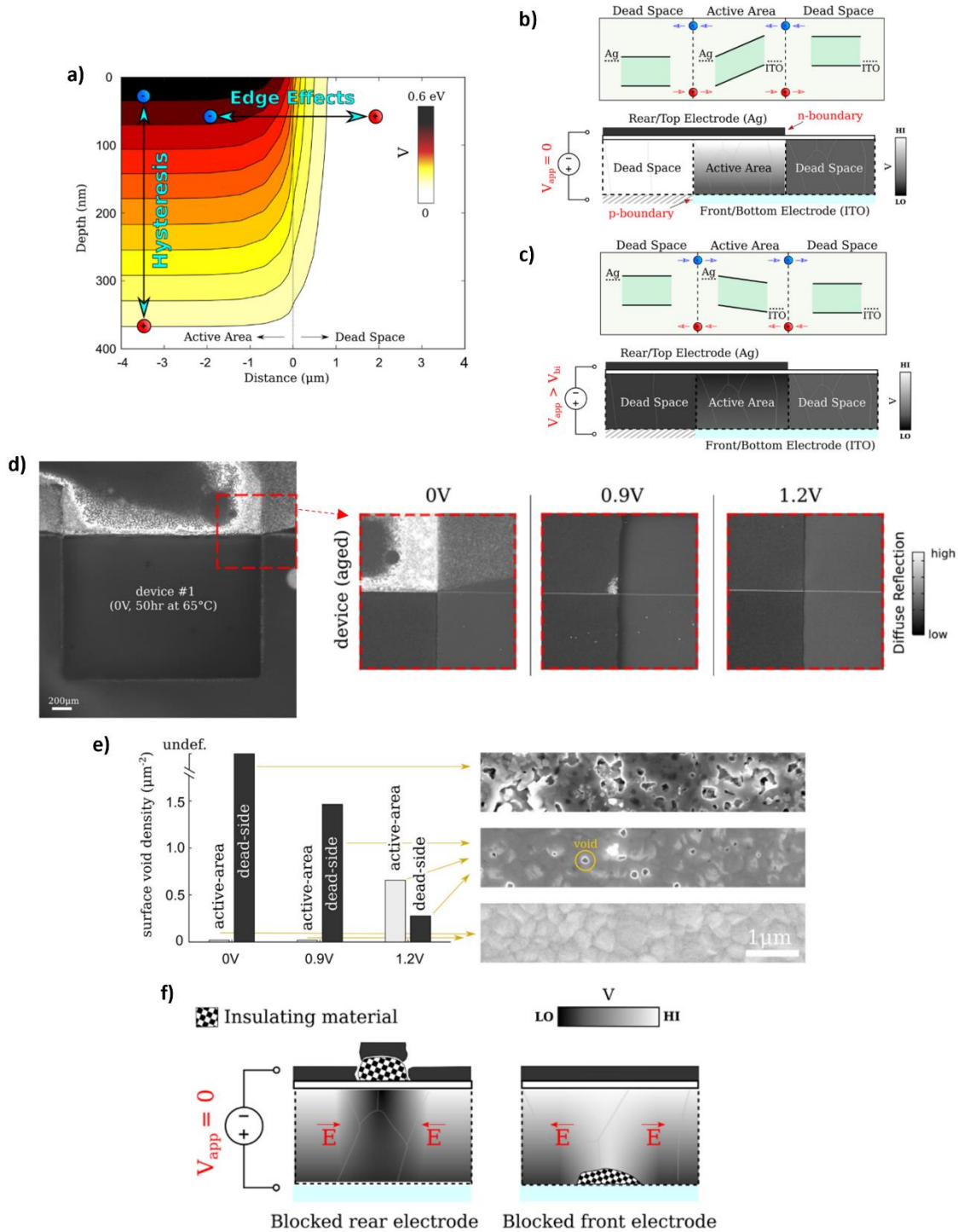
Figure 1.7: Lateral Ion-Induced Degradation.[63] *a) internal potential for a simulated PSC at the edge of the active area. No bias was applied. Only the built-in potential. (b and c) perovskite layer electronic bands for different applied voltages. d) PL images light-soaked devices at different applied voltages, for 50 h under 1 sun illumination and at 65°C. e) top-view SEM images of perovskite films after aging and peeling off of the top electrode for both active and dead areas. Images show the density of*

void present on the perovskite surface for light-soaked samples for 25 h at 65°C for different voltage bias applied. f) Illustration
demonstrating the impact of a local contaminants that can influence the internal potential and trigger lateral ion migration.

Thiesbrummel et al. demonstrated that the initial intrinsic degradation of PSCs under light bias results from the field screening induced by mobile ions.[64,65] Under light bias, the mobile ion density increases, leading to a redistribution of the internal field. Charge extraction becomes less efficient and photogenerated carriers accumulate in the perovskite layer, resulting in a drop in *FF* and especially in J_{SC} (Figure 1.8a and b). Increasing the scan speed allows better charge extraction, as mobile ions do not have time to reach the transport layers and accumulate (Figure 1.8c and d).[65] The longer the device is aged under continuous illumination, the greater the difference between the steady-state and the ion-freeze. It should be noted that the size if the active area of the cell makes no difference to this early degradation process.
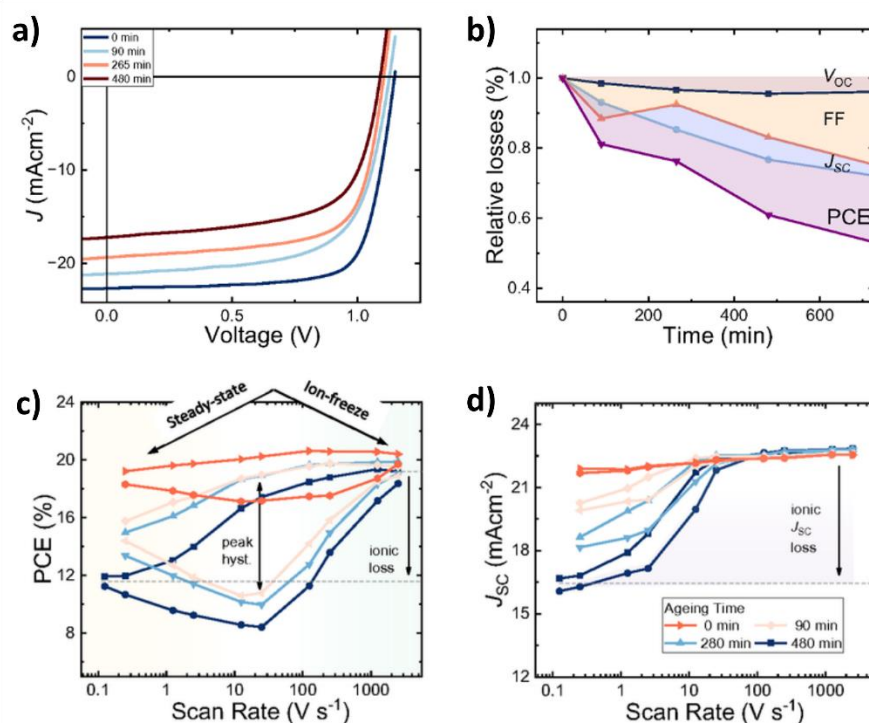
Figure 1.8: Mobile Ions-Induced Field Screening.[64] *a) Steady-state J-V curves of a CsFAMA-based PSC before and after certain times under continuous illumination at V_{OC}. The measurement was carried out at slow scan speeds (10 mV/s) to reach the steady state of the device. b) Relative V_{OC}, FF, J_{SC} and PCE losses recorded at different times during the aging test, in steady-state mode. c) Efficiency and d) J_{SC} extracted from J-V measurements, for various scan-speeds and different stages of devices aging.*

Additionally, under illumination, halide ions are more susceptible to drift compared to cations or metal species because they have lower activation energy.[66] Halide can segregate, creating iodide-rich (or bromide-rich) regions,[51,67–69] and leading to a localized band gap reduction (or increase, respectively). Such changes can induce V_{OC} losses, and the creation of recombination centers.[62, 49,51,70]

When subjected to illumination or an applied voltage, halides undergo oxidation, with a preference for iodide due to its relatively lower oxidation potential compared to bromide or chloride.[66] As a result, the oxidation of iodide plays a key role in determining halide phase segregation. The sketch in Figure 1.9a describes light-induced halide segregation process, governed by iodides. First, iodide ions (I-) present on the surface of the perovskite get oxidized to volatile I_2 permitting it to leave the crystal and creating a halide vacancy (V_X). I_2 diffuses through the material and can be reduced in regions where electrons accumulate at vacant sites within the material. In addition, asymmetric illumination (from one side), leads to the creation of an iodide oxidation rate gradient, as iodide close to the illumination area will be preferentially oxidized (Figure 1.9b). Finally, as preferential oxidation primarily occurs in regions with a significant population of photogenerated holes, such as those with elevated quasi-fermi level splitting (QFLS), oxidized iodine tends to migrate towards regions with lower QFLS. In other words, they accumulate in areas with a high density of electronic defects and a scarcity of holes. Consequently, this leads to the creation of iodine-rich domains in regions where the initial photoluminescence intensity was low. This model easily explains the increase in PL peak intensity and the downward shift of the band gap under light exposure, as well as the I-rich and Br-rich domains observed after degradation. [62,51,68,69,71]
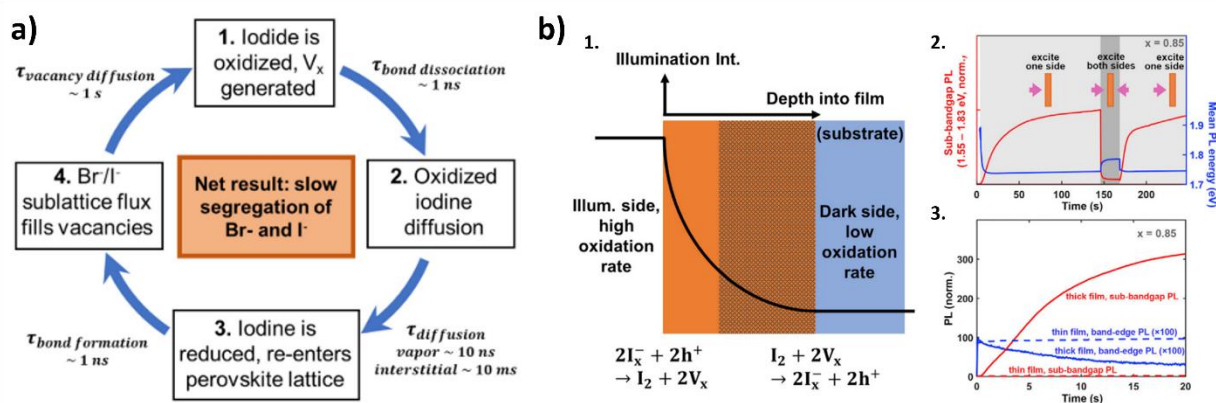
Figure 1.9: Iodide Oxidation and Halide Redistribution *a) Sketch of the Iodide oxidation and reduction leading to halide redistribution and segregation, and b) iodide oxidation rate for asymmetric (1 side) or symmetric (2 sides) illumination.*[66]

In summary, under prolonged illumination, perovskite exhibits a considerable ionic rearrangement throughout the material bulk, which may lead to degradation.

1.2.4 Encapsulation Methods and Passivating Layers to Enhance the PSCs Stability

Shi et al. used gas chromatography and mass spectrometry analyses to identify the volatile compounds released from perovskite material under thermal stress, and found species such as CH_3I, CH_3Br, and NH_3.[72] They showed that pressure-tight encapsulation leads to an equilibrium setting that prevents more degradation products from being formed, [23,72,73] therefore effectively prevents the perovskite from decomposition reactions. As a proof, their cells did not exhibit any efficiency degradation after 1800 hours of DH testing, or 75 cycles of humidity freeze testing. [72] Additionally, exposure to light can generate

additional decomposition products. For instance, I_2 gas resulting from iodide oxidation can escape from the perovskite and reacts with the metal contact, reducing its conductivity.[22,45] Therefore, a robust encapsulation is essential to protect the silver electrode and prevent degradation due to oxygen or moisture.[74,75] Belich et al. proposed an encapsulation method using PMMA/MoO_{3-x}/Epoxy/Glass. With this approach, they achieved significant improvements in the stability of PSC, both in ambient air and operational conditions. The cells retained 92.9% of their initial efficiency (up to 19%) after 1000 h under 1 sun illumination at MPPT it ambient air (30-60% RH).[73] Similarly, prior to using a standard encapsulation based on glass/glass packaging and edge sealant, Zhou et al. developed a multiple-barrier (inert Bi metal electrode/Al_2O_3/parylene stack) to prevent perovskite decomposition and metal degradation. With the addition of this thin film encapsulation, CsFA-based cells maintained 90% of their initial efficiency (20.5%) even after continuous operation at 45 °C for 5200 h and 93% of their initial efficiency after continuous operation at 75 °C for 1000 h under 1 sun illumination.[76]

Furthermore, Wang et al. introduced butylammonium into the CsFA perovskite to enhance the light stability of the devices.[40] Starting the test with efficiencies around 17%, these cells retained nearly 80% of their "post burn-in" efficiency after 1000 hours in air and almost 4000h when encapsulated with a hot-melt polymer foil and a glass coverslip. Comparatively, non-encapsulated devices exhibited efficiency degradation, primarily associated with a significant decrease in J_{SC} (Figure 1.10a-e). This degradation can be attributed to the continuous perovskite decomposition and outgassing when exposed to light. In summary, when proper encapsulation is employed, impressive stability results are achievable.
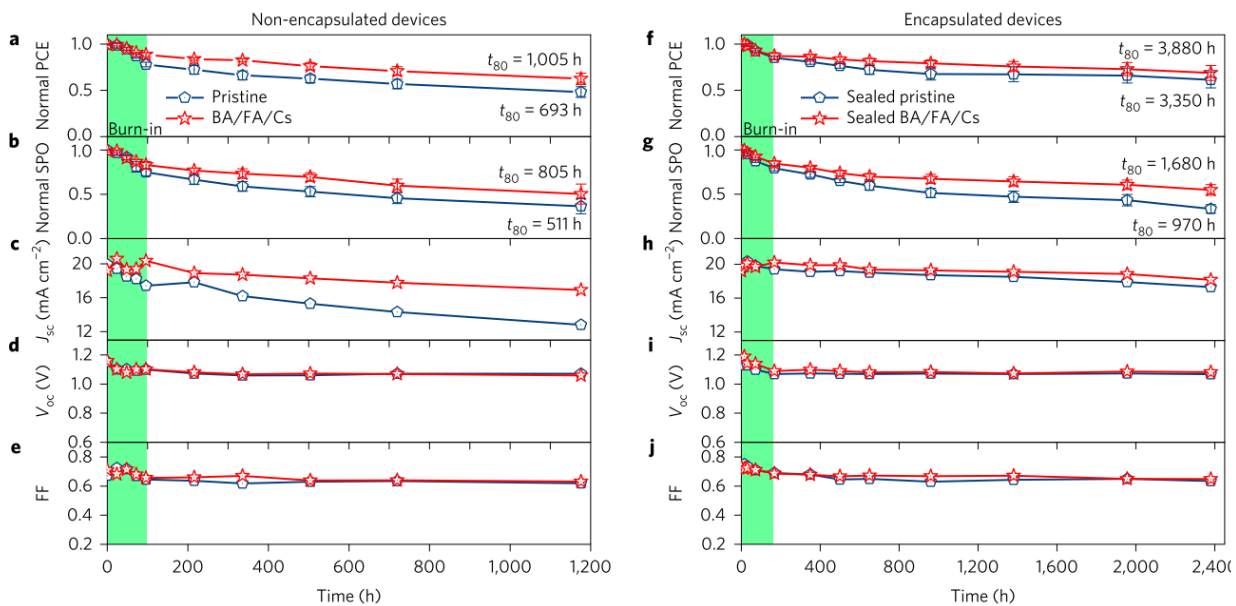
Figure 1.10: Light-Soaking Stability of CsFA and CsFABA Perovskite-Based Devices. *Results of non-encapsulated and encapsulated devices based on CsFA are plotted in blue and red for CsFABA perovskite.[40] Devices were exposed to continuous illumination (xenon-lamp, 76mWcm^{-2}, ~45 RH%, no UV cutter), at open-circuit. Evolution of the J-V parameters of the champion devices throughout the test are presented as follow: (a,f) normal efficiency, (b,g), stabilized power output (SPO), (c-h) J_{SC}, (d, i) V_{OC} and (e,j) FF. Cell stack: glass/FTO/SnO$_2$/C$_{60}$/perovskite/spiro-OMeTAD (with Li-TFSI and tBP additives)/Au*

In addition to the imperative need for encapsulation, device engineering can further enhance the performance of PSCs, particularly under operational conditions. For instance, by passivating the NiO_X/perovskite interface with 1,3-bis(diphenylphosphino)propane (DPPP), Li et al. achieved a champion device with an initial efficiency of 23%, which stabilized at 23.5% after maximum power point tracking under continuous illumination at 40°C for over 3500 hours. This device showed no degradation even during a light soaking test at open-circuit and 85°C for more than 1500 hours.[77] For these aging test, the devices were encapsulated with glass and UV-curable resin, and placed in N_2 environment. Bi et al. developed a low-dimensional diffusion barrier between the perovskite and the Ag contact to reduce ion diffusion. After encapsulation, the perovskite module, with an initial efficiency exceeding 15% and an active area of 36 cm^2, successfully passed both DH and LS tests, with efficiency losses of less than 5% and 9%, respectively, after 1000 hours of testing. [78] By adding long chain alkylamine ligands into the perovskite precursor solution, Zheng et al. demonstrated no loss in PCE after 1000 hours of operation stability testing, thanks to the improvement in the optoelectronic properties of the absorber and the reduction of ion migration.[79] Finally, Babics et al. reported a year-long outdoor performance of a perovskite/silicon tandem solar cell,[80] which is particularly significant as it reflects realistic and promising results achieved in harsh environmental conditions, including relatively high ambient temperatures throughout the year (from 20 to 40°C), high humidity (60% to 90% RH), and intense solar irradiance (above 2240 kWh m^{-2} per year). After one year of testing, the device retained 80% of its initial efficiency.

1.3 NiO_X as a promising HTM for industry applications

Focusing on hole transport materials, high efficiencies have been obtained with extremely thin organic hole transport material (HTMs) such as Poly(4-butyltriphenylamine) (poly-TPD),[27,81,82] Poly[*bis*(4-phenyl)(2,4,6-trimethylphenyl)amine] (PTAA),[79] carbazole-based self-assembled monolayers (SAM).[83–86] For small area (<1 cm^2), these devices often outperform those with inorganic HTM in terms of efficiency.[87] However, the deposition of < 5 nm thick organic layers over large scale by solution processes, such as spin coating, dip coating, slot-die coating, is challenging and prone to pinholes formation, especially in the case of textured surfaces such as those used by the Si PV industry. In this regard, the development of vacuum-deposited HTM offers a promising approach to deposit thin films at high throughput over large areas in a controllable and reproducible way. Notably, NiO_x can be deposited by various methods such as pulsed laser deposition,[88] solution processing,[89–91] nanoparticle dispensing,[92,93] or sputtering.[81,94–97] The latter method is well-known at the industrial level, is suitable for both upscaling and conformal deposition on various textured substrates, and offers the possibility to fabricate high efficiency mini-modules[98] and perovskite/Si tandem devices.[81,96,97,99]

Overall, NiO_x is an attractive material for hole extraction in solar cells as it is naturally *p*-type doped (oxygen-rich) [100–102] and it has a suitable valence band alignment with typical lead iodide perovskite absorbers, as

well as a high conduction band offset with the perovskite conduction band (bandgap ~3.6 eV) thus ensuring charge carrier selectivity. NiO$_x$ can also be doped to improve hole conductivity, notably with different cations such as Li,[103,104] Mg,[105,106] Al,[107] Cs,[108,109] Cu,[110,111] Na$_2$S[112] or with N$_2$ gas during the sputtering of a Ni target to form a Ni$_y$N layer.[113]
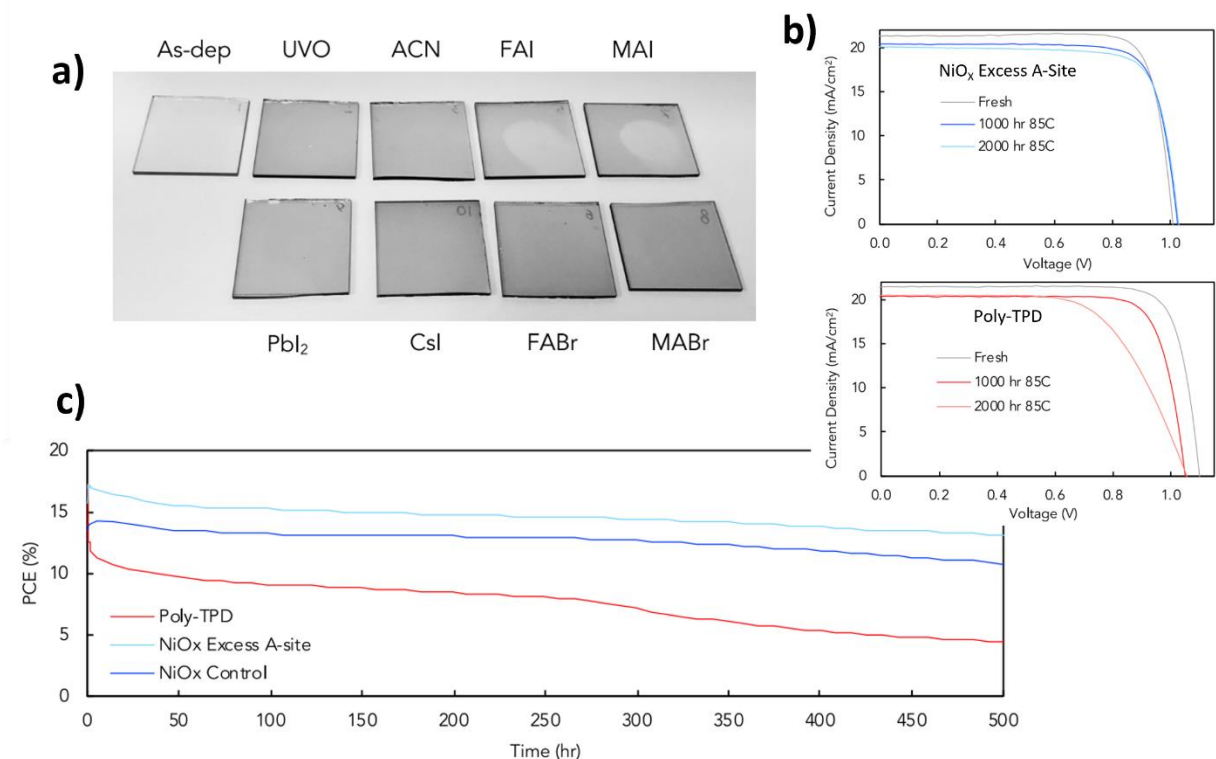

Figure 1.11: Characterization and Stability Analysis of NiO$_X$-Based Perovskite Solar Cells. *a) picture of a NiO$_X$ film as-dep and NiO$_X$ treated with UVO and various perovskite precursors (FAI, FABr, MAI, MABr, PbI$_2$, and CsI) dissolved in anhydrous acetonitrile. b) J-V curves of device based on NiOx/perovskite with A-site in excess (top graph) and poly-TPD/perovskite control solution (bottom graph) for different times at 85°C. c) Operational stability of unencapsulated perovskite solar cells based on either NiOx or Poly-TPD as HTM and a perovskite solution with or without A-site cation in excess. Stability test was performed under 0.77 sun intensity, at 55°C, under N$_2$ atmosphere.[114]*

Promising stability results have been demonstrated when exposing cells with spin-coated NiO$_x$ nanoparticles to various stresses (thermal,[43,74,115] damp heat,[74,116] light soaking[115,116] and temperature cycling).[74,75] Further reports show thermal and light-soaking stability for cells with NiO$_x$ deposited by atomic layer deposition[28] and sputtering.[96,117] However, some intrinsic issues remain in NiO$_x$-based perovskite devices, especially due to the reactive Ni^{3+} when in contact with the perovskite. By treating the NiO$_x$ surface with UV-ozone, the film becomes darker and the concentration of Ni^{3+} increases. As it can be seen of the Figure 1.11a, applying a FAI or MAI solution onto this oxidized film led to a discoloration of the NiO$_x$ surface to match the original as-deposited film. Boyd et al. showed that a redox reaction occurs at the interface between the Ni^{23+} from the NiO$_x$ and the cations from perovskites,[114] leading to the formation of an A-site deficient lead bromide/iodide phase at the surface. This defective surface accelerates interfacial recombination, thus reducing the V_{OC} of the cells. In fact, several studies attribute the limited achievable

V_{OC} with NiO$_X$ to non-radiative recombination at the NiO$_X$/perovskite interface.[118,119,87,120] In the same way, Peng et al. demonstrated that a passivation of the NiO$_X$ surface is required to decrease Ni^{3+} concentration at the NiO$_X$/perovskite interface and avoid redox reaction between I$^-$ from the perovskite and Ni^{3+} from the NiO$_X$.[121] They employed a thin layer of phenylethylamine iodide (PEAI) to neutralize the Ni^{3+} on the surface of sputtered NiO$_X$ through redox reactions. Others interlayers such as PN4N,[118] 1,3-bis(diphenylphosphino)propane (DPPP),[77] 4-iodo-2,3,5,6-tetrafluorobenzoic acid (I-TFBA)[122] or 4',4'''-(1,3,4-Oxadiazole-2,5-diyl)bis(N,N-bis(4-methoxyphenyl)-[1,1'-biphenyl]-4-amine)[123] can passivate the defects at the NiO$_X$/perovskite interface and enhance strongly the stability of the device. Additionally, to mitigate undesired redox reactions at the NiO$_X$/perovskite interface, Itzhak et al. proposed to protect the sputtered NiO$_X$ surface with a thin Ni$_y$N layer sputtered from a Ni target in Ar and N$_2$ gas flows.[113] This passivating layer protects the NiO/perovskite interface and avoids the reduction of Ni^{3+} ions. Moreover, Du et al. proposed a surface redox engineering method to stabilize the surface of the electron beam evaporated NiO$_X$. By doing an oxidation step of the surface with an Ar plasma followed by a reduction with nitric acid (HNO$_3$), they managed to eliminate the detrimental Ni^{4+} and -OH species while preserving Ni^{3+} and Ni^{2+}.[124] A deep understanding of this redox reaction at the NiO$_X$/perovskite interface as well as the development of strategy to delay this undesired reaction will be discussed in this thesis (Chapter 3 and 4).

1.4   Structure of the thesis

The thesis study the impact of two main tests, required by the IEC-61265 protocol, on PSCs performances. Chapters 3 and 4 focus on the damp heat test (performed at 85°C with 85% relative humidity), while Chapter 5 concentrates on the light soak test, involving prolonged exposure to continuous illumination and high temperatures. All the experimental details needed for this work can be found in Chapter 2. The thesis is organized as follows:

Chapter 2 describes the perovskite solar cell (PSC) fabrication process, from glass substrate to encapsulated devices, as well as the setups used for accelerated aging tests. Measuring instruments and methods used to characterize both devices and materials, in order to assess degradation mechanisms, are also presented.

Chapter 3 gives a deep understanding of NiO$_X$-induced degradation in PSCs. Characterized by S-shaped *J-V* curves, these devices exhibit a significant drop in performance after a few hours of <u>damp heat</u> (DH) test. Finally, this chapter demonstrates that temperature accelerates the degradation reaction and leads to chemical and property changes in the material.

Chapter 4 offers a robust and reproducible solution for addressing the stability issues presented in the previous chapter. By controlling the NiO$_X$ stoichiometry and enhancing film quality, devices with improved

DH stability were successfully demonstrated, passing over 5000 hours of DH testing, while maintaining a fill factor above 73%.

Chapter 5 provides an overview of the degradation mechanisms occurring under light (and heat) exposure in NiO$_X$-based PSCs. Through a layer-by-layer study, this chapter gives detailed insights into the degradation mechanisms taking place within the solar cell, from transport materials to contacts, thus emphasising the impact of each material of the cells. Additionally, it explores the influence of perovskite composition under light and heat. Finally, it investigates light and heat-induced degradation in complete devices and studies the role of one passivating molecule and one additive.

Chapter 6 summarize the key findings of this work and offers perspectives for future research in this field, with a view to bringing this technology into industrial application as soon as possible.

1.5   Contribution to the field

NiO$_X$ is the primary hole transport material used in the industry due to its efficient deposition process at low temperatures. It can be sputtered onto large areas, forming uniform layers. Understanding how NiO$_X$ behaves within perovskite solar cells (PSCs) offers essential insights into addressing potential industrial challenges. To move towards the commercialization of PSCs, these cells must pass degradation tests defined by the International Electrotechnical Commission. The two primary tests are damp heat (DH) and light soaking (LS). This thesis first investigates NiO$_X$ behavior under DH.

In the DH test, cells are placed in a climatic chamber at 85°C and 85% relative humidity. With proper encapsulation, this test essentially becomes a thermal test. However, this research reveals that NiO$_X$-based PSCs can degrade under temperature-induced stress. Advanced characterization techniques were employed to identify the source of this degradation. It was found that in inert environments and under thermal stress, the NiO$_X$ hole transport layer loses its p-type properties, and this degradation is irreversible. This extensive investigation resulted in a published paper, as first author, and can be find in the Chapter 3 of this thesis.

Furthermore, efforts to address this degradation have led to the development of a new deposition method, enabling the production of NiO$_X$-based PSCs capable of passing the DH test up to five consecutive times. Since the proposed strategies align with industrial methods, this research could pave the way for the integration of this technology into the photovoltaic energy market. This work resulted in peer-reviewed article as first author.

In parallel, industrial companies are urging researchers to swiftly tackle the challenge of light-induced degradation at elevated temperatures. This test is a major concern that must be resolved before solar cells can be commercialized and deployed worldwide. In this context, the behavior of cells under light soaking at 35°C and 65°C has been examined, and the importance of the encapsulation has been discussed. The final chapter presents relevant insights that should be implemented to pass this critical test.

In summary, this work offers valuable insights into the degradation pathways induced by the combination of light and high temperatures. It provides promising approaches and methods to mitigate this degradation. Additionally, the cells studied are suitable for tandem applications and are fabricated with layers compatible with industrial processes.

2. Experimental chapter

This chapter gives an overview of the materials, methods, and techniques used throughout the thesis to study the degradation of perovskite solar cells. It provides the detailed recipe of each perovskite solution used, the process of fabricating and encapsulating solar cells, methods and techniques employed for material and cell analysis. Additionally, it presents the specific setups used to study the degradation processes in detail.

2.1 Solar cells fabrication

2.1.1 Material

PbI_2 (99.99%), $PbBr_2$ (99.99%) and MeO-2PACz (>98.0%) were purchased from TCI, FAI and FABr (99.99%) from Dyenamo, CsI (99.99%) from Alfa Aesar, MABr from Greatcell Solar, 99.99%, C_{60} from Creaphys. All the other chemicals were purchased from Sigma-Aldrich.

2.1.2 Solutions preparation

$Cs_{0.17}FA_{0.83}Pb(I_{0.83}Br_{0.17})_3$ 10 % PbI_2 excess

The $Cs_{0.17}FA_{0.83}Pb(I_{0.83}Br_{0.17})_3$ perovskite solution was prepared in a glovebox by mixing three solutions. For the first solution, 1.5M of PbI_2 and 1.22 M CsI were dissolved in Dimethylsulfoxide (DMSO) at 70°C. For the second solution, 1.5M of PbI_2 and 1.22 M FAI were dissolved in Dimethylformamide (DMF):DMSO (4:1 as a volume ratio) at 70°C. For the third solution 1.5M of $PbBr_2$, 1.01 M FABr and 0.207 M CsBr were dissolved in DMSO. Once dissolved, the three solutions were mixed in the ratio 17:66:17. 100 µL of the mixed solution was spin-coated with a 2-step program: 10s at 1000 rpm with 200 rpm/s, then 37 s at 6000 rpm with 1000 rpm/s. 5s before the end of the program, 300 µL of ethyl acetate was quickly dripped on the sample. The as-deposited perovskite films were dried for 2 min at 60°C, then annealed for 30 min at 120°C inside the glovebox.

$Cs_{0.17}FA_{0.83}Pb(I_{0.83}Br_{0.17})_3$ with 0.5 % PbI_2 excess

The perovskite solution was prepared in the glovebox by dissolving 0.745 M of PbI_2, 0.255 M of $PbBr_2$, 0.169 M of CsI and 0.826 M of FAI in 2-methyl pyrazine (2-MP):DMSO (3:2). 100 µL of solution was spin-coated with a 2-step program: 10s at 1000 rpm with 200 rpm/s, then 25 s at 5000 rpm with 1200 rpm/s. 5s before the end of the program, 300 µL of chlorobenzene (CB) was quickly dripped on the sample. The as-deposited perovskite films were dried for 5 min at 60°C, then annealed for 30 min at 120°C inside the glovebox.

$Cs_{0.17}FA_{0.75}MA_{0.08}Pb(I_{0.87}Br_{0.13})_3$ with 0.5 % PbI_2 excess

The perovskite solution was prepared in the glovebox by dissolving 1.243 M of PbI_2, 0.217 M of $PbBr_2$, 0.254 M of CsI, 1.087 M of FAI and 0.109 M of MABr in DMF:DMSO (4:1). 100 µL of solution was spin-coated with a 2-step program: 5s at 500 rpm with 200 rpm/s, then 20 s at 5000 rpm with 1200 rpm/s. 15s before the end of the program, 300 µL of CB was quickly dripped on the sample. The as-deposited perovskite films were directly annealed for 30 min at 100°C inside the glovebox.

$Cs_{0.04}FA_{0.8}MA_{0.16}Pb(I_{0.83}Br_{0.17})_3$ with 0.7 % PbI_2 excess

The stoichiometric $Cs_{0.04}FA_{0.8}MA_{0.16}Pb(I_{0.83}Br_{0.17})_3$ perovskite solution was prepared in a glovebox by mixing the three following solutions. For the first solution, 1.43 M of PbI_2 and 1.36 M of FAI were dissolved in DMF:DMSO (4:1). For the second one, 1.43 M of $PbBr_2$ and 1.36 M of MABr were dissolved in DMF:DMSO (4:1). For the third one, 1.5 M of CsI was dissolved in DMSO. Once dissolved, the three solutions were mixed with 830:170:40 volume ratio. 100 µL of the mixed solution was spin-coated with a 1-step program: 35s at 3500 rpm with 2000 rpm/s. 15s before the end of the program, 300 µL of anisole was quickly dripped on the sample. The as-deposited perovskite films were annealed for 15 min at 100°C inside the glovebox.

In the case where pentaflourobenzylphosphonic acid (pFBPA) was used as an additive, 2 mM of it was added to the perovskite precursor.

$Cs_{0.05}(MA_{0.17}FA_{0.83})_{0.95}Pb(I_{0.83}Br_{0.17})_3$ used for mini-module fabrication.

The solution-processed was deposited according to Saliba et al.[34] The perovskite film was spin coated from a precursor solution of DMF/DMSO (4:1 v:v). Chlorobenzene was used as the antisolvent and dripped on the substrate before the end of the spin-coating step. Substrates were subsequently annealed.

2.1.3. Cells fabrication

<u>1 cm^2 single junction cell fabrication</u>

P-i-n single junction perovskite solar cells were fabricated on commercial 2.5 x 2.5 cm glass/ITO substrates (Kintec, sheet resistance 7 Ω/sq). A thin NiO_x layer was RF sputtered from a NiO_x or $Ni_{0.99}Cs_{0.01}O_x$ target (Disc AG, target diameter 100 mm) in an Oerlikon Clusterline cluster tool on top of ITO after an oxygen

plasma cleaning in a RIE chamber (power 250 W, O2 flow 50 sccm, working pressure 100 mTorr, time 60s). Both NiO_X and $Cs:NiO_X$ were sputtered at 150 W, under different gas flow: either in pure Ar (150 sccm) or in Ar/O_2 atmosphere (120 sccm Ar / 30 sccm $Ar_{0.95}$-$O2_{0.05}$). The chuck temperature was set to 60°C.Prior to device fabrication, NiO_X, O_2-NiO_X, $Cs:NiO_X$, and O_2-$Cs:NiO_X$ films were annealed in air at 300°C for 30 min. To make the NiO/organic HTM bilayers, solutions of various hole transporting layers were prepared and deposited by spin coating in a nitrogen-filled glovebox. 100 μl of filtered PTAA solution (2 mg/ml in toluene, 6000 rpm for 30 s, static spin-coating), 60 μL of Poly-TPD (2 mg/ml in chlorobenzene, 5000 rpm for 30 s, dynamic spin coating), or 70 μL of MeO-2PACz (1mM in ethanol, sonicated 15 min before use, 3000 rpm for 30s, static spin-coating) were dropped on the NiOx substrates and the organic films were then dried in the glovebox at 100°C for 10 min. For PTAA and poly-TPD based samples, 50 μL of filtered PFN-Br (0.5 mg/mL in methanol, 5000 rpm for 30s, dynamic spin-coating) was spin coated on top to improve the wettability of the perovskite. When employing SiO_X nanoparticles, 50 μl of a 0.2% weight solution of SiO_X-np, having a diameter of 20 nm, in ethanol was statically spin-coated at 2000 rpm. Films were annealed for 10 minutes at 100°C afterwards. The perovskite solution was spin coated using a program detailed above and annealed accordingly. 1 nm of LiF and 20 nm of C60 were thermally evaporated in an Angstrom evaporator at 400°C and 700°C respectively, with a deposition rate of 0.1 Å/s and 0.2 Å/s respectively (base pressure $5x10^{-8}$ mbar, working pressure 3-$4x10^{-7}$ mbar) and the thickness was monitored by dedicated quartz crystal microbalances. The substrate holder was held at room temperature. 10 nm of tin oxide ($SnO2$) was then deposited by atomic layer deposition (ALD) in a Oxford Instruments FlexAL ALD system at 100°C using Tetrakis(dimethylamino)tin(IV), (99.99%-Sn, Strem Chemicals) and water as precursors. 110 nm of ITO was then sputtered in a Oerlikon Clusterline cluster tool at 750W in a Ar/Ar-O2 flow (25/8 sccm) at 80°C. Finally, 120 nm of silver was evaporated at a rate between 0.2 and 1 Å/s through a shadow mask in a home-made evaporator.

<u>Mini-modules fabrication</u>

Mini-modules were fabricated on 5x5 cm^2 ITO glass (Kintec) following the same deposition methods as perovskite cells except for the top electrode. A stack of ITO (60 nm)/Ag (50 nm)/ITO (50 nm) as a top electrode was sputtered in a Oerlikon Clusterline cluster tool. The modules have 5 sub-cells and each sub-cell has a width of 7.2 mm. Laser patterning was performed with a Trumpf fs laser (515nm). The patterned withs of P1, P2 and P3 are 20, 115, and 110 μm, respectively. A geometric form factor was around 94.8% with a dead width of 373μm. An aperture area of module is 14.6cm^2.

2.1.4 Encapsulation

Encapsulation is necessary to pass the IEC 61215 stability tests, including thermal cycling (from -40°C to +85°C), damp heat test (1000h under 85°C and 85% humid air), and UV-light soaking (UV irradiation at wavelength between 280nm and 400nm at 15 kWh/m2). Thin film encapsulation or UV-cured epoxy edge seal are used by many research groups to encapsulate the device but are expensive and fragile. Glass-glass encapsulation with an edge sealant and a lamination foil is a more robust encapsulation method. The main barrier against moisture ingress is the edge sealant based on a butyl rubber. The lamination foil is required

to have a refractive index matching between the glass and the device and it may partially or completely block the UV light. It should not react with the cell or release chemicals that are harmful to the perovskite. EVA (ethylene vinyl acetate), the most used in silicon PV technology, cannot be adopted for perovskite because it releases with time acetic acid, which causes degradation of the perovskite. Surlyn is too stiff and causes delamination. On the contrary, polyolefin is not harmful to the perovskite and has a suitable elastic modulus.22

<u>Encapsulation method</u>

For damp heat and light soaking tests, the devices were encapsulated between two 5x5 cm^2 glasses, including a polyolefin DNP-CVF lamination foil and a butyl edge sealant (Helioseal PVS 101), after connecting adhesive conductive tape to the device terminals (Figure 2.1). The lamination process was carried out in a 3S laminator at 120°C with a maximum pressure of 0.6 bar.
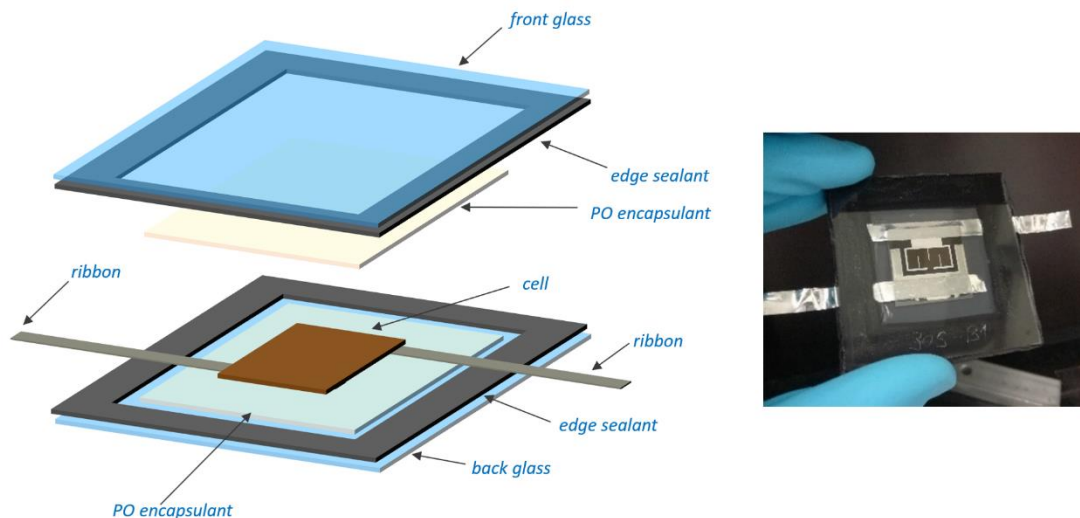

Figure 2.1 PSCs Encapsulation *Scheme*

2.2 Devices characterization

<u>The current density-voltage (*J-V*)</u> curves of perovskite solar cells were measured under simulated air mass AM1.5 G spectrum with an irradiance of 1000 W/m^2 using a Wacom two-lamps (Ha and Xe) AAA class sun simulator. A mask with an aperture area of 1.04 cm^{-2} was used to define the active area of the solar cell. Reverse and forward *J-V* scans were measured from -0.2 V to 1.2 V with a scan rate of 100 mV/s, before and after tracking the maximum power point of the cell for 300 s. Low-light *J-V* measurements were also done using neutral density filters. For *J-V*(T) measurements, a Peltier controller was used to vary the temperature of the measured device. The external quantum efficiency of the cells was measured with a

home-built lock-in amplified (Stanford-Research) spectral response set-up in J_{SC} condition, under a monochromatic halogen light source emitting from 230 to 800 nm.

External quantum efficiency (EQE) spectra were obtained using a custom-made spectral response setup. The cells were illuminated, at J_{SC} conditions, with a chopped light thanks to a grating monochromator. The response of the samples was recorded using two lock-in amplifiers. The light beam was subjected to modulation at a frequency of 217 Hz and had a beam size of 2 mm². No bias light was applied during the measurement.

1D drift-diffusion simulations were performed on SCAPS-1D software.[125] A NiO_x-based perovskite solar cell model was built including absorptance file measured on our NiO_x, with a band gap of 3.66 eV.

Photoluminescence peak measurements were performed on a MonoVista CRS+ instrument from Spectroscopy & Imaging GmbH. A green laser with a wavelength of 514 nm was employed.

Photoluminescence mapping PL images were acquired in a custom setup. The setup is based on two LED types: blue (450 nm Osram GD CS8PM1.14) for perovskite excitation, and infrared (850 nm Osram SFH 4715AS) for silicon excitation. The imaging is performed by a ThorLabs Kiralux 1.3 MP NIR-Enhanced CMOS Camera, with selectable filters to block the excitation illumination. The incident photon flux is about 10 mA/cm2 for the blue illumination and 25mA/cm2 for the infrared illumination.

The high-resolution images were acquired by a Micro Vu Vertex 311 UC dimensional analysis station. It combines a 2D translation stage and a camera. It performs multiple image acquisitions at different positions and reconstructs the full image. It can perform images in transmission, and under dark field and bright field (axial) illumination. The imaging system uses red LEDs for illumination and a grayscale camera.

2.3 Films characterization

Absorptance spectra were calculated from the total transmittance and total reflectance spectra measured with a PerkinElmer Lambda 950 UV-VIS-NIR spectrophotometer equipped with an integrating sphere. Film thicknesses were measured with both a profilometer (KLA-Tencor P-15 Profiler) and an ellipsometer (J. A.Woollam Co).

High-resolution X-ray photoelectron spectroscopy (XPS) depth profile measurements were conducted using an Axis Supra instrument, from Kratos Analytical, which utilized a monochromatic Al Kα X-ray source. The pass energy was configured at 20 eV with a 0.1 eV step size. To minimize charging effects, the samples were appropriately electrically grounded. Etching of the sample was accomplished using an argon ion beam. The oxidation states of NiO were determined through fitting components corresponding to the electronic states of N^0 (from Ni metal), Ni^{2+} (from the cubic rock-salt structure NiO), and Ni^{3+} (from the NiOOH), following the methodology outlined by Biesinger et al.[126,127]

The measurements and fitting were done by Dr. Mounir Mensi. His contribution is gratefully acknowledged.

X-ray reflectivity (XRR) and grazing incidence X-ray diffraction (GI-XRD) measurements were conducted using a Panalytical X'Pert MRD diffractometer equipped with a parallel beam mirror and a point detector. In the XRR measurement the incident beam slit was set to 1/32° and a 0.04 rad Soller slit was used at the detector side to minimize X-ray beam divergence. The measurements were performed in a 2θ range of XXX-YYY with a step of ZZZ. Data analysis and fitting were carried out using the X'Pert Reflectivity software. For the XRD measurements, the incident beam slit setting was 1/2°. The measurements were conducted in a 2θ range of XXX-YYY with a step of ZZZ.

XRR, GI-XRD and some of the XRD measurements, fitting and analyses were performed by Dr. Ivan Marozau.

Tauc plot: In Chapter 5, the perovskite absorber band gap was calculated using Tauc plots based on UV-Vis spectroscopy. The intercept on x-axis of the $(\alpha h v)^2$ vs hv plot provides the band gap value (α is the absorption coefficient calculated from UV-Vis, and $hv = 1240/\text{wavelength}$ is the photon energy).

Atomic force microscopy (AFM) measurements were carried out using a Digital Instruments Nanoscope 3100 system manufactured by Bruker. An AdvanceTEC cantilever with a spring constant of 45 N/m from Nanosensors was employed for these measurements in an ambient air environment. The samples were securely positioned on an x, y, z stage for stability. The scanning process was performed at a speed of 0.6 Hz, covering a scan range of 5 µm.

Secondary electron microscopy (SEM) images were taken using a Zeiss Gemini 2 microscope, which was equipped with an Energy-Dispersive X-ray (EDX) detector. The microscope typically operated with a 3 keV incident electron beam. To obtain the top view images, the samples were horizontally fixed to a holder using conductive tape.

SEM images were taken by Dr. Quentin Jeangros and Dr. Florent Sahli.

Transmission electron microscopy (TEM) analysis: NiOx films were sputtered on Si TEM supports with 10 nm-thin SiN windows, before then annealing some of the films at 300 °C. The films were then analysed at 200 kV by transmission electron microscopy, namely by selected area diffraction, scanning TEM bright-field and high-angle annular dark-field imaging and energy-dispersive X-ray spectroscopy in a FEI Tecnai Osiris operated at 200 kV. STEM EDX was performed using four windowless Super-X SDD EDX detectors integrated into the pole piece with 0.9 srad solid angle.

TEM measurements and analyses were performed by Dr. Quentin Jeangros.

Electrochemical impedance spectroscopy was carried out on 100 nm-thick NiO_x films deposited on ITO using a Bio-Logic SP-300 potentiostat with a built-in EIS function, following a reported procedure.[128] A sinusoidal 15 mV AC signal that was scanned between 1 Hz and 1 MHz was superimposed on each DC potential step. The measurements were performed in a 3-electrode configuration using a Ag/AgCl (sat. KCl) reference electrode, a graphite rod counter-electrode and the NiO_x on ITO as working electrode, in an

aqueous solution with 50 mM $K_3Fe(CN)_6$, 350 mM $K_4Fe(CN)_6$, 1 M Na_2SO_4 (pH 8.4). The applied potential was converted to the reversible hydrogen electrode (RHE) using the Nernst equation (1):

$$V_{RHE} = V_{Ag/AgCl} + 0.059 \times pH + 0.197 \qquad (1)$$

The EIS data were modelling with the Zview software (Scribner Associates) using a Randles circuit. For each NiO_x condition, the measurement was repeated on 3 samples and the average capacitance was taken for the Mott-Schottky plots. In the linear region of Mott–Schottky plot, a simple linear regression model (2) was applied to perform Mott–Schottky analysis:

$$C^{-2} = \frac{2}{q\varepsilon\varepsilon_0 A^2 N_A}\left(V - V_{fb} - \frac{kT}{q}\right) (2)$$

where C is capacitance, q is elementary charge, ε is dielectric constant (taking 12 for NiO_x),[129] ε_0 is vacuum permittivity, A is surface area, N_A is acceptor density, V is applied potential, V_{fb} is flat-band potential which is the electrochemical potential at which there is no band bending, equaling the semiconductor Fermi level divided by the electron charge, k is Boltzmann constant and T is absolute temperature.

The measurements and fittings were performed by Dr. Yongpeng Liu.

2.4 Accelerated aging tests

2.4.1 Damp Heat

Damp heat degradation test on glass-glass laminated devices were run in a Weiss Technik Temperature&Humidity test chamber set at 85°C and 85% relative humidity.

2.4.2 Solar Simulators

The so-called Cicci chamber is a LED-light-soaker made by Cicci Research (Figure 2.2). Spectrum is calibrated using a photodetector reference cell and UV, VIS, IR intensity can be changed separately. The spectrum is presented Figure 2.4. Unencapsulated cells were placed in a sealed box under a continuous N_2 flow. A temperature controller was set at 25°C, while the actual temperature of the cells under light was 35°C. The Arkeo all-in-1 setup consist of 16 channels in which 4 cells can be connected. Various programs, including Maximum Power Point Tracking (MPPT), can be employed during the light soaking tests and periodic *J-V* scans can be conducted throughout the test. For MPPT tests, cells were placed on a holder

inside the chamber and connected to different channels. Periodic *J-V* scans were also conducted throughout the test. For the open-circuit measurements, cells were simply placed of the floor of the chamber.
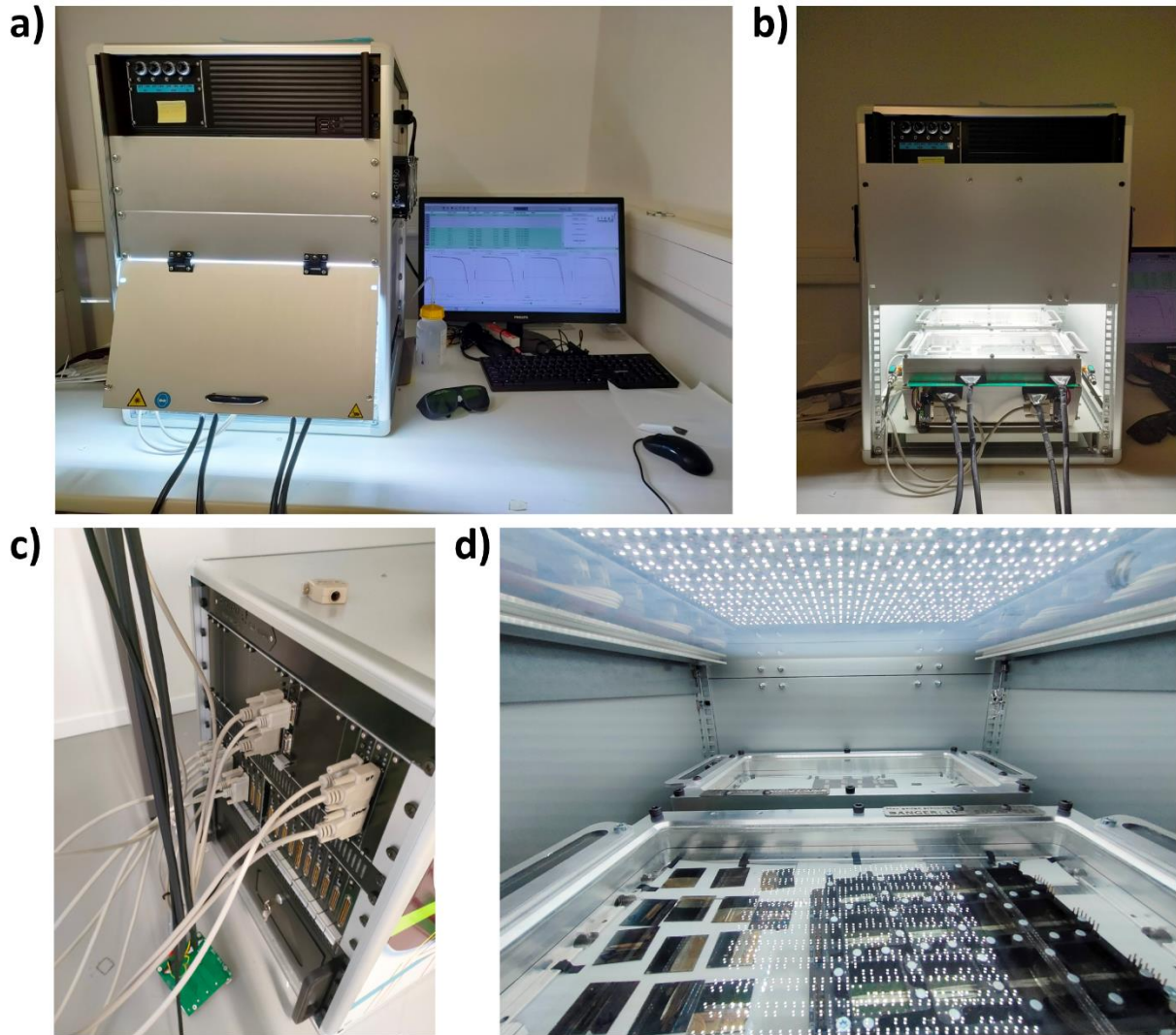

Figure 2.2: Cicci Light-Soaker Setup. *a) Cicci set-up, b) Cicci light soaker with the two sealed chambers, c) multichannel hardware, d) picture inside the light soaker, with the LEDs array on top and samples in the chambers on bottom.*

Light soaking at 65°C was carried out in the so-called Solaronix chamber, in ambient air (Figure 2.3). This system is composed of continuous light sources, such as a plasma lamp and additional halogen lamps, which are fitted with highly efficient reflectors to provide uniform and diffuse illumination to the sample area. The intensity of the lamps can be controlled using the Fadec software. The spectrum is presented Figure 2.5. Throughout the tests, the solar modules were exposed to steady light at an irradiance level of 1000W/m^2. Prior to the test, cells were encapsulated using the method described above. A chiller set at 50°C was used to keep the device temperature at 65°C. For open-circuit measurements, cells were directly placed in the chamber, on a water-cooled aluminum plate, while for MPPT, the Arkeo setup was used, and cells were connected to the channels via cables.
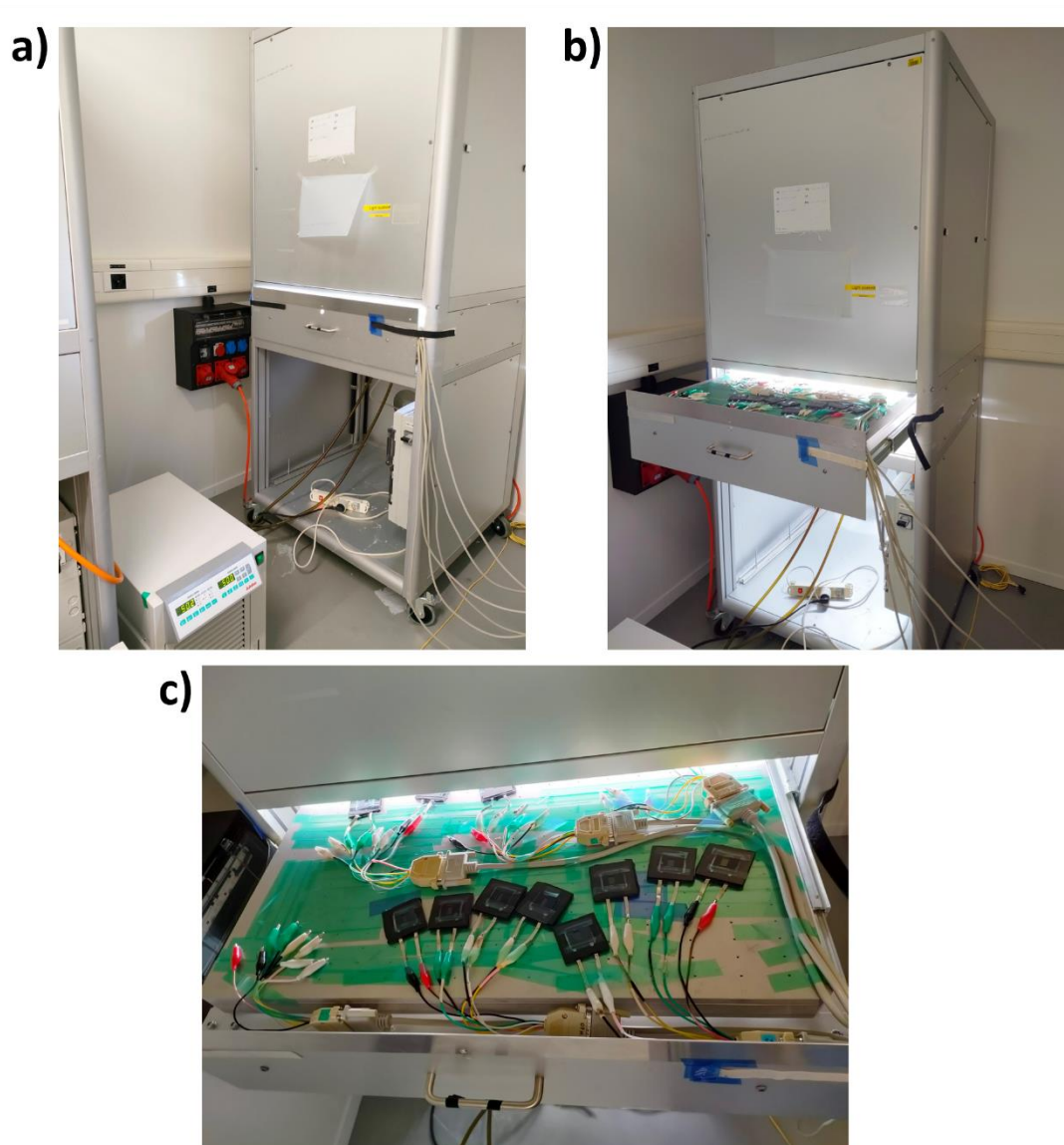

Figure 2.3 Solaronix Lght-Soaker Setup. *a) Solaronix chamber, with the chiller on the lef end side of the picture, b and c) pictures of the encapsulated cells connected to the Arkeo MPPT program.*
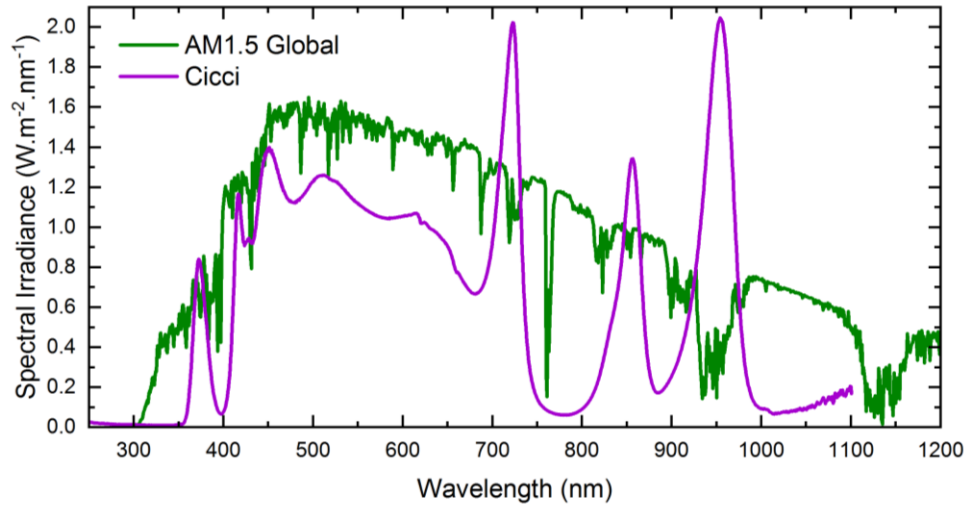
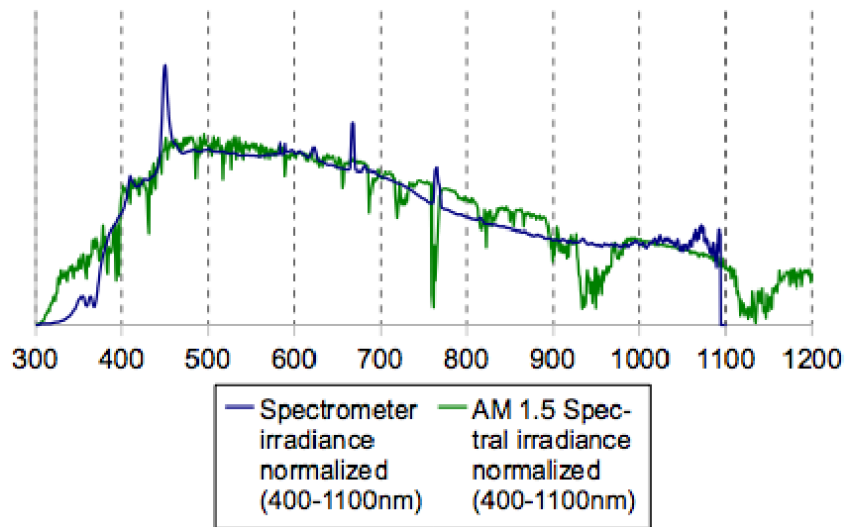**Figure 2.4: Cicci and AM1.5 Global Spectra**

Figure 2.5: Solaronix and AM1.5 Global Spectra

3. Understanding and Mitigating the Degradation of Perovskite Solar Cells based on a Nickel Oxide Hole Transport Material During Damp Heat Testing

Abstract

The development of stable materials, processable on large areas, is a prerequisite for perovskite industrialization. Beyond the perovskite absorber itself, this should also guide the development of all other layers in the solar cell. In this regard, the use of NiO_X as a hole transport material (HTM) offers several advantages, as it can be deposited with high throughput on large areas and on flat or textured surfaces via sputtering, a well-established industrial method. However, NiO_X may trigger the degradation of perovskite solar cells (PSCs) when exposed to environmental stressors. Already after 100 hours of damp heat stressing, a strong fill factor (*FF*) loss appears in conjunction with a characteristic S-shaped *J-V* curve. By performing a wide range of analyses on cells and materials, completed by device simulation, the cause of the degradation is pinpointed, and mitigation strategies are proposed. When NiO_X is heated in an air-tight environment, its free charge carrier density drops, resulting in a band misalignment at the NiO_X/perovskite interface and in the formation of a barrier impeding holes extraction. Adding an organic layer between the NiO_X and the perovskite enables higher performances but not long-term thermal stability, for which reducing the NiO_X thickness is necessary.

3.1 Introduction

Since 2009, the efficiency of perovskite solar cells (PSCs) has steadily improved, reaching 26.1%,[10] rivaling silicon-based solar cells, although at much smaller device size. Perovskite/silicon (PK/Si) tandem architecture is a promising route to low-cost devices that can surpass the efficiency limit of Si single-junction solar cells.[7] To be commercially viable, PSCs must demonstrate stability, especially for tandem applications. Meeting standard degradation tests, like damp heat, UV-light soaking, and thermal cycling, is essential. Vacuum-deposited hole transport materials (HTM), like NiO$_X$, offer scalability[98] and conformal deposition for efficient large-area devices.[81,96,97,99] NiO$_X$, being naturally p-type doped,[100–102] is suitable for charge carrier selectivity. Promising stability results have been observed with NiO$_X$ in various stress conditions, but challenges remain due to redox reactions at the NiO$_X$/perovskite interface, which affect cell performance.[114] This chapter focuses on the understanding of the NiO$_X$-based PSCs degradation under damp heat test, and proposes solutions to mitigate this degradation.

3.2 Experimental details

The main advantage of employing NiO$_X$ as HTM lies in the film uniformity and high yield of working devices (i. e. not shunted) when scaling the fabrication to larger cells (> 1 cm^2) and modules, compared to organic HTMs, which are typically only a few nm thick and thus more prone to pinholes. To combine the coating uniformity of the NiO$_X$ with the lower non-radiative recombination of organic HTMs, a bilayer stack based on NiO$_X$ and a self-assembled monolayer (SAM) is used. Indeed, the phosphonic acid in the organic HTM, MeO-2PACz, is expected to bind conformally and uniformly to the NiO$_X$ surface to lead to a pinhole-free HTM bilayer,[130] while at the same time, pinholes in the SAM film would not be critical, as the underlying NiO$_X$ prevents shunting.[131]

For this study, a 1. 63 eV band gap Cs$_{0.17}$FA$_{0.83}$Pb(I$_{0.83}$Br$_{0.17}$)$_3$ perovskite light absorber was chosen due to its intrinsically good thermal stability and resilience against moisture.[74,75,116] RF sputtered NiO$_X$, MeO-2PACz SAM,[83] and a bilayer NiO$_X$/MeO-2PACz[131] were use as HTM. Prior to device fabrication, the RF-sputtered NiO$_X$ layer was annealed in air at 300°C for 15 minutes. This step slightly increases the crystallinity of the layer (small variation in peak intensity and similar crystallographic contrast and grain size according to transmission electron microscopy, in Figure 3.1) but mainly decreases its absorptance and makes its surface more hydrophilic. The p-i-n stack was completed in a semi-transparent design (LiF/C$_{60}$/SnO$_2$/ITO/Ag top stack) compatible with tandem implementation. A sketch of the device stack is displayed in Figure 3.2a. For the damp heat test, devices were encapsulated in a glass/glass packaging, as described in Chapter 2, section 2.1.4.
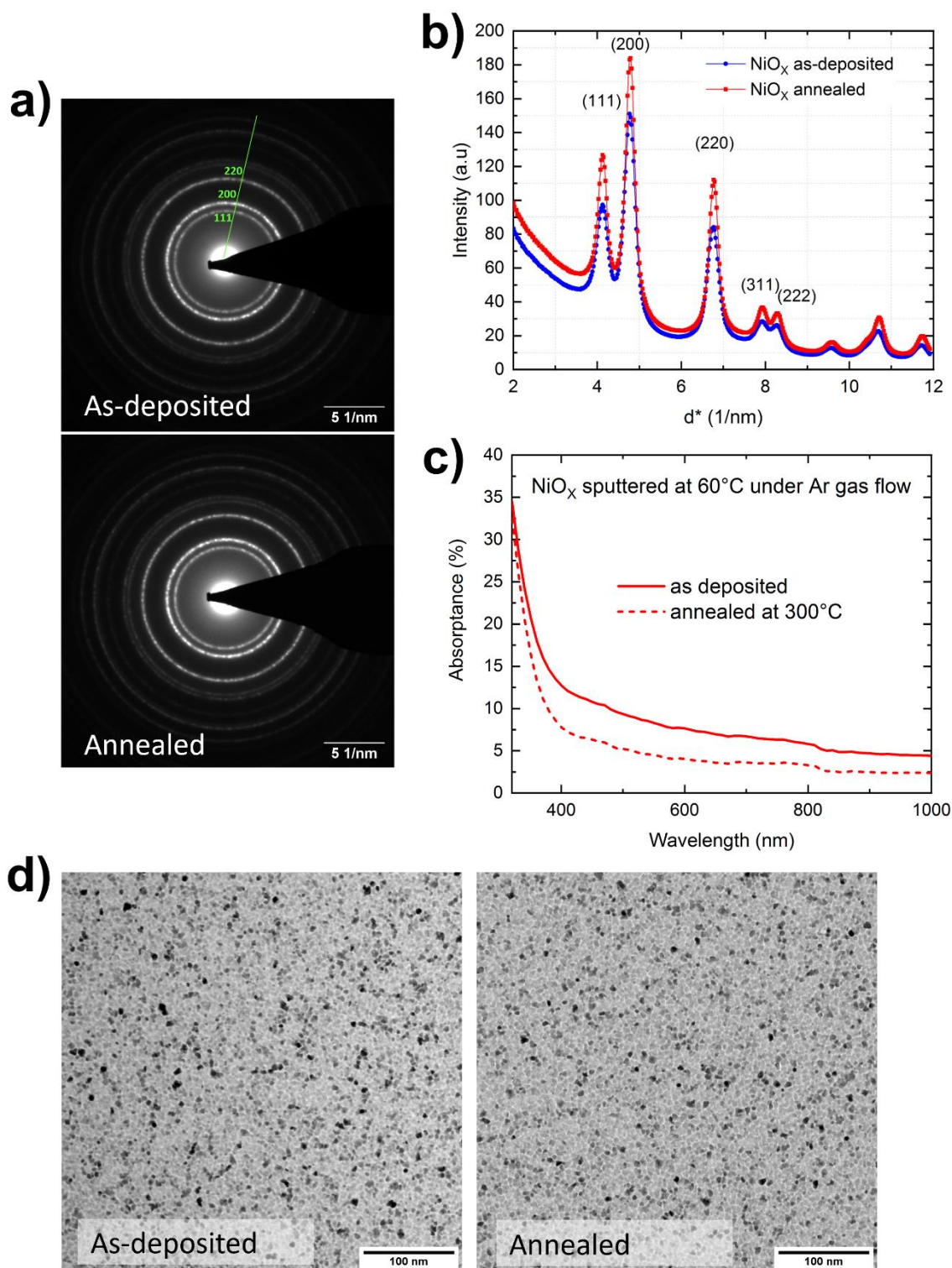
Figure 3.1:Characterization of NiOₓ Thin Films. *a) selected-area electron diffraction (SAED) patterns of 20-nm thick NiOₓ film deposited on a Cu/C TEM grid, b) radial profile plot of both as-deposited and annealed NiOₓ crystalline planes extracted from the SAED patterns. Each set of lattice planes is labelled. c) absorptance spectra of NiOₓ film on glass before and after*

annealing at 300°C in ambient air. d) Scanning transmission electron microscopy (STEM) bright-field imaging of 20-nm thick NiOX film deposited on a Cu/C TEM grid.

3.3 Results and discussion

3.3.1 Initiale performances

The highest efficiencies for these semi-transparent cells (1.04 cm^2) were obtained using MeO-2PACz, reaching a PCE close to 16%, thanks to a high V_{OC} up to 1120 mV (Figure 3.2b and Figure 3.3). However, when increasing the device area from 1 cm^2 to about 14 cm^2, an inversion of the trend is observed. The devices containing NiO$_X$ (with or without a MeO-2PACz layer) outperformed the MeO-2PACz-only devices,
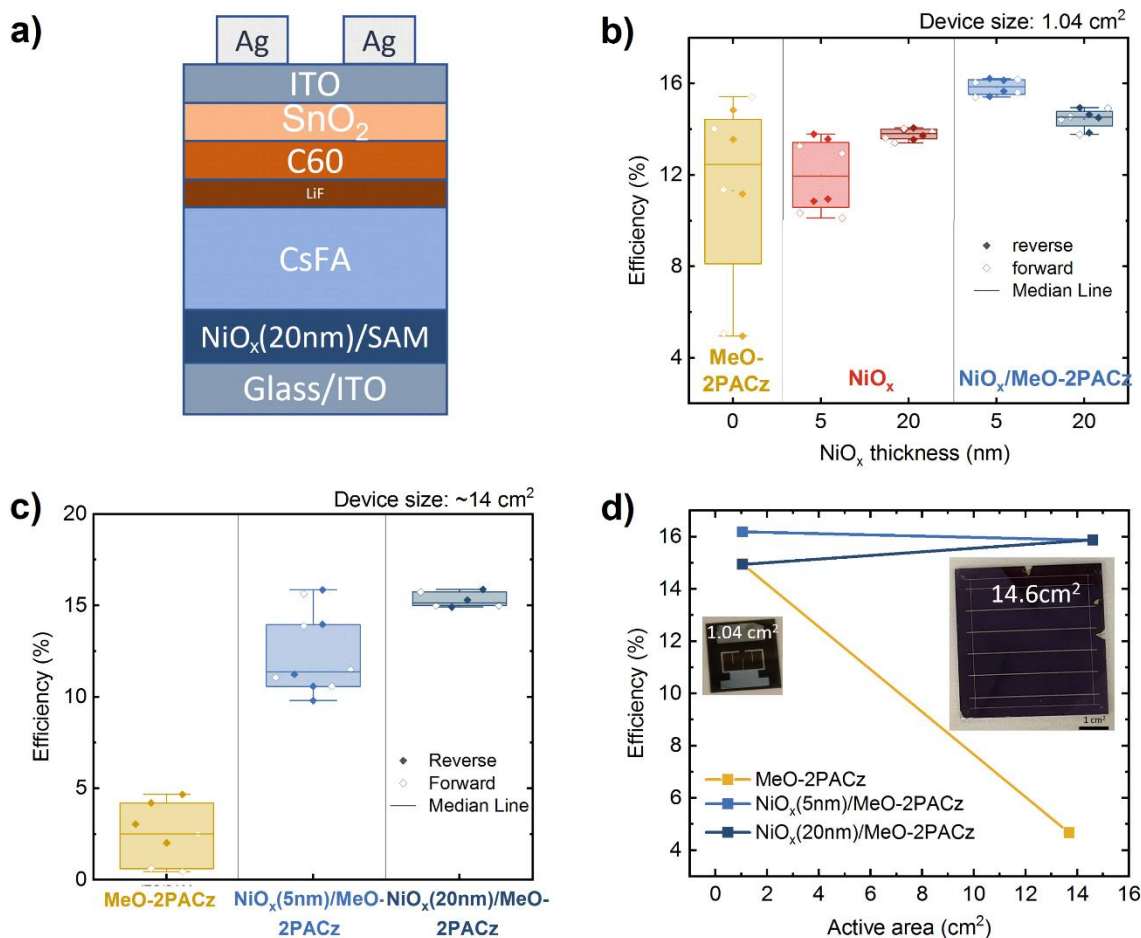

Figure 3.2: Efficiency and Structure Analysis of Perovskite Solar Cells and Mini-Modules. *a) Structure of the p-i-n PSC studied. Devices efficiency of b) 1 cm^2 semi-transparent PSCs and c) 14 cm^2 perovskite mini-modules for various HTM stacks, and d) efficiency of champion perovskite devices for different HTM and active area size. Pictures of the 1.04 cm^2 and 14.6 cm^2 semi-transparent perovskite solar devices on 2.5 x 2.5 cm and 5 x 5 cm glass substrates are also presented.*

mainly due to electrical shunts affecting the latter (Figure 3.2c and Figure 3.4). In conjunction with the wider spread of efficiencies in small area devices, incomplete coverage of the transparent conductive oxide (TCO) by the MeO-2PACz is most probable, leading to shunts which are more likely to occur on larger area devices (Figure 3.2b and c). Indeed, even on small cells (1 cm^2), the proportion of shunted devices is much higher when MeO-2PACz is used alone as HTM rather than in a bilayer with NiO$_X$. At low illumination, all devices based on MeO-2PACz show shunts while those with the bilayer 20 nm NiO$_X$ /MeO-2PACz show perfect diode behaviour (Figure 3.4a). From these results, the use of a continuous sputtered NiO$_X$ underlayer is required for reproducibility and upscaling. The best average performance for the minimodule (5 segments in series) was obtained for the bilayer structure consisting of 5 - 20 nm sputtered NiO$_X$ in combination with MeO-2PACz. Reducing the thickness of the sputtered NiO$_X$ to 5 nm yielded the highest *FF*s and efficiencies for both small and large area devices. However, a likely incomplete coverage of the thin NiO$_X$ still led to a significant yield scattering on 14 cm^2 minimodules in the case of 5 nm NiO$_X$ (Figure 3.2c, d). Figure 3.4 highlights that with 5 nm NiO$_X$ /MeO-2PACz the shunt resistance of the cells increases compared to MeO-2PACz only, but less than for 20 nm NiO$_X$ /MeO-2PACz. This entails that the best compromise between efficiency, scalability and reproducibility is obtained when combining 20 nm NiO$_X$ with MeO-2PACz.
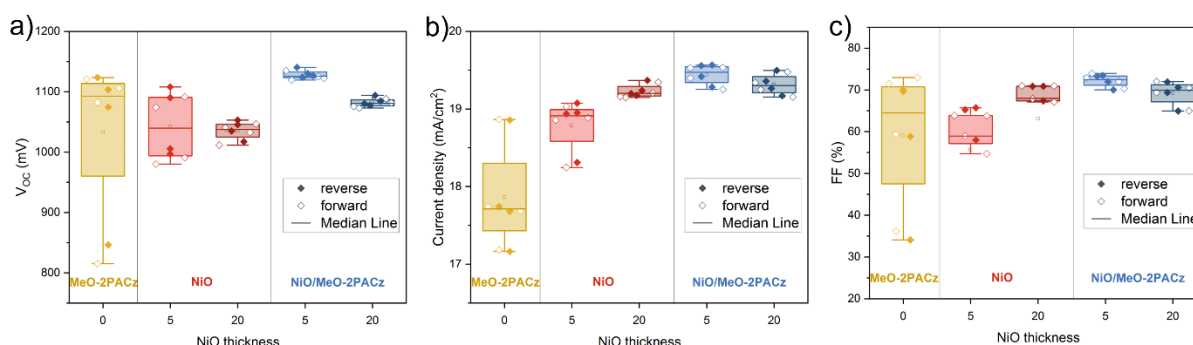

Figure 3.3: J-V parameters of the 1.04 cm² cells presented in Figure 3.2. *a) V$_{OC}$, b) J$_{SC}$ and c) FF.*
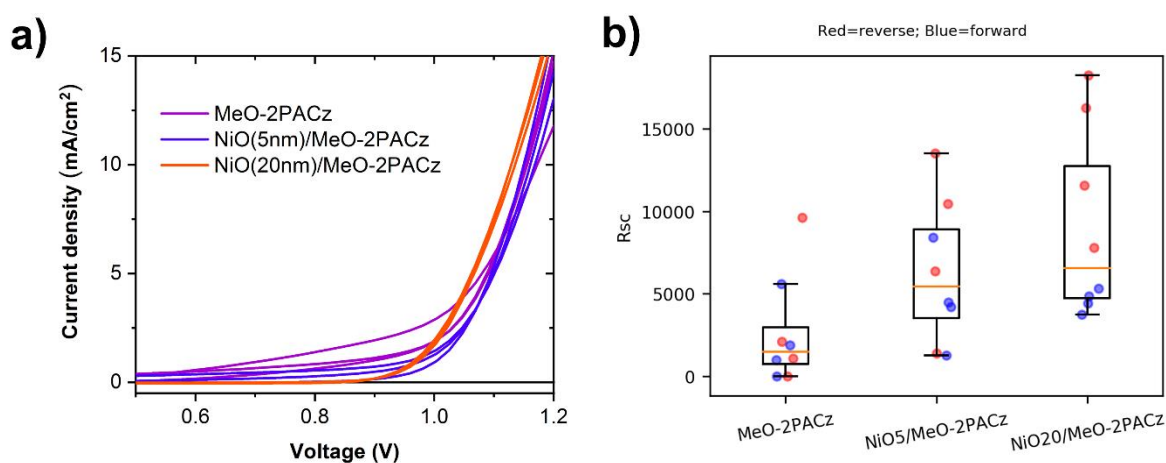

Figure 3.4: Effect of the HTM Choice on Shunt Resistance in Semi-Transparent Perovskite Solar Cells. *a) Dark reverse J-V curves of semi-transparent 1cm^2 PSCs based on MeO-2PACz (purple curves), NiO(5nm)/MeO-2PACz (blue curves), and NiO(20nm)/MeO-2PACz (red curves) as HTM; b) shunt resistance of those same cells under 1 sun. As it can be seen, the NiO$_X$ layer helps increasing the shunt resistance.*

3.3.2 Solar cell thermal stability

Reliability tests were performed on the aforementioned devices by subjected them to prolonged damp heat (DH) tests in accordance with IEC 61215 standard tests (85°C and 85% relative humidity, for 1000 h in the dark). To withstand the test, the samples were encapsulated between 2 glasses with a moisture-blocking edge seal and a thermoplastic polyolefin sheet on each side of the device as lamination foil (Figure 3.5a and Chapter 2, section 2.1.4). Previous examples with similarly sized cells (~1 cm^2) using such a lamination have shown little to no degradation over 1000h.[74] The results are presented in the Figure 3.5: J-V curves before (solid lines) and after the DH test (dashed lines) are plotted in Figure 3.5b, whereas the evolution of the efficiencies at different DH times is shown on the Figure 3.5c. The MeO-2PACz devices retained 95% of their initial efficiency after the test, with only a small drop in FF (Figure 3.5Figure 3.5:, blue curve). The other two combinations degraded rapidly within the first 500 h, primarily through a loss in FF and J_{SC} (Figure 3.5, pink and purple curves). The degraded devices exhibited a pronounced S-shape and finished the test at 40% of their initial efficiency. Complementary tests using polymeric HTM such as Poly[bis-(4-phenyl)-(2,4,6-trimethylphenyl)-amin] (PTAA) and Poly(N,N'-bis-4-butylphenyl-N,N'-bisphenyl)benzidine (Poly-TPD) also resulted in minimal loss of FF after 1000 hours of damp heat (Figure 3.6), indicating that the degradation is mostly linked to the presence of NiO$_X$ in the system.
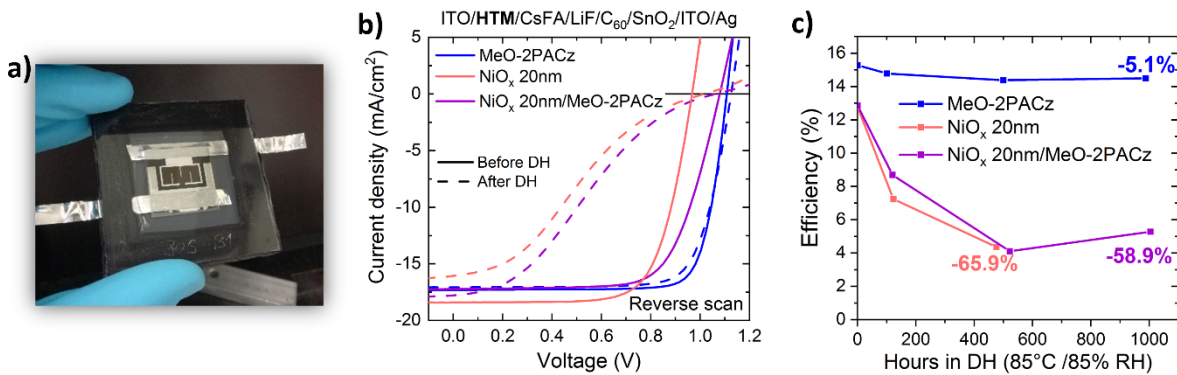

Figure 3.5: Damp heat stability results of PSCs for various HTM: a) Encapsulated 1.04 cm^2 semi-transparent PSC. (b) reverse J-V curves just after encapsulation (solid lines) and J-V curves of the same cells after 1000h in the DH chamber (85°C / 85% RH, dashed lines). (c) efficiency of the encapsulated cells (from J-V) during DH stress and percentage of efficiency losses at the end of the DH test.
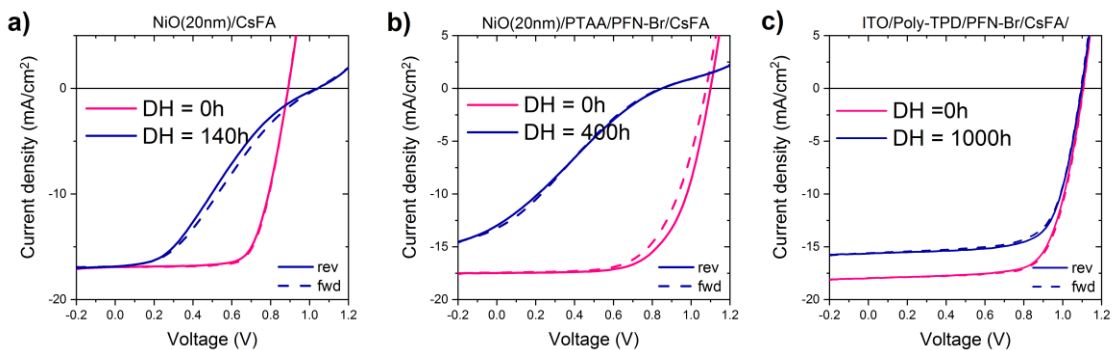

Figure 3.6: J-V curves of semi-transparent PSCs before and after DH degradation as a function of the HTM: a) NiO(20 nm), b) NiO(20 nm)/PTAA/PFN-Br, c) Poly-TPD/PFN-Br. Stack: ITO/HTM/CsFA/LiF/C$_{60}$/SnO$_2$/ITO/Ag. Active area: 1.04 cm^2.

The origin of the *FF* losses was then investigated. Boyd et al. showed that a redox-reaction between Ni^{3+} and the organohalides causes the formation of an amorphous inorganic PbX$_2$ layer at the interface, which reduces the V_{OC} of the cell.[114] The authors mitigated the formation of the PbX$_2$ layer by compensating the lost organohalides through the addition of ~3% additional organohalides. This strategy was adopted, and the stability of cells was tested with various organohalide concentrations (in this case FAI) in the precursor ink (Figure 3.7a, b, and c). Cells with an excess of FAI indeed showed a higher open-circuit voltage (but worse *FF* and *J$_{SC}$*), whereas stoichiometric and PbI$_2$-rich samples showed better *FF* and *J$_{SC}$* but a lower V_{OC}. During DH testing, in all cases, a thermally activated degradation occurred, with a stronger degradation for the organohalide-rich composition. It has been further verified whether the overall perovskite formulation impacts the degradation mechanism by varying its composition. Absorbers with different bandgaps were investigated, testing the impact of I/Br ratio and methylammonium was introduced to form a triple-cation perovskite absorber (Figure 3.7d and e), varying the A site composition. Finally, the impact of the preparation method was also analyzed: solution-processed absorbers were compared to perovskites produced using a hybrid method, where CsBr and PbI$_2$ were co-evaporated, followed by spin coating of a FAI/FABr solution, and interdiffusion during subsequent annealing (Figure 3.7f). Likewise, bilayer devices with NiO$_X$ were fabricated in combination with PTAA or MeO-2PACz SAM and tested in the same conditions (Figure 3.7d and e). In all the above cases, the degradation proceeded at a comparable rate within the first 100 h of DH. It was concluded from these experiments that the degradation proceeds irrespective of the deposition method, or the exact composition and nature of the organohalides (MA or FA, I or Br), and is accelerated with an excess of organohalide in the system. The presence of an interlayer between the NiO$_X$ and the perovskite also does not prevent this degradation. The fact that the degradation proceeds faster at elevated temperatures, indicates that it is a thermally accelerated process (at room temperature, encapsulated devices show a similar degradation but after several weeks).
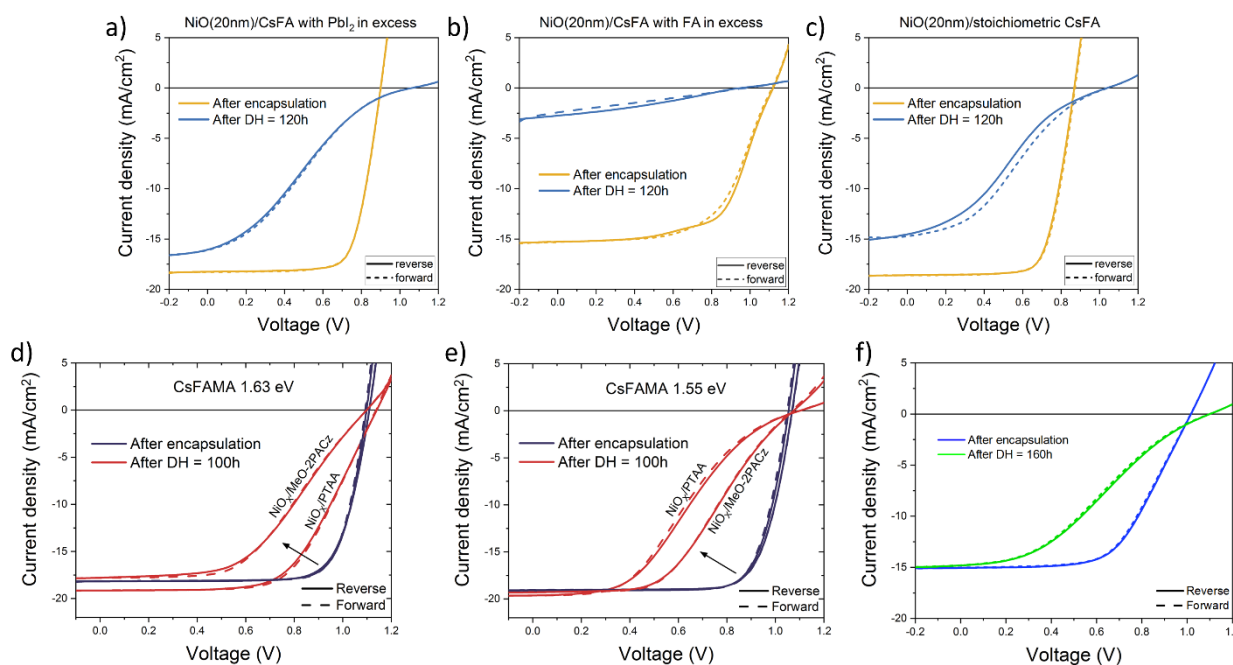

Figure 3.7: J-V curves of semi-transparent PSCs before and after DH degradation for various perovskite compositions and HTMs: *a) CsFA with PbI$_2$ in excess, b) CsFA with FA cation in excess, c) CsFA stoichiometric, d) CsFAMA with 17% of Br*

leading to a band gap of 1.63eV, e) CsFAMA with 5% of Br for a band gap of 1.55eV, f) hybrid-processed perovskite (CsBr/PbI$_2$ template first evaporated then FAI/FABr spin coated). Stack a, b, c, f: ITO/NiO(20 nm)/Perovskite/LiF/C$_{60}$/SnO$_2$/ITO/Ag. Stack d, f: ITO/NiO(20 nm) + MeO-2PACz or PTAA/CsFAMA/LiF/C$_{60}$/SnO$_2$/ITO/Ag. Active area: 1.04 cm^2.
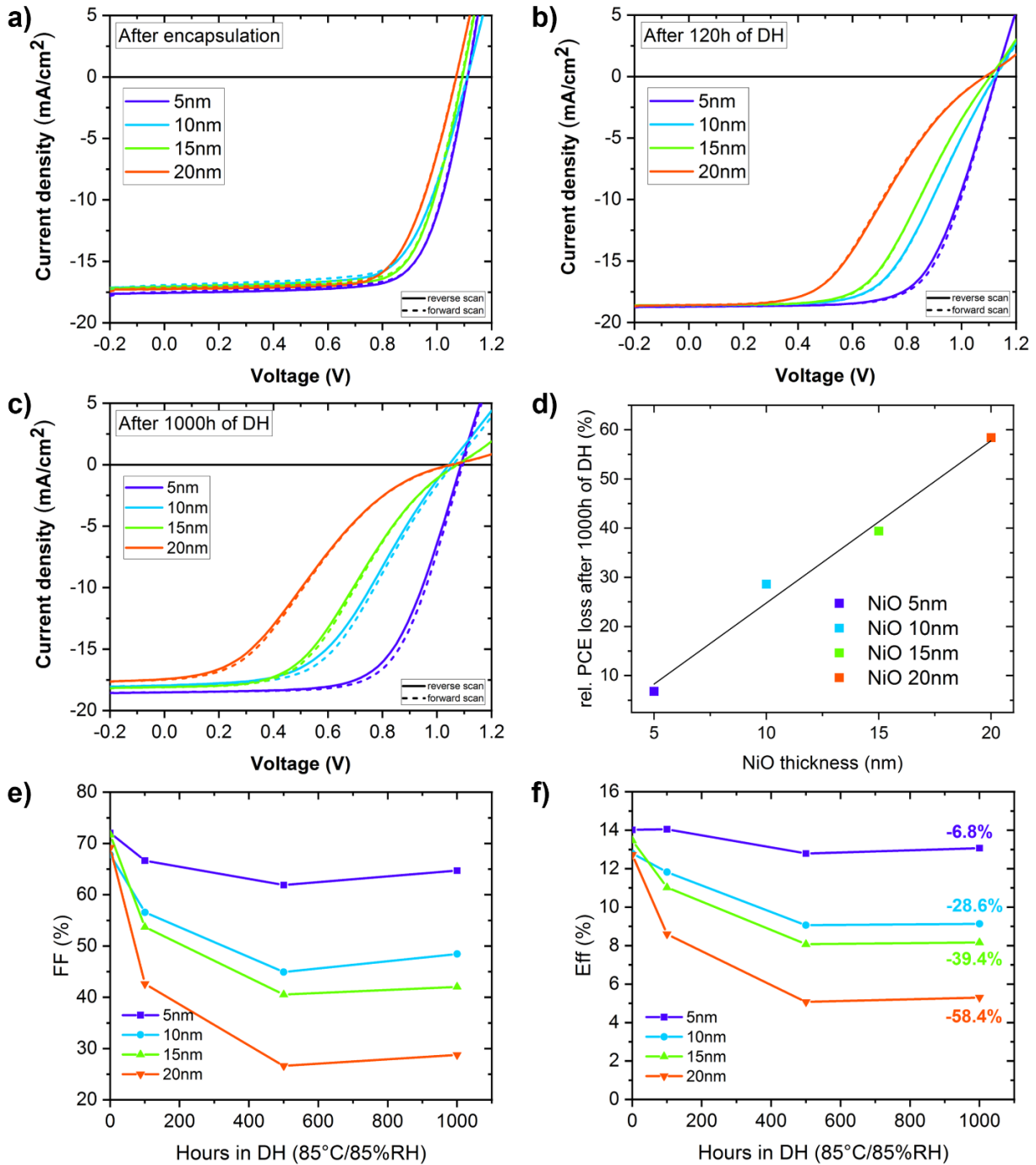

Figure 3.8: DH degradation of encapsulated cells based on NiO$_X$/MeO-2PACz for different thicknesses of the NiO$_X$ (5-10-15-20 nm). *J-V curves of the cells a) before starting the DH test, b) after 120 h into DH; c) after 1000 h into DH, d) relative efficiency loss after 1000 h of DH as a function of the NiO thickness, e) fill factor and f) efficiency plots of those same cells throughout the test.*

Next, the above-identified best candidates were used for large-scale deposition (NiO_X/MeO-2PACz) and the NiO_X thickness was varied (Figure 3.8). The cell degradation during DH was investigated for NiO_X thicknesses between 5 nm and 20 nm. Reverse and forward *J-V* scans are plotted on the Figure 3.8a (DH = 0 h), b (DH = 120 h) and c (DH = 1000 h). Relative efficiency loss at the end of the test as a function of the NiO_X thickness, and the evolution of both *FF*s and efficiencies according to the time in the DH chamber are showed in Figure 3.8d, e and f, respectively. It can be observed that: 1) the degradation proceeds more rapidly within the first 100 h for thicker NiO_X (Figure 3.8b, e and f); 2) the degradation is linear with the NiO_X thickness (Figure 3.8d) and 3) the degradation is dominated by a reduction in *FF*, with an increasingly evident S-shape in the *J-V* curve over time (Figure 3.8c and e). It should be noted that all results presented in this paper are from cells illuminated from the substrate side (glass/HTM) as they show higher performances.

Since in tandem device the perovskite top cell is illuminated from the other side, these same cells were also measured from film side throughout the DH test and results are shown in Figure 3.9. Lower currents were measured when the cells were illuminated for the film side because C_{60} is less transparent than NiO_X (Figure 3.9c and d). Additionally, as depicted in Figure 3.9a and b, the difference in efficiency between measurements from the substrate side and film side diminishes after 1000 hours of DH testing compared to before the test. This decrease is attributed to a lower J_{SC} when measured after 1000h of DH testing in a substrate side illumination configuration, while a higher J_{SC} is observed in measurements with film side illumination. In fact, at the end of the DH test, significantly more pronounced degradation is observed in the EQE when the device is measured from the substrate side (Figure 3.9c). This result confirms that the degradation primarily occurs at the NiO_X/perovskite interface rather than at the perovskite/C_{60} one. It's noteworthy that below 450 nm, the EQE increases after the DH test for film side illumination, which can be accounted for by a slight reduction in ITO absorption due to aging.
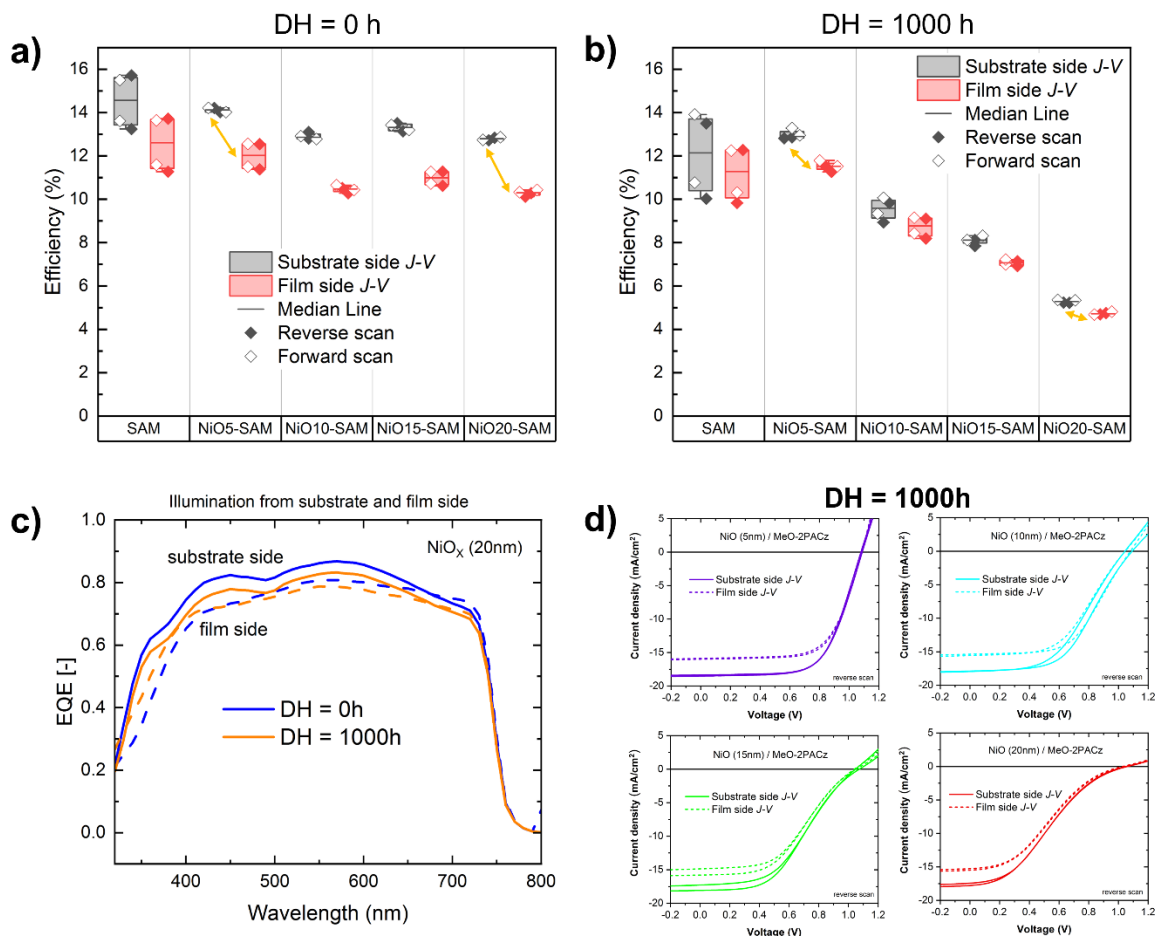
Figure 3.9: Electrical results of the cells presented in Figure 3.8 and measured from the substrate and the film side. *a) Efficiency before and b) after the DH test. c) External quantum efficiency (EQE) of a cell based on 20 nm NiO$_X$ from both film and substrate side just before the DH test (DH = 0h, blue lines) and at the end of the test (DH = 1000h, orange lines). EQE from the substrate side are plotted with solid lines while dashed lines correspond to EQE from the film side of the device. d) J-V curves of the cells throughout the test for the two illumination sides (film: dotted curves and substrate side: solid curves).*

3.3.3 Origin of the efficiency loss

The origin of the emerging loss has been investigated, and it has been hypothesized that the reduction in *FF* may either indicate a reduction of carrier mobility, e.g., due to de-doping of a transport layer or the formation of a barrier or a combination of both. To confirm the hypothesis of a barrier formation, the behavior of the recombination within the cell as a function of applied bias was first investigated. In an ideal cell, the photoluminescence quantum yield (PLQY) of the absorber is expected to drop deeply only below the maximum power point.[132–134] While the performance of perovskite solar cells has been constantly improving, these devices are not yet at their radiative limit, but instead dominated by non-radiative recombination.[135] In this scenario, the PLQY serves only as a proxy to measure the number of carriers present in the absorber and a steep reduction in PLQY (upon reducing the voltage below V_{OC}) can be associated with efficient carrier transport out of the perovskite absorber.
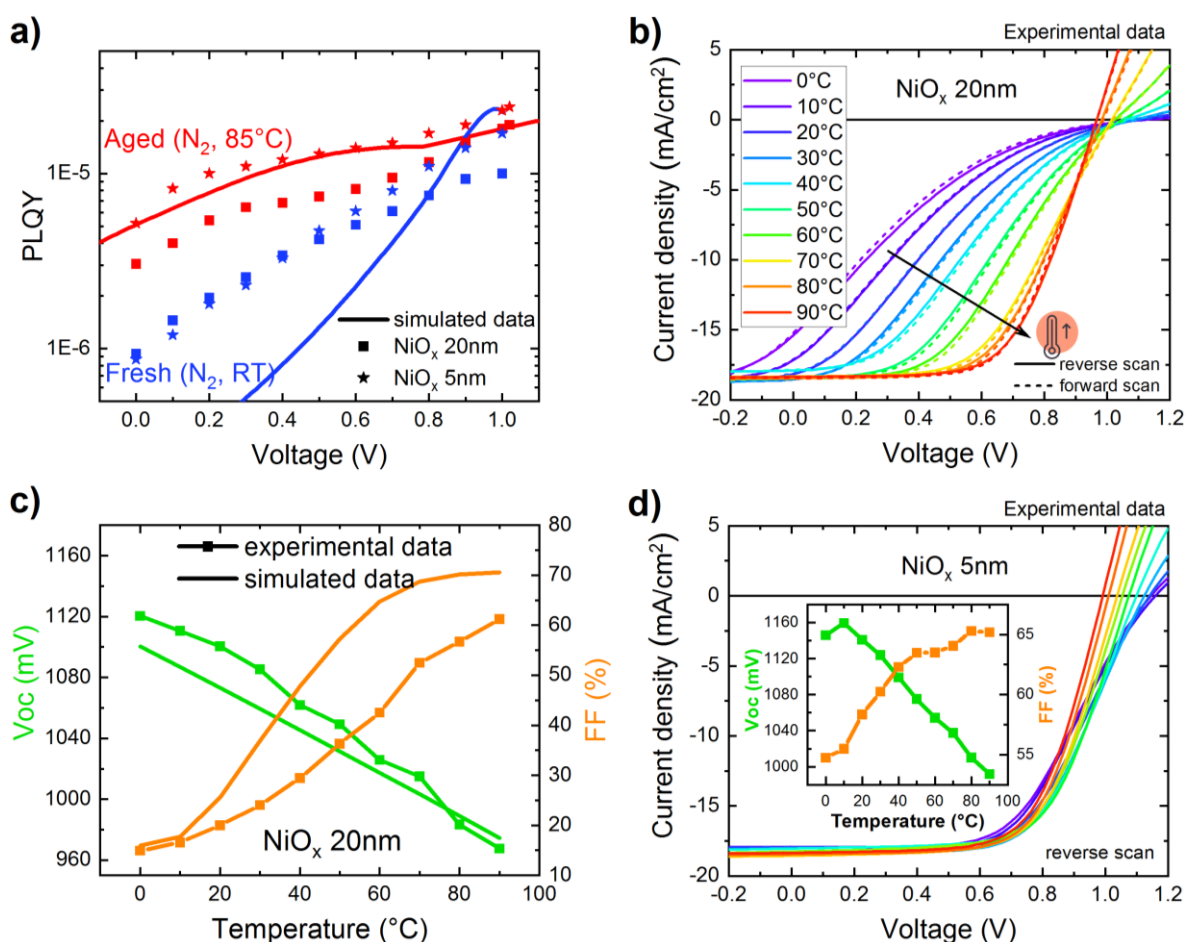

Figure 3.10: Photoluminescence Quantum Yield, Degradation Behavior, and Electrical Performance in NiOX-Based Perovskite Solar Cells. *a) PLQY(V) of PSCs with a NiO$_X$ thickness of 5 and 20 nm (dotted lines refer to experimental measures whereas solid lines refer to simulated data), b) J-V(T) of NiO$_X$(20 nm)/MeO-2PACz-based perovskite solar cell after 1000h of DH, c) V$_{OC}$ and FF extracted from the Fig. 4b plotted in parallel with the data simulated with SCAPS software and d) J-V(T) and V$_{OC}$(T)/FF(T) plots of NiO$_X$(5 nm)/MeO-2PACz-based perovskite solar cell after 1000h of DH.*

Such measurements were performed on fresh and aged (at 85°C, under N$_2$ atmosphere for > 100h) solar cells for 5 and 20 nm-thick NiO$_X$ (including MeO-2PACz) devices (Figure 3.10a). The slope of the PLQY as a

function of applied voltage is steeper for the fresh samples and reduced upon increasing the latter (blue symbols). Furthermore, for the aged samples, the samples with a thicker NiO$_X$ (red square symbols) also exhibit a lower PLQY ($\approx$ 2x) across the whole voltage range, indicative of stronger non-radiative recombination. These results suggest that a barrier for hole extraction forms upon DH testing and scales with the NiO$_X$ layer thickness. This point will be validated further.In a system where phonon-scattering is limiting charge transport within the carrier bands, a reduction of the *FF* upon increasing temperature would be expect, whereas in the case of hopping transport or an electronic barrier, an increase in *FF* is to be expected with higher temperatures. Therefore, temperature-dependent *J-V* measurements were carried out, varying the temperature between 0 and 90°C for two thicknesses of NiO$_X$ modified with MeO-2PACz. The results are shown in Figure 3.10b-d. A linear reduction in the open-circuit voltage is observed, in line with $V_{OC} \propto k_B T$ for the two tested NiO$_X$ thicknesses of 5 and 20 nm (Figure 3.10b, c, d and Figure 3.11). On the other hand, the fill factor increased for both bilayer systems from 55% to 65% (15% to 60%) for the aged 5 nm (20 nm) thick NiO$_X$/MeO-2PACz bilayer cells.
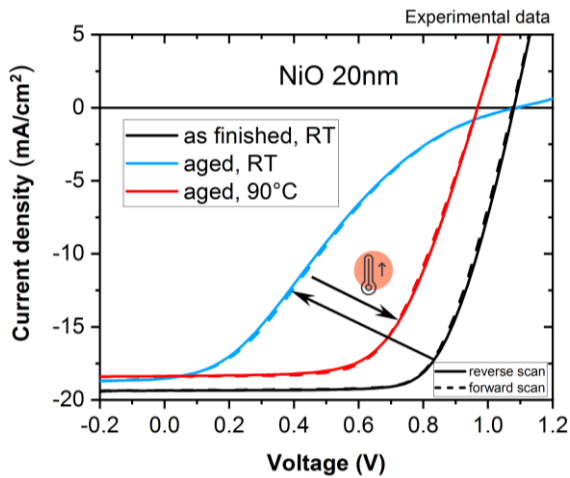

Figure 3.11: S-shape in the J-V curve removed when heating the NiO-based PSC.

To understand the underlying mechanism, the solar cell stack was simulated on SCAPS-1D[125] with the parameters given in **Table 1**, which are representative of a device at room temperature (Figure 3.12a). Increasing temperature would imply a comparable trend in V_{OC} but a mild reduction of *FF* rather than an increase (Figure 3.12b). A hole extraction barrier has hence been introduced by increasing the bandgap of the NiO$_X$ from 3.66 eV to 3.85 eV, in line with results from optical absorption measurements on fresh and aged (85°C, N$_2$ atmosphere) NiO$_X$ samples. Aged NiO$_X$ had a lower density of sub-bandgap states and a higher bandgap, as extracted from a Tauc analysis[136] (Figure 3.12c, d, and e). Solely increasing the bandgap in the simulation, however, did not lead to the characteristic S-shape obtained after degradation (Figure 3.12f, purple line). Only the combination of bandgap widening and a simultaneous decrease in doping concentration accurately describe the experimental data (Figure 3.10c).
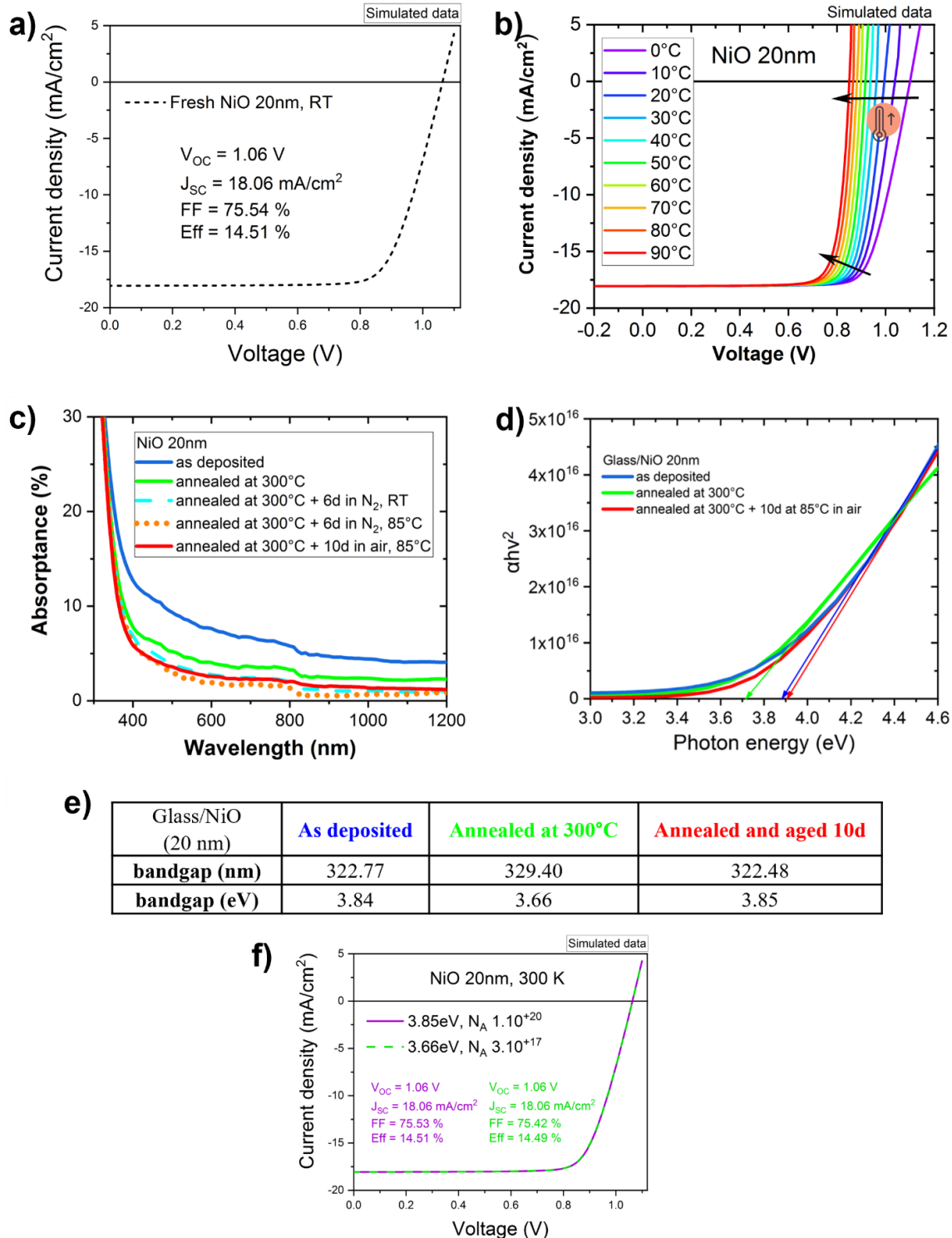
Figure 3.12: Simulation, Analysis, and Band Gap Effects in NiO$_X$-Based Perovskite Solar Cells. *a) J-V simulation on SCAPS of NiO-based perovskite solar cell model. (SCAPS ref model NiO 3.66 eV, NA = 1.01 x 10^{+20} cm^{-3}, 300 K). b) Simulated J-V temperature variation of fresh NiO-based PSC (NiO 20 nm, band gap 3.66 eV, N$_A$ 1.04 x 10^{+20} cm^{-3})- c) Absorptance spectra, d) Tauc plot and e) extracted band gap of NiO depending on its storage. f) Simulated J-V curve of a NiO-based device at room temperature depending on the NiO$_x$ band gap (3.66 eV or 3.85 eV) and the doping level of the NiO$_X$ (1x10^{+20} cm^{-3} or 3x10^{+17} cm^{-3}). Changing the band gap or the doping concentration does not lead to an S-shaped J-V curve.*

The fact that the barrier width plays a critical role, as it can be seen by the stronger *FF* reduction in the case of 20 nm of NiO$_X$ compared to 5 nm of NiO$_X$, also hints towards an additional effect stemming from a reduced conductivity in the NiO$_X$ layer upon aging in DH conditions. R. Karsthof et al. demonstrated that changes in electrical transport properties in NiO$_X$ are caused by the diffusion of Ni vacancies.[137] Over-stoichiometric films tend to equilibrate with the surrounding atmosphere by losing excess O$_2$-ions. In addition, Z. Peng et al. demonstrated that Ni^{3+} are detrimental to the NiO$_X$/perovskite interface. I$^-$ from the perovskite reduces Ni^{3+} from the NiO$_X$ to Ni^{2+} leading to a decrease in conductivity.[121] To gain insights into the changes in dopant concentration and Fermi level position during damp heat, surface and bulk composition were studied on 100 nm thick NiO$_X$ films, one freshly annealed in air (as used in a solar cell) and another aged at 85°C in nitrogen for 100 h (to simulate the thermal stress on an air-tight encapsulated device).
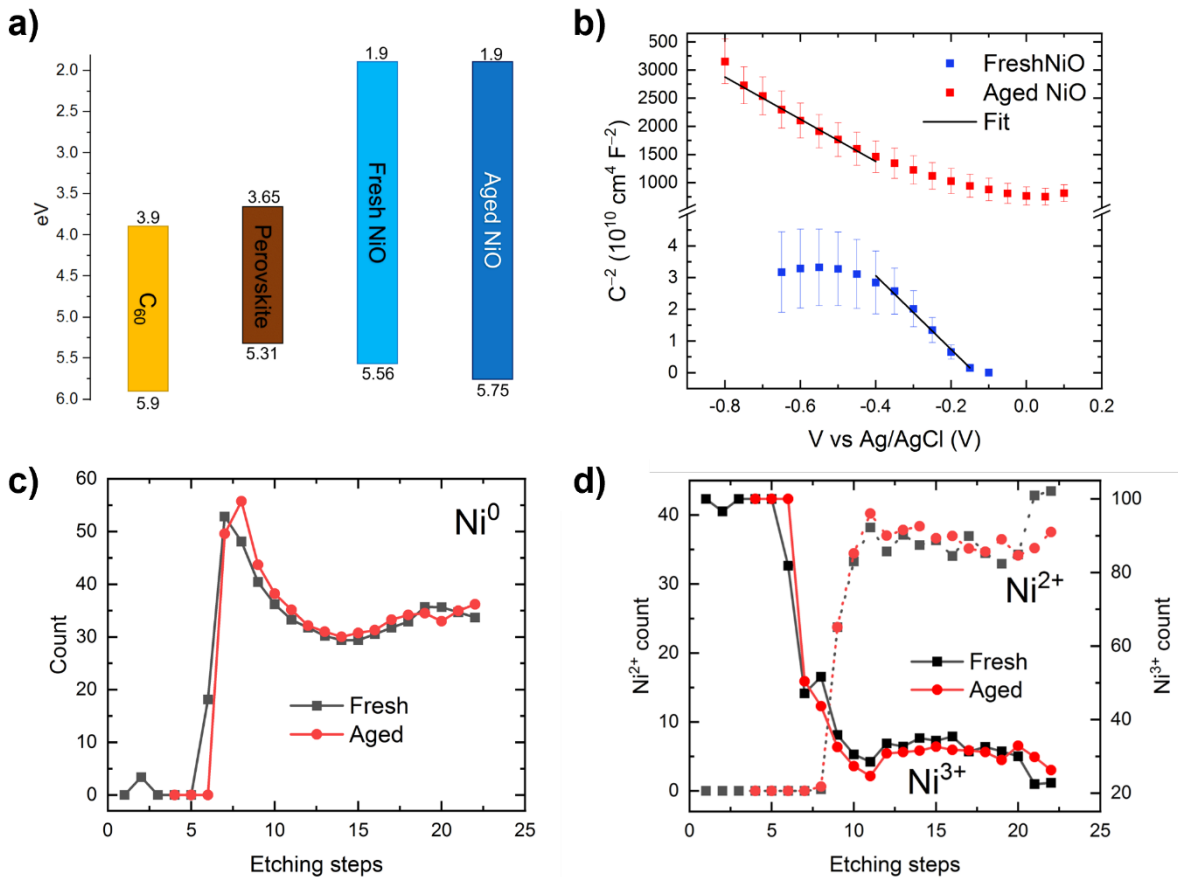

Figure 3.13: Chemical Analyses of NiO$_X$. *a) Schematic representation of the band edge positions of the NiO$_X$/Perovskite/C$_{60}$ stack according to the aging of the NiO$_X$. Values are based on EIS measurements, Tauc plot and literature and b) linear fitting of the Mott-Schottky plots of the fresh and aged NiO$_X$ based on the average capacitance values measured on 3 samples, c) concentration of metal nickel (Ni^0) and d) Ni^{2+}, Ni^{3+} nickel cations within the Pk/NiO$_X$ fresh and aged samples. Oxidation states of the NiO$_X$ were extracted from the Ni2p$_{3/2}$ peak measured by XPS depth profiling.*

As the conductivity of the NiO$_X$ is too low for being measured by Hall effect, electrochemical impedance spectroscopy has been performed and a Mott-Schottky analysis were done on those samples.[128] NiO$_X$/Perovskite/C$_{60}$ band diagram and Mott-Schottky plots of the fresh and aged NiO$_X$ are presented Figure 3.13. The acceptor concentration N$_A$ of the freshly annealed NiO$_X$ was estimated from the slope of

the Mott-Schottky plot to be on the order of 1×10^{20} cm^{-3}, value similar to literature reports for NiO$_X$ films annealed in air at 300°C.[95,138,139] For the NiO$_X$ aged at 85°C under nitrogen, the doping level dropped to 3×10^{17} cm^{-3} (Table 2). From the intercept of the Mott-Schottky plot, a small shift of the Fermi level can be observed, from 4.56 eV for the fresh NiO$_X$ to 4.65 eV for the aged material (Figure 3.13a and b). Using these values for aged NiO$_X$ in the simulation, the S-shape observed for the 20 nm-thick NiOx devices can be reproduced. Furthermore, the absence of S-shape (only a moderate increase in R$_{OC}$) is also accurately simulated when the NiO$_X$ thickness is reduced to 5 nm (Figure 3.14). To note, the drastic loss of free charge carriers does not lead to an S-shape in the simulated *J-V* curves unless the valence band is shifted downwards (Figure 3.12f, green dashed line). Supported by the simulated PLQY(V) data (Figure 3.10a, solid lines), it can be concluded that the drop in *FF* and the appearance of an S-shape result from the combined formation of a barrier hindering hole extraction at the NiO$_X$/perovskite interface and the decreased conductivity of the NiO$_X$ in these oxygen-poor conditions.
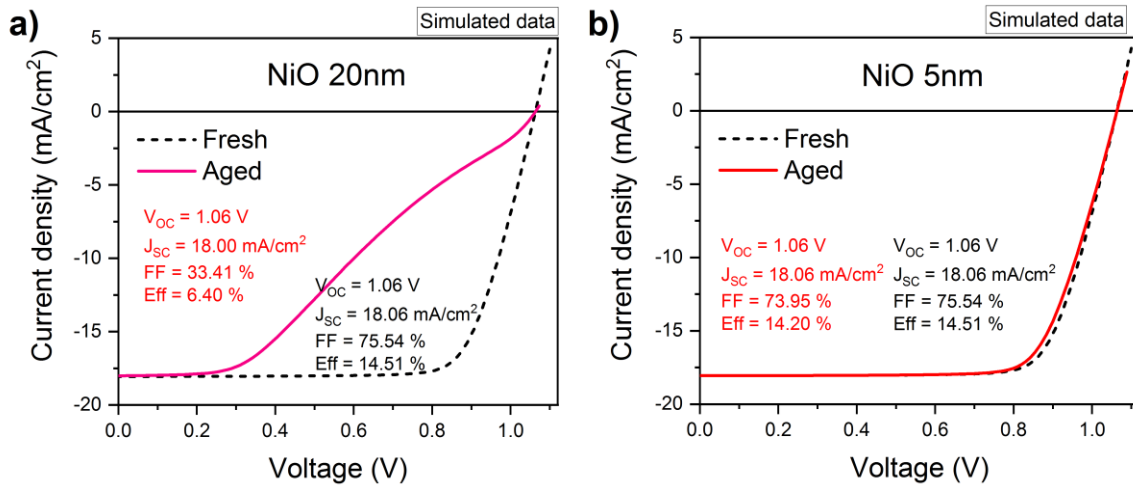

Figure 3.14: Simulated J-V curves of fresh (black curve) and aged (red curve) NiOx-based PSCs, depending on the thickness of the NiOx: *a) 20 nm and b) 5 nm. To reproduce the aged devices, both the band gap and the carrier concentration have been changed, from 3.66 eV to 3.85 eV and from $1\times10^{+20}$ cm^{-3} or $3\times10^{+17}$ cm^{-3} respectively.*

In order to understand this drastic drop in conductivity from fresh to aged NiO$_X$ samples, the oxidation state of the NiO$_X$ before and after aging has been studied by X-ray photoelectron spectroscopy (XPS). High-resolution Ni2p$_{3/2}$ XPS depth profiling was conducted on fresh and aged perovskite (~500 nm) on NiO$_X$ (20 nm) to get insight on the composition of the NiO$_X$ at the perovskite interface as well as in the NiO$_X$ bulk.[126,127] Results are plotted in Figure 3.13c, d and Figure 3.15.

First, Ni^0 signal was detected at the perovskite/NiO$_X$ interface, and its amount decreased with the etching time, i.e., further away from the perovskite and into the NiO$_X$ bulk. This behaviour is opposite to what normally observed in the XPS depth profiling of metal oxides, i.e. the metallic component is expected to increase with the etching time as the ion beam preferentially removes oxygen, and therefore reduces metal oxides to metals. Thus, this behaviour supports the findings of Boyd and co-workers that a redox reaction takes place at the interface between NiO$_X$ and perovskite.

Moreover, the Ni^0 signal at the interface is 5% higher for the aged perovskite/NiO$_X$ sample than for the fresh sample, thus the redox reaction rate is increased by temperature, as expected.

To come to the doping, the concentration of Ni^{3+} species, from which the doping stems, is about 5% lower in the aged sample than in the fresh one, while the Ni^{2+} concentration increases with aging. Therefore, the lower Ni^{3+}/Ni^{2+} ratio for the aged sample is consistent with the loss in doping concentration inferred from the Mott-Schottky analysis and spectroscopy data.

It can be concluded that at 85°C under inert atmosphere or with an air-tight encapsulation, NiO$_X$ p-type conductivity degrades, while the film becomes at the same time more transparent, and finally NiO$_X$ suffers from reduction with iodide in the neighbouring perovskite likely being oxidized to iodine. The combination of all these phenomena leads to the formation of a barrier for hole extraction, which is proportional to the thickness of the NiO$_X$.
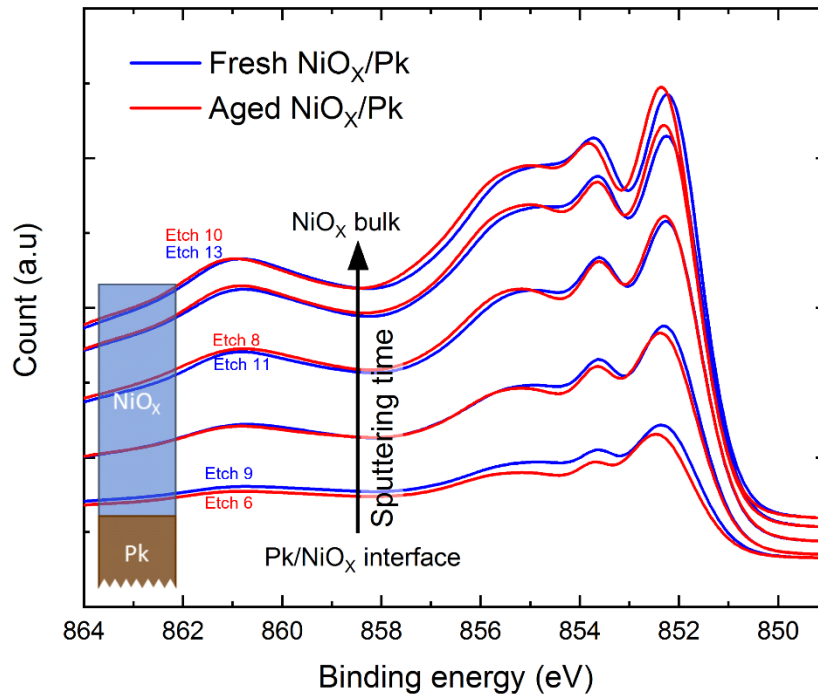

Figure 3.15: XPS of the fresh (blue lines) and aged (red lines) Perovskite/NiO$_X$ samples at different etching steps. *To remove rapidly the perovskite, the first three etches were performed at high speed (350s/etch, ca. ~20nm/min in the perovskite). The followings were performed at much lower speed (90s/etch, ca. ~1.6nm/min in the NiO$_X$ to carefully analyse the perovskite/NiO$_X$ interface and the bulk of the thin NiO$_X$. Since we noticed that the etching speed of the aged sample was faster than the fresh one, we superposed the 2 plots accordantly to get rid of this variation. Here, steps 9 to 13, and 6 to 10 have been plotted for the fresh and the aged samples, respectively. On the graph, the curves with lower intensities correspond to the XPS measurement of the NiO$_X$ near the interface with the perovskite, whereas the very top curves correspond to the measurement of the NiO$_x$ bulk.*

Using a bilayer stack shows better results than when the NiO$_X$ is directly in contact with the perovskite (Figure 3.8 for the bilayer vs. Figure 3.16 for NiO$_X$ alone). On one hand, MeO-2PACz delays the redox reaction between the NiO$_X$ and the perovskite, and on the other hand, the valence band of the organic HTM seems to counterbalance the band alignment mismatch between the NiO$_X$ and the perovskite, allowing a better charge extraction. However, it can be noted that this effect works mainly for NiO$_X$ thicknesses below 10 nm. This result seems reasonable as the extracted photogenerated holes will still

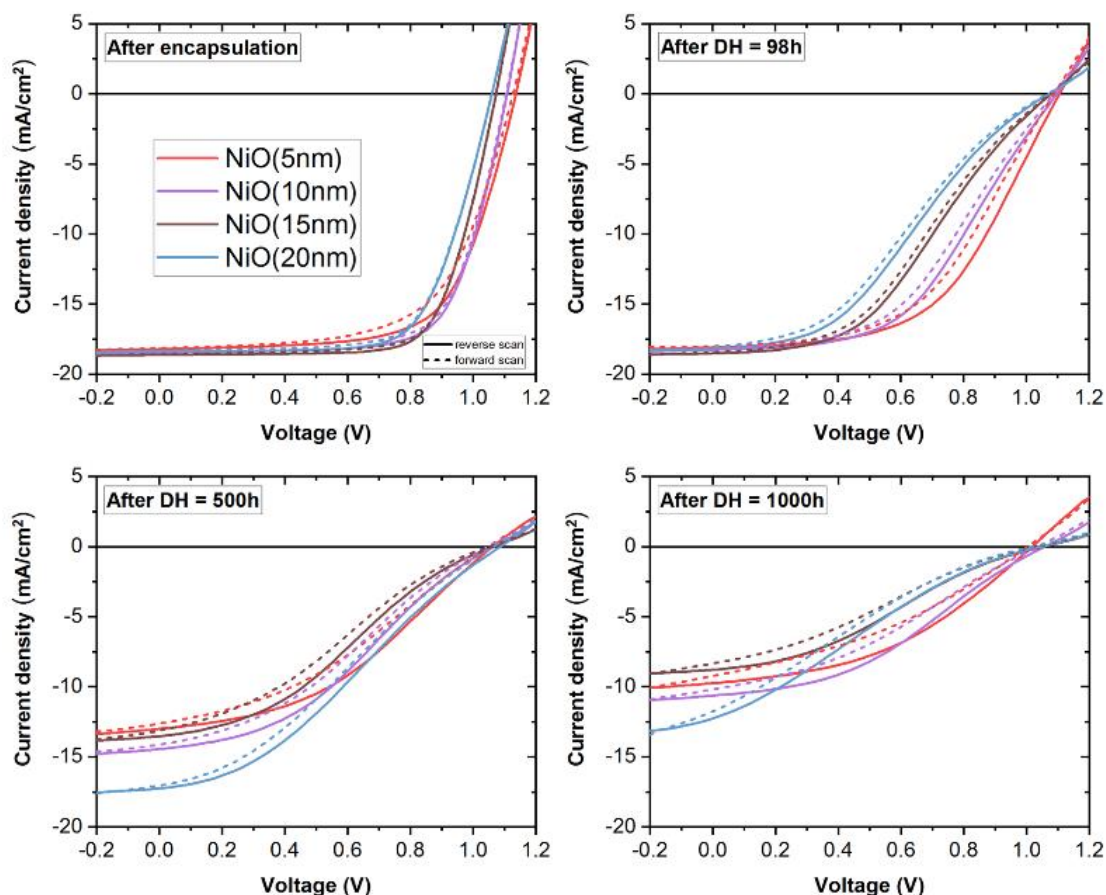accumulate at the NiO$_X$/SAM interface due to the deeper valence band and poorer conductivity of the aged NiO$_X$.

Figure 3.16: J-V Curves of Perovskite Devices Based on Different NiO Thicknesses During DH Test.

3.3 Conclusion

In summary, this chapter reports the thermal degradation of semi-transparent perovskite solar cells with sputtered NiO$_X$ as a hole transport layer upon damp-heat testing. The yield of devices featuring as HTM either a thin NiO$_X$ layer or a self-assembled monolayer is poor when the active area is 1.04 cm^2, which was associated with imperfect coverage of the thin HTM layers atop of the TCO. Thickening the NiO$_X$ layer improves reproducibility, but the cell performance drops during the damp-heat testing due to the formation of a barrier that scales with the thickness of the NiO$_X$ layer. The cause of this extraction barrier was investigated using a combination of temperature-dependent and bias-dependent measurements. Electrochemical impedance spectroscopy results, supported by simulations of solar cells *J-V* data, indicate that this barrier results from the downward shift of the NiO$_X$ valence band combined with a loss of charge carriers in the NiO$_X$ in damp heat conditions, due to a Ni^{3+} reduction to Ni^{2+} from the iodide of the

perovskite. Using a bilayer consisting of 5 nm of NiO_X and a self-assembled monolayer, similar efficiencies on 1 cm^2 cells and on 14 cm^2 minimodules (16.2% and 14.4%, respectively) were demonstrated, thanks to a higher V_{OC} and a pinhole-free HTM, even on large area devices. Furthermore, enhanced stability was achieved, as the bilayer HTM devices retain >94% efficiency after 1000 h at 85°C, 85% R.H.

While reducing the NiO_X thickness and using it as an HTM in a bilayer configuration with a SAM has significantly enhanced thermal stability, the fundamental issues regarding the intrinsic instability of the NiO_X material have not been resolved. Considering this, the upcoming chapter introduces a sputtering method to control the film's stoichiometry and morphology. This approach results in devices passing DH testing five times without performance losses. This chapter aims to offer an deep understanding of the impressive stability improvement achieved.

TABLES

Table 1: SCAPS simulation data [88,140–143]

	NiO fresh	NiO aged	Perovskite	C60	NiO/Pk	Pk/C60
thickness (nm)	20	20	500	30		
bandgap (eV)	3.66	3.85	1.63	2		
electron affinity (eV)	1.9		3.65	3.9		
dielectric permittivity (relative)	12		30	4.2		
CB effective density of states $(1/cm^3)$	1.00E+17		1.50E+18	8.00E+19		
VB effective density of states $(1/cm^3)$	1.00E+20		1.50E+18	8.00E+19		
electron thermal velocity (cm/s)	1.00E+07		1.00E+07	1.00E+07		
hole thermal velocity (cm/s)	1.00E+07		1.00E+07	1.00E+07		
electron mobility (cm^2/Vs)	1.00E-06		1.00E+00	8.00E-02		
hole mobility (cm^2/Vs)	3.00E-02		1.00E+00	3.50E-03		
donor density ND $(1/cm^3)$	0.00E+00		1.00E+12	1.00E+18		
acceptor density NA $(1/cm^3)$	1.01E+20	3.01E+17	1.00E+14	0.00E+00		
defects:						
total density $(1/cm^3)$	1.00E+15	1.00E+15	2.50E+14	1.00E+15	5.00E+09	2.00E+10
capture cross-section electrons (cm^2)	1.00E-15	1.00E-15	1.00E-15	1.00E-15	1.00E-15	1.00E-15
capture cross-section holes (cm^2)	1.00E-15	1.00E-15	1.00E-15	1.00E-15	1.00E-15	1.00E-15
radiative recombination coefficient (cm^3/s)			6.00E-11			
Metal work function	flat band					
Rs $(Ohm.cm^2)$	7.00E+00					
spectrum	AM1.5G 1 sun					

Table 2: Mott-Schottky measurement on fresh and aged NiOx samples

	NiO fresh	**NiO aged**
E(V vs Ag/AgCl)	-0.13744	-0.0462
E(V vs RHE)	0.556505	0.647744
E(V vs NHE)	0.05956	0.1508
E(eV vs vacuum)	-4.56	-4.65
Doping concentration $(1/cm^3)$	1.01E+20	3.01E+17

4. Stabilizing the chemistry of NiO$_X$ in Perovskite Solar Cells to pass the Damp Heat test

Abstract

Following the degradation mechanisms identified in Chapter 3, this new chapter introduces an approach to adjust the exact chemistry of the NiO$_X$ film by manipulating the gas flow during the sputtering deposition process and by incorporating Cs as a dopant. Through this control of the layer chemistry, the optimized NiO$_X$-based perovskite solar cells (PSCs) exhibit remarkable stability with devices remaining stable over 5000 hours of damp heat (DH) testing. To gain a comprehensive understanding of the improved stability, an extensive XPS analysis was conducted on both the surface and bulk of NiO$_X$. This analysis revealed that the concentration of Ni^{3+} in the NiO$_X$ film, which is detrimental to the stability of perovskite solar cells, was twice as high as that in the optimized NiO$_X$. When in contact with the perovskite and subjected to aging at 85°C, a decrease in Ni^{3+} was observed at the NiO$_X$/perovskite interface, indicating a redox reaction. In contrast, an opposing trend was measured for the optimized layer. Furthermore, the film characterization concluded that the NiO$_X$ film exhibited higher porosity and susceptibility to contamination and chemical alterations over time at elevated temperatures.

4.1 Introduction

The previous chapter reported that undoped NiO$_X$ induces a strong degradation at elevated temperatures in an oxygen-free environment, leading to the formation of an extraction barrier at the NiO$_X$/perovskite

interface.[144] Particularly, the free carrier concentration drops by three orders of magnitude, and the valence band of NiO_X shifts downwards. With aging in an oxygen-free environment, NiO_X loses Ni^{3+} and O^{2-} species, leading to an increase in the thermally more stable Ni^{2+}.[137, 145] To resolve this thermal stability issue, the NiO_X layer should be stabilized such that its conductivity and valence band do not shift during aging. Ni^{3+} species are required to ensure good hole conductivity, nevertheless, their concentration must be controlled to avoid redox reactions with the neighboring perovskite.[114] Several research papers have explored the enhancement of the NiO_X conductivity by introducing various components into the film, such as Al,[146] Cs,[108] Mg,[105] Na_2S,[112] Li,[147,148] and O.[100] However, none of these studies investigated the thermal stability of the modified films at temperatures above 55°C. In this chapter, the performance and stability of cesium-doped NiO_X are investigated, also at elevated temperatures relevant for damp heat testing. Here, an approach is proposed to adjust the chemistry of the NiO_X film by manipulating the gas flow during the sputtering deposition process and incorporating Cs as a dopant.

4.2 Experimental details

Here, 20 nm of NiO_X was deposited by RF sputtering under an Ar atmosphere from a NiO_X target. This NiO_X film was deposited on a glass/indium tin oxide (ITO) substrate as hole transport layer. After a 30-minute annealing step at 300°C to improve the optoelectronic properties of the NiO_X layer and enhance the wetting of the perovskite absorber, a $Cs_{0.17}FA_{0.83}Pb(I_{0.83}Br_{0.17})_3$ (CsFA) perovskite solution was deposited by spin coating. To complete the inverted planar perovskite solar cell (PSC), C_{60}, SnO_2, and ITO were deposited by thermal evaporation, atomic layer deposition (ALD), and DC sputtering, respectively. Finally, Ag fingers were evaporated to fabricate 1 cm^2 semi-transparent devices. A sketch of the device stack is shown in Figure 4.1a. The finished devices were then encapsulated in a glass/glass package, including a thermoplastic lamination foil and a butyl rubber edge sealant to protect them from moisture ingress (see Chapter 2, section 2.1.4).
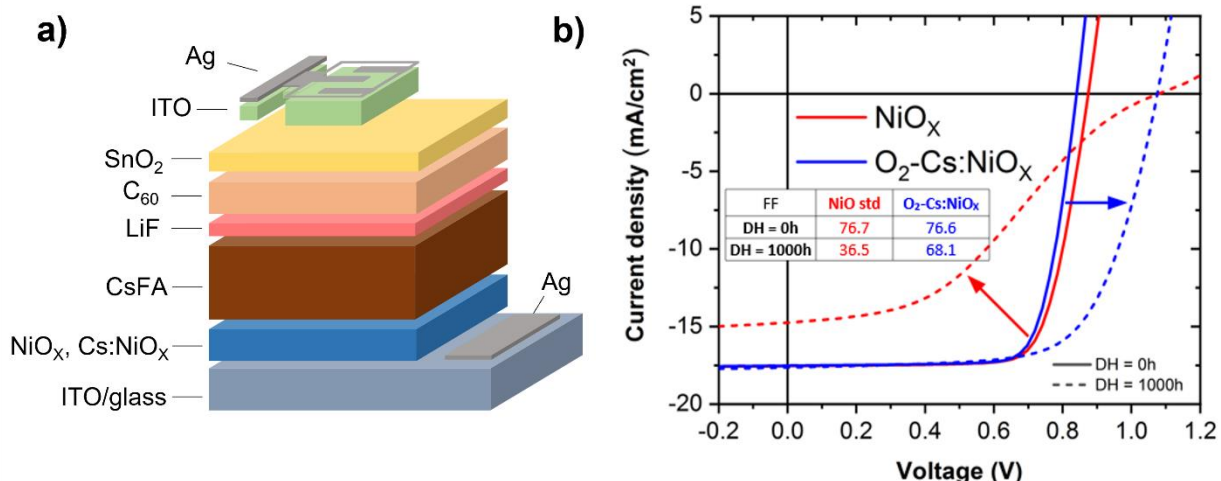
Figure 4.1: Performance Comparison of NiOₓ and O₂-Cs:NiOₓ as HTM in Semi-Transparent Perovskite Solar Cells. *a) device architecture of the semi-transparent inverted planar PSC based on NiOₓ or Cs:NiOₓ as HTM), b) J-V curves of encapsulated semi-transparent PSCs as a function of the HTM used: undoped NiOₓ and O₂-Cs:NiOₓ (red and blue curves respectively). The active surface is 1cm².*

To stabilize the layer, NiO_X was sputtered in the presence of O_2 to increase the oxygen-to-nickel ratio in NiO_X.[149,137,150,100] In order to increase the Ni^{3+} concentration and thus enhance the hole conductivity, NiO_X was also alloyed with Cs by sputtering a $Ni_{0.99}Cs_{0.01}O_X$ target under an Ar/O_2 gas flow mixture. With the insertion of Cs the creation of a Ni^{3+} for each Cs^+ replacing a Ni^{2+} in the lattice is expected. Hereafter, the NiO_X and $Cs:NiO_X$ sputtered with an oxygen partial pressure (120 sccm Ar / 30 sccm $Ar_{(0.95)}$-$O_{2(0.05)}$) are named O_2-NiO_X and O_2-$Cs:NiO_X$, respectively. The original NiO_X sputtered in pure Ar (150 sccm) is named undoped-NiO_X. They were all sputtered in the same chamber, at 150 W.

4.3 Results and discussion

In terms of optical properties, as deposited O_2-$Cs:NiO_X$ film is much less transparent than undoped NiO_X (Figure 4.2). However, after an annealing at 300°C, the absorptance of both films decreases to reach similar levels. In devices, O_2-$Cs:NiO_X$-based PSCs show statistically lower initial efficiencies (12% on average, versus 12.6% for undoped NiOx) due to a lower V_{OC} (-50 mV on average, Figure 4.3a, d). However, similar *FF* and J_{SC} are achieved (Figure 4.3b and c). Despite the lower initial performance, O_2-$Cs:NiO_X$-based devices gain in efficiency compared to NiO_X-based PSCs after 1000h of damp heat (DH) testing (Figure 4.1b and Figure 4.4). For both types of cells, the V_{OC} increases rapidly in the first hours of DH test. While the *FF* of the undoped NiO_X cells drops to below 50% within the first 100h of testing, the *FF* of the O_2-$Cs:NiO_X$-based cells remains stable and decreases by less than ~10% after 1000h.
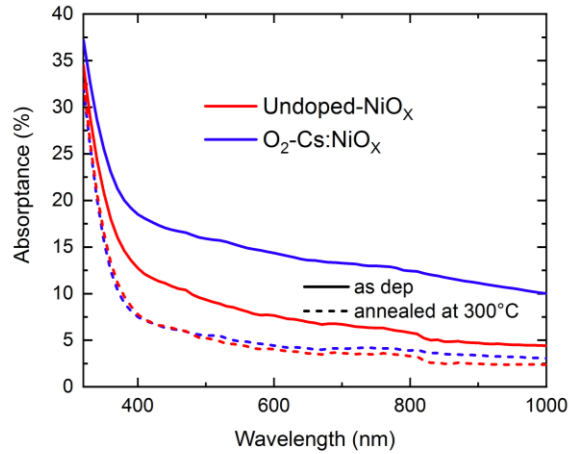
Figure 4.2: Absorptance Spectra of NiO$_X$ and O$_2$-CS:NiO$_X$. *undoped-NiO$_X$ (red curves) and doped-NiO$_X$ (blue curves) films before and after annealing at 300°C in ambient air.*
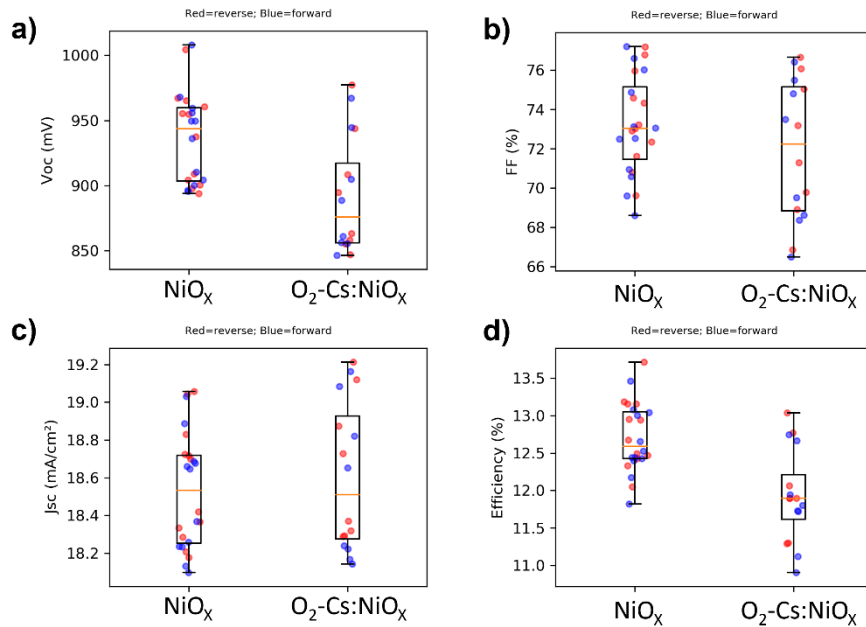

Figure 4.3: J-V parameters of as-deposited PSCs depending on the doping of the NiO$_X$. *Un-doped NiO$_X$ (150 sccm Ar / 0 sccm Ar-O$_2$) and O$_2$ and Cs-doped NiO$_X$: O$_2$-Cs:NiO (120 sccm Ar / 30 sccm Ar-O$_2$).*
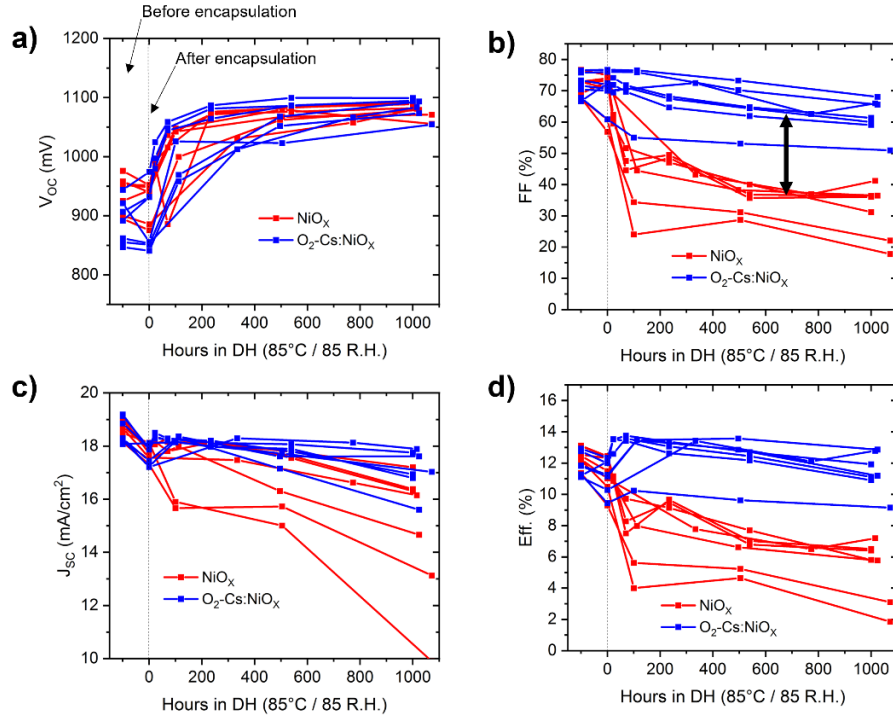
Figure 4.4: J-V performances of PSCs based on 20 nm NiO$_X$ and O$_2$-Cs:NiO$_X$ at different times of DH testing. *a) J$_{SC}$, b) FF, c) V$_{OC}$, d) Eff. DH = -100h corresponds to the J-V measurement done on the as-finished device , whereas DH = 0h refers to the measurement after encapsulation. Right after the encapsulation, the devices show lower efficiencies due to a J$_{SC}$ and V$_{OC}$ drops. This degradation caused by the encapsulation process is reversible after a few hours in the DH chamber, as it can be seen in Figures S3a and c. To show statistics, 14 cells from 4 different batches are plotted.*

4.3.1 Film characterization

To get some insights into the possible differences in the crystallinity of the O$_2$-Cs:NiO$_X$ films and the undoped NiO$_X$, transmission electron microscopy (TEM) and grazing incident X-ray diffraction (GI-XRD) analyses were performed. The XRD pattern in Figure 4.5a show that the NiO$_X$ crystallites are randomly oriented. The intensity of the O$_2$-Cs:NiO$_X$ peaks is lower than that of the NiO$_X$ peaks. This result indicates a poorer crystallinity induced by the Cs-doping. The incorporation of Cs into the lattice is confirmed by the shift in the XRD peaks to lower 2θ angles for the O$_2$-Cs:NiOx sample compared to the NiO$_X$ film (Figure 4.5a). This result indicates an expansion of the lattice, in agreement with the insertion of larger Cs$^+$ ions into the NiO$_X$ lattice. The incorporation of Cs was also confirmed by Energy-dispersive X-ray spectroscopy (EDX), which indicated the presence of about 0.5%at of Cs in the sputtered film (Figure 4.6). Although a small lattice distortion is noticed, both NiO$_X$ and O$_2$-Cs:NiO$_X$ films show similar morphology in STEM dark-field images (Figure 4.5b, c). Grains size is slightly larger for O$_2$-Cs:NiOx (6.9 nm on average, versus 5.5 nm for NiO$_X$, manually measured with Fiji software on more than 30 grains per image). A density of 5.6 g/cm^3 was calculated from X-ray reflectivity (XRR) data for O$_2$-NiO$_X$ deposited on silicon, against 4.9 g/cm^3 for NiO$_X$, indicating that the latter is much less dense than the O$_2$-NiO$_X$ one. Atomic force microscopy (AFM) reveals a roughness of 2.6 nm for the O$_2$-NiO$_X$ film on silicon while the NiO$_X$ film appeared twice rougher (5.0 nm), as shown in Figure 4.5 d and e. As the sputtering of the O$_2$-Cs:NiO$_X$ was done in the same

conditions as for O$_2$-NiO$_X$, (same gas flow and similar deposition rates), a denser and smoother layer is also expected for O$_2$-Cs:NiO$_X$ compared to NiO$_X$.
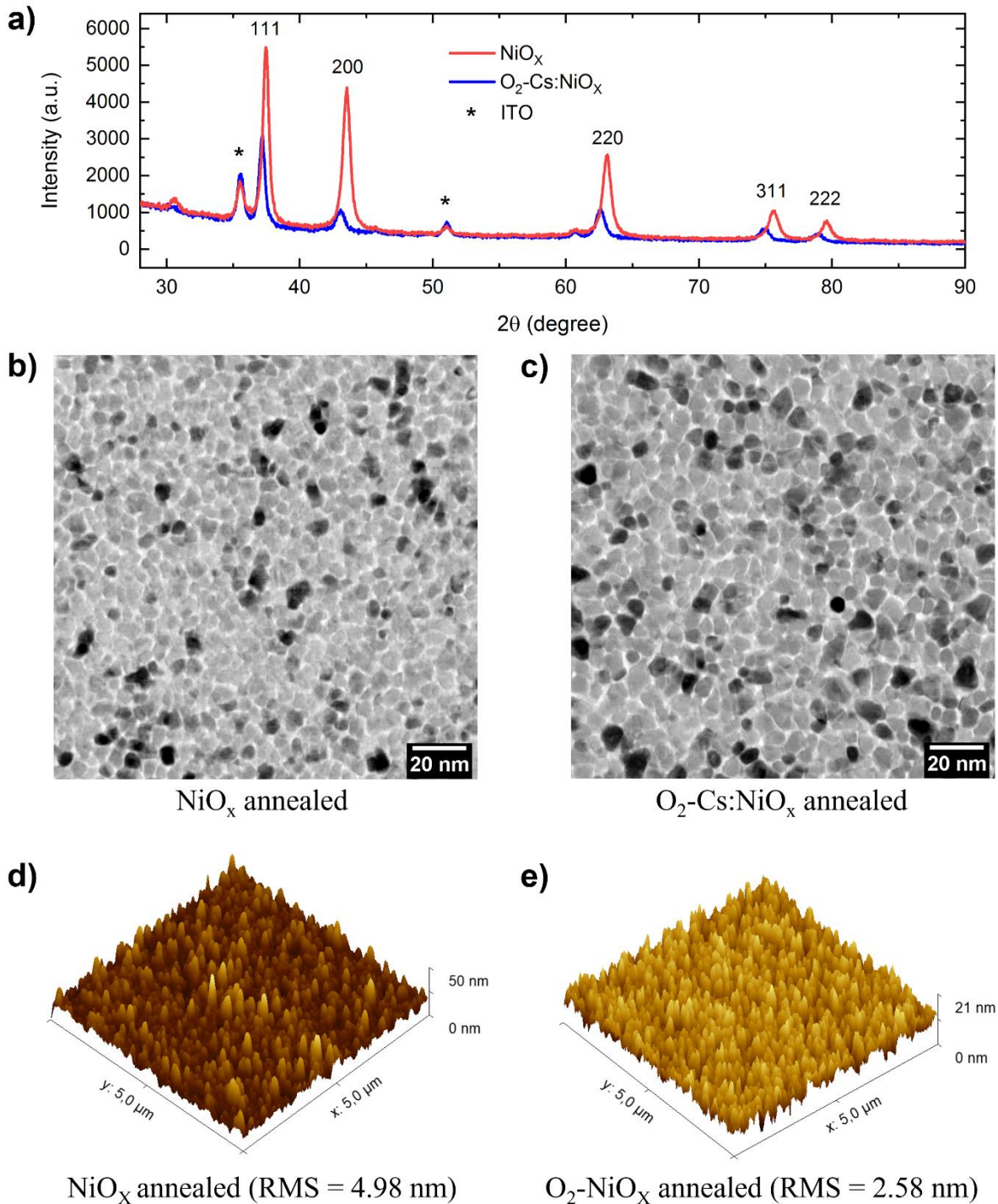

Figure 4.5: Characterization of NiO$_X$ and O$_2$-Cs:NiO$_X$ Thin Films and Their Microstructures. *a) Grazing incidence measurement (0.3°) of 100 nm thick NiO$_x$ (red) and O$_2$-Cs:NiO$_x$ (black) film on ITO substrate, b) STEM bright-field image of annealed NiO$_x$ and c) NiCsO$_x$ film. D) AFM images of both annealed NiO$_x$ and e) O$_2$-NiO$_X$ deposited on glass/ITO substrates.*
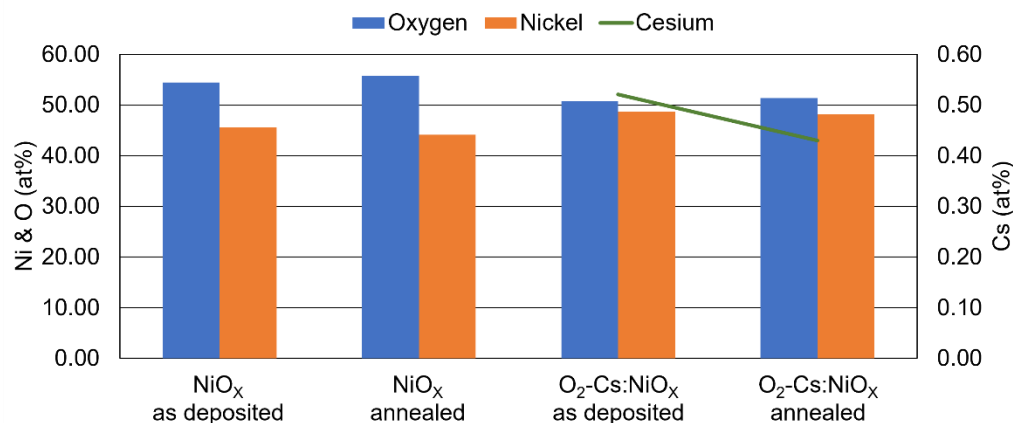
Figure 4.6: Atomic Concentrations of Ni, O, and Cs from STEM EDX of NiO$_X$ and O$_2$-Cs:NiO$_X$ 20 nm Thick Films Deposited on TEM Grids. *For both materials, EDX measurements were done on both as-deposited and annealed films. Annealing was done in air at 300°C for 30 min.*

4.3.2 Chemical analysis of the NiO films

To gain insights into the surface chemistry of the NiO$_X$, O$_2$-NiO$_X$ and O$_2$-Cs:NiO$_X$ films, X-ray photoelectron spectroscopy (XPS) was conducted on fresh films and "aged" films, i.e. films annealed in nitrogen at 85°C for one week (Figure 4.7). In a second time, an XPS depth profiling study was conducted to analyze the evolution of the Ni2p$_{3/2}$ signal from the surface of the NiO$_X$ films down to the ITO interface and to compare the amount of Ni^{3+} in the different samples. (Figure 4.10).

The contributions from the Ni metal, oxide, oxy-hydroxides, and hydroxide were identified based on the approach of Biesinger et al.[126] The XPS results on the surface of the fresh and aged nickel oxide films are presented in Figure 4.7, Figure 4.8 and Figure 4.9. Comparing the Ni 2p signal in Figure 4.7a, c, e and Figure 4.8, it can be seen that a distinct contribution from metallic Ni is present only in the fresh NiO$_X$ film. The aged NiO$_X$ sample does not show this contribution and at the same time has a higher Ni^{2+} and lower Ni^{3+} contribution, which could both indicate an oxidation of the Ni^0 by the interstitial or adsorbed oxygen present in the film and released during the 85°C test (as it will be discussed later).

In the case of the O$_2$-NiO$_X$ and O$_2$-Cs:NiO$_X$ films, an opposite trend is observed, with the Ni^{2+} decreasing and the Ni^{3+} increasing with the aging. As to the amount of Ni^{3+} states on the fresh surfaces, NiO$_X$ showed a higher quantity of Ni^{3+} (40 %) compared to O$_2$-NiO$_X$ and O$_2$-Cs:NiO$_X$ films (21-23%, Figure 4.8). It is interesting to note that all the samples reached a similar level of Ni^{3+} on the surface after one week at 85°C in nitrogen (about 33 +/- 2 %), with a decrease in the case of NiO$_X$ and an increase in the case of the O$_2$-NiO$_X$ and O$_2$-Cs:NiO$_X$ films.
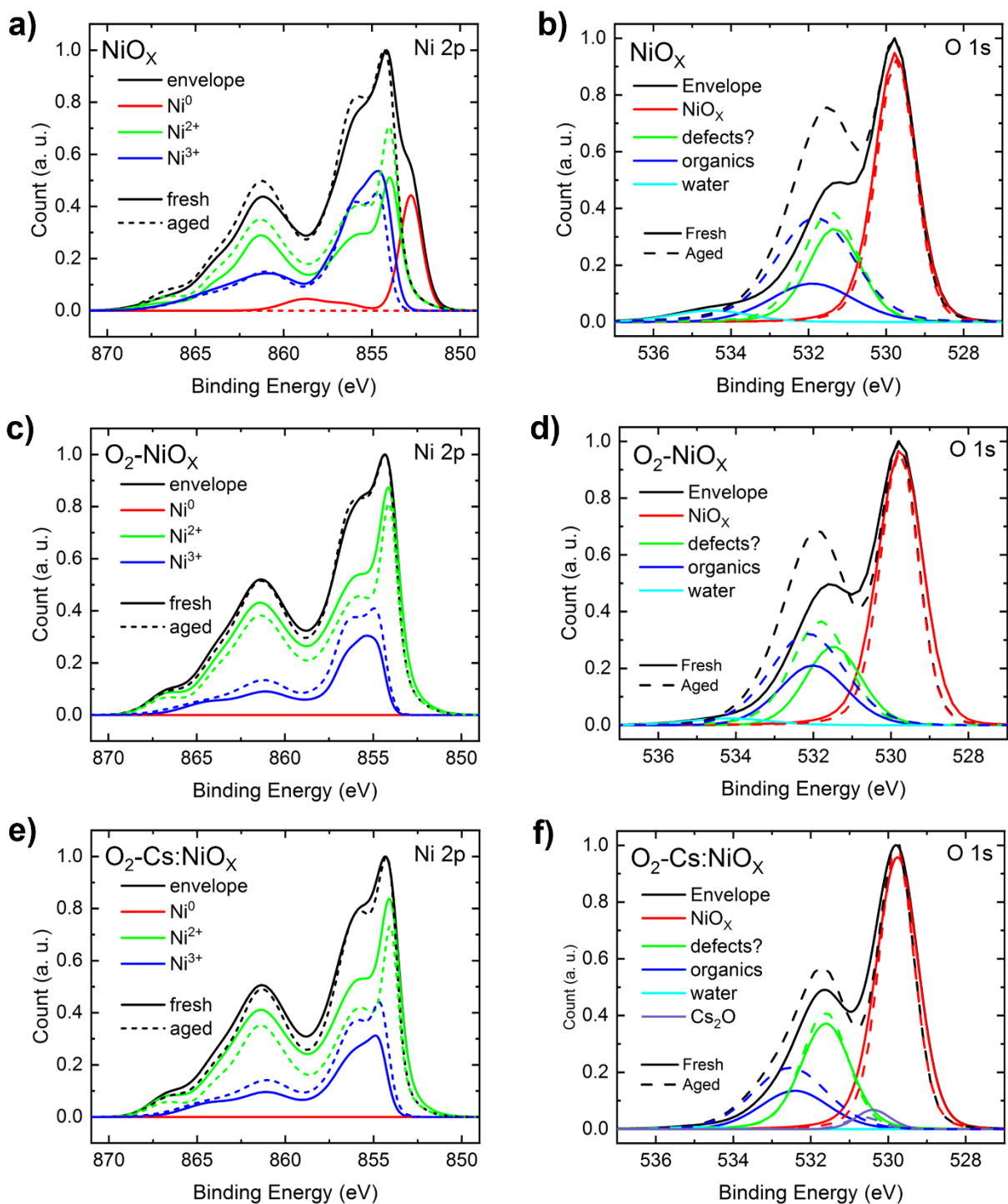
Figure 4.7: XPS Measurements Taken on the Surface of Each Fresh and Aged Samples: *NiO_X (a-b), O_2-NiO_X (c-d) and O_2-Cs:NiO_X(e-f). For each sample, the global Ni 2p and O 1s envelopes and the peaks corresponding to the various contributions are plotted on the same graph. The Ni^0 contribution in Ni 2p spectra is plotted in red, Ni^{2+} in green and Ni^{3+} in blue. For the O 1s spectra, the O contribution from NiO is plotted in red, O from defects or hydroxides (as discussed in the text) in green, O from organics in dark blue, O from H_2O in light blue, and O from Cs_2O in purple.*
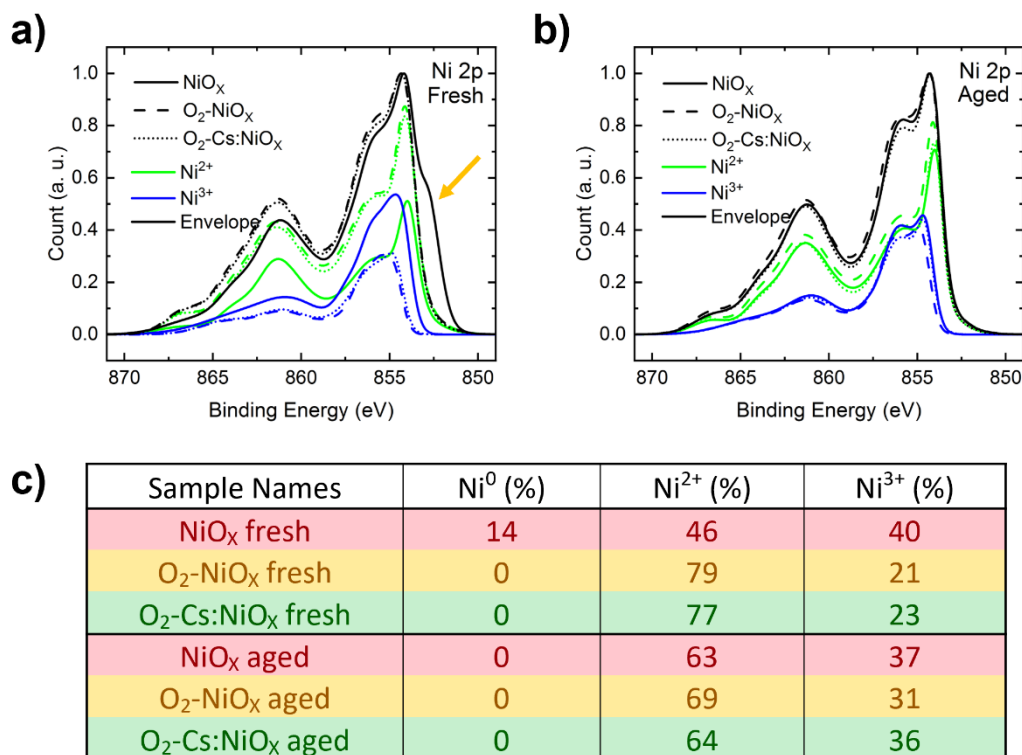
Figure 4.8: Ni 2p XPS Surface Analysis and Deconvolution for Each Oxidation State (Ni⁰, Ni²⁺ and Ni³⁺) for NiOₓ, O₂-NiOₓ and O₂-Cs:NiOₓ Films. *Ni 2p envelopes, Ni²⁺ and Ni³⁺peaks deconvoluted for each a) fresh and b) aged HTM are plotted. Table c) presents the integrated values for each contribution, in the different HTMs, before and after aging at 85°C in an inert atmosphere. The Ni⁰ contribution in the NiOₓ film is shown by an arrow.*

The O 1s peak consists of two distinct peaks (Figure 4.7b, d, f and Figure 4.9). The peak at the binding energy of 529.78 eV, which remains constant for all samples, before and after aging, corresponds to the oxygen of the NiO. The second peak at higher binding energies displays more variation after aging, particularly with respect to the increase in intensity compared to the main peak. The deconvolution of this peak results in four components: organic contamination, adsorbed water, a small contribution of the oxygen from Cs_2O in the Cs:NiOₓ sample, and the remaining contribution around 531.4 eV, labeled as defects in the figures. A few hypotheses were tested for the peak at 531.4 eV. If the peak at 531.4 eV originated from oxygen in NiOOH, the Ni:O ratio would be 33:66 but a ratio of 40:60 is observed instead. This ratio matches well Ni_2O_3, but the binding energy is lower than expected for this oxide, which would be around 531.7-531.8 eV.[151] Instead, it could correspond to oxygen close to nickel vacancies (and therefore called defects in the figures) or adsorbed oxygen, as reported by Biesinger.[126]

The defect concentration, associated to the O defects peak, was larger for the fresh NiOₓ sample (see graphs and table in Figure 4.9a, b and c). After aging, this concentration increased for all samples, to reach a similar value, although the increase was small for the NiOₓ film. Moreover, a noticeable shift towards higher energies was observed in the case of NiOₓ and O₂-NiOₓ with aging, but not for O₂-Cs-NiOₓ (Figure

4.7b, d, f, green curves). This observation suggests that the incorporation of Cs into the lattice restricts chemical changes, resulting in a more stable layer.
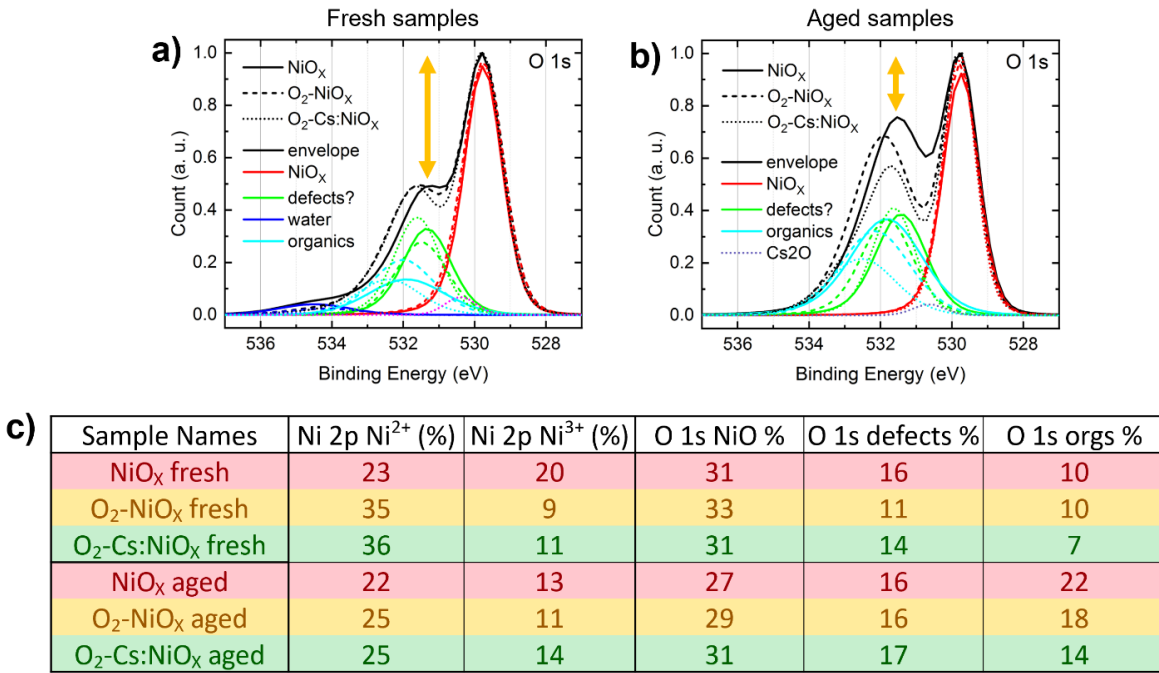

Sample Names	Ni 2p Ni^{2+} (%)	Ni 2p Ni^{3+} (%)	O 1s NiO %	O 1s defects %	O 1s orgs %
NiO$_X$ fresh	23	20	31	16	10
O$_2$-NiO$_X$ fresh	35	9	33	11	10
O$_2$-Cs:NiO$_X$ fresh	36	11	31	14	7
NiO$_X$ aged	22	13	27	16	22
O$_2$-NiO$_X$ aged	25	11	29	16	18
O$_2$-Cs:NiO$_X$ aged	25	14	31	17	14

Figure 4.9: XPS Analysis of O 1s Spectra for NiO$_X$, O$_2$-NiO$_X$, and O$_2$-Cs:NiO$_X$ Surfaces Before and After Aging at 85°C. a) O *1s spectra of fresh samples and (b) aged one. Each O peak contribution are plotted in the same graph to highlight the shifts. Table c) presents the deconvoluted values obtained for each O and Ni contributions.*

Additionally, the O 1s peak associated with organic contamination in the NiO$_X$ sample was much higher than for the O$_2$-NiO$_X$ and the O$_2$-Cs:NiO$_X$ (Figure 4.7b, d, f, dark blue curves). After aging, this organic contribution increased for all the samples but the most for the NiO$_X$ film and the least for the O$_2$-Cs:NiO$_X$. This means that some carbon contamination came to the surface either with the aging at 85°C or during the measurement (as the transfer, from sealed box to XPS tool has been done in air). Moreover, on the NiO$_X$ sample, a clear shoulder of the envelope (around 534-536 eV) indicates the presence of water. However, aside from this sample, the fitting of water for the two other sample is prone to uncertainty as the line shape used to fit the other components will naturally affect the tail of the O1s manifold, where the water is potentially present. It seems likely that the fast sputtering in pure Ar (5 min deposition to reach a thickness of 20 nm, as measured by profilometry) resulted in a more porous and defective film compared to the slower sputtering in mixed Ar/O$_2$ (about 25 min for thickness of 20 nm) and more prone to adsorb water and organic contamination. With respect to all the contributions to the high binding energy O1s signal (defective sites, organic contamination, water), it is clear that the O$_2$-Cs:NiO$_X$ film remained relatively stable during the aging as opposed to the NiO$_X$.
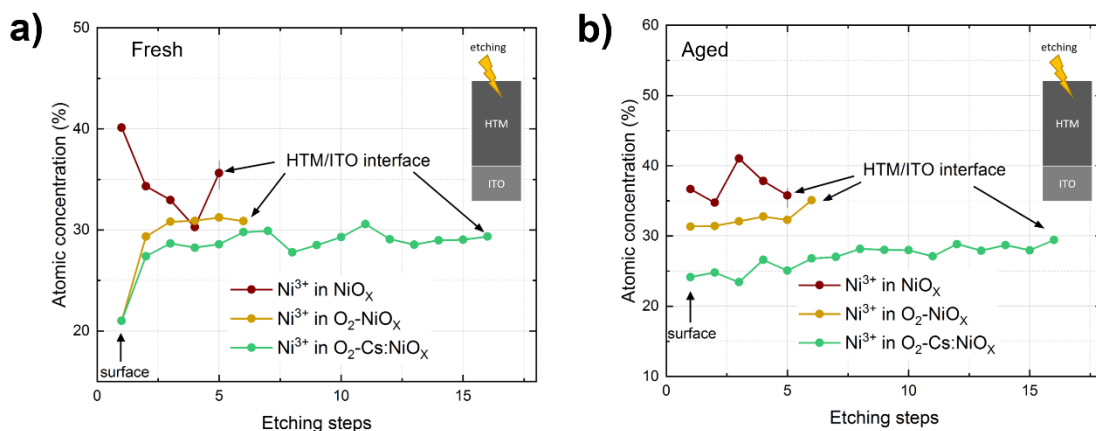
Figure 4.10: Ni³⁺ Concentration in NiOₓ, O₂-NiOₓ and O₂-Cs:NiOₓ Films. *The atomic concentrations of Ni³⁺ species determined through XPS depth profile analysis for fresh and aged NiOₓ, O₂-NiOₓ and O₂-Cs:NiOₓ films previously sputtered on glass/ITO substrates. Aged samples were placed in inert atmosphere at 85°C for one week. In each case, XPS measurements were conducted initially on the film surface and subsequently after performing multiple etching steps to reveal insights into the bulk composition. It's worth noting that identical etching parameters were applied to all the samples. However, the thickness removed with each etching step varied among the HTM/ITO samples due to differences in film density, as discussed in the main text. The XPS results presented here are derived from data collected from the surface of each HTM film to the HTM/ITO interface The identification of the ITO interface was facilitated by detecting Sn peaks, with the interface position defined as Ni/Sn = 50%. It is evident from these results that only five etching steps were required to reach the ITO surface in the case of NiOₓ samples, while O₂-Cs:NiOₓ demanded 16 steps, underscoring the lower density of NiOₓ compared to O₂-Cs:NiOₓ.*

While all the films had the same thickness based on profilometry data, XPS depth profiles indicate that a higher number of etching steps was required to reach the ITO interface in the case of O_2-Cs:NiOₓ (Figure 4.10), i.e. the etching of NiOₓ was 3 times faster than the etching of O_2-NiOₓ or O_2-Cs:NiOₓ films. This finding supports the XPS surface analyses and XRR results, indicating a lower density for the NiOx film, and a greater propensity to absorb water and organic contaminants.

The depth profiling of the Ni³⁺ signal in Figure 4.10 shows a low and steady concentration throughout the bulk of the O_2-Cs:NiOₓ, after a steep increase below the surface, and no change upon aging at 85°C. Conversely, for the NiOₓ film the amount of Ni³⁺ is high and poorly uniform in the fresh sample, while it seems to equilibrate throughout the bulk upon aging, still remaining much higher than for the O_2-Cs:NiOₓ film.

4.3.3 Chemical analysis of the NiO films covered with perovskite

The chemical properties of the NiO films may change when in contact with perovskite, especially upon aging at 85°C. Therefore, depth profiling XPS analyses were also conducted on NiOₓ, O_2-NiOₓ and O_2-Cs:NiOₓ films coated with a perovskite layer (Figure 4.11). A quick etching using an argon ion beam was done through the perovskite to reach the NiO interface, then the etching proceeded at a slower pace throughout the NiO films to reach the ITO interface (etching details are written in the Figure 4.11 caption). The dashed lines in Figure 4.11 indicate where the interface with the perovskite (and the ITO) was estimated, based on the drop of the Pb XPS signal (the etching step where Pb and Ni (or Ni and Sn) are

equal). The Ni^{3+} concentration measured in the NiO_X sample dropped of about 10 % after aging (Figure 4.11a) while in both modified-NiO_X films, higher concentrations of Ni^{3+} were measured after aging, particularly in the case of O_2-Cs:NiO_X (Figure 4.11b, c). As presented in Chapter 3, a significant drop in Ni^{3+} concentration was observed at the NiO_X/perovskite interface accompanied by a marked increase in Ni^0, sign of redox reaction (Figure 4.11d). Typically metal oxides are getting reduced to metal due to the preferential sputtering of oxygen, hence one would expect to observe a reduction of the NiO to Ni^0. However, the opposite trend is found, indicating that metallic Ni was already present in the samples, and with a higher concentration at the interface with perovskite. One hypothesis could be that in the presence of perovskite, nickel ions are reduced to metallic nickel while iodide ions are oxidized to iodine. As opposed to the NiO_X results, the O_2-Cs:NiO_X sample shows a much lower Ni^0 peak after aging and a higher Ni^{3+} concentration at the interface with the perovskite, showing that the redox reaction was mitigated in this case.
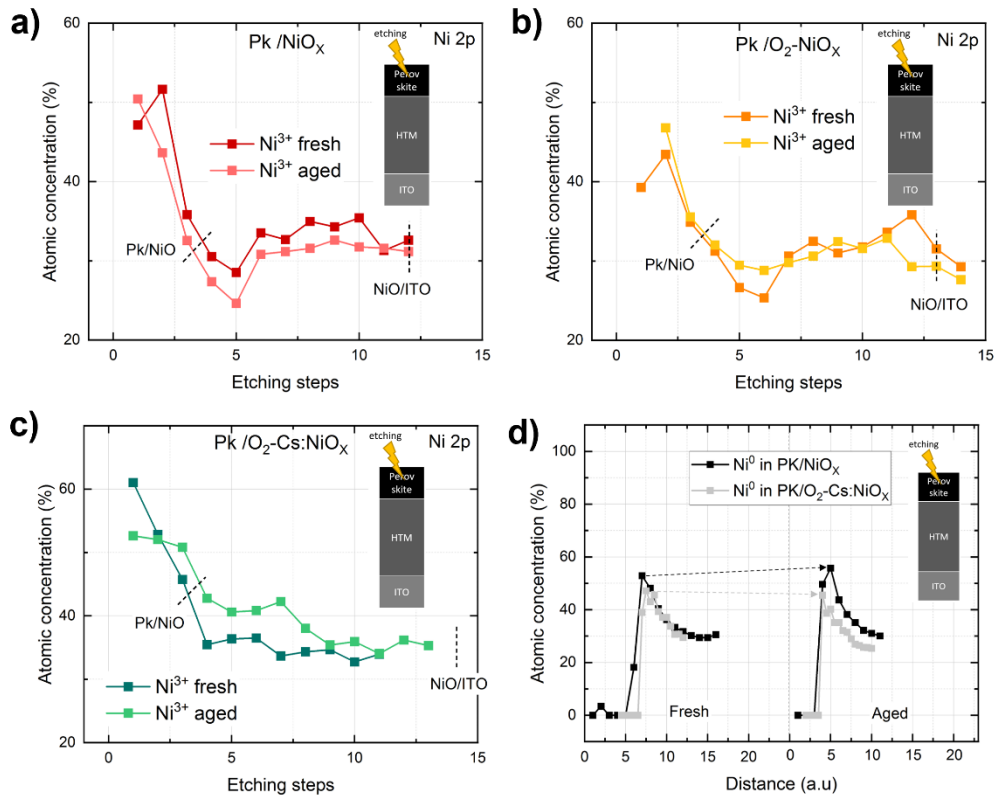

Figure 4.11: Depth Profiting XPS Analyses of the Three Different NiO in Contact with the Perovskite, for Fresh and Aged Samples. *From the obtained Ni 2p spectra, Ni^{3+} contribution is plotted for a) Pk/NiO_X, b) Pk/O_2-NiO_X and c) Pk/O_2-Cs:NiO_X samples (d) Ni^0 oxidation state is plotted for Pk/NiO_X and Pk/O_2-NiO_X before and after aging. To remove rapidly the perovskite, the first three etches were performed at high speed (350s/etch, ca. ~20nm/min in the perovskite). The followings were performed at much lower speed (90s/etch, ca. ~1.6nm/min in the NiO to carefully analyze the perovskite/NiO interface and the bulk of the thin NiO. Since it was noticed that the etching speed of the aged sample was faster than the fresh one, the two plots were superposed accordantly to get rid of this variation.*

It can be concluded that NiO_X tends to reduce with aging thus oxidizing the neighboring perovskite layer compared to the two doped-NiO_X films. This implies a higher reactivity for NiO_X, due to a higher Ni^{3+} concentration.

4.3.4 Devices performances

In terms of solar cells, the initial performances of cells with NiO_X and O_2-Cs:NiO_X were very similar, as shown in Figure 4.1b. To assess the impact of using O_2 gas during sputtering in comparison to introducing Cs, devices based on Cs:NiO_X sputtered under pure Ar conditions were fabricated. The initial performances are plotted in Figure 4.12a. Except for a slightly lower V_{OC} with O_2-Cs:NiO_X, the devices made on either NiO_X, Cs:NiO_X or O_2-Cs:NiO_X exhibited similar current-voltage (*J-V*) characteristics. However, in contrast to the DH behaviour of O_2-Cs:NiO_X (Figure 4.1b) the characteristic S-shaped *J-V* curve seen in undoped-NiO_X (Chapter 3) became evident also for Cs:NiO_X-based cells (represented by the red and green curves, respectively, in Figure 4.12). While Cs doping alone modestly improved the *FF* after 1000h of DH, it is worth noting that the presence of O_2 gas during sputtering is crucial for enhancing performance after DH testing, particularly due to a much more stable *FF*.
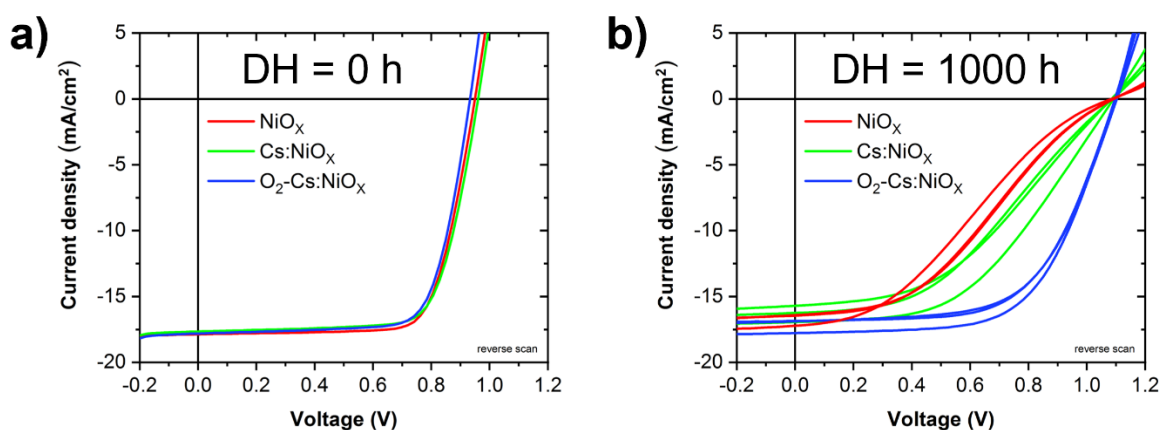

Figure 4.12: J-V Performance of Encapsulated PSCs with Various NiO as HTMs Before and After 1000 Hours of Damp Heat Testing. *a) after encapsulation - DH = 0 h, and (b) after 1000 h of DH testing.*

Since the presence of O_2 during sputtering has been shown to be essential for the long-term stability of PSCs, devices based on O_2-NiO_X and O_2-Cs:NiO_X were compared after DH testing. To improve the initial performances, and especially the V_{OC}, a MeO-2PACz self-assembled monolayer (SAM) was applied on top of the HTM layer to improve the interface with the perovskite. Figure 4.13 presents the *FF* obtained for each HTM condition, at different times of DH testing. Fresh devices initially showed similar *FF* values, with a slight dispersion, possibly due to imperfect SAM coverage. However, after subjecting the devices to 2000 hours of DH testing, those based on NiO_X experienced a significant drop in *FF* to less than 55% due to a strong increase in R_{OC} and the emergence of an S-shaped *J-V* curve (Figure 4.13c). Note that the *FF* value remained decent after 2000h of DH test, thanks to the presence of SAM at the NiO_X/perovskite interface. As previously discussed in the Chapter 3, the presence of organic layer at this interface delays the redox reaction, and thus helps to lower the S-shaped curve. In contrast, devices based on O_2-doped NiO_X exhibited *FF* values above 70%. O_2-Cs:NiO_X-based PSCs displayed the highest *FF* values, reaching up to 73%. This trend became even more pronounced after 5100 hours of DH testing. The best *J-V* scan of the O_2-Cs:NiO_X-based device exhibited 73.5% *FF* value after more than 5100 hours under DH, while the *FF* of the O_2-NiO_X-based cells decreased to an average of 67%. These results certainly underscore the lattice stabilization effect of Cs incorporation, as previously discussed. Overall, by finely tuning the stoichiometry

and enhancing the film quality, devices with improved DH stability were demonstrated, passing over 5000 hours of DH testing with, with even a slight gain in efficiency when compared to the as-encapsulated reference value (Figure 4.14). In more details, after encapsulation (DH = 0h), the device efficiency dropped around 2% due to a decrease in J_{sc}. This J_{sc} variation could be caused by a combination perovskite degradation due to the lamination process and the reflection of light at the front glass interface. After the first 160 hours under DH, the device efficiency increased as a result of a V_{oc} enhancement of up to 100 mV. This large increase can be explained by the passivation of the NiO/perovskite, as also noticed in other chapters.
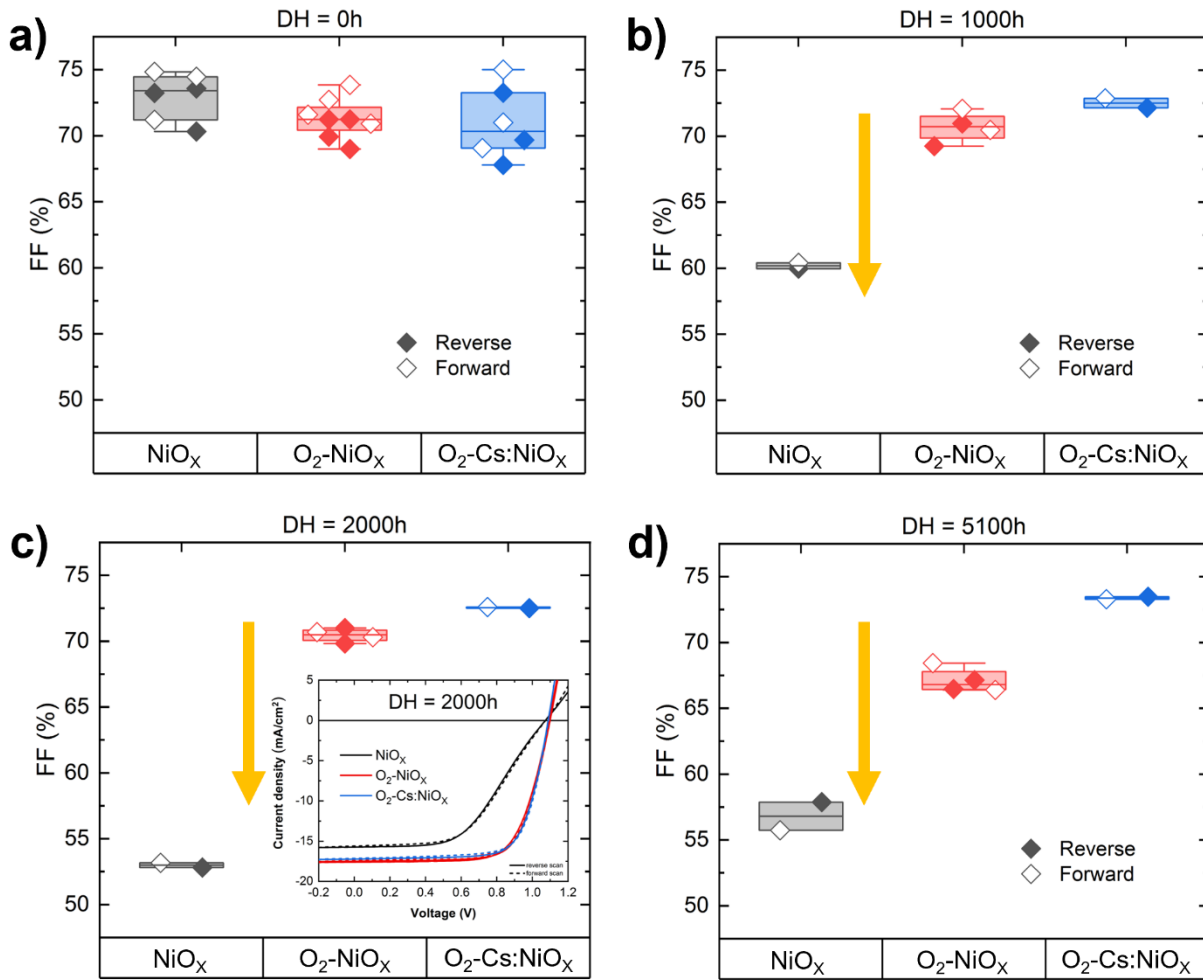
Figure 4.13: FF of PSCs using NiO/MeO-2PACz bilayer as HTM During the Damp Heat test. Three NiO compositions were investigated. *After (a) encapsulation, (b) 1000 h and (c) 2000 h and (d) 5100h in DH chamber, for different HTMs. J-V of the devices after 2000h of DH are inserted in the (c).*
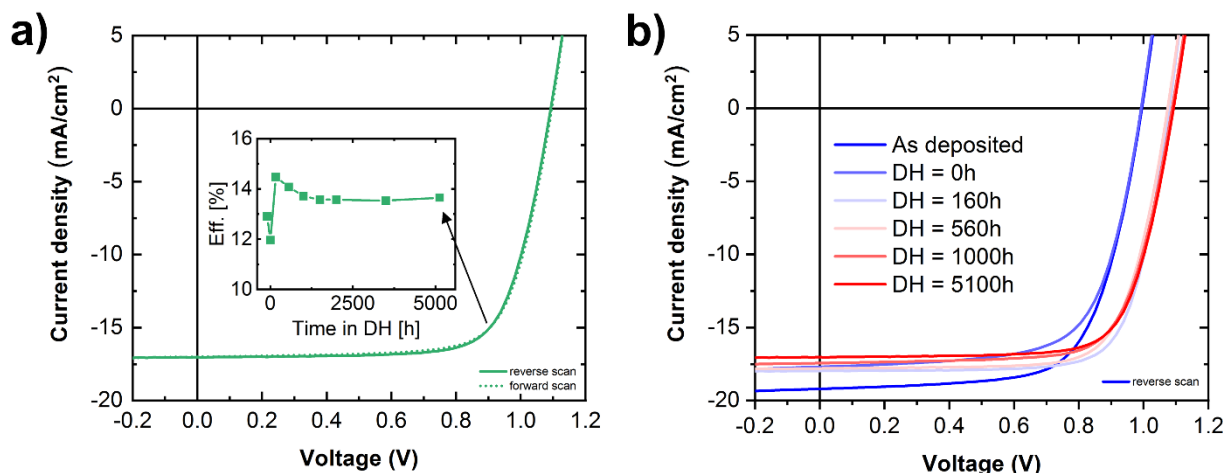
Figure 4.14: Record DH stability device based on O₂-Cs:NiOₓ/MeO-2PACz as HTM. *a) reverse and forward J-V curve of O₂-Cs:NiOₓ-based PSCs after more than 5100 hours of DH testing, with a final efficiency of 13.67% and a FF of 73.47% and efficiencies value of this device taken at different time during the test. b) reverse J-V curve of the record cell at various DH time. DH = 0h corresponds to the measurement after encapsulation.*

4.4 Conclusion

In summary, this study revealed that a porous NiOₓ layer leads to an increased presence of defects and Ni³⁺. Consequently, the film becomes more susceptible to water adsorption, contamination, and perovskite oxidation. However, by carefully controlling the sputtering process through deposition in a mixture of Ar and O₂ gases (instead of pure Ar), the concentration of Ni³⁺ species can be reduced, the surface made smoother and the NiOₓ layer denser. Furthermore, the introduction of the large Cs element (by sputtering from a Cs:NiOₓ target) resulted in the creation of more stable layers, thereby enhancing the overall device stability due to a denser and more amorphous microstructure, which seems to stabilize the Ni oxidation state upon DH aging. As a result, a O₂-Cs:NiOₓ-based PSC was shown to pass five times the IEC 61215 damp heat test requirements (<5%rel change in PCE). These results show pathways to stabilize perovskite solar cells that can be implemented at the industrial level.

Having successfully addressed the stability of NiOₓ-based PSCs stability under damp heat conditions, the following chapter will investigate the stability of these devices when subjected to a combination of elevated temperatures and light exposure. This specific test, known as the light soaking test, is one of the most critical assessments to pass for PSCs. Light activates ion migration, leading to processes such as halide phase segregation, ion accumulation at the interfaces, and inhomogeneous electric field, all of which can cause irreversible cell damage. Moreover, under elevated temperatures, and despite the

presence of adequate encapsulation, as demonstrated in the previous chapter on DH testing, light-induced degradation becomes significantly more severe. A comprehensive understanding of these degradation mechanisms is essential for the production of reliable photovoltaic panels based on perovskite materials.

5. Light-Induced Degradation of Perovskite Solar Cells

Abstract

In addition to the rapid progress in terms of efficiency, the long-term operational stability of perovskite solar cells (PSCs) remains a critical challenge that must be overcome to ensure their commercialization. Perovskite cells undergo irreversible decomposition upon light exposure, a process that intensifies when cells are subjected to both illumination and elevated temperatures. An extensive study was conducted to comprehensively understand the roles and impacts of each material within the cells. First, precise control over the perovskite composition is crucial. PbI_2 accelerates degradation reaction under light and heat exposure, meaning an accurate control over the perovskite stoichiometry is required for enhanced stability. Furthermore, the utilization of CsFAMA triple-cations formulation, with a minor fraction of MA, does not appear to be a limitation for stability, when used in a stoichiometric perovskite composition. Second, a redox reaction occurs at the NiO_X/perovskite interface. Effective mitigation strategies such as employing dopants within NiO_X or incorporating interlayers give encouraging results. Third, the intrinsic ionic properties of the perovskite semiconductor facilitate ion mobility. Under continuous illumination, ions migrate and accumulate at interfaces and edges of the active area of the cells, leading to first reversible degradation and then irreversible phase segregation followed by strong degradation. Fourth, the incorporation of pFBPA as an additive in the perovskite precursor solution and the use of a hydrophilic SiO_X nanoparticles layer between a hydrophobic self-assembled monolayer (SAM) and the perovskite layer, both aimed at enhancing efficiency, are shown to lead to significant and irreversible instabilities after few hours of light exposure. These instabilities manifest in a loss of J_{SC}. Last, the silver electrodes show severe damage after light soaking, attributed to exposure to I_2 vapor resulting from the outgassing of volatile species from the perovskite. Finally, various pathways to extend the operational stability of PSCs are discussed: these involve the meticulous control of the perovskite composition, effective interface engineering, and the implementation of protective layers.

5.1   Introduction

In order to improve the long-term stability of PSCs under light exposure, a deep understanding of the degradation mechanisms occurring within the solar cell is required. As discussed in the introduction chapter, perovskite solar cells (PSCs) can experience various degradation processes, including perovskite decomposition, outgassing of certain species, ion migration, and halide segregation, particularly when exposed to a combination of light and elevated temperatures.

Given that a solar cell is a superposition of different materials that interact with one another, investigating their behavior under light exposure on a layer-by-layer basis appears to hold significant value. UV-VIS spectroscopy, combined with photoluminescence spectroscopy and X-ray diffraction measurements were carried out on different materials stacks to assess their intrinsic stability under light soaking. Additionally, the literature suggests that PbI_2 plays a critical role in triggering perovskite decomposition. Therefore, an examination of the impact of the perovskite composition on this process is presented. Furthermore, to have a complete overview of the degradation, the behavior of full-stack devices under light and heat is studied, and the role of one passivating molecule and one additive on the stability is discussed. Lastly, the enhancement of the NiO_X/perovskite interface has been investigated, exploring methods to improve its stability.

5.2   Results and discussion

5.2.1 Assessing light-induced degradation in PSC layer by layer

To start, the degradation of bare NiO_x hole transport materials (HTMs) on either glass or glass/ITO substrates was studied. The samples were encapsulated in a glass/glass packaging as described in section 2.1.4 (Figure 5.1).

Absorptance spectra were measured in the "fresh" state after encapsulation and following two weeks of light exposure under a 1-sun illumination at 35 °C (Cicci setup, "aged" state). A picture of the devices inside the chamber is presented in Figure 5.1. There were no detectable shifts in the absorptance spectra for both NiO_X and $Cs:NiO_X$ (Figure 5.2).

Then, the stability of PbI_2 under light has been investigated (Figure 5.2). A strong increase in the absorptance spectra was visible for wavelengths above 514 nm in evaporated PbI_2 samples after light soaking (both for PbI_2 on glass and on glass/ITO, represented by the red and green curves in Figure 5.2, respectively). Given that PbI_2 has a band gap of 2.41 eV, it absorbs photons with wavelengths equal or lower than 514 nm. Interestingly, the absorptance at wavelengths >514 nm jumped from 5% to 30% after light soaking for PbI_2 on glass and from 8% to 56% for PbI_2 on ITO, indicating a photodecomposition of the PbI_2 material into metallic lead (Pb^0) and I_2 gas, a process that seems to be accelerated by the presence of ITO.[53,54,152]

Figure 5.1: Picture of the Different Samples in the Cicci Chamber at Room Temperature under LED Arrays.

To get closer to a realistic situation, the previous experiment was repeated for ITO/NiO$_X$/perovskite samples, both with double and triple cation perovskites (with the same bandgap of 1.63 eV) as well as with Cs:NiO$_X$. Perovskites were also deposited onto bare glass/ITO as comparison. The first CsFA formulation contained a nominal 10% excess of PbI$_2$ (Figure 5.3a) while the second CsFA and the CsFAMA were closer to the stoichiometric proportions (with a 0.5% excess of PbI$_2$, Figure 5.3b and c). In *Figure 5.1*, stoichiometric CsFA and CsFAMA look purplish and light bluish, respectively. PbI$_2$ excess-CsFA looks darker. The impact of the PbI$_2$ excess will be detailed in the next section. Absorptance, XRD and PL data are presented in Figure 5.3*.*
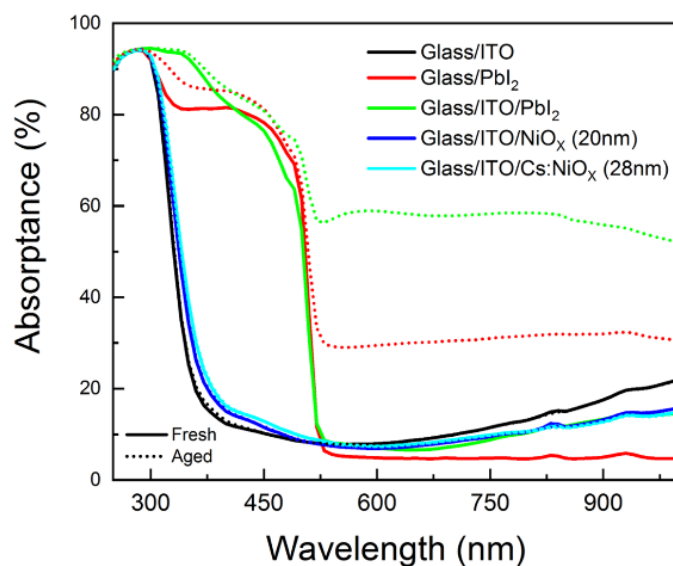
Figure 5.2: Absorptance measurements of ITO, NiO$_X$, PbI$_2$ before and after light soaking. *Light soaking was done in 1-sun conditions at room temperature for two weeks.*
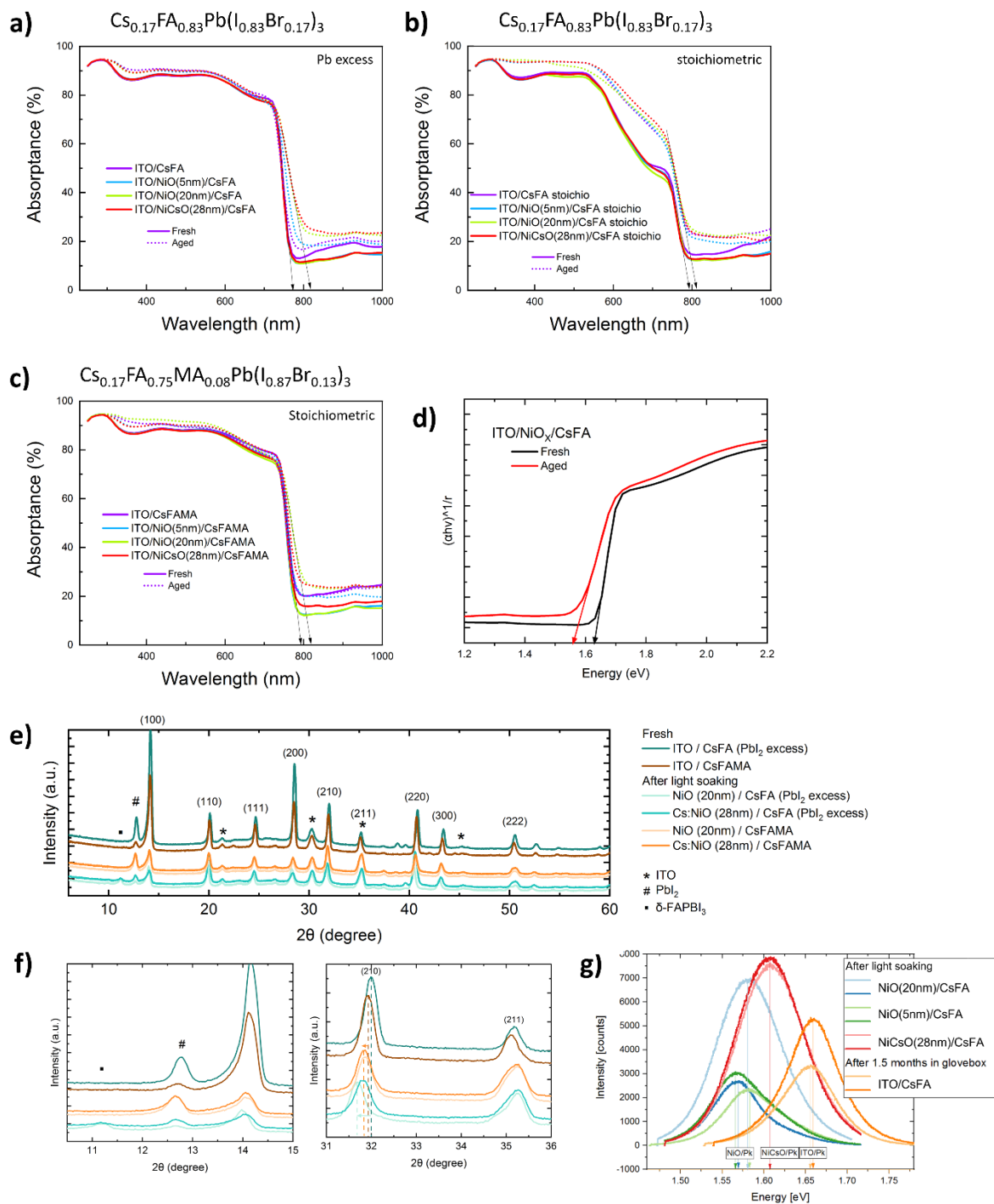
Figure 5.3: Characterization of Perovskite and HTM Interactions through Spectroscopic and Structural Analysis. *absorptance spectra of a) PbI_2 excess-CsFA, stoichiometric (b) CsFA and (c) CsFAMA perovskites on various substrates (ITO, NiO_X, $Cs:NiO_X$), d) Tauc plots of the ITO/NiO_X/CsFA sample, before and after two weeks of light soaking, to illustrate the determination of the perovskite's band gap. e) XRD pattern of HTM/perovskite stacks before and after light-induced aging under 1 sun intensity. The peaks of ITO were used to align the scans for the different samples. The plots in Figure f) are magnified views of Figure e), providing enhanced clarity on both the emerging δ-FAPbI$_3$ phase and the shift in perovskite peak for distinct HTM configurations. g) The PL peak intensity of CsFA perovskite layers coated on ITO, NiO_X or $Cs:NiO_X$ substrates after light soaking or storage in the glovebox for 1.5 month. Two samples per condition are plotted.*

First of all, aged perovskite-based samples show higher absorptance values compared to fresh ones, and this across the entire wavelength range (Figure 5.3a, b and c). This increase is similar to the data measured for aged PbI_2 samples (Figure 5.2) and was independent of the HTM used. This gain in absorptance is most likely due to photodecomposition of PbI_2. Note that absorption spectra are lower at wavelengths between 520 and 750 nm for stoichiometric CsFA, due to a thinner perovskite film. The perovskite absorber band gap was calculated using Tauc plots based on UV-Vis spectroscopy (as shown in Figure 5.3d). The curves exhibit a less steep slope near the perovskite band gap (approximately ranging from 730 nm to 800 nm) after light soaking. This results in a reduction of the perovskite band gap. This reduction is more pronounced for PbI_2 excess-CsFA (Figure 5.3a) compared to the two other perovskites (Figure 5.3b and c). Moreover, the band gap of the PbI_2 excess-CsFA perovskite on ITO remains unaltered whereas on ITO/NiO_X (20nm), it decreases from 1.63 eV to 1.57 eV (Figure 5.3a). One possible explanation suggested in literature could be the deprotonation and redox reactions involving organohalides in the perovskite and Ni^{3+} species in the NiO_X layer.[114,144,153] This interfacial reaction, exacerbated by light, may degrade the perovskite and change its absorption onset. A trend in the degradation may support this hypothesis: thicker NiO_X layers were found to result in a more significant reduction in the band gap measured by UV-Vis-NIR spectroscopy.

It is interesting to note that this relationship between NiO_X thickness and band gap shift was not as straightforward in the PL data (Figure 5.3g). After 1.5-month in the glovebox, PbI_2 excess-CsFA on ITO exhibited no changes in band gap, while on NiO_X (or Cs:NiO_X), the perovskite band gap shifted to lower energy after two weeks of light exposure. It is worth noting that band gap values differs slightly between absorptance and PL measurements due to the Stoke shift.[154]. The difference between bandgap values extracted from UV-Vis-NIR absorption and PL may be explained the formation of a heterogeneous microstructure, with highly luminescent domains controlling the PL signal.[51] Overall, less variations in band gap were measured before and after light exposure for the stoichiometric CsFA and CsFAMA devices, underscoring lower chemical changes either due to the lower amount of PbI_2 or the presence of MA.

To complete the analysis, XRD data was collected and plotted in Figure 5.3e and f. Due to the insertion of the MA cation into the lattice, the perovskite peaks of the CsFAMA samples are shifted to lower angles than those of the CsFA samples. Regardless of the presence of PbI_2 in all the samples, three crucial findings can be observed: First, for both PbI_2-excess CsFA and stoichiometric CsFAMA samples, the perovskite peak intensity significantly decreased after the light soaking and the PbI_2 peak intensity increased. In the CsFAMA case, the PbI_2 peak became almost as large as that of the perovskite (100). Second, the emergence of a distinct peak around 11.2° for the two light-soaked PbI_2-excess CsFA samples. This peak is attributed in the literature to the δ-non-photoactive hexagonal phase of the $FAPbI_3$ perovskite, also called "yellow phase".[31,155] This yellow phase, prevalent in $FAPbI_3$ perovskite at room temperature, detrimentally affects solar cell performance and is normally avoided by mixing FA with other cations such as Cs or MA.[30] Third, the perovskite peak shifted to lower angles after aging, signifying an expansion of the perovskite lattice (Figure 5.3e, f). The largest shift was observed for the NiO_X/CsFA sample. The creation of an I-rich perovskite could explain this lattice variation and the band gap decrease observed by UV-VIS-NIR and PL spectroscopies.

Next, the stability of the perovskite absorber capped with the top contact and electrode was studied. 20 samples based on glass/ITO/NiO/CsFAMA/C_{60} stacks were prepared. The perovskite precursor used,

$Cs_{0.04}FA_{0.8}MA_{0.16}Pb(I_{0.83}Br_{0.17})_3$, was the standard one used in our laboratory. XRD data is plotted in *Figure 5.11*. It contained 0.7% PbI_2 excess and 2,3,4,5,6-Pentafluorobenzylphosphonic acid (p-FBPA) as an additive.[16] Details about this molecule will be discussed later. To isolate the individual contribution of each upper layer on stability, incomplete devices with either just SnO_2 as top layer, or SnO_2/ITO were fabricated. As a comparison, some samples with the complete stack $SnO_2/ITO/Ag$ were also produced. As in the previous experiments, samples were encapsulated but the encapsulation foil was omitted in this experiment for simplicity. A total of five samples were prepared per each condition. For each set, half of the samples were exposed to light from the film side, while the remaining half were exposed from the substrate side. The devices were placed in a light soaking chamber at 65°C for one week (Solaronix setup). A scheme of the experiment is presented in Figure 5.4 along with an image of the laminated samples. Importantly, shadow masks were used to selectively expose to light only the active area of the device to light.
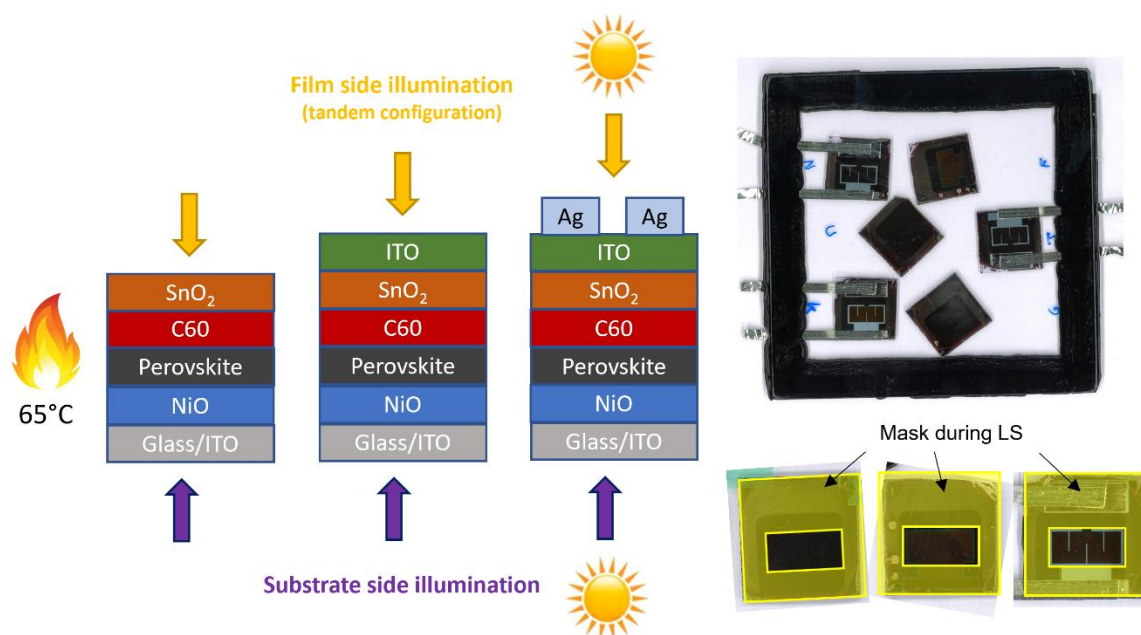
Figure 5.4: Stacks of the Device Architecture Studied and Picture of the Laminated Samples.

Figure 5.5 shows the PL intensity map, optical micrographs and PL spectra of some partial devices completed up to the SnO_2 layer after one week under light. A pronounced degradation is evident based on the contrast in the optical images: the degradation pattern is precisely where the aperture mask was positioned. Regions that were shadowed by the mask kept their initial contrast. This degradation is even more noticeable in devices illuminated from the film side (i.e., in a substrate configuration). The active area is brighter and PL spectroscopy reveals a perovskite band gap of 1.61 eV. This value is 0.3 eV lower than the fresh perovskite band gap, highlighting the formation of I-rich emissive regions within the absorber material.[51] When illuminating through the substrate (superstrate configuration, bottom insets of Figure 5.5), degradation is less obvious with a band gap of approximately 1.62 eV after one week of light soaking.
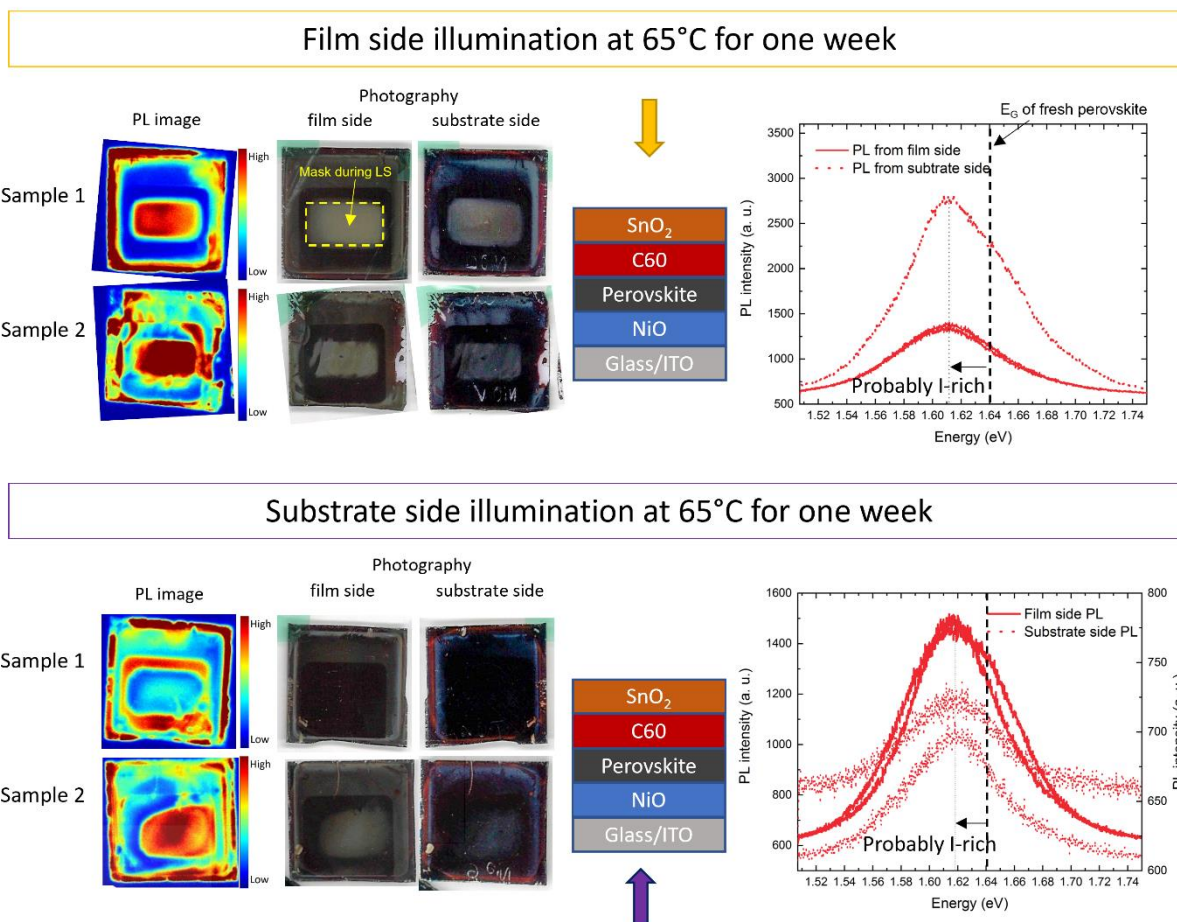
Figure 5.5: Characterization of Encapsulated Devices Until SnO$_2$ layer, Following Light Soaking at Elevated Temperatures. *PL intensity mapping, film/substrate side photography and sketch of the of encapsulated devices after one week of light soaking at 65°C with a mask centered on the substrate (yellow square). Devices were incomplete and finished with the SnO$_2$ layer. The figure is divided in two parts. On the top, the devices were illuminated from the film side, while the bottom figures show the results after light-soaking from the substrate side.*

The PL intensity in the illuminated area increased for most samples irrespective of the light bias orientation, while these regions became optically brighter in the micrographs. Bandgap shifts are less severe than without the C$_{60}$/SnO$_2$ stack. Still, the slight changes in the perovskite luminescence peak indicate that the SnO$_2$ layer is not fully protecting the perovskite and the PL bandgap shifts to lower value, likely as a result of phase segregation. This shift may explain the PL increase as a result of charge funneling to the emissive I-rich regions.[51]

Also, volatile species likely escape from the perovskite, leading to a lower PL intensity when illuminating and probing the PL signal from the film side (top panel in Figure 5.5).[45,52,156] This results indicate that the light soaking direction has an impact on the degradation process: a faster degradation occurs when the perovskite is illuminated in substrate conditions. This may be rationalized by the fact that most of the photons are absorbed near the perovskite/C$_{60}$/SnO$_2$ interface, which may lead to stronger structural rearrangements close to this interface and the subsequent outgassing of volatile species from this region. When illumination conditions are reversed, meaning when the film is illuminated in a superstrate

configuration (bottom panel in *Figure 5.5*), changes in the perovskite films occur preferentially close to the glass/ITO/HTM stack: the latter forms an impermeable barrier, which slows down degradation.
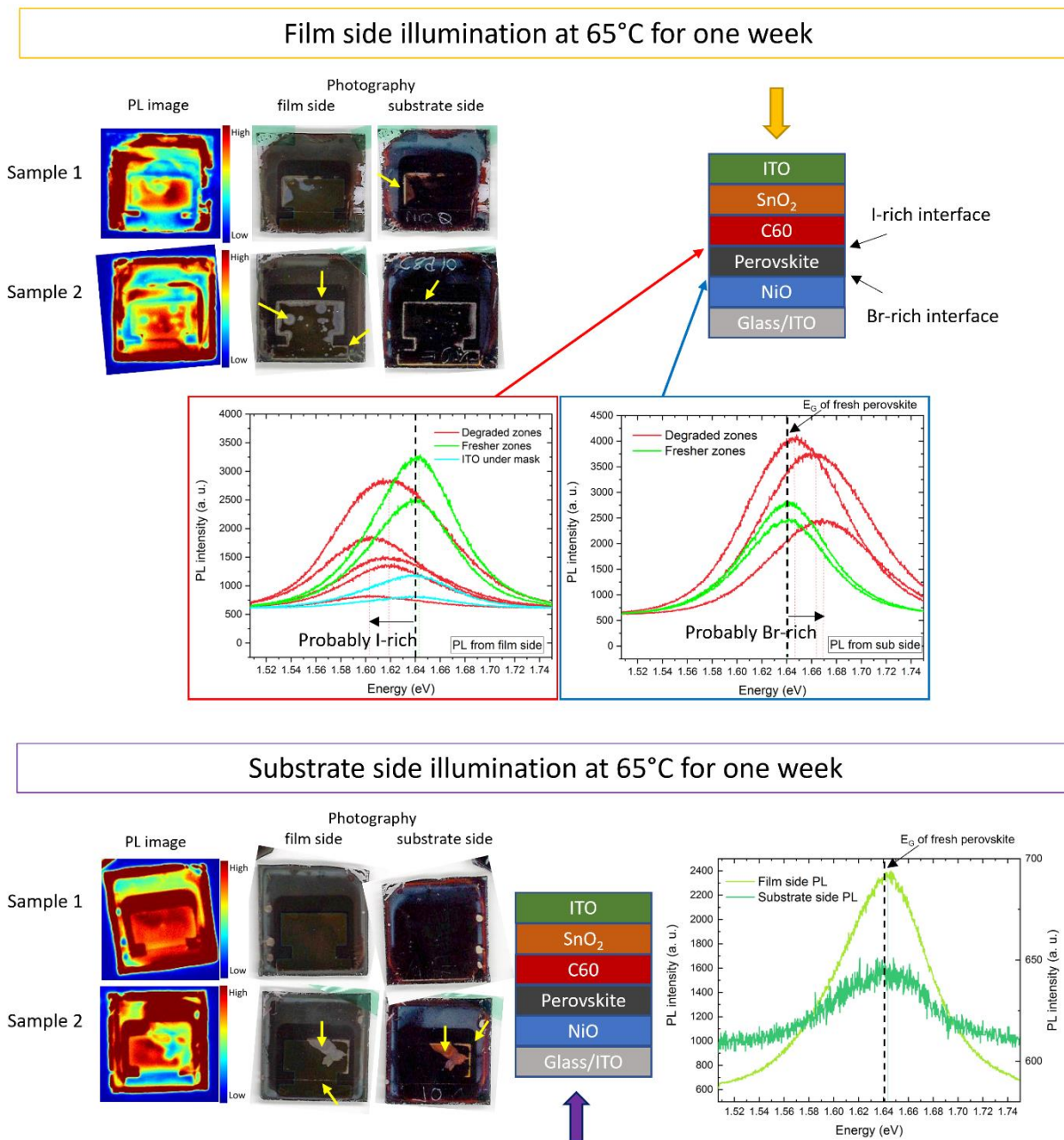

Figure 5.6: Characterization of Encapsulated Devices Until ITO layer, Following Light Soaking at Elevated Temperatures. *The impact of the top stack during light soaking was investigated here with devices finished with SnO_2/ITO layers. The Ag grid was deliberately missing. These encapsulated devices were light soaked from either the film side (top part of the figure) or the substrate side (bottom part) through a shadow mask for one week (170 h) at 65°C. The stack of the devices is presented for each light soaking condition and the light direction is represented with an arrow. PL intensity, photographic, and sketch of the devices are displayed for each illumination side alongside PL spectra.*

The next experiment of this study was to sputter a 120 nm thick ITO layer on top of C_{60}/SnO_2 and to investigate the stability of the stack under illumination and exposing the encapsulated device to one week of light soaking at 65°C (Figure 5.6). Like before, illumination from the film side resulted in more

pronounced damage than an illumination from the substrate side. Notably, examining samples illuminated from the film side, it was noticeable that the ITO perimeter appeared optically brighter and with a lower PL intensity, even in areas not exposed to light. This change may be attributed to the formation of PbI_2. Also PL spectroscopy from the film side of the device showed a shift from 1.64 eV in pristine regions to 1.60 eV in degraded regions. On the contrary, PL measurements from the substrate side demonstrated an increase in band gap, from 1.64 eV in pristine regions to 1.67 eV in the more degraded regions. This result seems to indicate that in the degraded parts of the active area, the interface with C_{60} became iodide-rich while the interface with the NiO_x became bromide-rich as result of a phase segregation process. This phenomenon was not detected with partial stacks.

On the one hand, the fact that degradation follows the edge of the ITO could be attributed to the thickness gradient in the sputtered TCO. Since the TCO is thinner at the edges, it potentially fails to provide sufficient protection to the perovskite underneath from light exposure, leading to preferential degradation in those areas. On the other hand, as degradation follows the ITO edges even below the aperture mask (i.e. in an area not exposed to light), it seems more likely that lateral ion migration, induced by the electric potential difference inside and outside of the active area, is the cause of this degradation.[63]
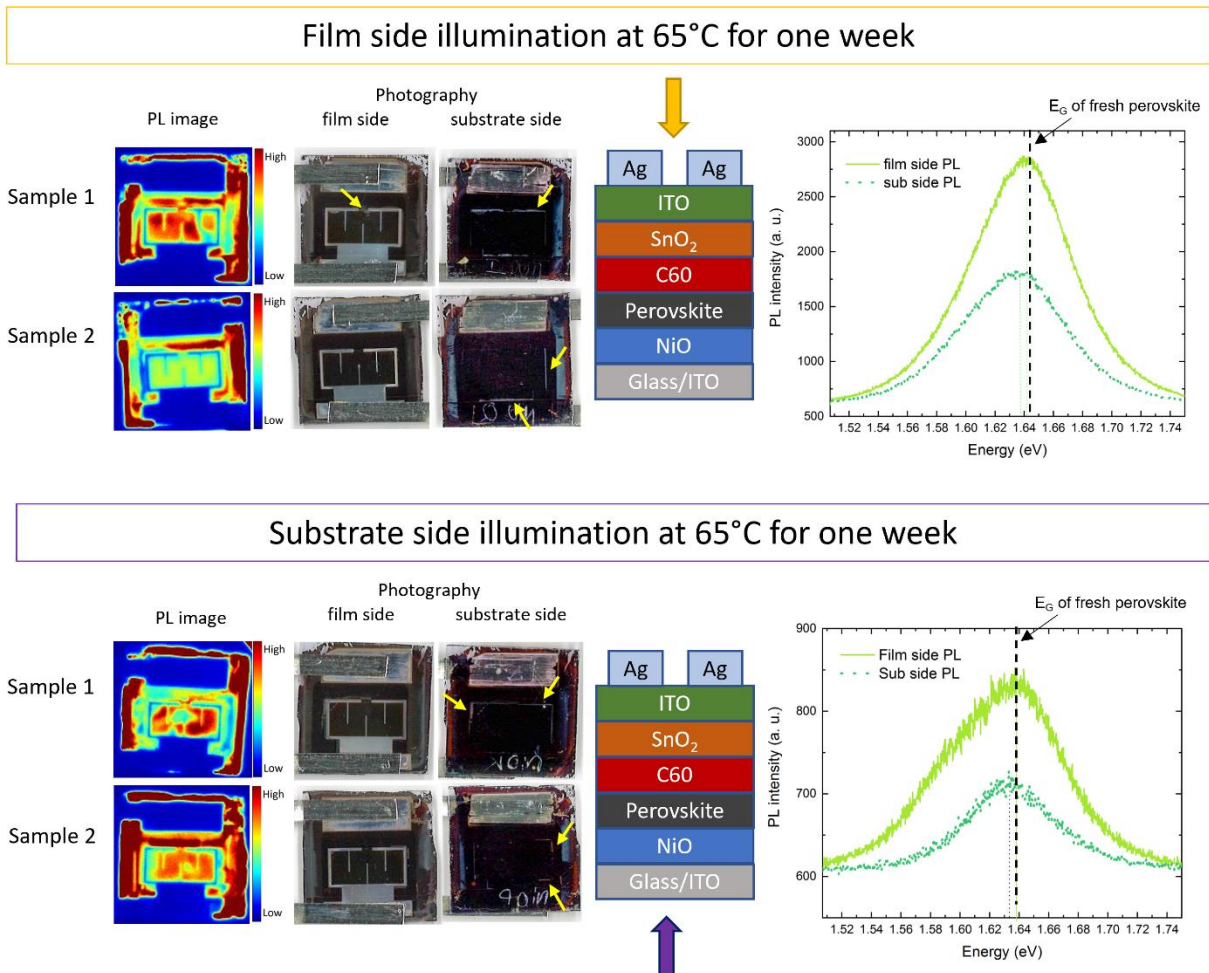
Figure 5.7: Characterization of Encapsulated Devices with the Complete PSC Stack, Following Light Soaking at Elevated Temperatures. *PL intensity mapping, film and substrate side photography and sketch of the encapsulated PSCs*

It is worth noting that degradation could also be promoted by macroscopic defects in the active area. The presence of prominent dots in the active area of sample 2 under film side illumination, or the appearance of a flake in the case of sample 2 when illuminated from the substrate side (Figure 5.6) may be attributed to the presence of dust particles and flaws. To mitigate this potential issue, additional precautions need to be implemented to reduce the likelihood of surface contamination during the manufacturing process of these devices.

The last condition of this study was the full semi-transparent device: ITO/NiO/perovskite/C$_{60}$/SnO$_2$/ITO/Ag. PL data and images of the devices are presented Figure 5.7. The full stack degraded less after one week under light compared to partial stacks. The band gap measured from PL was around 1.64 eV for both samples irradiated from the film and the substrate side. However, by looking deeper on the pictures taken from the substrate side of the devices, yellowish lines at the edges of the active area and on the laser scribe line are visible, again likely due to PbI$_2$ formation as a result of lateral migration of ions and preferential outgassing at the edges of the active area where the top electrode is thinner.

The Ag lines also degraded due to an oxidation by I$_2$ vapors.[44,157] From SEM images of the silver grid taken after 900h of light soaking from the film side (Figure 5.8), AgI$_x$ spikes formed at the edges of the Ag fingers.[45,158–160,161] In line with literature, these results indicate that the perovskite is losing iodine in the form of likely I$_2$ vapors and that these vapors eventually attack the Ag electrode.

In summary, the impact of light soaking was studied for each layer of the stack and their combinations. First, it was observed that the direct contact between NiO$_X$ and the perovskite caused more severe optical changes different from those of perovskite/ITO stacks. This degradation is likely attributed to redox reactions between nickel ions and organohalides as discussed in Chapter 4. Second, PbI$_2$ was found to decompose rapidly under light, an effect that seems to dictate the light-soaking stability of the perovskite material. This effect may screen other compositional parameters (e.g. presence of MA). This point will be discussed further in the next sections of this chapter (5.2.1). Third, the SnO$_2$ and TCO electrode layer deposited on top of the perovskite protect the perovskite by slowing down the release of volatile species. Fourth, when the electrode is present, lateral differences in the electric field at the edges of the active area lead to ion migration and accumulation, which eventually leads to a decomposition of the perovskite layer in these regions. Finally, the Ag electrode oxidizes over time as it becomes exposed to I$_2$ vapors released by the perovskite. The next sections will now focus on full devices, with the goal of relating degradation results to mechanisms triggered by individual layers or their combinations.
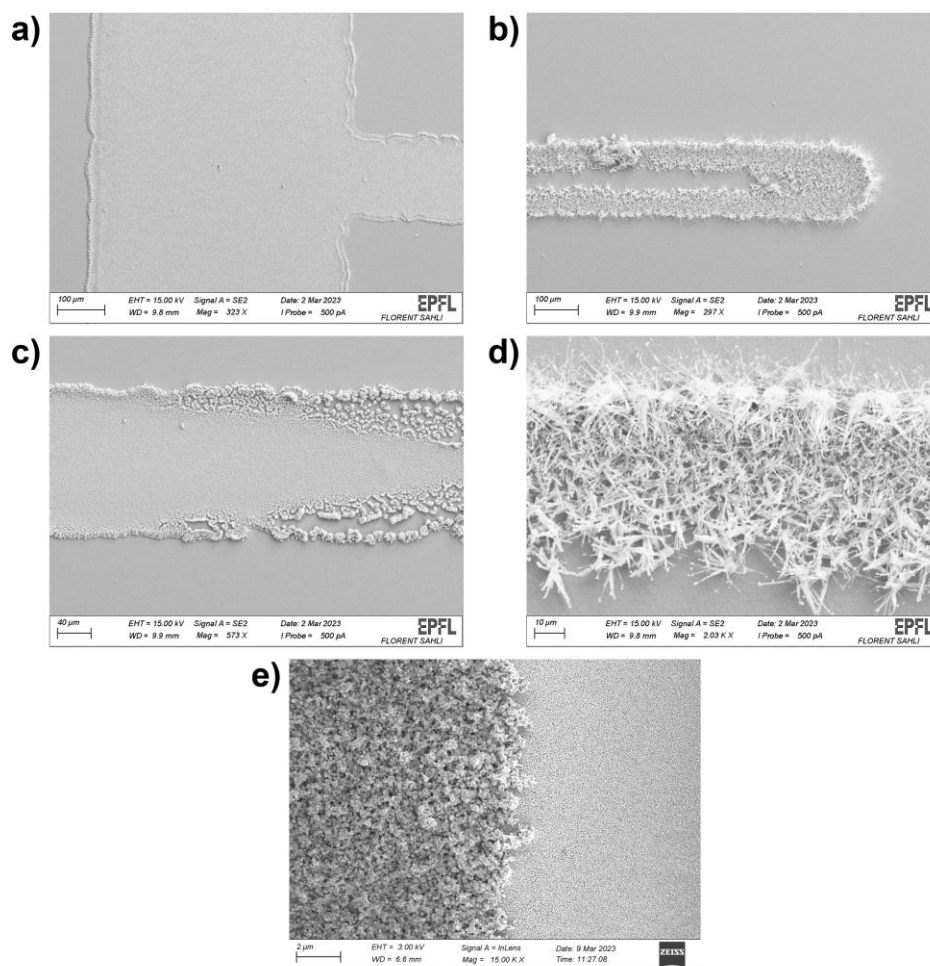
Figure 5.8: SEM top-view image of Ag finger after 900h of light soaking from the film side at 35°C. *The narrow part of the fingers appeared much more impacted by the degradation induced by I$_2$ vapor.*

5.2.2 Impact of the perovskite composition on light soaking stability in perovskite solar cells

The role of an excess in organohalide or PbI$_2$ was evaluated in light soaking tests with three modified Cs$_{0.17}$FA$_{0.83}$Pb(I$_{0.83}$Br$_{0.17}$)$_3$ compositions. The first solution was prepared with a 10% PbI$_2$ deficit (or FAI excess), the second with a 10% PbI$_2$ excess, and the third with a stoichiometric ratio. The solar cells consisted of semi-transparent device stack (NiO/PK/C$_{60}$/SnO$_2$/ITO/Ag grid) and were encapsulated in a glass/glass packaging as described in 2.1.4. To minimize variations resulting from the lamination process, eight cells were encapsulated in the same glass/glass packaging employing two large pieces of tempered glass (13 cm x 13 cm). To enhance statistical significance, 2 or 3 cells per condition were encapsulated within the same packaging.
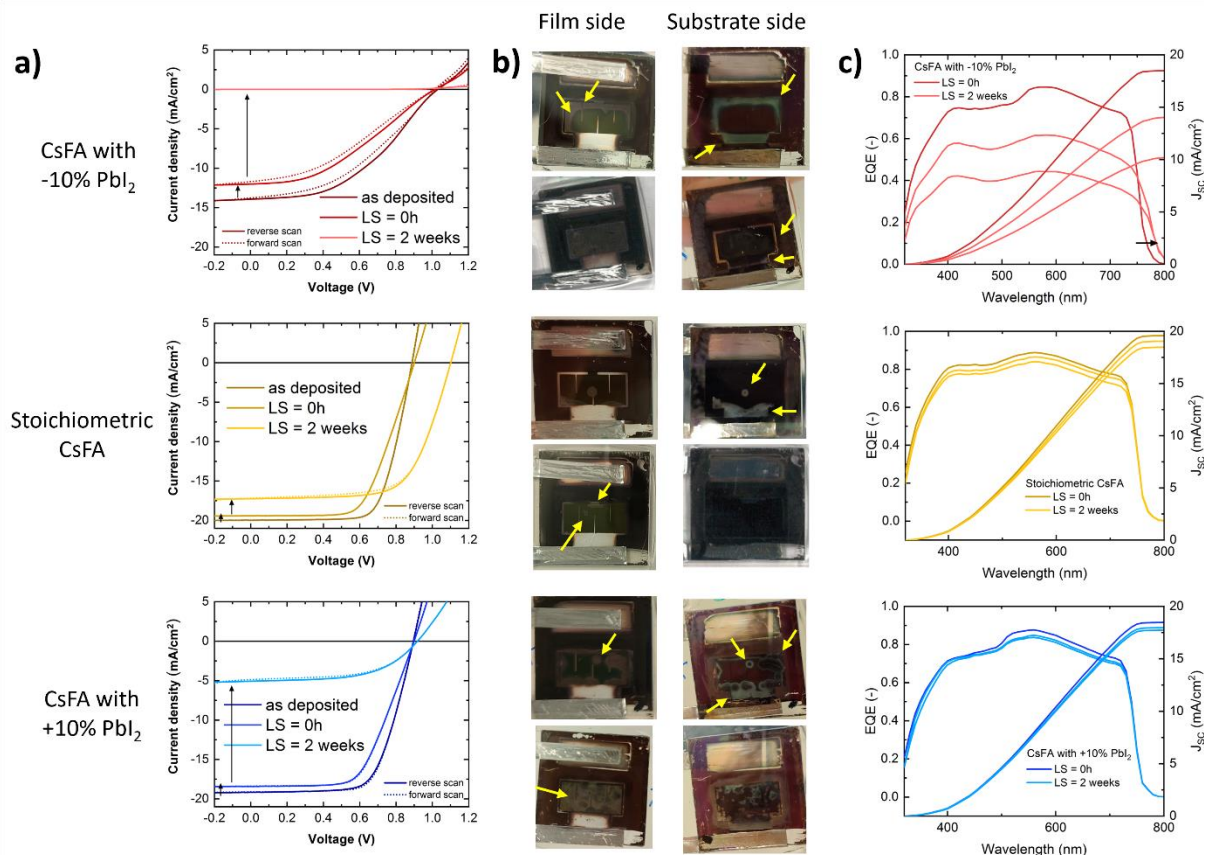
Figure 5.9: Impact of PbI₂ Concentration on Perovskite Device Stability Under Light-Soaking Conditions. *The figure presents the degradation results of cells after two weeks (336h) of light soaking under 1 sun illumination at MPPT and 65°C for various PbI₂ concentrations in the perovskite solution. The stack on each encapsulated cell is the following: NiO/PK/C₆₀/SnO₂/ITO/Ag fingers. Only the active areas of the cells were light soaked from the substrate side (NiOx) using an aperture mask. a) J-V curves of PSCs as deposited, after encapsulation and after the light soaking. The J-V scans were measured in superstrate configuration. b) Visual degradation of the cells after light soaking, as depicted by pictures taken from both the film and substrate side of the devices for each PbI₂ concentration. c) EQE curves from the substrate side of the cells, before and after the stress tests.*

Looking at *J-V* data before encapsulation, after encapsulation and after light soaking, a slight decrease in efficiency, marked by an increase in R_{OC} along with a decrease in J_{sc}, is evident in all the devices after the encapsulation process, irrespective of the perovskite composition (as shown in Figure 5.9a). The changes in J_{sc} may stem from a change in the device optics induced by the encapsulation process, while *FF* changes may be due to resistive losses induced by the ribbons. Subsequently, the active areas of the cells were light soaked from the substrate side (NiO$_x$) using an aperture mask. The test was run under 1 sun illumination in the Solaronix chamber at 65°C, and devices were under maximum power point tracking (MPPT), for two weeks (corresponding to 336h hours). Figure 5.9 and Figure 5.10 present *J-V* scans, pictures of the cells and EQE plots after light soaking test.

For the CsFA perovskite-based devices with a 10% PbI₂ deficit, the efficiency dropped to 0% after two weeks under operation (Figure 5.9a). From Figure 5.9b it can be seen that the degradation started at the edges of the active area, i.e. at the ITO/Ag edges. Notably, the silver grid seems to have entirely disappeared while discolored regions are visible at the active area boundaries. As discussed above, volatile halide species escaping from the perovskite may reach the Ag top contact and form AgI$_x$,[44,43] while the lateral migration of ions triggers degradation at the edges of the active area.[63] Furthermore, from EQE, the

band gap of this perovskite decreased from 1.62 eV to 1.56 eV after two weeks of light soaking, suggesting a loss of bromide from the perovskite absorber [49,69] EQEs measured after the degradation test showed that spectral response dropped significantly (Figure 5.9c). When comparing this information to the J_{sc} values obtained from J-V measurements, it seems that a barrier is impeding carrier extraction.

For the +10% PbI$_2$ perovskite composition, significant and visible degradation occurred across the entire active area surface, with some yellow parts indicating the presence of PbI$_2$. The devices showed a dramatic drop in current, and the Ag grid became less visible, also in this case. PbI$_2$ is likely to have acted as a source of degradation (see section above) and of mobile iodine species.[54,45] Contrary to the PbI$_2$ deficient condition, the spectral response of the samples containing an excess of PbI$_2$ within the perovskite absorber showed almost no variation (<1mA/cm^2 loss after the light soaking test, Figure 5.9c bottom inset), while the J_{sc} values extracted from J-V measurements dropped significantly. Two hypotheses can be put forward: 1) degradation could have created a large number of electronic trap states throughout the perovskite bulk and a high number of mobile ions, enhancing recombination under high regimes of illumination and leading to a screening of the electric field;[49,62,64] 2) degradation leads to a loss of active area. Regarding this second point, the EQE data shown in Figure 5.9c was acquired from regions that appeared fresh. On the contrary, the J-V measurements were conducted across the entire active area using a 1.04 cm^2 mask, meaning it included electrically dead regions that did not contribute to the generation of current. Indeed, *Figure 5.10* shows the difference in spectral response between a pristine region and a degraded one in the same cell, with no current being extracted from the later.
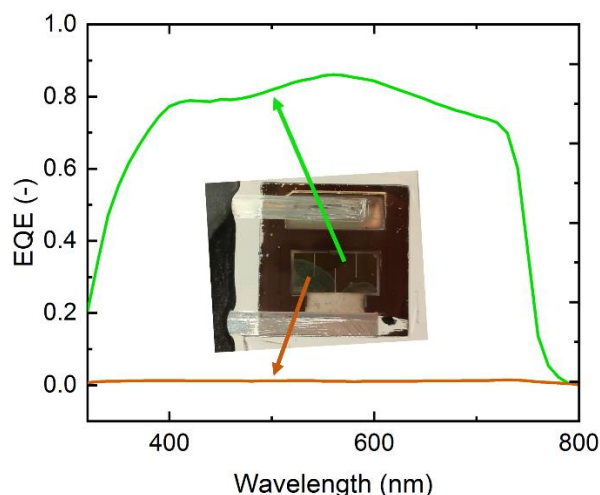

Figure 5.10: Spatial Variations in EQE Response Reflect Degradation Heterogeneity in Light-Soaked Perovskite Cells. *Here is plotted EQE curves of one of the cells presented in Figure 5.9 after light soaking degradation. EQE measurements were taken from different regions within the active area. The results reveal that the most degraded regions exhibit a significantly weakened spectral response (EQE close to 0), indicating a substantial loss of current generation. Conversely, in fresher regions, current extraction remains feasible, demonstrating a better response to light.*

Finally, with less visible degradation in the devices, the stoichiometric perovskite composition demonstrated the most promising results in term of light stability, (Figure 5.9b). The loss in J_{sc} was lower than other compositions and the *FF* increased slightly by 4% (from 62.16% to 66.19%) thanks to a lower R$_{OC}$ at the end of the test. Interestingly, the loss in J_{sc} was in part compensated by a significant gain in V_{oc} of about 200 mV. This gain in V_{oc} can be attributed to a passivation of trap states at the NiO/perovskite interface induced by the light soaking conditions.[162,163] The champion cell maintained an efficiency of

12.56% after two weeks of operation at 65°C. Still, even if this perovskite composition was more stable under light and heat, a degradation of the silver electrode was still observed.[27,43,74]

In summary, the PbI_2 concentration in the perovskite film has a significant impact on the operational stability of PSCs at elevated temperatures. To achieve more stable results during light soaking, it is imperative to use a stoichiometric perovskite composition. The cells lost mainly in J_{sc}, which can be explained by two effects: carrier extraction issues e.g. linked to field-screening induced by mobile ions. Also edges of the active area were found to degrade, highlighting the accumulation of mobile ions. Additionally, the metal electrode was found to be particularly prone to degradation as a result a reaction with volatile iodine species.

5.2.3 Impact of SiO_X and pFBPA on the light soaking stability

Several modifications were made by our group to demonstrate 2-terminal perovskite/Si tandems reaching an efficiency of >30%.[16,164] First, SiO_X-nanoparticles were deposited on the hydrophobic Me-4PACz SAM prior to the perovskite coating to improve its quality. This spin-coated layer of SiOx NPs improves the wetting of the perovskite solution, reducing pinholes and electrical shunts. Additionally, the incorporation of a 2,3,4,5,6-Pentafluorobenzylphosphonic acid (p-FBPA) additive into the perovskite precursor solution can drastically boost the V_{OC} and passivate the perovskite interface with the C_{60}.[16] As the ultimate goal is to demonstrate high efficiency devices with long term stability, both SiO_X and pFBPA were used here and their impact on the light-soaking stability of devices was investigated.

For this study, self-assembled monolayers (SAM) (either MeO-2PACz[83] or Me-4PACz[86]) and/or sputtered 20-nm NiO_X were used as HTM and coated on top of commercial glass/ITO substrates. A 500 nm thick triple halide stoichiometric perovskite ($Cs_{0.04}FA_{0.8}MA_{0.16}Pb(I_{0.83}Br_{0.17})_3$) was then spin-coated on top, followed with the standard 20 nm C_{60} / 10 nm ALD SnO_X / 120 nm ITO / 130 nm layer Ag fingers stack. The X-ray diffraction pattern of a fresh cell is shown in Figure 5.11. No PbI_2 peak is detected as a stoichiometric solution was used.
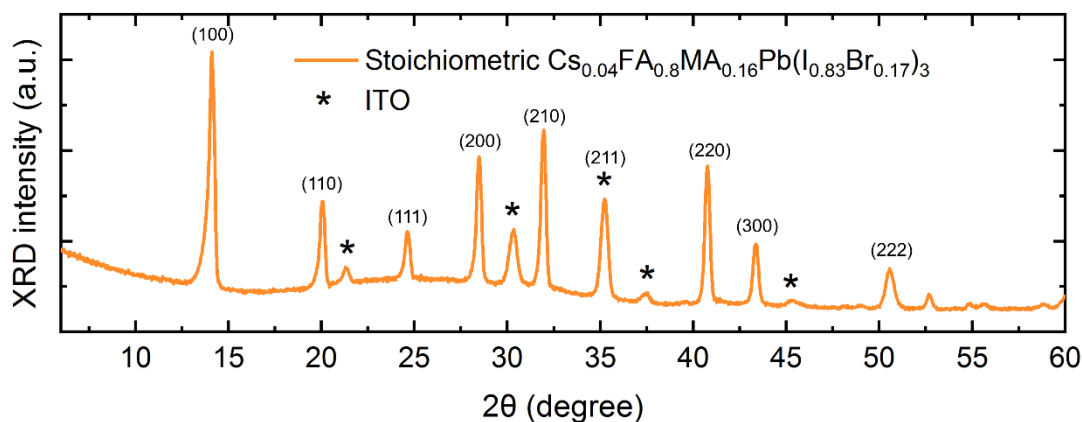

Figure 5.11: X-Ray Diffraction Pattern of a PSC Based on a Stoichiometric $Cs_{0.04}FA_{0.8}MA_{0.16}Pb(I_{0.83}Br_{0.17})_3$ Perovskite Solution.

For protection against oxygen and humidity ingress, the devices were encapsulated with our standard process. To facilitate the investigation of different degradation mechanisms, semi-transparent cells were exposed to light from either from the substrate (NiO$_X$) or the film (C$_{60}$) side, in the Solaronix chamber, under ambient air conditions. The cells were light soaked at open circuit for over 300 hours at 65°C under a 1 sun illumination.

After less than 400 hours of illumination from the substrate side through an aperture mask, significant degradation was observed in the active area of the encapsulated devices. The degradation systematically initiated from the edges of the active area and/or from defects like pinholes (Figure 5.12 and Figure 5.13a). Notably, the degradation pattern followed that of the ITO layer (Figure 5.13c, d), even in non-illuminated regions. This effect was more pronounced in cases where the ITO pattern and the Ag grid were misaligned (Figure 5.13d). Overall, these modes of degradation were observed before, also with individual layers. Degradation starting at impurities and at the edges of the devices govern the visual changes observed here and these can be linked to the accumulation of mobile ions passed a certain threshold beyond which the perovskite starts to decompose. The EQE of the device dropped significantly over time under light (Figure 5.13e), mostly as a result of the formation of large inactive regions within the device, as highlighted in Figure 5.13f. Overall, the devices degraded quickly, requiring further investigations of the impact of each new building block of the stack.

Figure 5.12: Encapsulated Cells After > 400 h of Substrate Side Light Soaking at 65°C and at V$_{OC}$ in the Solaronix Chamber. *Stack: glass/ITO/NiO$_X$/(SiOx)/CsFAMAPb(IBr)$_3$ + pFBPA/C$_{60}$/SnO$_2$/ITO/Ag.*
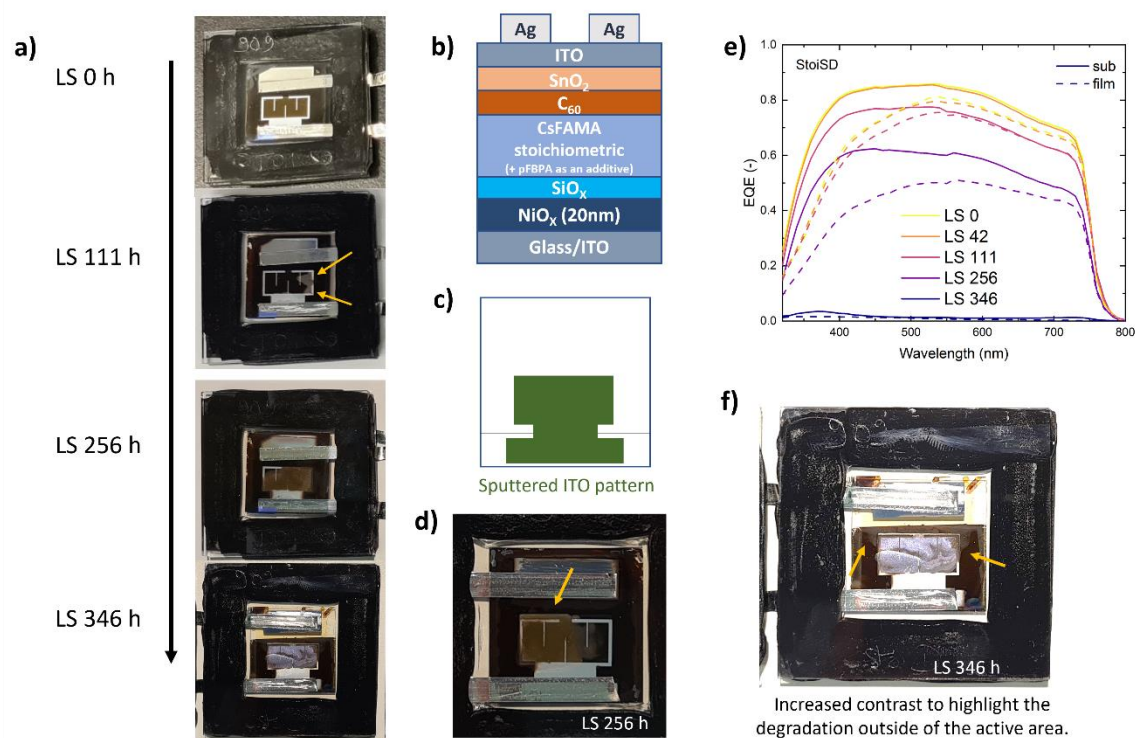
Figure 5.13: Degradation Progress of Perovskite Solar Cells Under Extended Light Soaking. *Encapsulated cells were light soaked from the substrate side (NiO$_X$ side) through a mask at 65°C and at V$_{OC}$. a) pictures of a degraded cell at different times under light, b) the device architecture of the studied devices, c) a sketch of the sputtered ITO on the device, which is defining the active area, d) a picture of a cell where ITO and Ag were misaligned. With this photo, it can be clearly seen that the degradation follows the ITO pattern, even when it is out of the active and illuminated area; e) EQE curves of the cell presented in the picture a) at different time after light soaking and f) picture of this same cell after 346h of light soaking. Contrast has been slightly modified to highlight the degradation starting outside of the active area.*

Impact of pFBPA additive

To isolate potential factors contributing to this degradation, SiO$_X$ was excluded from this batch. As previously discussed, higher V$_{OC}$ were obtained for the fresh pFBPA-based devices (Figure 5.14c, time 0).[16] Moreover, throughout the test period and in particular during the first 200 hours of light soaking, all devices exhibited an impressive *V*$_{oc}$ gain of around 130 mV for devices illuminated from the film side (C$_{60}$) and up to 180 mV when illuminated from the substrate side, thanks to a good passivation of the trap states during light soaking, at the most defective interface (e.g. NiO$_X$/perovskite one).[162,163] However, from *J-V* scans, devices containing pFBPA in the perovskite precursor solution exhibited a drop in performance over 50% after less than 100 hours of light soaking, mainly due to a significant drop in *J*$_{SC}$ and *FF*. Initially, *J*$_{SC}$ was around 19 mA.cm^{-2} on average, but it dropped to less than 10 mA.cm^{-2} after only 130 hours of light soaking. In addition, the integrated current extracted from EQE measurements varied from 19.44 mA.cm^{-2} before the test, to 13.80 mA.cm^{-2} after 320 hours of light soaking (Figure 5.14 orange curves). Despite similar trends, a mismatch in current from *J-V* and EQE measurement was noticed at the end of the test.[64] *FF* dropped also dramatically to less than 45% on average after the end of the test. No shunt was observed during dark *J-V* measurements.

On the contrary, cells that did not contain pFBPA demonstrated better resilience to light-induced degradation. The J_{sc} of those cells are plotted in turquoise in Figure 5.14 for different times under light. As in pFBPA-based devices, the steeper drop in J_{sc} occurred during the first 200 hours of light exposure. However, devices without pFBPA exhibited a much slower degradation in current and still had 15-17 mA.cm^{-2} after 1200 hours. As previously explained, the reduction in J_{SC} during the degradation test can be attributed to several factors, from the loss of active area due to a local decomposition of the perovskite to carrier extraction limitations induced by mobile ions.[64] In the case of aged pFBPA devices, our laboratory demonstrated that peeling the top contact (Ag/ITO/SnO$_2$/C$_{60}$), cleaning the surface with alcohols, and subsequently reapplying the top-electrode stack led to a recovery of the initial performance, without the passivation effect normally obtained with the pFBPA (~80mV improvement). This finding suggests that degraded pFBPA hinders carrier extraction at perovskite/C$_{60}$ interface.[164]

Regarding the impact of the illuminated side, no drastic difference in stability was observed between superstrate and substrate conditions after light exposure (Figure 5.14 solid vs. dashed lines). However, visual degradation highlighted strong differences. Similar to Figure 5.13, a substrate side illumination of the cells led to intense degradation in the active area and more specifically where the TCO was sputtered, while a film side illumination appeared less detrimental. Figure 5.15 depicts the visual degradation of pFBPA-based cells for each of the illumination configurations. After only 170 hours under light, substrate side illumination led to severe degradation on the active area. Finally, it should be noted degradation seemed to nucleate from few critical defects, indicating that process cleanliness is an important factor that also needs to be taken into account.
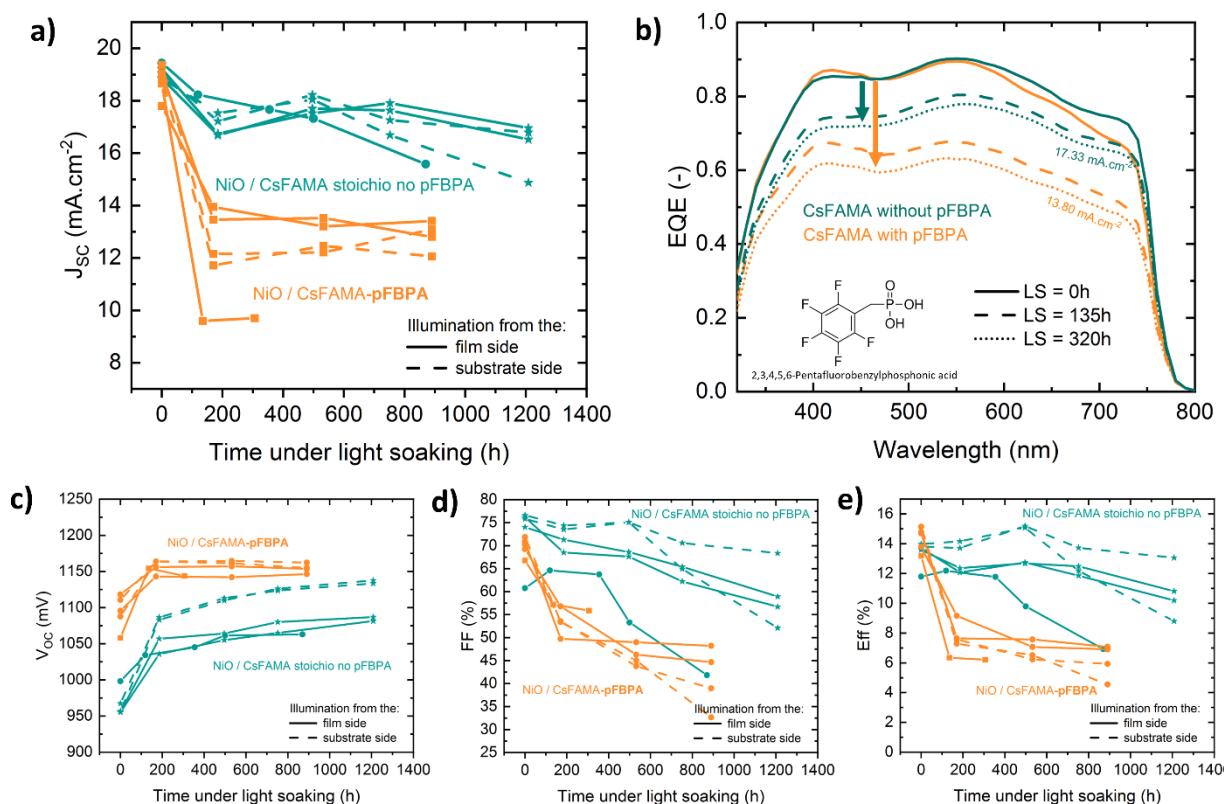

Figure 5.14: Impact of pFBPA on the Light Soaking Stability of PSCs. *Light soaking conditions: Cicci setup, LED arrays, at V$_{OC}$, 35°C, N$_2$, without any encapsulation, and no masking during the light soaking. Stack: NiO/CsFAMA (with or without pFBPA)/C$_{60}$/LiF/SnO$_2$/Ag. a) J$_{SC}$ plot of the average value of the reverse and forward J-V scan at different time during the light*

soaking test, and b) EQE measured after encapsulation, and after some time under light (film side LS) for devices with and without pFBPA in the perovskite precursor solution. The incorporation of pFBPA does not change the perovskite band gap but lead to a slight decrease of the perovskite absorber thickness (by ~50 nm).[164] c) V_{OC}, d) FF and e) Eff of the average value of the reverse and forward J-V scan at different time during the light soaking test
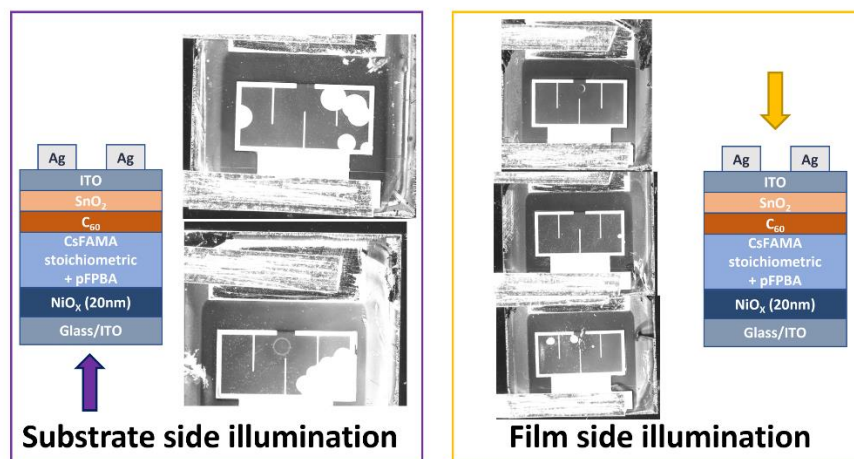
Figure 5.15: Microview Images of pFBPA-based PSCs for the Two Illumination Configurations

Impact of SiO$_X$ wetting agent

Here PSCs were made with the following architecture: NiO$_X$/Me-4PACz/SiO$_X$/stoichiometric CsFAMA without pFBPA/C$_{60}$/ SnO$_2$/IZO or ITO/Ag. Cells were placed under light soaking at open circuit in an N$_2$ chamber without any encapsulation at 35°C (Cicci chamber). No shadow mask was used during light soaking. A picture of each condition is presented in Figure 5.16. Regardless of the TCO used, strong degradation in the form of degraded islands was evident when illuminating from the substrate side (NiO$_X$), while an oxidation of the Ag grid could be noticed when illuminating from the other side. EQE measurements reveal that almost no current could be extracted from the highly degraded zones (Figure 5.16b and c), while more than 19 mA.cm^{-2} was measured in the non-degraded areas. The use of a smaller mask (here 0.16 cm^2) on the non-degraded zones during J-V measurement allowed us to measure a J_{sc} up to 16 mA.cm^{-2}. When measuring the whole active area, only 12 mA.cm^{-2} could be measured by J-V.
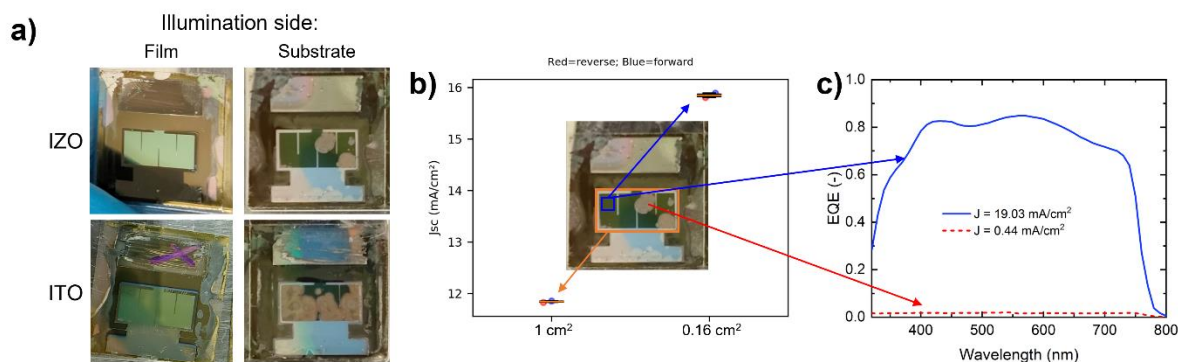
Figure 5.16: Comparative Analysis of Light-Soaking-Induced Degradation Patterns in Perovskite Solar Cells Between the Two Illumination Sides. *a) a top view pictures of PSCs taken after 500 hours of light soaking in an N$_2$ atmosphere These images reveal differences in the degradation pattern depending on the illumination side and the type of TCO used. The structure of the cells was the following: NiO$_X$ / Me-4PACz / SiOx / stoichiometric CsFAMA without pFBPA / C$_{60}$ / SnO$_2$ / IZO or ITO / Ag; b)*

To go deeper in the understanding of the influence of the illumination-side, XRD analyses were conducted, also on samples based on NiO$_X$ or Cs:NiO$_X$ without SiO$_X$ for comparison. XRD patterns and pictures of the cells are presented in Figure 5.17. First, clear differences can be seen from the images in Figure 5.17c. The active area of the cells light-soaked from the substrate side presented strong and well visible degradation in the active area in the form of brownish regions nucleating from few degradation sources, while the Ag grid looked relatively unchanged. Moreover, the emergence of a PbI$_2$ peak was visible in the XRD patterns for cells light-soaked from the substrate side and based on SiO$_X$ (Figure 5.17a). This indicates that the degraded area regions are made of PbI$_2$. Conversely, devices light-soaked through the film side had no degradation in the active area, regardless of the use of SiO$_X$, and the XRD pattern did not shown any PbI$_2$.

SEM top-view images revealed that the top TCO appeared to be "wavy" in degraded areas (Figure 5.18), suggesting that the perovskite underneath underwent some outgassing as it degraded to PbI$_2$, thus leading to TCO buckling. Furthermore, a top view image of areas without visible degradation exhibited no signs of defects, cracks, or pinholes (Figure 5.19), while comparable images captured in a degraded region displayed bright spots predominantly observed at grain boundaries (small features that appeared on top of the buckling effect discussed above).

From all the different analysis, it can be concluded that substrate side illumination of SiO$_X$-based devices leads to perovskite degradation, with PbI$_2$ formation and delamination of the top electrode.
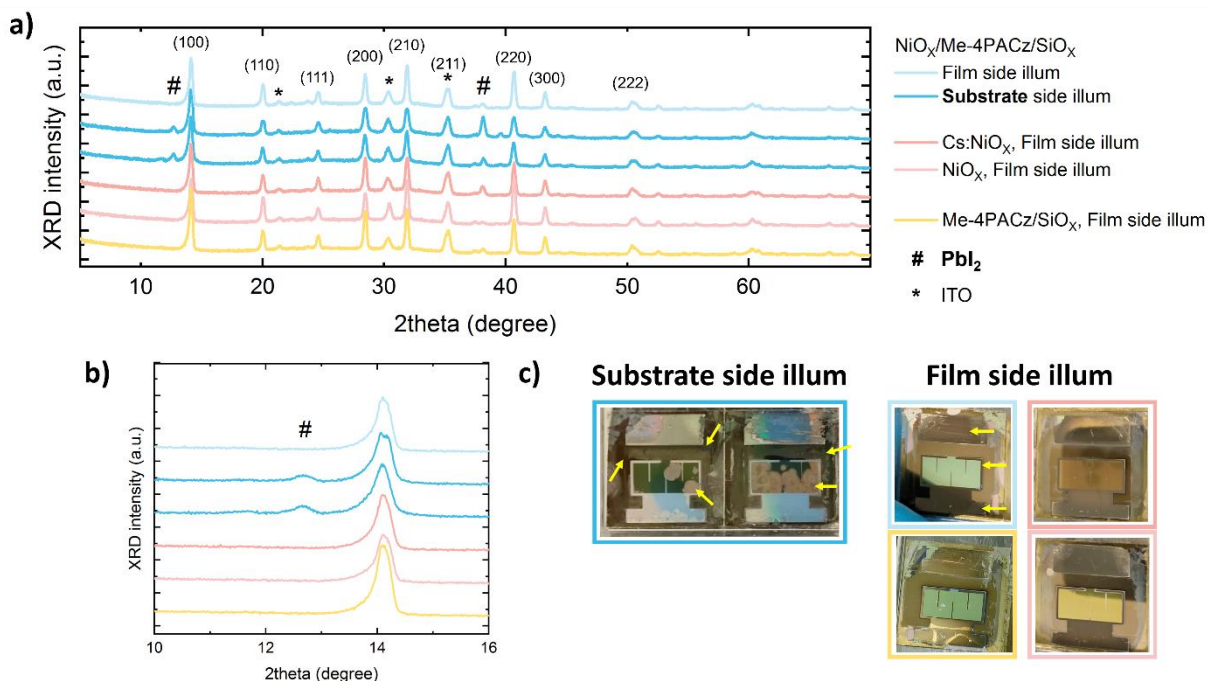

Figure 5.17: XRD Analysis of Perovskite Solar Cells with Various HTMs and SiO$_X$ Under Different Illumination Conditions. *The impact of the use of SiO$_X$ and the one of the illumination side during 900h of light soaking in the Cicci setup was studied. Device were fully illuminated: no shadow mask during light soaking All the cells are based on the stoichiometric*

CsFAMA solution without addition of pFBPA. a) XRD pattern plotted from 2ϑ =5° to 70°, b) zoom-in of figure a) to show the emergence of a PbI$_2$ peak for the two samples containing SiO$_X$-np and light-soaked from the substrate side. c) picture of cells for different illumination side during the light soaking.
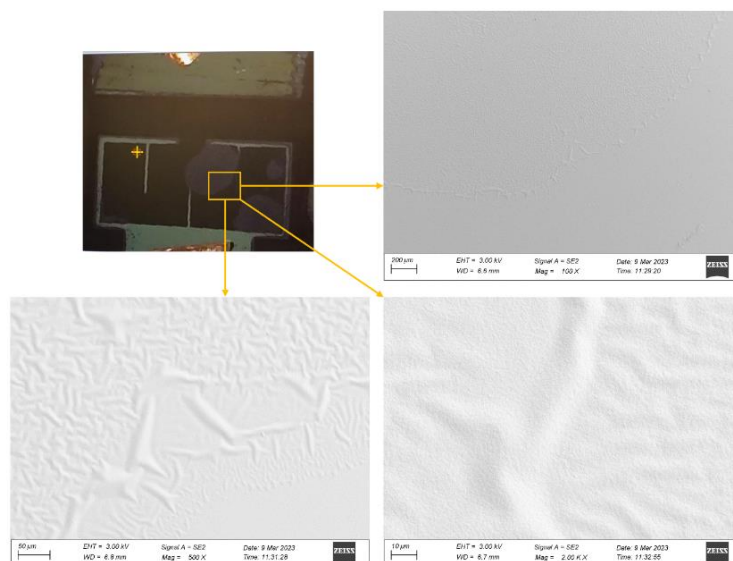

Figure 5.18: SEM Top View Images of a Degraded Cell After 900h of Light Soaking from the Substrate Side in the Cicci Chamber.
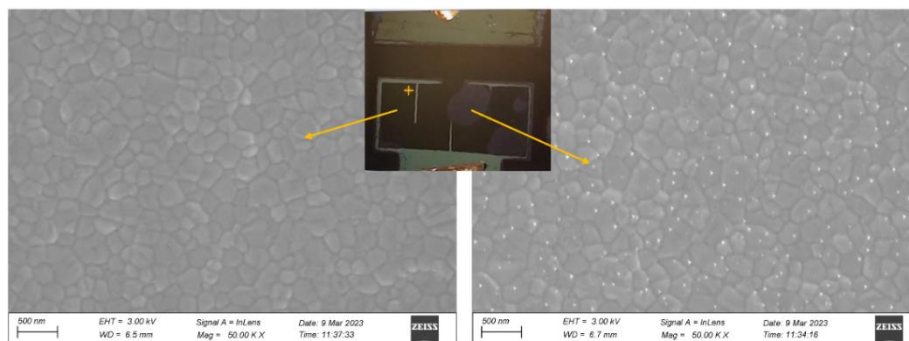

Figure 5.19: Top View SEM Images of a PSC After 900h of Light Soaking Through the Substrate Side. *The cell was exposed to light with a 1 sun intensity at 35°C at open circuit in an N$_2$ atmosphere. Images were taken from regions that did not appear to degrade visually (left) and from regions that changed optically during light soaking (right).*

Overall, cells without SiO$_X$ exhibited improved stability when compared to those containing SiO$_X$. To gain a better understanding, the evolution of the *J-V* parameters was measured at different times during the light soaking for PSC based of NiO$_X$, NiO$_X$/Me-4PACz, or NiO$_X$/Me-4PACz/SiO$_X$ stacks, as presented in Figure 5.20. A significant drop in efficiency was recorded for the three cells containing SiO$_X$, mainly due to a dramatic drop in *J$_{sc}$* (and *FF*), especially for the one light soaked through the HTM side. In fact, the *J$_{sc}$* decreased from 20.5 mA cm^{-2} to less than 14 mA.cm^{-2} for devices exposed to 870 hours in substrate conditions, and even further to 9 mA.cm^{-2} for devices light soaked in a superstrate configuration. In comparison NiO$_X$/Me-4PACz and NiO$_X$-only devices exhibited improved stability with substantially lower *J$_{sc}$* drop. However, in contrast to NiO$_X$ alone, NiO$_X$/Me-4PACz experienced stronger *J$_{SC}$* losses, up to 5 mA.cm^{-2}. Although only four cells per condition are presented here, these findings align with data obtained from

others batches. Notably, larger drops in performance were consistently observed in devices utilizing MeO-2PACz or Me-4PACz (with NiO$_X$). During light soaking under open-circuit conditions, the electric field is minimal, and photo-generated carriers are not extracted. Instead, they diffuse towards the contacts, accumulate, and can deteriorate both the charge transport layers and the perovskite absorber.[165] This degradation might be more pronounced in devices with higher carrier concentrations, such as those based on self-assembled monolayers, as they experience fewer non-radiative recombination and consistently demonstrate higher V$_{OC}$ values (+100 mV) compared to those based solely on NiO$_X$. To facilitate a more accurate comparison, it is advisable to subject devices to light soaking at MPPT instead of open circuit.

As it can be seen in *Figure 5.16*, perovskite located outside the active region appears lighter, less smooth and even somewhat blurred in cells with SiO$_X$ compared to those without nanoparticles. It appeared that the presence of the SiO$_X$ wetting layer accelerated degradation The presence of some adsorbed water on the surface of the SiO$_X$ nanoparticles (deposited from a diluted alcohol solution but initially dispersed in water) may trigger the generation of PbI$_2$ at the interface with the perovskite, and in turn the buckling of the top electrode seen by SEM. If this form of degradation is due to the water present in the SiOx nanoparticles, it is not surprising that it extends across the entire surface of the samples. However, it is the delamination of the top TCO to make it even more visible. Still the exact influence of the nanoparticles
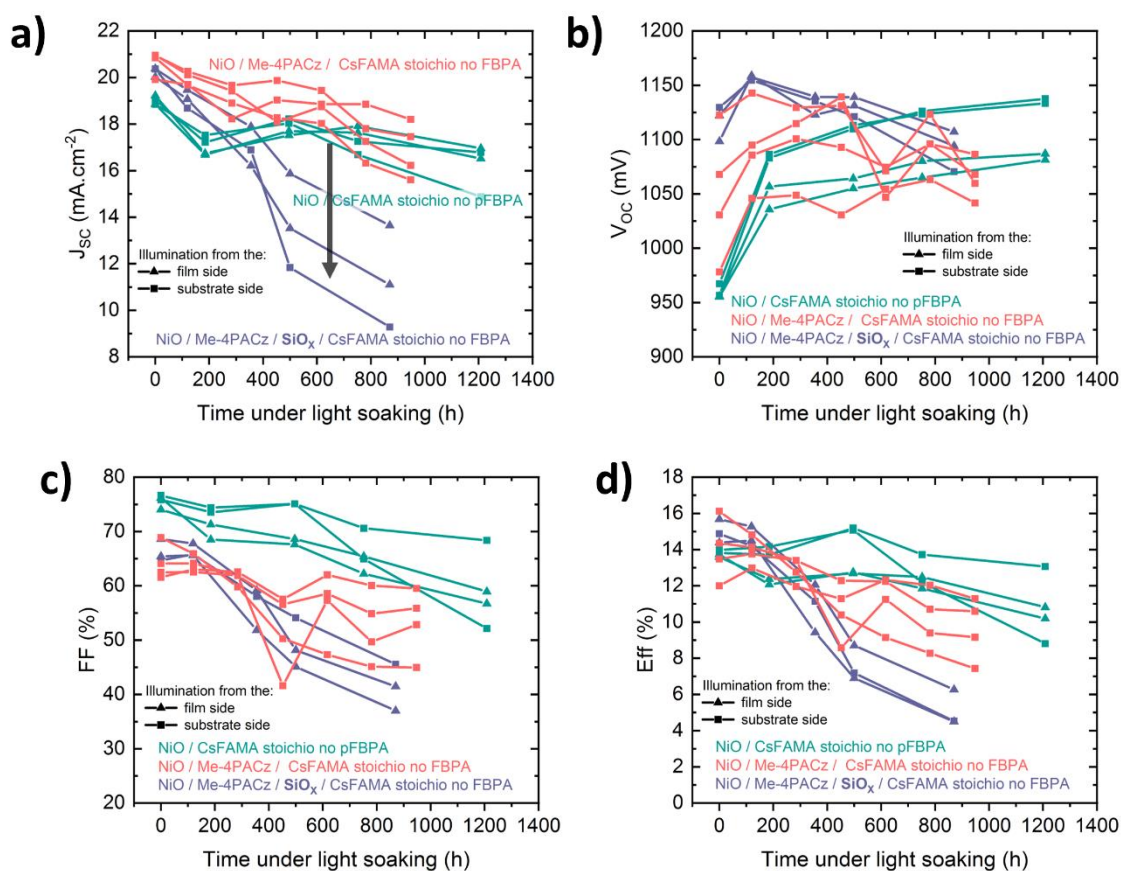

Figure 5.20: J-V Parameters of PSCs Throughout the Light Soaking Test at 35°C. *Cells were put in the Cicci chamber, in N$_2$ atmosphere, without any encapsulation or shadow mask. (a) J$_{SC}$, (b) V$_{OC}$, (c) FF and (d) Eff.*

on the light-soaking stability of the PSCs remains unclear at this stage. The SiO_X solution must be prepared in a water-free environment for reliable PSC stability testing.

5.2.4 Impact of the TCO electrode

Next, the impact of the TCO electrode on degradation was investigated. To test this, a fresh batch of cells using different transparent conductive oxide (TCO) materials was fabricated. Our standard poly-crystalline ITO was compared with an amorphous sputtered IZO. In addition, the sputtering power of the standard ITO (normally sputtered at 750 W) was also reduced to 375 W to investigate potential sputtering-induced damage. Here, pFPBA was introduced in the perovskite precursor solution while SiO_X was not used. After encapsulation, the cells were illuminated from the substrate side at 65°C and left at open circuit in the Solaronix light soaking chamber.

As observed in Figure 5.21, degradation occurs irrespective of the TCO composition or sputtering power. Within 136 hours of light exposure, degradation manifested across all samples and started from point defects and at the active area boundaries. As light soaking extended, degradation propagated further. Beyond 500 hours, massive degradation emerged in all cells, exclusively where the TCO was sputtered and primarily within the illuminated active area, irrespective of the specific TCO material used. The areas that degraded exhibited a lighter or yellowish hue, indicative of lead iodide formation. Notably, the silver grid became barely visible due to its reaction with I_2 between 136 and 347 hours of light exposure.
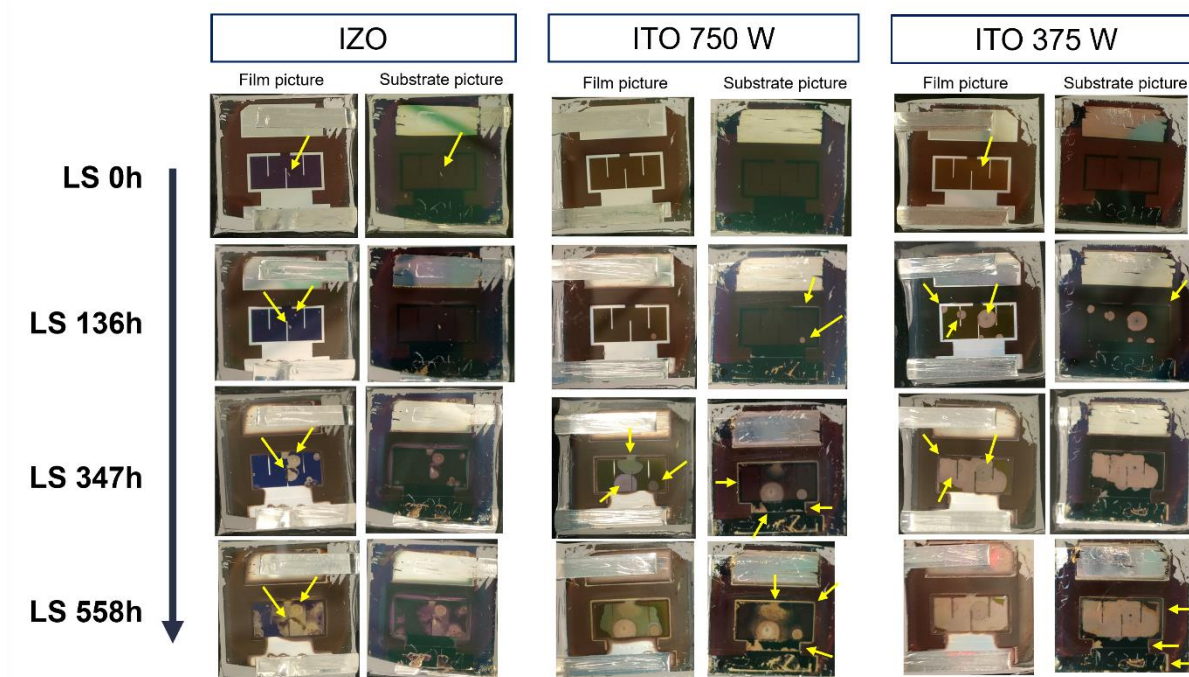

Figure 5.21: Picture of the Cells Throughout the Light Soaking Test, for Different TCO.

Moreover, yellow lines are visible at the boundaries of the TCO. As discussed earlier, this degradation is likely to stem from a lateral ion migration driven by the electric potential difference between inside and outside the active area. To assess this point, the ITO pad was extended beyond the illuminated area. Results are presented in Figure 5.22. Apart from the silver grid that is a bit impacted, no degradation can

be seen in the active area when the ITO is larger than the illuminated area (Figure 5.22a). However, degradation is well visible at the edges of the active area for the samples with ITO as large as the illuminated area. This assessment underscores the role of the lateral ion migration in the light-induced degradation. Finally, to summarize this part, the nature of the TCO did not impact the degradation pathway.
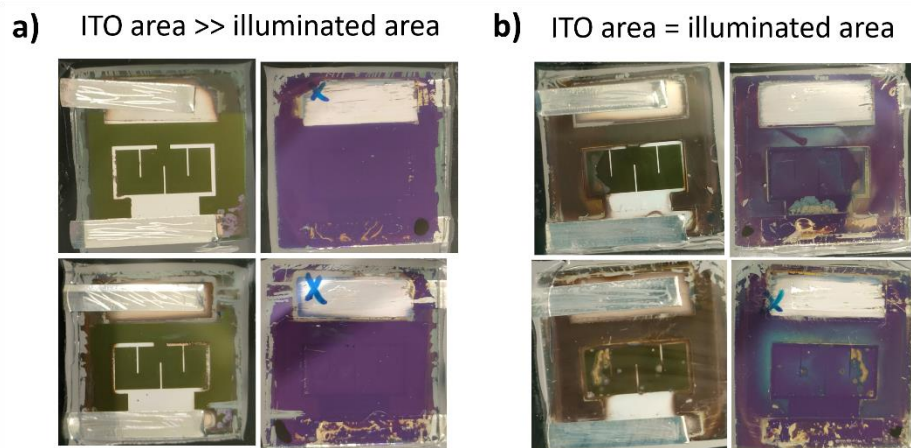

a) ITO area >> illuminated area   **b)** ITO area = illuminated area

Figure 5.22: Picture of PSCs Light Soaked from the Film Side for 560 h in the Solaronix at 65°C. *a) picture of cells with a top ITO sputtered on a much larger area than the illuminated area, b) picture of cells with a top ITO as large as the active area of the cells. Film and substrate side are showing for each device.*

5.2.5 Mitigation of the redox reaction at the NiOₓ/perovskite interface

Deprotonation and redox reactions involving organic iodides in the perovskite and Ni^{3+} species in the NiO_X layer is well documented in the literature.[114,144,153] This interfacial reaction, exacerbated by light, lead to strong current decrease. Recent publication has introduced the use of 1,3-bis(diphenylphosphino)propane (DPPP) as an interlayer to passivate the NiO_X/perovskite interface and enhance both efficiency and stability.[77] Moreover, doping the NiO_X with oxygen has been shown to improve the thermal stability of NiO_X-based PSCs, as discussed in the Chapter 4. To gain insights into the impact of these modifications on the light-stability, a study comparing NiO_X, NiO_X/DPPP and O_2-NiO_X-based devices under light was conducted at different temperatures. From the results discussed previously, the perovskite used here was the stoichiometric CsFAMA $Cs_{0.04}FA_{0.8}MA_{0.16}Pb(I_{0.83}Br_{0.17})_3$ and neither pFBPA nor SiO_X was used. No top TCO was used, and opaque Ag contact was evaporated directly on top of the SnO_X. The variation in *J-V* parameters over time under light exposure at 35°C and 65°C are presented in Figure 5.23 and Figure 5.25, respectively. At 35°C, unencapsulated cells were placed in the Cicci chamber under N_2 atmosphere. At 65°C, to prevent continuous perovskite outgassing due to elevated temperatures, the cells were encapsulated (see section 2.1.4) and subjected to the Solaronix light setup.
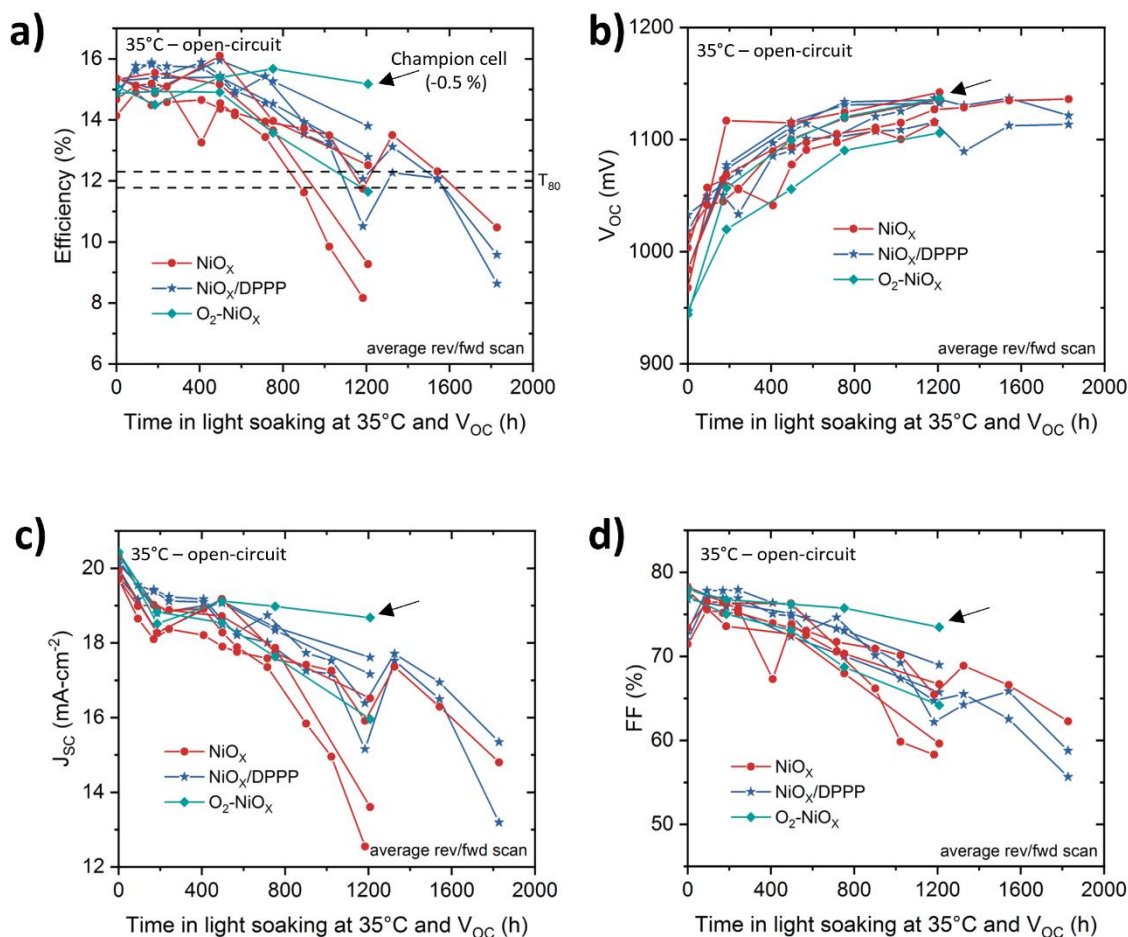
Figure 5.23: *J-V* **parameters of opaque PSCs Based on NiO$_X$, O$_2$-NiO$_X$ and NiO$_X$/DPPP during light soaking at** <u>**35°C**</u> **and at open-circuit.** *Light Soaking was conducted in the Cicci chamber under N$_2$ flow, and 1 sun illumination. No shadow mask was used during light soaking. The stack of the devices is the following: HTM/CsFAMA/C$_{60}$/SnO$_2$/Ag. The active area is 1 cm². a) Efficiency, b) V$_{OC}$, c) J$_{SC}$, and d) FF of the cells during the test are presented.*

Devices incorporating DPPP as an interlayer showed similar initial efficiencies to baseline devices.[77] During the first 500 hours of light soaking at 35°C, DPPP-based devices displayed increased performance, achieving up to a +1% absolute efficiency boost, primarily attributed to enhancements in both V_{OC} and J_{SC} (Figure 5.23). Notably, DPPP-based devices exhibited a similar to milder degradation in J_{SC} and *FF* compared to baseline devices, ultimately showing less than a 20% degradation relative to their initial efficiency after over 1000 hours of light exposure. Still, more statistics will be needed to fully determine whether the presence of the DPPP interlayer really improves the light soaking stability of NiO$_x$-based devices.

At 65°C, light soaking of DPPP-based devices initially exhibited a similar performance increase as observed at 35°C (+1.1% absolute after 100 hours) during the first 200 hours of testing (Figure 5.25). However, after this initial boost, these devices experienced a strong drop in efficiency, characterized by steep *FF* and J_{SC} decrease. Despite the notable stability improvement during the first hundred hours, DPPP-based devices exhibited a T$_{80}$ comparable to that of NiO$_X$ baseline devices (less than 300 hours). They ended up the test

with low J$_{SC}$ and FF, and the emergence of a characteristic S-shaped *J-V* curve, indicative of a barrier impeding carrier extraction.
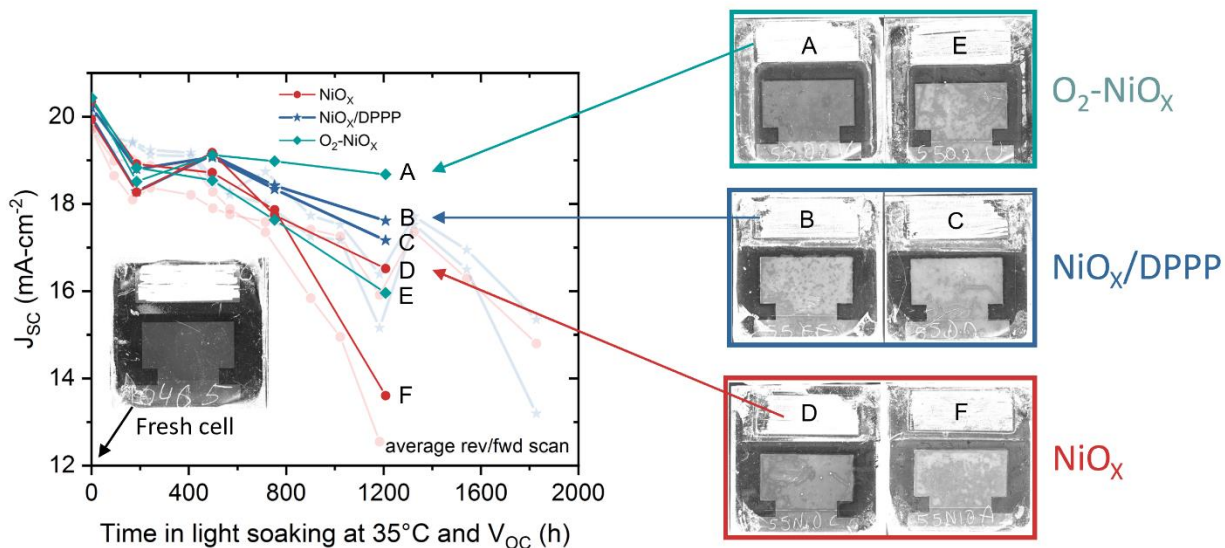

Figure 5.24: *J*$_{SC}$ Variations and Microview Images of Fresh and Aged Devices for 6 of the Cells Presented in Figure 5.23. *The images were taken from the substrate side. The aged cells were light-soaked for 1200 hours at 35°C in N$_2$.*

O$_2$-NiO$_X$-based-device demonstrated superior stability at 35°C when compared to the two others HTM compositions. The champion device experienced only 0.5% degradation in efficiency relative to its initial performance after more than 1200 hours under 1 sun (see arrows in Figure 5.23). Although some J$_{SC}$ decrease was partially offset by an increase in V$_{OC}$, reduction in current was less pronounced compared to the other conditions.

Figure 5.24 displays microview images of the cells taken after 1200 hours of light soaking at 35°C. In these optical images, distinct contrast regions in the active area of each aged cell are evident when compared to the fresh device. This visual degradation suggests the presence of phase segregation, likely attributable to mobile ions. Notably, the champion device based on O$_2$-NiO$_X$ exhibits the least observable degradation in these images. Conversely, NiO$_X$/DPPP-based devices appear quite bright across nearly the entire active area, despite their good stability performance.

Finally, O$_2$-NiO$_X$-based-device exhibited promising operational stability under light and heat conditions (Figure 5.25). Similar to DPPP devices, the O$_2$-NiO$_X$ configuration experienced an initial efficiency increase during the first 650 hours of testing, attributed to improvements in all *J-V* parameters. T$_{80}$ was reached after 540 hours of testing at 65°C. However, after the 400th hour of the test, both J$_{SC}$ and FF exhibited a linear decrease. While doping NiO$_X$ with oxygen delayed degradation, it did not prevent it entirely. Nevertheless, the *FF* drop was much slower than that observed in the baseline NiO$_X$. However, further data will be necessary to confirm these trends.
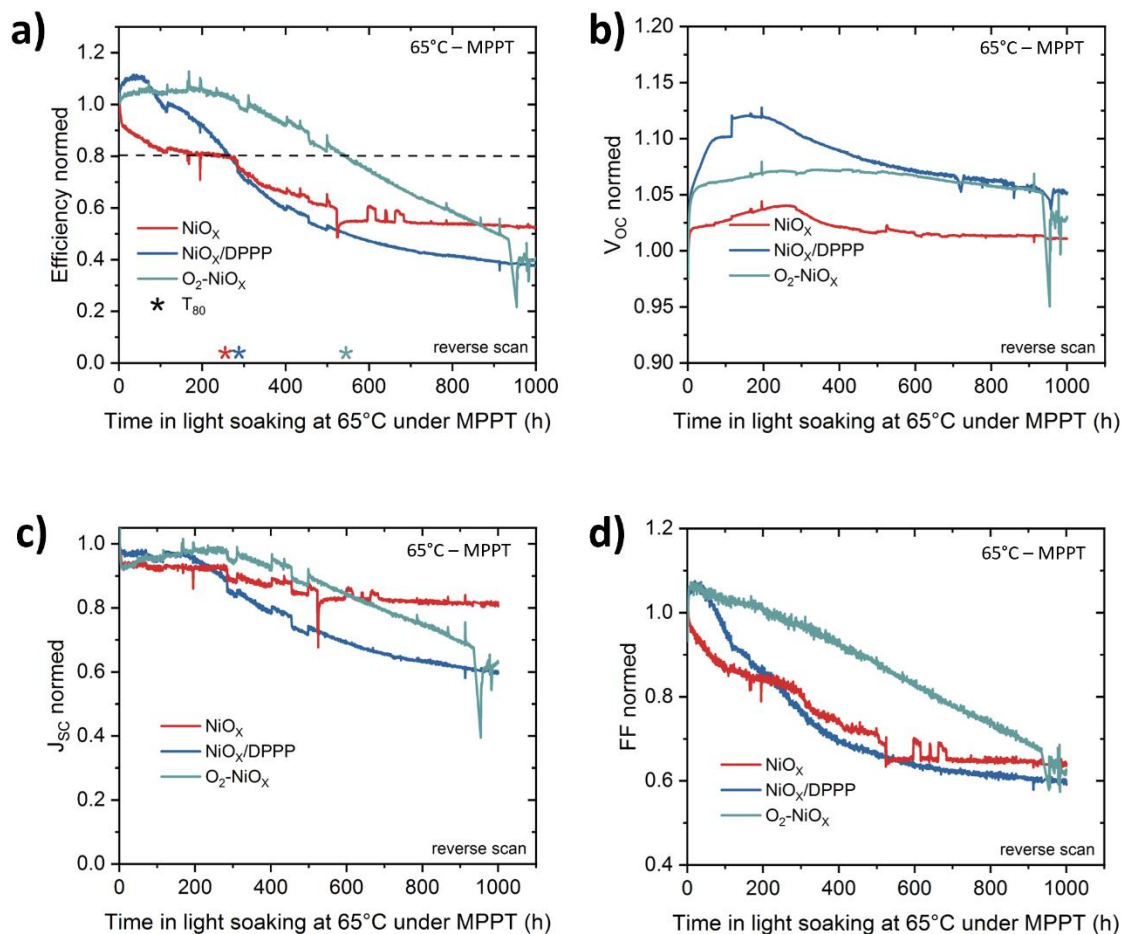
Figure 5.25: *J-V* parameters of encapsulated opaque PSCs Based on NiO$_X$, O$_2$-NiO$_X$ and NiO$_X$/DPPP during light soaking at 65°C and at MPPT. *Light Soaking was conducted in the Solaronix chamber under N$_2$ flow, and 1 sun illumination. No shadow mask was used during light soaking. The stack of the devices is the following: HTM/CsFAMA/C$_{60}$/SnO$_2$/Ag. The active area is 1 cm^2. a) Efficiency, b) V$_{OC}$, c) J$_{SC}$, and d) FF of the cells during the test are presented.*

5.3 Conclusion and Outlook

In this chapter, light and heat induced degradation in perovskite solar cells was studied, first using a layer-by-layer approach and then by investigating different device configurations, to identify each degradation pathway. The findings highlight several crucial factors affecting the stability of PSCs and recommendations are provided here to mitigate these instability issues. First, to enhance the PSCs stability, a precise control over the perovskite composition is of paramount importance: the perovskite layer should be as stoichiometric as possible without PbI$_2$ excess. Indeed, PbI$_2$ degrades under light, which leads to mobile ions generation and eventually the release of I$_2$ vapors that can attack metal layers. Second, the C$_{60}$/SnO$_2$ layers alone do not provide sufficient protection to the perovskite. Employing impermeable capping layers, particularly denser and thicker SnO$_2$ layer, may effectively delay the degradation, e.g. through the

introduction of -OH terminated nucleation promoting layers below the SnO$_2$.[27] Third, while the ITO slows down the release of volatile species from the perovskite by acting as an extra barrier, mobile ions may accumulate at the edges of the ITO-defined active area, which may eventually lead to a decomposition of the perovskite layer once a certain threshold of mobile ions has been reached. The switch from small pixel devices to large devices of industrial dimensions should effectively mitigate the issue. Fourth, redox reaction occurring at the NiO$_X$/perovskite interface pose a significant challenge. Employing dopants within NiO$_X$ or incorporating interlayers proved effective mitigation strategies. Fifth, silver electrodes are susceptible to severe damage upon exposure to light, primarily due to I$_2$ vapor released from perovskite outgassing. To delay this degradation, advanced encapsulation methods involving encapsulant foils and ALD protective layers, such as polyolefin and ALD-Al$_2$O$_3$, can be employed. Last, the incorporation of pFBPA as an additive in the perovskite precursor solution and the use of a hydrophilic SiO$_X$ nanoparticles layer aimed at enhancing efficiency can result in significant instabilities that need to be further investigated.

The time devoted to this study did not allow a fully understanding all the degradation mechanisms. It would be intriguing to use more advanced characterization techniques, such as photoluminescence and electroluminescence measurements, on both fresh and aged devices. These investigations would provide valuable insights into perovskite degradation and the loss of contact within the top stack. Additionally, conducting XPS analysis on the perovskite surface after the removal of the top contact from both fresh and aged devices could yield a more comprehensive understanding of degradation from a chemical perspective. Regarding the SiO$_X$-induced degradation, new formulation, in dry atmosphere, will be tried. Careful consideration and optimization of these materials are necessary.

In conclusion, achieving long-term operational stability in PSCs requires meticulous control of materials, effective interface engineering, and the implementation of protective layers. As perovskite solar technology advances, addressing these challenges will be pivotal to unlocking its full potential.

6. Conclusions and Perspectives

In this concluding chapter, we provide a concise overview of the key findings regarding the use of NiO_X-based contacts in perovskite solar cells (PSCs). Our primary focus has been to investigate the factors affecting their stability under heat and light exposure conditions. We then summarise and outline various possibilities for enhancing the durability of these cells, especially to withstand exposure to light at elevated temperatures.

6.1 Conclusions

6.1.1 Enhancing the thermal stability of PSCs

Chapter 3 primarily focused on addressing the thermal degradation of sputtered NiO_X-based PSCs. When using a thin NiO_X layer (~5nm) or a self-assembled monolayer (SAM) as hole transport layer (HTM), the devices exhibited poor yield, especially in the case of large active areas (> 1 cm²). This was associated with imperfect coverage of the thin HTM layers on the transparent conductive oxide (TCO). Thickening the NiO_X layer improved reproducibility but introduced a performance drop during damp-heat testing. This drop in performance was attributed to the formation of an extraction barrier, the extent of which correlated with the thickness of the NiO_X layer. To understand the origin of this barrier, a deep study was carried out, involving temperature and bias-dependent measurements, electrochemical impedance spectroscopy, and device simulations.

The key findings of this investigation revealed that the extraction barrier resulted from a combination of factors, including a downward shift of the NiO_X valence band and a loss of charge carriers in the NiO_X layer, a process that accelerates at elevated temperatures and in an inert atmosphere. This loss was attributed to the reduction of Ni^{3+} to Ni^{2+} due to interactions with the iodide of the perovskite. As a solution, a bilayer structure consisting of a 5 nm NiO_X layer, and a self-assembled monolayer was introduced. With this approach, similar efficiencies in both 1 cm² cells and 14 cm² minimodules were achieved, thanks to a higher V_{OC} and a pinhole-free HTM. Most importantly, this bilayer configuration significantly enhanced the stability of the PSCs, with these devices retaining over 94% efficiency after 1000 hours of exposure to 85°C and 85% relative humidity.

Chapter 4 introduced an effective strategy for addressing the intrinsic instability of NiO_X material. The study demonstrated that a porous NiO_X layer, presented in Chapter 3 and sputtered in pure argon flow, exhibited increased defects and a higher presence of Ni^{3+}. These porous layers were more prone to water adsorption, contamination, and perovskite oxidation. To mitigate these issues, a controlled sputtering process was introduced, involving the deposition of NiO_X in a mixture of argon and oxygen gases. This precise control over the sputtering process resulted in the reduction of Ni^{3+} species, surface smoothing, and densification of the NiO_X layer.

Furthermore, the incorporation of cesium by sputtering from a Cs:NiOx target produced more stable Cs-doped NiO_X layers. Besides stabilizing the Ni^{3+}/Ni^{2+} ratio over time, oxygen/cesium doping give also denser films. Most notably, the introduction of Cs led to the development of O_2-Cs:NiO_X-based PSCs that successfully passed the IEC 61215 damp-heat test requirements, exhibiting less than a 5% relative change in power conversion efficiency after more than 5100 hours of test.

These findings offer pathways to improve the thermal stability of PSCs based on NiO_x, using an industrially compatible deposition method and enabling the manufacturing of large-area devices.

6.1.2 Light Soaking Stability

Having successfully addressed the stability of NiO_X-based PSCs under damp heat conditions, **Chapter 5** investigated the different degradation paths of these devices when subjected to a combination of elevated temperatures and light exposure, the most critical test to pass for PSCs.

First of all, the composition of the perovskite layer is of primary importance. The perovskite must be as stoichiometric as possible to avoid rapid degradation. Under light, excess PbI_2 undergoes photodecomposition, leading to the release of I_2 vapors that are likely to attack the metal electrode. Second, the SnO_2 layer is insufficient as gas barrier and does not prevent outgassing of the photodecomposition products. Employing impermeable capping layers, particularly denser and thicker SnO_2 layers, is required to provide a more effective barrier. Third, while ITO acts as an additional barrier by slowing the release of volatile species from the perovskite, results revealed that mobile ions may accumulate at the edges of the ITO-defined active area, eventually leading to perovskite layer decomposition. Transitioning from small pixel devices to large devices of industrial dimensions effectively mitigates this issue. Fourth, the redox reactions occurring at the NiO_X/perovskite interface emerged as a significant challenge. Results have revealed that employing dopants within NiO_X (here O_2-NiO_X) or incorporating interlayers (DPPP) could be an effective mitigation strategy. Fifth, metal electrodes are susceptible to severe damage when exposed to light, primarily arising from I_2 vapor released during perovskite outgassing. Advanced encapsulation methods and implementation of protective layers could

help to delay this degradation. Finally, the study also revealed that the incorporation of pFBPA as an additive in the perovskite precursor solution, combined with the use of a hydrophilic SiO_X nanoparticles layer aimed at enhancing efficiency, can result in significant degradation.

In conclusion, the path to achieving long-term operational stability in perovskite solar cells is multifaceted, demanding meticulous control of materials, effective interface engineering, and the implementation of protective layers. Further efforts are necessary to resolve perovskite instability in order to bring this promising technology to the market.

.

6.2 Perspectives

The main challenge in the research and development of perovskite photovoltaic cells remains to achieve the necessary stability.

One of the major problems facing perovskite photovoltaic systems is the metal-halide reaction. In that regard, as iodide is the most oxidizing halide[66] and Ag can diffuse easily through the cell layers, particularly at elevated temperatures,[43] metal-halide reactions are extremely likely. To overcome this reaction, alternatives to silver metal contacts have been proposed, combining a diffusion barrier of a few nm such as Cr,[166] Bi[76,167] and a less reactive but sufficiently conductive metal such as Cu,[168] which improves devices stability without suffering much from resistive losses. These strategies have been demonstrated only in single junction opaque devices using full-area metal electrodes do not require high conductivity but have not been transferred to perovskite / c-Si tandems with partial metal contacts - fingers and busbars. Therefore, in order to improve the stability of tandem devices, these alternative metal stacks should be tested in tandems. With the aim of improving device stability, Cu plating could also be developed. Fraunhofer ISE demonstrated the feasibility of the process on both PSC[169] and perovskite/c-Si tandem[170] devices. However, as the copper is more prone to oxidation than silver, some development must be done to delay this reaction, such as using an Ag/Cu mixture for instance. Additionally, this process requires improvement to make it more suitable for industrial-scale. Moreover, as I_2 vapor can oxidize metallic contacts from the top, advanced encapsulation methods involving encapsulant foils and atomic layer deposition (ALD) protective layers, such as polyolefin and ALD-Al_2O_3, can provide a solution to delay this degradation.

In theory, not only the metal stack can act as a diffusion, outgassing and penetration barrier. Each single layer of the device could be used to enhance the device stability, by acting as blocking layer against undesired species migration. In this respect, the top electrode stack commonly used in conventional inverted perovskite solar cells and tandems (C_{60} / ALD-SnO_2 / TCO) can be significantly improved. First of all, the commonly used C_{60} is an organic electron transport layer that has a very defective interface with

the perovskite, weakly bound to it and very permeable to halides. Thus, the implementation of an interface passivation layer between perovskite[171] and C_{60} and/or C_{60} doping[172] are a very promising strategy to both passivate defects and overcome perovskite / C_{60} reactions such as iodide migration into C_{60}. Additionally, self-oxidative species that protect perovskite absorbs such as phosphine and boron derivates (DPPP,[77] TPFB,[173]), hydrophobic (fluorine-derivatives) layers,[82] and compact interlayers like ALD-AlO$_X$[174] are promising candidates that improve the stability of perovskite solar cell by acting as ion and humidity blockers that we can implement in our baselines.

In the best scenario, a substitute to the expensive fullerene and fullerene-derivatives should be used, having a higher binding energy with perovskite and a defect-free interface is a necessity. However, identifying a transport layer with equivalent electron extraction capabilities, including proper band energetics, mobility, and high-quality interface passivation, is a challenging task. Although a few alternative candidates have been suggested in the literature, they have not yet achieved comparable performance to C_{60} in terms of electron extraction. These alternative materials include naphthalene[175,176] and perylene[177–179] derivatives.

Another layer than can be improved in the cell stack is ALD-deposited SnO_2. ALD growth requires functional groups (e.g., hydroxyls, amines) on the surface. However, organic materials such as C_{60} have a limited density of functional groups that can initiate ALD nucleation. Consequently, ALD-deposited layers grow on surfaces with insufficient functional groups, tend to be less compact and dense that doesn't offer substantial barrier properties. Enhancing the nucleation of SnOx through surface modification of C60 represents a promising strategy that we can explore without impeding electron transport at that interface. The introduction of -OH-terminated nucleation layers beneath SnOx, such as ethoxylated polymers (PEIE),[27] can effectively improve nucleation, resulting in a denser layer. This enhancement not only delays degradation but also strengthens the performance of PSCs.

Finally, also the TCO can be further investigated and improved. Commonly used TCOs are ITO and IZO. With a polycrystalline structure, ion, metal, and oxygen diffusion can occur in ITO material.[43] In this context, the use of amorphous TCO without grain boundaries seems to be a promising route to enhance barrier properties. In that regard, IZO is a possible candidate. It exhibits not only an amorphous nature without grain boundaries but also maintains high mobility even in its as-deposited state. Furthermore, considering the layering strategy, incorporating TCO materials such as ITO, IZrO, or newer options like new SCOT[180,181] between the SnOx layer and an amorphous TCO like IZO can result in improved barrier properties. Looking ahead, the exploration of next-generation high-mobility TCOs like IZrO, ICO, and IWO promising candidates to exploit the potential of tandems in terms of optoelectronics and stability.[182]

Finally, more degradation tests should be conducted directly on tandem devices, and not only on single junctions. Indeed, some degradation effects may be more detrimental in single junction than in tandem devices. For instance, higher shunt and reverse bias resilience has been observed in tandem configuration.[183] Additionally, the growth of perovskite top cell on glass or silicon substrates may lead to differences in layers crystallinity and stability.

To sum up, improving the barrier properties of the thin films in the stack by either substituting the materials with intrinsically more stable alternatives or by improving the growth kinetics of the materials

used is crucial to improve the devices stability. Once adequate protection is provided to the perovskite absorber and robust interfaces are established, the intrinsic stability of the perovskite absorber and its grain boundaries can be enhanced through compositional adjustments and the incorporation of additives. Recent investigations have explored the use of polymers and additives that wrap around the grains, resulting in significant improvements in stability.[184,185] Moreover, there remains a huge compositional space to be explored for organic-inorganic hybrid perovskites with variations in A-site cations (FA, MA, DMA, Cs, Rb), B-site cations (Pb, Sn, Ag, Bi), and halides (I, Br, Cl). This exploration demands intensive efforts in fabrication and characterization, and the adoption of automated tools such as solution preparation robots, processing robots, automated characterization techniques, and machine learning-assisted data analysis, is essential to expedite these developments.

List of Figures

List of Tables

Bibliography

(1)   IPCC. Summary for Policymakers: Synthesis Report. *Clim. Chang. 2023 Synth. Report. Contrib. Work. Groups I, II III to Sixth Assess. Rep. Intergov. Panel Clim. Chang.* **2023**, 1–34.

(2)   IEA. CO2 Emissions in 2022. *CO2 Emiss. 2022* **2023**. https://doi.org/10.1787/12ad1e1a-en.

(3)   IEA. Renewable Energy Market Update: Outlook for 2023 and 2024 - International Energy Agency. **2023**, 87.

(4)   Irena, M. T. *Renewable Generation Costs in 2022*; 2022.

(5)   Haegel, N. M.; Verlinden, P.; Victoria, M.; Altermatt, P.; Atwater, H.; Barnes, T.; Breyer, C.; Case, C.; De Wolf, S.; Deline, C.; Dharmrin, M.; Dimmler, B.; Gloeckler, M.; Goldschmidt, J. C.; Hallam, B.; Haussener, S.; Holder, B.; Jaeger, U.; Jaeger-Waldau, A.; Kaizuka, I.; Kikusato, H.; Kroposki, B.; Kurtz, S.; Matsubara, K.; Nowak, S.; Ogimoto, K.; Peter, C.; Peters, I. M.; Philipps, S.; Powalla, M.; Rau, U.; Reindl, T.; Roumpani, M.; Sakurai, K.; Schorn, C.; Schossig, P.; Schlatmann, R.; Sinton, R.; Slaoui, A.; Smith, B. L.; Schneidewind, P.; Stanbery, B. J.; Topic, M.; Tumas, W.; Vasi, J.; Vetter, M.; Weber, E.; Weeber, A. W.; Weidlich, A.; Weiss, D.; Bett, A. W. Photovoltaics at Multi-Terawatt Scale: Waiting Is Not an Option. *Science (80-.).* **2023**, *380* (6640), 39–42. https://doi.org/10.1126/science.adf6957.

(6)   Kost, C.; Shammugam, S.; Fluri, V.; Peper, D.; Memar, A. D.; Schlegel, T. Levelized Cost of Electricity- Renewable Energy Technologies June 2021. **2021**, No. June, 1–45.

(7)   Richter, A.; Hermle, M.; Glunz, S. W. Reassessment of the Limiting Efficiency for Crystalline Silicon Solar Cells. *IEEE J. Photovoltaics* **2013**, *3* (4), 1184–1191. https://doi.org/10.1109/JPHOTOV.2013.2270351.

(8)   The Full-Area Conversion Efficiency of HBC Modules Reaches 24.88%! Kingstone Energy Set Another World Record. **2023**.

(9)   27.42% Efficiency! The Conversion Efficiency of Kingstone Energy's HBC Battery Has Reached a New High. **2023**.

(10)   National Renewable Energy Laboratory. *Best Research-Cell Efficiency Chart*. https://www.nrel.gov/pv/assets/pdfs/best-research-cell-efficiencies.pdf.

(11)   Trina Solar. Trina Solar Breaks World Record for 25th Time by Setting N-Type Module Aperture Efficiency at 24.24%. **2023**.

(12)   Futscher, M. H.; Ehrler, B. Efficiency Limit of Perovskite/Si Tandem Solar Cells. *ACS Energy Lett.* **2016**, *1* (4), 863–868. https://doi.org/10.1021/acsenergylett.6b00405.

(13)   Szabó, G.; Park, N.-G.; De Angelis, F.; Kamat, P. V. Are Perovskite Solar Cells Reaching the Efficiency and Voltage Limits? *ACS Energy Lett.* **2023**, *8* (9), 3829–3831. https://doi.org/10.1021/acsenergylett.3c01649.

(14)   Werner, J.; Niesen, B.; Ballif, C. Perovskite/Silicon Tandem Solar Cells: Marriage of Convenience or True Love Story? – An Overview. *Adv. Mater. Interfaces* **2018**, *5* (1), 1–19. https://doi.org/10.1002/admi.201700731.

(15)   Wang, Z.; Song, Z.; Yan, Y.; Liu, S. (Frank); Yang, D. Perovskite—a Perfect Top Cell for Tandem Devices to Break the S–Q Limit. *Adv. Sci.* **2019**, *6* (7). https://doi.org/10.1002/advs.201801704.

(16)   Chin, X. Y.; Turkay, D.; Steele, J. A.; Tabean, S.; Eswara, S.; Jacobs, D.; Guesnay, Q.; Sahli, F.; Andreatta, G.; Boccard, M. Interface Passivation for 31.25%-Efficient Perovskite/Silicon Tandem Solar Cells. **2023**, *63* (July), 59–63. https://doi.org/10.1126/science.adg0091.

(17)   Qian, J.; Ernst, M.; Wu, N.; Blakers, A. Impact of Perovskite Solar Cell Degradation on the Lifetime Energy Yield and Economic Viability of Perovskite/Silicon Tandem Modules. *Sustain. Energy Fuels* **2019**, *3* (6), 1439–1447. https://doi.org/10.1039/c9se00143c.

(18)   Noh, J. H.; Im, S. H.; Heo, J. H.; Mandal, T. N.; Seok, S. Il. Chemical Management for Colorful, Efficient, and Stable Inorganic-Organic Hybrid Nanostructured Solar Cells. *Nano Lett.* **2013**, *13* (4), 1764–1769. https://doi.org/10.1021/nl400349b.

(19)   Hao, F.; Stoumpos, C. C.; Chang, R. P. H.; Kanatzidis, M. G. Anomalous Band Gap Behavior in Mixed Sn and Pb Perovskites Enables Broadening of Absorption Spectrum in Solar Cells. *J. Am. Chem. Soc.* **2014**, *136* (22), 8094–8099. https://doi.org/10.1021/ja5033259.

(20)   Sahli, F.; Kamino, B. A.; Werner, J.; Bräuninger, M.; Paviet-Salomon, B.; Barraud, L.; Monnard, R.; Seif, J. P.; Tomasi, A.; Jeangros, Q.; Hessler-Wyser, A.; De Wolf, S.; Despeisse, M.; Nicolay, S.; Niesen, B.; Ballif, C. Improved Optics in Monolithic Perovskite/Silicon Tandem Solar Cells with a Nanocrystalline Silicon Recombination Junction. *Adv. Energy Mater.* **2018**, *8* (6), 1–8. https://doi.org/10.1002/aenm.201701609.

(21)   Kumar, A.; Bansode, U.; Ogale, S.; Rahman, A. Understanding the Thermal Degradation Mechanism of Perovskite Solar Cells via Dielectric and Noise Measurements. *Nanotechnology* **2020**, *31* (36). https://doi.org/10.1088/1361-6528/ab97d4.

(22)   Boyd, C. C.; Cheacharoen, R.; Leijtens, T.; McGehee, M. D. Understanding Degradation Mechanisms and Improving Stability of Perovskite Photovoltaics. *Chem. Rev.* **2019**, *119* (5), 3418–3451. https://doi.org/10.1021/acs.chemrev.8b00336.

(23)   Zhang, D.; Li, D.; Hu, Y.; Mei, A.; Han, H. Degradation Pathways in Perovskite Solar Cells and How to Meet International Standards. *Commun. Mater.* **2022**, *3* (1). https://doi.org/10.1038/s43246-022-00281-z.

(24)   Niu, G.; Li, W.; Meng, F.; Wang, L.; Dong, H.; Qiu, Y. Study on the Stability of CH3NH3PbI3 Films and the Effect of Post-Modification by Aluminum Oxide in All-Solid-State Hybrid Solar Cells. *J. Mater. Chem. A* **2014**, *2* (3), 705–710. https://doi.org/10.1039/c3ta13606j.

(25)   Fu, Q.; Tang, X.; Huang, B.; Hu, T.; Tan, L.; Chen, L.; Chen, Y. Recent Progress on the Long-Term Stability of Perovskite Solar Cells. *Adv. Sci.* **2018**, *5* (5). https://doi.org/10.1002/advs.201700387.

(26)   Leguy, A. M. A.; Hu, Y.; Campoy-Quiles, M.; Alonso, M. I.; Weber, O. J.; Azarhoosh, P.; Van Schilfgaarde, M.; Weller, M. T.; Bein, T.; Nelson, J.; Docampo, P.; Barnes, P. R. F. Reversible Hydration of CH3NH3PbI3 in Films, Single Crystals, and Solar Cells. *Chem. Mater.* **2015**, *27* (9), 3397–3407. https://doi.org/10.1021/acs.chemmater.5b00660.

(27)   Raiford, J. A.; Boyd, C. C.; Palmstrom, A. F.; Wolf, E. J.; Fearon, B. A.; Berry, J. J.; McGehee, M. D.; Bent, S. F. Enhanced Nucleation of Atomic Layer Deposited Contacts Improves Operational Stability of Perovskite Solar Cells in Air. *Adv. Energy Mater.* **2019**, *9* (47), 1–9. https://doi.org/10.1002/aenm.201902353.

(28)   Seo, S.; Jeong, S.; Bae, C.; Park, N. G.; Shin, H. Perovskite Solar Cells with Inorganic Electron- and Hole-Transport Layers Exhibiting Long-Term (≈500 h) Stability at 85 °C under Continuous 1 Sun Illumination in Ambient Air. *Adv. Mater.* **2018**, *30* (29), 1–8. https://doi.org/10.1002/adma.201801010.

(29)   Divitini, G.; Cacovich, S.; Matteocci, F.; Cinà, L.; Di Carlo, A.; Ducati, C. In Situ Observation of Heat-Induced Degradation of Perovskite Solar Cells. *Nat. Energy* **2016**, *1* (1). https://doi.org/10.1038/NENERGY.2015.12.

(30)   Prathapani, S.; Choudhary, D.; Mallick, S.; Bhargava, P.; Yella, A. Experimental Evaluation of Room Temperature Crystallization and Phase Evolution of Hybrid Perovskite Materials. *CrystEngComm* **2017**, *19* (27), 3834–3843. https://doi.org/10.1039/c7ce00402h.

(31)   Ma, F.; Li, J.; Li, W.; Lin, N.; Wang, L.; Qiao, J. Stable α/δ Phase Junction of Formamidinium Lead Iodide Perovskites for Enhanced near-Infrared Emission. *Chem. Sci.* **2016**, *8* (1), 800–805. https://doi.org/10.1039/c6sc03542f.

(32)   He, J.; Li, T.; Liu, X.; Su, H.; Ku, Z.; Zhong, J.; Huang, F.; Peng, Y.; Cheng, Y. B. Influence of Phase Transition on Stability of Perovskite Solar Cells under Thermal Cycling Conditions. *Sol. Energy* **2019**, *188* (May), 312–317. https://doi.org/10.1016/j.solener.2019.06.025.

(33)   Wang, Y.; Zhao, Y.; Gao, F.; Chen, H.; Fan, Y.; Chen, Y.; Miao, Y.; Qin, Z.; Wang, X.; Liu, X.; Zhu, K. Sequential Cesium Incorporation for Highly Efficient Formamidinium-Cesium Perovskite Solar Cells. **2022**, 1–15.

(34)   Saliba, M.; Matsui, T.; Seo, J. Y.; Domanski, K.; Correa-Baena, J. P.; Nazeeruddin, M. K.; Zakeeruddin, S. M.; Tress, W.; Abate, A.; Hagfeldt, A.; Grätzel, M. Cesium-Containing Triple Cation Perovskite Solar Cells: Improved Stability, Reproducibility and High Efficiency. *Energy Environ. Sci.* **2016**, *9* (6), 1989–1997. https://doi.org/10.1039/c5ee03874j.

(35)   Yang, J.; Liu, X.; Zhang, Y.; Zheng, X.; He, X.; Wang, H.; Yue, F.; Braun, S.; Chen, J.; Xu, J.; Li, Y.; Jin, Y.; Tang, J.; Duan, C.; Fahlman, M.; Bao, Q. Comprehensive Understanding of Heat-Induced Degradation of Triple-Cation Mixed Halide Perovskite for a Robust Solar Cell. *Nano Energy* **2018**, *54* (October), 218–226. https://doi.org/10.1016/j.nanoen.2018.10.011.

(36)   Azmi, R.; Ugur, E.; Seitkhan, A.; Aljamaan, F.; Subbiah, A. S.; Liu, J.; Harrison, G. T.; Nugraha, M. I.; Eswaran, M. K.; Babics, M.; Chen, Y.; Xu, F.; Allen, T. G.; Rehman, A.; Wang, C.; Anthopoulos, T. D.; Schwingenschlögl, U.; Bastiani, M. De; Aydin, E.; Wolf, S. De. Damp Heat – Stable Perovskite Solar Cells with Tailored-Dimensionality 2D/3D Heterojunctions. **2022**, *1* (April), 73–77.

(37)   Yao, D.; Zhang, C.; Zhang, S.; Yang, Y.; Du, A.; Waclawik, E.; Yu, X.; Wilson, G. J.; Wang, H. 2D-3D Mixed Organic-Inorganic Perovskite Layers for Solar Cells with Enhanced Efficiency and Stability Induced by n-Propylammonium Iodide Additives. *ACS Appl. Mater. Interfaces* **2019**, *11* (33), 29753–29764. https://doi.org/10.1021/acsami.9b06305.

(38)   Li, M.; Yeh, H.; Chiang, Y.; Jeng, U.; Su, C.; Shiu, H.; Hsu, Y.; Kosugi, N.; Ohigashi, T.; Chen, Y.; Shen, P.; Chen, P.; Guo, T. Highly Efficient 2D / 3D Hybrid Perovskite Solar Cells via Low-Pressure Vapor-Assisted Solution Process. **2018**, *1801401*, 1–13. https://doi.org/10.1002/adma.201801401.

(39)   Gharibzadeh, S.; Nejand, B. A.; Jakoby, M.; Abzieher, T.; Hauschild, D.; Moghadamzadeh, S.; Schwenzer, J. A.; Brenner, P.; Schmager, R.; Haghighirad, A. A.; Weinhardt, L.; Lemmer, U.; Richards, B. S.; Howard, I. A.; Paetzold, U. W. Record Open-Circuit Voltage Wide-Bandgap

Perovskite Solar Cells Utilizing 2D / 3D Perovskite Heterostructure. **2019**, *1803699*, 1–10. https://doi.org/10.1002/aenm.201803699.

(40) Wang, Z.; Lin, Q.; Chmiel, F. P.; Sakai, N.; Herz, L. M.; Snaith, H. J. Efficient Ambient-Air-Stable Solar Cells with 2D-3D Heterostructured Butylammonium-Caesium-Formamidinium Lead Halide Perovskites. *Nat. Energy* **2017**, *2* (9), 1–10. https://doi.org/10.1038/nenergy.2017.135.

(41) Ke, W.; Mao, L.; Stoumpos, C. C.; Hoffman, J.; Spanopoulos, I.; Mohite, A. D.; Kanatzidis, M. G. Compositional and Solvent Engineering in Dion – Jacobson 2D Perovskites Boosts Solar Cell Efficiency and Stability. **2019**, *1803384*, 1–11. https://doi.org/10.1002/aenm.201803384.

(42) Isikgor, F. H.; Isikgor, F. H.; Furlan, F.; Liu, J.; Ugur, E.; Eswaran, M. K.; Subbiah, A. S.; Yengel, E.; Bastiani, M. De; Harrison, G. T.; Zhumagali, S.; Howells, C. T.; Aydin, E.; Wang, M.; Gasparini, N.; Allen, T. G.; Rehman, A.; Kerschaver, E. Van; Baran, D.; Mcculloch, I. Article Concurrent Cationic and Anionic Perovskite Defect Passivation Enables 27 . 4 % Perovskite / Silicon Tandems with Suppression of Halide Segregation Concurrent Cationic and Anionic Perovskite Defect. **2021**, 1566–1586. https://doi.org/10.1016/j.joule.2021.05.013.

(43) Boyd, C. C.; Cheacharoen, R.; Bush, K. A.; Prasanna, R.; Leijtens, T.; McGehee, M. D. Barrier Design to Prevent Metal-Induced Degradation and Improve Thermal Stability in Perovskite Solar Cells. *ACS Energy Lett.* **2018**, *3* (7), 1772–1778. https://doi.org/10.1021/acsenergylett.8b00926.

(44) Sahli, F.; Werner, J.; Kamino, B. A.; Bräuninger, M.; Monnard, R.; Paviet-Salomon, B.; Barraud, L.; Ding, L.; Diaz Leon, J. J.; Sacchetto, D.; Cattaneo, G.; Despeisse, M.; Boccard, M.; Nicolay, S.; Jeangros, Q.; Niesen, B.; Ballif, C. Fully Textured Monolithic Perovskite/Silicon Tandem Solar Cells with 25.2% Power Conversion Efficiency. *Nat. Mater.* **2018**, *17* (9), 820–826. https://doi.org/10.1038/s41563-018-0115-4.

(45) Fu, F.; Pisoni, S.; Jeangros, Q.; Sastre-Pellicer, J.; Kawecki, M.; Paracchino, A.; Moser, T.; Werner, J.; Andres, C.; Duchêne, L.; Fiala, P.; Rawlence, M.; Nicolay, S.; Ballif, C.; Tiwari, A. N.; Buecheler, S. I2 Vapor-Induced Degradation of Formamidinium Lead Iodide Based Perovskite Solar Cells under Heat-Light Soaking Conditions. *Energy Environ. Sci.* **2019**, *12* (10), 3074–3088. https://doi.org/10.1039/c9ee02043h.

(46) Eames, C.; Frost, J. M.; Barnes, P. R. F.; O'Regan, B. C.; Walsh, A.; Islam, M. S. Ionic Transport in Hybrid Lead Iodide Perovskite Solar Cells. *Nat. Commun.* **2015**, *6* (May), 2–9. https://doi.org/10.1038/ncomms8497.

(47) Yuan, Y.; Huang, J. Ion Migration in Organometal Trihalide Perovskite and Its Impact on Photovoltaic Efficiency and Stability. *Acc. Chem. Res.* **2016**, *49* (2), 286–293. https://doi.org/10.1021/acs.accounts.5b00420.

(48) Brennan, M. C.; Draguta, S.; Kamat, P. V.; Kuno, M. Light-Induced Anion Phase Segregation in Mixed Halide Perovskites. *ACS Energy Lett.* **2018**, *3* (1), 204–213. https://doi.org/10.1021/acsenergylett.7b01151.

(49) Hoke, E. T.; Slotcavage, D. J.; Dohner, E. R.; Bowring, A. R.; Karunadasa, H. I.; McGehee, M. D. Reversible Photo-Induced Trap Formation in Mixed-Halide Hybrid Perovskites for Photovoltaics. *Chem. Sci.* **2015**, *6* (1), 613–617. https://doi.org/10.1039/c4sc03141e.

(50) Li, N.; Luo, Y.; Chen, Z.; Niu, X.; Zhang, X.; Lu, J.; Kumar, R.; Jiang, J.; Liu, H.; Guo, X.; Lai, B.; Brocks, G.; Chen, Q.; Tao, S.; Fenning, D. P.; Zhou, H. Microscopic Degradation in Formamidinium-Cesium

Lead Iodide Perovskite Solar Cells under Operational Stressors. *Joule* **2020**, *4* (8), 1743–1758. https://doi.org/10.1016/j.joule.2020.06.005.

(51)   Caprioglio, P.; Caicedo-Dávila, S.; Yang, T. C. J.; Wolff, C. M.; Peña-Camargo, F.; Fiala, P.; Rech, B.; Ballif, C.; Abou-Ras, D.; Stolterfoht, M.; Albrecht, S.; Jeangros, Q.; Neher, D. Nano-Emitting Heterostructures Violate Optical Reciprocity and Enable Efficient Photoluminescence in Halide-Segregated Methylammonium-Free Wide Bandgap Perovskites. *ACS Energy Lett.* **2021**, *6* (2), 419–428. https://doi.org/10.1021/acsenergylett.0c02270.

(52)   Juarez-Perez, E. J.; Ono, L. K.; Maeda, M.; Jiang, Y.; Hawash, Z.; Qi, Y. Photodecomposition and Thermal Decomposition in Methylammonium Halide Lead Perovskites and Inferred Design Principles to Increase Photovoltaic Device Stability. *J. Mater. Chem. A* **2018**, *6* (20), 9604–9612. https://doi.org/10.1039/c8ta03501f.

(53)   Dawood, R. I.; Forty, A. J.; Tubbs, M. R. The Photodecomposition of Lead Iodide. *Proc. R. Soc. London. Ser. A. Math. Phys. Sci.* **1965**, *284* (1397), 272–288. https://doi.org/10.1098/rspa.1965.0063.

(54)   Holovský, J.; Peter Amalathas, A.; Landová, L.; Dzurňák, B.; Conrad, B.; Ledinský, M.; Hájková, Z.; Pop-Georgievski, O.; Svoboda, J.; Yang, T. C. J.; Jeangros, Q. Lead Halide Residue as a Source of Light-Induced Reversible Defects in Hybrid Perovskite Layers and Solar Cells. *ACS Energy Lett.* **2019**, *4* (12), 3011–3017. https://doi.org/10.1021/acsenergylett.9b02080.

(55)   Jacobsson, T. J.; Correa-Baena, J. P.; Halvani Anaraki, E.; Philippe, B.; Stranks, S. D.; Bouduban, M. E. F.; Tress, W.; Schenk, K.; Teuscher, J.; Moser, J. E.; Rensmo, H.; Hagfeldt, A. Unreacted PbI2 as a Double-Edged Sword for Enhancing the Performance of Perovskite Solar Cells. *J. Am. Chem. Soc.* **2016**, *138* (32), 10331–10343. https://doi.org/10.1021/jacs.6b06320.

(56)   Bi, D.; Tress, W.; Dar, M. I.; Gao, P.; Luo, J.; Renevier, C.; Schenk, K.; Abate, A.; Giordano, F.; Correa Baena, J. P.; Decoppet, J. D.; Zakeeruddin, S. M.; Nazeeruddin, M. K.; Grätzel, M.; Hagfeldt, A. Efficient Luminescent Solar Cells Based on Tailored Mixed-Cation Perovskites. *Sci. Adv.* **2016**, *2* (1). https://doi.org/10.1126/sciadv.1501170.

(57)   Park, B. wook; Kedem, N.; Kulbak, M.; Lee, D. Y.; Yang, W. S.; Jeon, N. J.; Seo, J.; Kim, G.; Kim, K. J.; Shin, T. J.; Hodes, G.; Cahen, D.; Seok, S. Il. Understanding How Excess Lead Iodide Precursor Improves Halide Perovskite Solar Cell Performance. *Nat. Commun.* **2018**, *9* (1), 1–8. https://doi.org/10.1038/s41467-018-05583-w.

(58)   Liu, F.; Dong, Q.; Wong, M. K.; Djurišić, A. B.; Ng, A.; Ren, Z.; Shen, Q.; Surya, C.; Chan, W. K.; Wang, J.; Ng, A. M. C.; Liao, C.; Li, H.; Shih, K.; Wei, C.; Su, H.; Dai, J. Is Excess PbI2 Beneficial for Perovskite Solar Cell Performance? *Adv. Energy Mater.* **2016**, *6* (7), 1–9. https://doi.org/10.1002/aenm.201502206.

(59)   Matsui, T.; Yamamoto, T.; Nishihara, T.; Morisawa, R.; Yokoyama, T.; Sekiguchi, T.; Negami, T. Compositional Engineering for Thermally Stable, Highly Efficient Perovskite Solar Cells Exceeding 20% Power Conversion Efficiency with 85 °C/85% 1000 h Stability. *Adv. Mater.* **2019**, *31* (10), 3–8. https://doi.org/10.1002/adma.201806823.

(60)   Otero-Martínez, C.; Fiuza-Maneiro, N.; Polavarapu, L. Enhancing the Intrinsic and Extrinsic Stability of Halide Perovskite Nanocrystals for Efficient and Durable Optoelectronics. *ACS Appl. Mater. Interfaces* **2022**, *14* (30), 34291–34302. https://doi.org/10.1021/acsami.2c01822.

(61)   Kim, G. Y.; Senocrate, A.; Wang, Y. R.; Moia, D.; Maier, J. Photo-Effect on Ion Transport in Mixed Cation and Halide Perovskites and Implications for Photo-Demixing**. *Angew. Chemie - Int. Ed.* **2021**, *60* (2), 820–826. https://doi.org/10.1002/anie.202005853.

(62)   DeQuilettes, D. W.; Zhang, W.; Burlakov, V. M.; Graham, D. J.; Leijtens, T.; Osherov, A.; Bulović, V.; Snaith, H. J.; Ginger, D. S.; Stranks, S. D. Photo-Induced Halide Redistribution in Organic-Inorganic Perovskite Films. *Nat. Commun.* **2016**, *7* (May). https://doi.org/10.1038/ncomms11683.

(63)   Jacobs, D. A.; Wolff, C. M.; Chin, X.; Artuk, K.; Ballif, C.; Jeangros, Q. Lateral Ion Migration Accelerates Degradation in Halide Perovskite Devices. *Energy Environ. Sci.* **2022**, 1–4. https://doi.org/10.1039/D2EE02330J.

(64)   Thiesbrummel, J.; Gutierrez-partida, E.; Camargo, F.; Peters, K.; Lang, F.; Riedl, T.; Koch, N.; Snaith, H. Ion Induced Field Screening Governs the Early Performance Degradation of Perovskite Solar Cells. *Res. Sq.* **2023**, 1–20.

(65)   Thiesbrummel, J.; Le Corre, V. M.; Peña-Camargo, F.; Perdigón-Toro, L.; Lang, F.; Yang, F.; Grischek, M.; Gutierrez-Partida, E.; Warby, J.; Farrar, M. D.; Mahesh, S.; Caprioglio, P.; Albrecht, S.; Neher, D.; Snaith, H. J.; Stolterfoht, M. Universal Current Losses in Perovskite Solar Cells Due to Mobile Ions. *Adv. Energy Mater.* **2021**, *11* (34). https://doi.org/10.1002/aenm.202101447.

(66)   Kerner, R. A.; Xu, Z.; Larson, B. W.; Rand, B. P. The Role of Halide Oxidation in Perovskite Halide Phase Separation. *Joule* **2021**, *5* (9), 2273–2295. https://doi.org/10.1016/j.joule.2021.07.011.

(67)   Suchan, K.; Just, J.; Becker, P.; Rehermann, C.; Merdasa, A.; Mainz, R.; Scheblykin, I. G.; Unger, E. L. Broad Distribution of Local I/Br Ratio in Illuminated Mixed Halide Perovskite Films Revealed by Correlative X-Ray Diffraction and Photoluminescence. **2021**, No. February.

(68)   Yoon, S. J.; Draguta, S.; Manser, J. S.; Sharia, O.; Schneider, W. F.; Kuno, M.; Kamat, P. V. Tracking Iodide and Bromide Ion Segregation in Mixed Halide Lead Perovskites during Photoirradiation. *ACS Energy Lett.* **2016**, *1* (1), 290–296. https://doi.org/10.1021/acsenergylett.6b00158.

(69)   Knight, A. J.; Borchert, J.; Oliver, R. D. J.; Patel, J. B.; Radaelli, P. G.; Snaith, H. J.; Johnston, M. B.; Herz, L. M. Halide Segregation in Mixed-Halide Perovskites: Influence of A-Site Cations. *ACS Energy Lett.* **2021**, *6* (2), 799–808. https://doi.org/10.1021/acsenergylett.0c02475.

(70)   Xu, Z.; Kerner, R. A.; Harvey, S. P.; Zhu, K.; Berry, J. J.; Rand, B. P. Halogen Redox Shuttle Explains Voltage-Induced Halide Redistribution in Mixed-Halide Perovskite Devices. *ACS Energy Lett.* **2022**, 513–520. https://doi.org/10.1021/acsenergylett.2c02385.

(71)   Li, R.; Chen, B.; Ren, N.; Wang, P.; Shi, B.; Xu, Q.; Zhao, H.; Han, W.; Zhu, Z.; Liu, J.; Huang, Q.; Zhang, D.; Zhao, Y.; Zhang, X. CsPbCl3-Cluster-Widened Bandgap and Inhibited Phase Segregation in a Wide-Bandgap Perovskite and Its Application to NiOx-Based Perovskite/Silicon Tandem Solar Cells. *Adv. Mater.* **2022**, *34* (27), 1–8. https://doi.org/10.1002/adma.202201451.

(72)   Shi, L.; Bucknall, M. P.; Young, T. L.; Zhang, M.; Hu, L.; Bing, J.; Lee, D. S.; Kim, J.; Wu, T.; Takamure, N.; McKenzie, D. R.; Huang, S.; Green, M. A.; Ho-Baillie, A. W. Y. Gas Chromatography-Mass Spectrometry Analyses of Encapsulated Stable Perovskite Solar Cells. *Science (80-.).* **2020**, *368* (6497). https://doi.org/10.1126/science.aba2412.

(73)   Belich, N. A.; Petrov, A. A.; Ivlev, P. A.; Udalova, N. N.; Pustovalova, A. A.; Goodilin, E. A.; Tarasov, A. B. How to Stabilize Standard Perovskite Solar Cells to Withstand Operating Conditions under an Ambient Environment for More than 1000 Hours Using Simple and Universal Encapsulation. *J.*

Energy Chem. **2023**, *78*, 246–252. https://doi.org/10.1016/j.jechem.2022.12.010.

(74)   Cheacharoen, R.; Boyd, C. C.; Burkhard, G. F.; Leijtens, T.; Raiford, J. A.; Bush, K. A.; Bent, S. F.; McGehee, M. D. Encapsulating Perovskite Solar Cells to Withstand Damp Heat and Thermal Cycling. *Sustain. Energy Fuels* **2018**, *2* (11), 2398–2406. https://doi.org/10.1039/c8se00250a.

(75)   Cheacharoen, R.; Rolston, N.; Harwood, D.; Bush, K. A.; Dauskardt, R. H.; McGehee, M. D. Design and Understanding of Encapsulated Perovskite Solar Cells to Withstand Temperature Cycling. *Energy Environ. Sci.* **2018**, *11* (1), 144–150. https://doi.org/10.1039/c7ee02564e.

(76)   Zhou, J.; Liu, Z.; Yu, P.; Tong, G.; Chen, R.; Ono, L. K.; Chen, R.; Wang, H.; Ren, F.; Liu, S.; Wang, J.; Lan, Z.; Qi, Y.; Chen, W. Modulation of Perovskite Degradation with Multiple-Barrier for Light-Heat Stable Perovskite Solar Cells. *Nat. Commun.* **2023**, *14* (1), 6120. https://doi.org/10.1038/s41467-023-41856-9.

(77)   Li, C.; Wang, X.; Bi, E.; Jiang, F.; Park, S. M.; Li, Y.; Chen, L.; Wang, Z.; Zeng, L.; Chen, H.; Liu, Y.; Grice, C. R.; Abudulimu, A.; Chung, J.; Xian, Y.; Zhu, T.; Lai, H.; Chen, B.; Ellingson, R. J.; Fu, F.; Ginger, D. S.; Song, Z.; Sargent, E. H.; Yan, Y. Rational Design of Lewis Base Molecules for Stable and Efficient Inverted Perovskite Solar Cells. *Science (80-.).* **2023**, *379* (6633), 690–694. https://doi.org/10.1126/science.ade3970.

(78)   Bi, E.; Tang, W.; Chen, H.; Wang, Y.; Barbaud, J.; Wu, T.; Kong, W.; Tu, P.; Zhu, H.; Zeng, X.; He, J.; Kan, S. ichi; Yang, X.; Grätzel, M.; Han, L. Efficient Perovskite Solar Cell Modules with High Stability Enabled by Iodide Diffusion Barriers. *Joule* **2019**, *3* (11), 2748–2760. https://doi.org/10.1016/j.joule.2019.07.030.

(79)   Zheng, X.; Hou, Y.; Bao, C.; Yin, J.; Yuan, F.; Huang, Z.; Song, K.; Liu, J.; Troughton, J.; Gasparini, N.; Zhou, C.; Lin, Y.; Xue, D. J.; Chen, B.; Johnston, A. K.; Wei, N.; Hedhili, M. N.; Wei, M.; Alsalloum, A. Y.; Maity, P.; Turedi, B.; Yang, C.; Baran, D.; Anthopoulos, T. D.; Han, Y.; Lu, Z. H.; Mohammed, O. F.; Gao, F.; Sargent, E. H.; Bakr, O. M. Managing Grains and Interfaces via Ligand Anchoring Enables 22.3%-Efficiency Inverted Perovskite Solar Cells. *Nat. Energy* **2020**, *5* (2), 131–140. https://doi.org/10.1038/s41560-019-0538-4.

(80)   Babics, M.; De Bastiani, M.; Ugur, E.; Xu, L.; Bristow, H.; Toniolo, F.; Raja, W.; Subbiah, A. S.; Liu, J.; Torres Merino, L. V.; Aydin, E.; Sarwade, S.; Allen, T. G.; Razzaq, A.; Wehbe, N.; Salvador, M. F.; De Wolf, S. One-Year Outdoor Operation of Monolithic Perovskite/Silicon Tandem Solar Cells. *Cell Reports Phys. Sci.* **2023**, *4* (2). https://doi.org/10.1016/j.xcrp.2023.101280.

(81)   Xu, J.; Boyd, C. C.; Yu, Z. J.; Palmstrom, A. F.; Witter, D. J.; Larson, B. W.; France, R. M.; Werner, J.; Harvey, S. P.; Wolf, E. J.; Weigand, W.; Manzoor, S.; Van Hest, M. F. A. M.; Berry, J. J.; Luther, J. M.; Holman, Z. C.; McGehee, M. D. Triple-Halide Wide-Band Gap Perovskites with Suppressed Phase Segregation for Efficient Tandems. *Science (80-.).* **2020**, *367* (6482), 1097–1104. https://doi.org/10.1126/science.aaz4639.

(82)   Wolff, C. M.; Canil, L.; Rehermann, C.; Ngoc Linh, N.; Zu, F.; Ralaiarisoa, M.; Caprioglio, P.; Fiedler, L.; Stolterfoht, M.; Kogikoski, S.; Bald, I.; Koch, N.; Unger, E. L.; Dittrich, T.; Abate, A.; Neher, D. Perfluorinated Self-Assembled Monolayers Enhance the Stability and Efficiency of Inverted Perovskite Solar Cells. *ACS Nano* **2020**, *14* (2), 1445–1456. https://doi.org/10.1021/acsnano.9b03268.

(83)   Al-Ashouri, A.; Magomedov, A.; Roß, M.; Jošt, M.; Talaikis, M.; Chistiakova, G.; Bertram, T.; Márquez, J. A.; Köhnen, E.; Kasparavičius, E.; Levcenco, S.; Gil-Escrig, L.; Hages, C. J.; Schlatmann,

R.; Rech, B.; Malinauskas, T.; Unold, T.; Kaufmann, C. A.; Korte, L.; Niaura, G.; Getautis, V.; Albrecht, S. Conformal Monolayer Contacts with Lossless Interfaces for Perovskite Single Junction and Monolithic Tandem Solar Cells. *Energy Environ. Sci.* **2019**, *12* (11), 3356–3369. https://doi.org/10.1039/c9ee02268f.

(84)   Aktas, E.; Phung, N.; Köbler, H.; González, D. A.; Méndez, M.; Kafedjiska, I.; Turren-Cruz, S. H.; Wenisch, R.; Lauermann, I.; Abate, A.; Palomares, E. Understanding the Perovskite/Self-Assembled Selective Contact Interface for Ultra-Stable and Highly Efficient p-i-n Perovskite Solar Cells. *Energy Environ. Sci.* **2021**, *14* (7), 3976–3985. https://doi.org/10.1039/d0ee03807e.

(85)   Farag, A.; Feeney, T.; Hossain, I. M.; Schackmar, F.; Fassl, P.; Küster, K.; Bäuerle, R.; Ruiz-Preciado, M. A.; Hentschel, M.; Ritzer, D. B.; Diercks, A.; Li, Y.; Nejand, B. A.; Laufer, F.; Singh, R.; Starke, U.; Paetzold, U. W. Evaporated Self-Assembled Monolayer Hole Transport Layers: Lossless Interfaces in p-i-n Perovskite Solar Cells. *Adv. Energy Mater.* **2023**, *13* (8). https://doi.org/10.1002/aenm.202203982.

(86)   Al-Ashouri, A.; Köhnen, E.; Li, B.; Magomedov, A.; Hempel, H.; Caprioglio, P.; Márquez, J. A.; Vilches, A. B. M.; Kasparavicius, E.; Smith, J. A.; Phung, N.; Menzel, D.; Grischek, M.; Kegelmann, L.; Skroblin, D.; Gollwitzer, C.; Malinauskas, T.; Jošt, M.; Matič, G.; Rech, B.; Schlatmann, R.; Topič, M.; Korte, L.; Abate, A.; Stannowski, B.; Neher, D.; Stolterfoht, M.; Unold, T.; Getautis, V.; Albrecht, S. Monolithic Perovskite/Silicon Tandem Solar Cell with >29% Efficiency by Enhanced Hole Extraction. *Science (80-.).* **2020**, *370* (6522), 1300–1309. https://doi.org/10.1126/science.abd4016.

(87)   Chen, W.; Zhou, Y.; Chen, G.; Wu, Y.; Tu, B.; Liu, F. Z.; Huang, L.; Ng, A. M. C.; Djurišić, A. B.; He, Z. Alkali Chlorides for the Suppression of the Interfacial Recombination in Inverted Planar Perovskite Solar Cells. *Adv. Energy Mater.* **2019**, *9* (19), 1–10. https://doi.org/10.1002/aenm.201803872.

(88)   Irwin, M. D.; Buchholz, D. B.; Hains, A. W.; Chang, R. P. H.; Marks, T. J. P-Type Semiconducting Nickel Oxide as an Efficiency-Enhancing Anode Interfacial Layer in Polymer Bulk-Heterojunction Solar Cells. *Proc. Natl. Acad. Sci. U. S. A.* **2008**, *105* (8), 2783–2787. https://doi.org/10.1073/pnas.0711990105.

(89)   Steirer, K. X.; Ndione, P. F.; Widjonarko, N. E.; Lloyd, M. T.; Meyer, J.; Ratcliff, E. L.; Kahn, A.; Armstrong, N. R.; Curtis, C. J.; Ginley, D. S.; Berry, J. J.; Olson, D. C. Enhanced Efficiency in Plastic Solar Cells via Energy Matched Solution Processed NiO x Interlayers. *Adv. Energy Mater.* **2011**, *1* (5), 813–820. https://doi.org/10.1002/aenm.201100234.

(90)   Jeng, J. Y.; Chen, K. C.; Chiang, T. Y.; Lin, P. Y.; Tsai, T. Da; Chang, Y. C.; Guo, T. F.; Chen, P.; Wen, T. C.; Hsu, Y. J. Nickel Oxide Electrode Interlayer in CH3NH3PbI 3 Perovskite/PCBM Planar-Heterojunction Hybrid Solar Cells. *Adv. Mater.* **2014**, *26* (24), 4107–4113. https://doi.org/10.1002/adma.201306217.

(91)   Hu, L.; Peng, J.; Wang, W.; Xia, Z.; Yuan, J.; Lu, J.; Huang, X.; Ma, W.; Song, H.; Chen, W.; Cheng, Y. B.; Tang, J. Sequential Deposition of CH3NH3PbI3 on Planar NiO Film for Efficient Planar Perovskite Solar Cells. *ACS Photonics* **2014**, *1* (7), 547–553. https://doi.org/10.1021/ph5000067.

(92)   Yin, X.; Que, M.; Xing, Y.; Que, W. High Efficiency Hysteresis-Less Inverted Planar Heterojunction Perovskite Solar Cells with a Solution-Derived NiOx Hole Contact Layer. *J. Mater. Chem. A* **2015**, *3* (48), 24495–24503. https://doi.org/10.1039/c5ta08193a.

(93)   Zhu, Z.; Bai, Y.; Zhang, T.; Liu, Z.; Long, X.; Wei, Z.; Wang, Z.; Zhang, L.; Wang, J.; Yan, F.; Yang, S. High-Performance Hole-Extraction Layer of Sol-Gel-Processed NiO Nanocrystals for Inverted Planar Perovskite Solar Cells. *Angew. Chemie* **2014**, *126* (46), 12779–12783. https://doi.org/10.1002/ange.201405176.

(94)   Cui, J.; Meng, F.; Zhang, H.; Cao, K.; Yuan, H.; Cheng, Y.; Huang, F.; Wang, M. CH3NH3PbI3-Based Planar Solar Cells with Magnetron-Sputtered Nickel Oxide. *ACS Appl. Mater. Interfaces* **2014**, *6* (24), 22862–22870. https://doi.org/10.1021/am507108u.

(95)   Guziewicz, M.; Grochowski, J.; Borysiewicz, M.; Kaminska, E.; Domagala, J. Z.; Rzodkiewicz, W.; Witkowski, B. S.; Golaszewska, K.; Kruszka, R.; Ekielski, M.; Piotrowska, A. Electrical and Optical Properties of NiO Films Deposited by Magnetron Sputtering. *Opt. Appl.* **2011**, *41* (2), 431–440.

(96)   Hou, Y.; Aydin, E.; De Bastiani, M.; Xiao, C.; Isikgor, F. H.; Xue, D. J.; Chen, B.; Chen, H.; Bahrami, B.; Chowdhury, A. H.; Johnston, A.; Baek, S. W.; Huang, Z.; Wei, M.; Dong, Y.; Troughton, J.; Jalmood, R.; Mirabelli, A. J.; Allen, T. G.; Van Kerschaver, E.; Saidaminov, M. I.; Baran, D.; Qiao, Q.; Zhu, K.; De Wolf, S.; Sargent, E. H. Efficient Tandem Solar Cells with Solution-Processed Perovskite on Textured Crystalline Silicon. *Science (80-.).* **2020**, *367* (6482), 1135–1140. https://doi.org/10.1126/science.aay0262.

(97)   De Bastiani, M.; Mirabelli, A. J.; Hou, Y.; Gota, F.; Aydin, E.; Allen, T. G.; Troughton, J.; Subbiah, A. S.; Isikgor, F. H.; Liu, J.; Xu, L.; Chen, B.; Van Kerschaver, E.; Baran, D.; Fraboni, B.; Salvador, M. F.; Paetzold, U. W.; Sargent, E. H.; De Wolf, S. Efficient Bifacial Monolithic Perovskite/Silicon Tandem Solar Cells via Bandgap Engineering. *Nat. Energy* **2021**, *6* (2), 167–175. https://doi.org/10.1038/s41560-020-00756-8.

(98)   Di Giacomo, F.; Castriotta, L. A.; Kosasih, F. U.; Di Girolamo, D.; Ducati, C.; Di Carlo, A. Upscaling Inverted Perovskite Solar Cells: Optimization of Laser Scribing for Highly Efficient Mini-Modules. *Micromachines* **2020**, *11* (12), 1–13. https://doi.org/10.3390/mi11121127.

(99)   Kamino, B. A.; Paviet-Salomon, B.; Moon, S. J.; Badel, N.; Levrat, J.; Christmann, G.; Walter, A.; Faes, A.; Ding, L.; Diaz Leon, J. J.; Paracchino, A.; Despeisse, M.; Ballif, C.; Nicolay, S. Low-Temperature Screen-Printed Metallization for the Scale-Up of Two-Terminal Perovskite-Silicon Tandems. *ACS Appl. Energy Mater.* **2019**, *2* (5), 3815–3821. https://doi.org/10.1021/acsaem.9b00502.

(100)   Niu, G.; Wang, S.; Li, J.; Li, W.; Wang, L. Oxygen Doping in Nickel Oxide for Highly Efficient Planar Perovskite Solar Cells. *J. Mater. Chem. A* **2018**, *6* (11), 4721–4728. https://doi.org/10.1039/c8ta00161h.

(101)   Nishihara, Y.; Chikamatsu, M.; Kazaoui, S.; Miyadera, T.; Yoshida, Y. Influence of O2 Plasma Treatment on NiOx Layer in Perovskite Solar Cells. *Jpn. J. Appl. Phys.* **2018**, *57* (4), 04FS07. https://doi.org/10.7567/JJAP.57.04FS07.

(102)   Egerton, R. F. Electron Energy-Loss Spectroscopy in the TEM. *Reports Prog. Phys.* **2009**, *72* (1). https://doi.org/10.1088/0034-4885/72/1/016502.

(103)   Hou, D.; Zhang, J.; Gan, X.; Yuan, H.; Yu, L.; Lu, C.; Sun, H.; Hu, Z.; Zhu, Y. Pb and Li Co-Doped NiOx for Efficient Inverted Planar Perovskite Solar Cells. *J. Colloid Interface Sci.* **2020**, *559*, 29–38. https://doi.org/10.1016/j.jcis.2019.09.087.

(104)   Nie, W.; Tsai, H.; Blancon, J. C.; Liu, F.; Stoumpos, C. C.; Traore, B.; Kepenekian, M.; Durand, O.;

Katan, C.; Tretiak, S.; Crochet, J.; Ajayan, P. M.; Kanatzidis, M.; Even, J.; Mohite, A. D. Critical Role of Interface and Crystallinity on the Performance and Photostability of Perovskite Solar Cell on Nickel Oxide. *Adv. Mater.* **2018**, *30* (5), 1–9. https://doi.org/10.1002/adma.201703879.

(105) Li, G.; Jiang, Y.; Deng, S.; Tam, A.; Xu, P.; Wong, M.; Kwok, H. S. Overcoming the Limitations of Sputtered Nickel Oxide for High-Efficiency and Large-Area Perovskite Solar Cells. *Adv. Sci.* **2017**, *4* (12), 1700463. https://doi.org/10.1002/advs.201700463.

(106) Chen, W.; Wu, Y.; Yue, Y.; Liu, J.; Zhang, W.; Yang, X.; Chen, H.; Bi, E.; Ashraful, I.; Grätzel, M.; Han, L. Efficient and Stable Large-Area Perovskite Solar Cells with Inorganic Charge Extraction Layers. *Science (80-.).* **2015**, *350* (6263), 944–948. https://doi.org/10.1126/science.aad1015.

(107) Nandy, S.; Maiti, U. N.; Ghosh, C. K.; Chattopadhyay, K. K. Enhanced P-Type Conductivity and Band Gap Narrowing in Heavily Al Doped NiO Thin Films Deposited by RF Magnetron Sputtering. *J. Phys. Condens. Matter* **2009**, *21* (11). https://doi.org/10.1088/0953-8984/21/11/115804.

(108) Chen, W.; Liu, F. Z.; Feng, X. Y.; Djurišić, A. B.; Chan, W. K.; He, Z. B. Cesium Doped NiOx as an Efficient Hole Extraction Layer for Inverted Planar Perovskite Solar Cells. *Adv. Energy Mater.* **2017**, *7* (19), 1–8. https://doi.org/10.1002/aenm.201700722.

(109) Yang, S.; Wang, L.; Gao, L.; Cao, J.; Han, Q.; Yu, F.; Kamata, Y.; Zhang, C.; Fan, M.; Wei, G.; Ma, T. Excellent Moisture Stability and Efficiency of Inverted All-Inorganic CsPbIBr2 Perovskite Solar Cells through Molecule Interface Engineering. *ACS Appl. Mater. Interfaces* **2020**, *12* (12), 13931–13940. https://doi.org/10.1021/acsami.9b23532.

(110) Haque, M. A.; Sheikh, A. D.; Guan, X.; Wu, T. Metal Oxides as Efficient Charge Transporters in Perovskite Solar Cells. *Adv. Energy Mater.* **2017**, *7* (20), 1–23. https://doi.org/10.1002/aenm.201602803.

(111) Bakr, Z. H.; Wali, Q.; Fakharuddin, A.; Schmidt-Mende, L.; Brown, T. M.; Jose, R. Advances in Hole Transport Materials Engineering for Stable and Efficient Perovskite Solar Cells. *Nano Energy* **2017**, *34* (November 2016), 271–305. https://doi.org/10.1016/j.nanoen.2017.02.025.

(112) Yao, Q.; Zhao, L.; Sun, X.; Zhu, L.; Zhao, Y.; Qiang, Y.; Song, J. Na2S Decorated NiOx as Effective Hole Transport Layer for Inverted Planar Perovskite Solar Cells. *Mater. Sci. Semicond. Process.* **2023**, *153* (April 2022), 107107. https://doi.org/10.1016/j.mssp.2022.107107.

(113) Itzhak, A.; He, X.; Kama, A.; Kumar, S.; Ejgenberg, M.; Kahn, A.; Cahen, D. NiN-Passivated NiO Hole-Transport Layer Improves Halide Perovskite-Based Solar Cell. *ACS Appl. Mater. Interfaces* **2022**, *14* (42), 47587–47594. https://doi.org/10.1021/acsami.2c11701.

(114) Boyd, C. C.; Shallcross, R. C.; Moot, T.; Kerner, R.; Bertoluzzi, L.; Onno, A.; Kavadiya, S.; Chosy, C.; Wolf, E. J.; Werner, J.; Raiford, J. A.; de Paula, C.; Palmstrom, A. F.; Yu, Z. J.; Berry, J. J.; Bent, S. F.; Holman, Z. C.; Luther, J. M.; Ratcliff, E. L.; Armstrong, N. R.; McGehee, M. D. Overcoming Redox Reactions at Perovskite-Nickel Oxide Interfaces to Boost Voltages in Perovskite Solar Cells. *Joule* **2020**, *4* (8), 1759–1775. https://doi.org/10.1016/j.joule.2020.06.004.

(115) Bai, S.; Da, P.; Li, C.; Wang, Z.; Yuan, Z.; Fu, F.; Kawecki, M.; Liu, X.; Sakai, N.; Wang, J. T. W.; Huettner, S.; Buecheler, S.; Fahlman, M.; Gao, F.; Snaith, H. J. Planar Perovskite Solar Cells with Long-Term Stability Using Ionic Liquid Additives. *Nature* **2019**, *571* (7764), 245–250. https://doi.org/10.1038/s41586-019-1357-2.

(116) Bush, K. A.; Palmstrom, A. F.; Yu, Z. J.; Boccard, M.; Cheacharoen, R.; Mailoa, J. P.; McMeekin, D.

P.; Hoye, R. L. Z.; Bailie, C. D.; Leijtens, T.; Peters, I. M.; Minichetti, M. C.; Rolston, N.; Prasanna, R.; Sofia, S.; Harwood, D.; Ma, W.; Moghadam, F.; Snaith, H. J.; Buonassisi, T.; Holman, Z. C.; Bent, S. F.; McGehee, M. D. 23.6%-Efficient Monolithic Perovskite/Silicon Tandem Solar Cells With Improved Stability. *Nat. Energy* **2017**, *2* (4), 1–7. https://doi.org/10.1038/nenergy.2017.9.

(117) Islam, M. B.; Yanagida, M.; Shirai, Y.; Nabetani, Y.; Miyano, K. NiOx Hole Transport Layer for Perovskite Solar Cells with Improved Stability and Reproducibility. *ACS Omega* **2017**, *2* (5), 2291–2299. https://doi.org/10.1021/acsomega.7b00538.

(118) Guo, Y.; Ma, J.; Wang, H.; Ye, F.; Xiong, L.; Lei, H.; Tan, Z. Overcoming Ni3+-Induced Non-Radiative Recombination at Perovskite-Nickel Oxide Interfaces to Boost Voltages in Perovskite Solar Cells. *Adv. Mater. Interfaces* **2021**, *8* (16), 1–7. https://doi.org/10.1002/admi.202100920.

(119) Wang, H.; Yuan, H.; Yu, J.; Zhang, C.; Li, K.; You, M.; Li, W.; Shao, J.; Wei, J.; Zhang, X.; Chen, R.; Yang, X.; Zhao, W. Boosting the Efficiency of NiOx-Based Perovskite Light-Emitting Diodes by Interface Engineering. *ACS Appl. Mater. Interfaces* **2020**, *12* (47), 53528–53536. https://doi.org/10.1021/acsami.0c16139.

(120) Mann, D. S.; Kwon, S.; Patil, P.; Na, S. Nano Energy Revivification of Nickel Oxide-Perovskite Interfaces via Nickel Nitrate to Boost Performance in Perovskite Solar Cells. *Nano Energy* **2023**, *106* (June 2022), 108062. https://doi.org/10.1016/j.nanoen.2022.108062.

(121) Peng, Z.; Zuo, Z.; Qi, Q.; Hou, S.; Fu, Y.; Zou, D. Managing the Double-Edged Sword of Ni3+ in Sputter-Deposited NiOx by Interfacial Redox Reactions for Efficient Perovskite Solar Cells. *ACS Appl. Energy Mater.* **2023**, *6* (3), 1396–1403. https://doi.org/10.1021/acsaem.2c03260.

(122) Zhang, C.; Shen, X.; Chen, M.; Zhao, Y.; Lin, X.; Qin, Z.; Wang, Y.; Han, L. Constructing a Stable and Efficient Buried Heterojunction via Halogen Bonding for Inverted Perovskite Solar Cells. *Adv. Energy Mater.* **2023**, *13* (2), 1–9. https://doi.org/10.1002/aenm.202203250.

(123) Lee, S.; Lee, J.; Park, H.; Choi, J.; Baac, H. W.; Park, S.; Park, H. J. Defect-Passivating Organic / Inorganic Bicomponent Hole-Transport Layer for High E Ffi Ciency Metal-Halide Perovskite Device. **2020**.

(124) Du, M.; Zhao, S.; Duan, L.; Cao, Y.; Wang, H.; Sun, Y.; Wang, L.; Zhu, X.; Feng, J.; Liu, L.; Jiang, X.; Dong, Q.; Shi, Y.; Wang, K.; Liu, S. (Frank). Surface Redox Engineering of Vacuum-Deposited NiOx for Top-Performance Perovskite Solar Cells and Modules. *Joule* **2022**, *6* (8), 1931–1943. https://doi.org/10.1016/j.joule.2022.06.026.

(125) Burgelman, M.; Nollet, P.; Degrave, S. Modelling Polycrystalline Semiconductor Solar Cells. *Thin Solid Films* **2000**, *361*, 527–532. https://doi.org/10.1016/S0040-6090(99)00825-1.

(126) Biesinger, M. C.; Payne, B. P.; Lau, L. W. M.; Gerson, A.; Smart, R. S. C. X-Ray Photoelectron Spectroscopic Chemical State Quantification of Mixed Nickel Metal, Oxide and Hydroxide Systems. *Surf. Interface Anal.* **2009**, *41* (4), 324–332. https://doi.org/10.1002/sia.3026.

(127) Biesinger, M. C.; Payne, B. P.; Grosvenor, A. P.; Lau, L. W. M.; Gerson, A. R.; Smart, R. S. C. Resolving Surface Chemical States in XPS Analysis of First Row Transition Metals, Oxides and Hydroxides: Cr, Mn, Fe, Co and Ni. *Appl. Surf. Sci.* **2011**, *257* (7), 2717–2730. https://doi.org/10.1016/j.apsusc.2010.10.051.

(128) Yang, F.; Zhou, X.; Plymale, N. T.; Sun, K.; Lewis, N. S. Evaluation of Sputtered Nickel Oxide, Cobalt Oxide and Nickel-Cobalt Oxide on n-Type Silicon Photoanodes for Solar-Driven O2(g) Evolution

from Water. *J. Mater. Chem. A* **2020**, *8* (28), 13955–13963. https://doi.org/10.1039/d0ta03725g.

(129)   Rao, K. V.; Smakula, A. Dielectric Properties of Cobalt Oxide, Nickel Oxide, and Their Mixed Crystals. *J. Appl. Phys.* **1965**, *36* (6), 2031–2038. https://doi.org/10.1063/1.1714397.

(130)   Phung, N.; Verheijen, M.; Todinova, A.; Datta, K.; Verhage, M.; Al-Ashouri, A.; Köbler, H.; Li, X.; Abate, A.; Albrecht, S.; Creatore, M. Enhanced Self-Assembled Monolayer Surface Coverage by ALD NiO in p-i-n Perovskite Solar Cells. *ACS Appl. Mater. Interfaces* **2022**, *14* (1), 2166–2176. https://doi.org/10.1021/acsami.1c15860.

(131)   Sun, J.; Shou, C.; Sun, J.; Wang, X.; Yang, Z.; Chen, Y.; Wu, J.; Yang, W.; Long, H.; Ying, Z.; Yang, X.; Sheng, J.; Yan, B.; Ye, J. NiOx-Seeded Self-Assembled Monolayers as Highly Hole-Selective Passivating Contacts for Efficient Inverted Perovskite Solar Cells. *Sol. RRL* **2021**, *5* (11), 1–8. https://doi.org/10.1002/solr.202100663.

(132)   Stolterfoht, M.; Caprioglio, P.; Wolff, C. M.; Márquez, J. A.; Nordmann, J.; Zhang, S.; Rothhardt, D.; Hörmann, U.; Amir, Y.; Redinger, A.; Kegelmann, L.; Zu, F.; Albrecht, S.; Koch, N.; Kirchartz, T.; Saliba, M.; Unold, T.; Neher, D. The Impact of Energy Alignment and Interfacial Recombination on the Internal and External Open-Circuit Voltage of Perovskite Solar Cells. *Energy Environ. Sci.* **2019**, *12* (9), 2778–2788. https://doi.org/10.1039/c9ee02020a.

(133)   Stolterfoht, M.; Le Corre, V. M.; Feuerstein, M.; Caprioglio, P.; Koster, L. J. A.; Neher, D. Voltage-Dependent Photoluminescence and How It Correlates with the Fill Factor and Open-Circuit Voltage in Perovskite Solar Cells. *ACS Energy Lett.* **2019**, *4* (12), 2887–2892. https://doi.org/10.1021/acsenergylett.9b02262.

(134)   Miller, O. D.; Yablonovitch, E.; Kurtz, S. R. Strong Internal and External Luminescence as Solar Cells Approach the Shockley-Queisser Limit. *IEEE J. Photovoltaics* **2012**, *2* (3), 303–311. https://doi.org/10.1109/JPHOTOV.2012.2198434.

(135)   Wolff, C. M.; Caprioglio, P.; Stolterfoht, M.; Neher, D. Nonradiative Recombination in Perovskite Solar Cells: The Role of Interfaces. *Adv. Mater.* **2019**, *31* (52). https://doi.org/10.1002/adma.201902762.

(136)   Tauc, J. Absorption Edge and Internal Electric Fields in Amorphous Semiconductors. *Mater. Res. Bull.* **1970**, *5* (8), 721–729. https://doi.org/10.1016/0025-5408(70)90112-1.

(137)   Karsthof, R.; Anton, A. M.; Kremer, F.; Grundmann, M. Nickel Vacancy Acceptor in Nickel Oxide: Doping beyond Thermodynamic Equilibrium. *Phys. Rev. Mater.* **2020**, *4* (3), 1–7. https://doi.org/10.1103/PhysRevMaterials.4.034601.

(138)   Thimsen, E.; Martinson, A. B. F.; Elam, J. W.; Pellin, M. J. Energy Levels, Electronic Properties, and Rectification in Ultrathin p-NiO Films Synthesized by Atomic Layer Deposition. *J. Phys. Chem. C* **2012**, *116* (32), 16830–16840. https://doi.org/10.1021/jp302008k.

(139)   Manceriu, L. M.; Colson, P.; Maho, A.; Eppe, G.; Nguyen, N. D.; Labrugere, C.; Rougier, A.; Cloots, R.; Henrist, C. Straightforward Prediction of the Ni1-XO Layers Stoichiometry by Using Optical and Electrochemical Measurements. *J. Phys. D. Appl. Phys.* **2017**, *50* (22). https://doi.org/10.1088/1361-6463/aa6e71.

(140)   Diekmann, J.; Caprioglio, P.; Rothhardt, D.; Arvind, M.; Unold, T.; Kirchartz, T.; Neher, D.; Stolterfoht, M. Pathways towards 30% Efficient Perovskite Solar Cells. *arXiv* **2019**, No. i.

(141) Ni, Z.; Bao, C.; Liu, Y.; Jiang, Q.; Wu, W. Q.; Chen, S.; Dai, X.; Chen, B.; Hartweg, B.; Yu, Z.; Holman, Z.; Huang, J. Resolving Spatial and Energetic Distributions of Trap States in Metal Halide Perovskite Solar Cells. *Science (80-.).* **2020**, *367* (6484), 1352–1358. https://doi.org/10.1126/science.aba0893.

(142) Kashir, A.; Jeong, H. W.; Lee, G. H.; Mikheenko, P.; Jeong, Y. H. Dielectric Properties of Strained Nickel Oxide Thin Films. *J. Korean Phys. Soc.* **2019**, *74* (10), 984–988. https://doi.org/10.3938/jkps.74.984.

(143) Ahmmed, S.; Aktar, A.; Rahman, M. F.; Hossain, J.; Ismail, A. B. M. A Numerical Simulation of High Efficiency CdS/CdTe Based Solar Cell Using NiO HTL and ZnO TCO. *Optik (Stuttg).* **2020**, *223* (May), 165625. https://doi.org/10.1016/j.ijleo.2020.165625.

(144) Dussouillez, M.; Moon, S.; Mensi, M.; Wolff, C. M.; Liu, Y.; Yum, H.; Kamino, B. A.; Walter, A.; Sahli, F.; Lauber, L.; Christmann, G.; Sivula, K.; Jeangros, Q.; Ballif, C.; Nicolay, S.; Paracchino, A. Understanding and Mitigating the Degradation of Perovskite Solar Cells Based on a Nickel Oxide Hole Transport Material during Damp Heat Testing. **2022**. https://doi.org/10.1021/acsami.3c02709.

(145) Yan, X.; Zheng, J.; Zheng, L. L.; Lin, G.; Lin, H.; Chen, G.; Du, B.; Zhang, F. Optimization of Sputtering NiOx Films for Perovskite Solar Cell Applications. *Mater. Res. Bull.* **2018**, *103* (March), 150–157. https://doi.org/10.1016/j.materresbull.2018.03.027.

(146) Shi, J.; Lai, L.; Zhang, P.; Li, H.; Qin, Y.; Gao, Y.; Luo, L.; Lu, J. Aluminum Doped Nickel Oxide Thin Film with Improved Electrochromic Performance from Layered Double Hydroxides Precursor in Situ Pyrolytic Route. *J. Solid State Chem.* **2016**, *241*, 1–8. https://doi.org/10.1016/j.jssc.2016.05.032.

(147) Chen, W.; Wu, Y.; Yue, Y.; Liu, J.; Zhang, W.; Yang, X.; Chen, H.; Bi, E.; Ashraful, I.; Grätzel, M.; Han, L. Efficient and Stable Large-Area Perovskite Solar Cells with Inorganic Charge Extraction Layers. *Science (80-.).* **2015**, *350* (6263), 944–948. https://doi.org/10.1126/science.aad1015.

(148) Traore, B.; Pedesseau, L.; Blancon, J. C.; Tretiak, S.; Mohite, A. D.; Even, J.; Katan, C.; Kepenekian, M. Importance of Vacancies and Doping in the Hole-Transporting Nickel Oxide Interface with Halide Perovskites. *ACS Appl. Mater. Interfaces* **2020**, *12* (5), 6633–6640. https://doi.org/10.1021/acsami.9b19457.

(149) Predanocy, M.; Hotový, I.; Čaplovičová, M. Structural, Optical and Electrical Properties of Sputtered NiO Thin Films for Gas Detection. *Appl. Surf. Sci.* **2017**, *395*, 208–213. https://doi.org/10.1016/j.apsusc.2016.05.028.

(150) Yan, X.; Zheng, J.; Zheng, L. L.; Lin, G.; Lin, H.; Chen, G.; Du, B.; Zhang, F. Optimization of Sputtering NiOx Films for Perovskite Solar Cell Applications. *Mater. Res. Bull.* **2018**, *103*, 150–157. https://doi.org/10.1016/j.materresbull.2018.03.027.

(151) Abu Bakar, W. A. W.; Othman, M. Y.; Ali, R.; Yong, C. K.; Toemen, S. The Investigation of Active Sites on Nickel Oxide Based Catalysts towards the In-Situ Reactions of Methanation and Desulfurization. *Mod. Appl. Sci.* **2009**, *3* (2), 35–43. https://doi.org/10.5539/mas.v3n2p35.

(152) Ho, K.; Wei, M.; Sargent, E. H.; Walker, G. C. Grain Transformation and Degradation Mechanism of Formamidinium and Cesium Lead Iodide Perovskite under Humidity and Light. *ACS Energy Lett.* **2021**, *6* (3), 934–940. https://doi.org/10.1021/acsenergylett.0c02247.

(153) Wu, T.; Ono, L. K.; Yoshioka, R.; Ding, C.; Zhang, C.; Mariotti, S.; Zhang, J.; Mitrofanov, K.; Liu, X.; Segawa, H.; Kabe, R.; Han, L.; Qi, Y. Elimination of Light-Induced Degradation at the Nickel Oxide-Perovskite Heterojunction by Aprotic Sulfonium Layers towards Long-Term Operationally Stable Inverted Perovskite Solar Cells. *Energy Environ. Sci.* **2022**, 4612–4624. https://doi.org/10.1039/d2ee01801b.

(154) Yang, F.; Wilkinson, M.; Austin, E. J.; O'Donnell, K. P. Origin of the Stokes Shift: A Geometrical Model of Exciton Spectra in 2D Semiconductors. *Phys. Rev. Lett.* **1994**, *72* (12), 1945–1945. https://doi.org/10.1103/physrevlett.72.1945.

(155) Yi, C.; Luo, J.; Meloni, S.; Boziki, A.; Ashari-Astani, N.; Grätzel, C.; Zakeeruddin, S. M.; Röthlisberger, U.; Grätzel, M. Entropic Stabilization of Mixed A-Cation ABX3 Metal Halide Perovskites for High Performance Perovskite Solar Cells. *Energy Environ. Sci.* **2016**, *9* (2), 656–662. https://doi.org/10.1039/c5ee03255e.

(156) Donakowski, A.; Miller, D. W.; Anderson, N. C.; Ruth, A.; Sanehira, E. M.; Berry, J. J.; Irwin, M. D.; Rockett, A.; Steirer, K. X. Improving Photostability of Cesium-Doped Formamidinium Lead Triiodide Perovskite. *ACS Energy Lett.* **2021**, *6* (2), 574–580. https://doi.org/10.1021/acsenergylett.0c02339.

(157) De Bastiani, M.; Van Kerschaver, E.; Jeangros, Q.; Ur Rehman, A.; Aydin, E.; Isikgor, F. H.; Mirabelli, A. J.; Babics, M.; Liu, J.; Zhumagali, S.; Ugur, E.; Harrison, G. T.; Allen, T. G.; Chen, B.; Hou, Y.; Shikin, S.; Sargent, E. H.; Ballif, C.; Salvador, M.; De Wolf, S. Toward Stable Monolithic Perovskite/Silicon Tandem Photovoltaics: A Six-Month Outdoor Performance Study in a Hot and Humid Climate. *ACS Energy Lett.* **2021**, *6*, 2944–2951. https://doi.org/10.1021/acsenergylett.1c01018.

(158) Choo, D. C.; Kim, T. W. Degradation Mechanisms of Silver Nanowire Electrodes under Ultraviolet Irradiation and Heat Treatment. *Sci. Rep.* **2017**, *7* (1), 1–12. https://doi.org/10.1038/s41598-017-01843-9.

(159) Wang, S.; Jiang, Y.; Juarez-Perez, E. J.; Ono, L. K.; Qi, Y. Accelerated Degradation of Methylammonium Lead Iodide Perovskites Induced by Exposure to Iodine Vapour. *Nat. Energy* **2017**, *2* (1), 1–8. https://doi.org/10.1038/nenergy.2016.195.

(160) Li, J.; Dong, Q.; Li, N.; Wang, L. Direct Evidence of Ion Diffusion for the Silver-Electrode-Induced Thermal Degradation of Inverted Perovskite Solar Cells. *Adv. Energy Mater.* **2017**, *7* (14), 1–8. https://doi.org/10.1002/aenm.201602922.

(161) Zhao, Y.; Heumueller, T.; Zhang, J.; Luo, J.; Kasian, O.; Langner, S.; Kupfer, C.; Liu, B.; Zhong, Y.; Elia, J.; Osvet, A.; Wu, J.; Liu, C.; Wan, Z.; Jia, C.; Li, N.; Hauch, J.; Brabec, C. J. A Bilayer Conducting Polymer Structure for Planar Perovskite Solar Cells with over 1,400 Hours Operational Stability at Elevated Temperatures. *Nat. Energy* **2022**, *7* (2), 144–152. https://doi.org/10.1038/s41560-021-00953-z.

(162) Mamun, A. Al; Ava, T. T.; Abdel-Fattah, T. M.; Jeong, H. J.; Jeong, M. S.; Han, S.; Yoon, H.; Namkoong, G. Effect of Hot-Casted NiO Hole Transport Layer on the Performance of Perovskite Solar Cells. *Sol. Energy* **2019**, *188* (February), 609–618. https://doi.org/10.1016/j.solener.2019.06.040.

(163) Tsai, H.; Asadpour, R.; Blancon, J. C.; Stoumpos, C. C.; Durand, O.; Strzalka, J. W.; Chen, B.; Verduzco, R.; Ajayan, P. M.; Tretiak, S.; Even, J.; Alam, M. A.; Kanatzidis, M. G.; Nie, W.; Mohite,

A. D. Light-Induced Lattice Expansion Leads to High-Efficiency Perovskite Solar Cells. *Science (80-.).* **2018**, *360* (6384), 67–70. https://doi.org/10.1126/science.aap8671.

(164) Turkay, D.; Artuk, K.; Chin, X.; Jacobs, D. A.; Moon, S.; Walter, A.; Mensi, M.; Andreatta, G.; Blondiaux, N.; Lai, H.; Fu, F.; Boccard, M.; Jeangros, Q.; Wolff, C. M.; Ballif, C. High-Efficiency (>30%) Monolithic Perovskite-Si Tandem Solar Cells with Flat Front-Side Wafers. **2023**.

(165) Khenkin, M. V.; Anoop, K. M.; Katz, E. A.; Visoly-Fisher, I. Bias-Dependent Degradation of Various Solar Cells: Lessons for Stability of Perovskite Photovoltaics. *Energy Environ. Sci.* **2019**, *12* (2), 550–558. https://doi.org/10.1039/c8ee03475c.

(166) Babu, V.; Fuentes Pineda, R.; Ahmad, T.; Alvarez, A. O.; Castriotta, L. A.; Di Carlo, A.; Fabregat-Santiago, F.; Wojciechowski, K. Improved Stability of Inverted and Flexible Perovskite Solar Cells with Carbon Electrode. *ACS Appl. Energy Mater.* **2020**, *3* (6), 5126–5134. https://doi.org/10.1021/acsaem.0c00702.

(167) Wu, S.; Chen, R.; Zhang, S.; Babu, B. H.; Yue, Y.; Zhu, H.; Yang, Z.; Chen, C.; Chen, W.; Huang, Y.; Fang, S.; Liu, T.; Han, L.; Chen, W. A Chemically Inert Bismuth Interlayer Enhances Long-Term Stability of Inverted Perovskite Solar Cells. *Nat. Commun.* No. 2019, 1–11. https://doi.org/10.1038/s41467-019-09167-0.

(168) Behrouznejad, F.; Shahbazi, S.; Taghavinia, N.; Wu, H. P.; Wei-Guang Diau, E. A Study on Utilizing Different Metals as the Back Contact of CH3NH3PbI3 Perovskite Solar Cells. *J. Mater. Chem. A* **2016**, *4* (35), 13488–13498. https://doi.org/10.1039/c6ta05938d.

(169) Hatt, T.; Kabakli, Ö.; Schulze, P. S. C.; Richter, A.; Glunz, S. W.; Glatthaar, M.; Goldschmidt, J. C.; Bartsch, J. Electroplated Copper Metal Contacts on Perovskite Solar Cells. *Sol. RRL* **2021**, *5* (9), 1–6. https://doi.org/10.1002/solr.202100381.

(170) Hatt, T.; Schulze, P. S. C.; Er-Raji, O.; Richter, A.; Efinger, R.; Schultz-Wittmann, O.; Heydarian, M.; Tutsch, L.; Goldschmidt, J. C.; Glatthaar, M.; Glunz, S. W.; Bartsch, J. Plated Copper Electrodes for Two-Terminal Perovskite/Silicon Tandem Solar Cells. *Sol. Energy Mater. Sol. Cells* **2022**, *246* (April), 111912. https://doi.org/10.1016/j.solmat.2022.111912.

(171) Ye, F.; Zhang, S.; Warby, J.; Wu, J.; Gutierrez-Partida, E.; Lang, F.; Shah, S.; Saglamkaya, E.; Sun, B.; Zu, F.; Shoaee, S.; Wang, H.; Stiller, B.; Neher, D.; Zhu, W. H.; Stolterfoht, M.; Wu, Y. Overcoming C60-Induced Interfacial Recombination in Inverted Perovskite Solar Cells by Electron-Transporting Carborane. *Nat. Commun.* **2022**, *13* (1). https://doi.org/10.1038/s41467-022-34203-x.

(172) Momblona, C.; Gil-Escrig, L.; Bandiello, E.; Hutter, E. M.; Sessolo, M.; Lederer, K.; Blochwitz-Nimoth, J.; Bolink, H. J. Efficient Vacuum Deposited P-i-n and n-i-p Perovskite Solar Cells Employing Doped Charge Transport Layers. *Energy Environ. Sci.* **2016**, *9* (11), 3456–3463. https://doi.org/10.1039/c6ee02100j.

(173) Gu, H.; Fei, C.; Yang, G.; Chen, B.; Uddin, M. A.; Zhang, H.; Ni, Z.; Jiao, H.; Xu, W.; Yan, Z.; Huang, J. Design Optimization of Bifacial Perovskite Minimodules for Improved Efficiency and Stability. *Nat. Energy* **2023**, *8* (7), 675–684. https://doi.org/10.1038/s41560-023-01254-3.

(174) Artuk, K.; Turkay, D.; Mensi, M. D.; Steele, J. A.; Jacobs, D. A.; Othman, M.; Chin, X. Y.; Moon, S.; Tiwari, A. N.; Hessler-wyser, A.; Jeangros, Q.; Ballif, C.; Wolff, C. M. A Universal Perovskite / C60 Interface Modification via Atomic Layer Deposited Aluminum Oxide for Perovskite Solar Cells and Perovskite- Silicon Tandems. **2023**.

(175) Kim, H. Il; Kim, M. J.; Choi, K.; Lim, C.; Kim, Y. H.; Kwon, S. K.; Park, T. Improving the Performance and Stability of Inverted Planar Flexible Perovskite Solar Cells Employing a Novel NDI-Based Polymer as the Electron Transport Layer. *Adv. Energy Mater.* **2018**, *8* (16), 1–7. https://doi.org/10.1002/aenm.201702872.

(176) Liu, W.; Shaikh, D. B.; Rao, P. S.; Bhosale, R. S.; Said, A. A.; Mak, A. M.; Wang, Z.; Zhao, M.; Gao, W.; Chen, B.; Lam, Y. M.; Fan, W.; Bhosale, S. V.; Bhosale, S. V.; Zhang, Q. Molecular Aggregation of Naphthalene Diimide(NDI) Derivatives in Electron Transport Layers of Inverted Perovskite Solar Cells and Their Influence on the Device Performance. *Chem. - An Asian J.* **2020**, *15* (1), 112–121. https://doi.org/10.1002/asia.201901452.

(177) Jiang, K.; Wu, F.; Yu, H.; Yao, Y.; Zhang, G.; Zhu, L.; Yan, H. A Perylene Diimide-Based Electron Transport Layer Enabling Efficient Inverted Perovskite Solar Cells. *J. Mater. Chem. A* **2018**, *6* (35), 16868–16873. https://doi.org/10.1039/c8ta06081a.

(178) Luo, Z.; Wu, F.; Zhang, T.; Zeng, X.; Xiao, Y.; Liu, T.; Zhong, C.; Lu, X.; Zhu, L.; Yang, S.; Yang, C. Designing a Perylene Diimide/Fullerene Hybrid as Effective Electron Transporting Material in Inverted Perovskite Solar Cells with Enhanced Efficiency and Stability. *Angew. Chemie - Int. Ed.* **2019**, *58* (25), 8520–8525. https://doi.org/10.1002/anie.201904195.

(179) Huang, J.; Gu, Z.; Zuo, L.; Ye, T.; Chen, H. Morphology Control of Planar Heterojunction Perovskite Solar Cells with Fluorinated PDI Films as Organic Electron Transport Layer. *Sol. Energy* **2016**, *133*, 331–338. https://doi.org/10.1016/j.solener.2016.04.017.

(180) Cruz, A.; Erfurt, D.; Wagner, P.; Morales-Vilches, A. B.; Ruske, F.; Schlatmann, R.; Stannowski, B. Optoelectrical Analysis of TCO+Silicon Oxide Double Layers at the Front and Rear Side of Silicon Heterojunction Solar Cells. *Sol. Energy Mater. Sol. Cells* **2022**, *236* (May 2021), 111493. https://doi.org/10.1016/j.solmat.2021.111493.

(181) Jay, F.; Gageot, T.; Pinoit, G.; Thiriot, B.; Veirman, J.; Cabal, R.; De Vecchi, S.; Favre, W.; Sciuto, M.; Gerardi, C.; Foti, M. Reduction in Indium Usage for Silicon Heterojunction Solar Cells in a Short-Term Industrial Perspective. *Sol. RRL* **2023**, *7* (8), 1–7. https://doi.org/10.1002/solr.202200598.

(182) Chavan, G. T.; Kim, Y.; Khokhar, M. Q.; Hussain, S. Q.; Cho, E. C.; Yi, J.; Ahmad, Z.; Rosaiah, P.; Jeon, C. W. A Brief Review of Transparent Conducting Oxides (TCO): The Influence of Different Deposition Techniques on the Efficiency of Solar Cells. *Nanomaterials* **2023**, *13* (7). https://doi.org/10.3390/nano13071226.

(183) Xu, Z.; Bristow, H.; Babics, M.; Vishal, B.; Aydin, E.; Azmi, R.; Ugur, E.; Yildirim, B. K.; Liu, J.; Kerner, R. A.; De Wolf, S.; Rand, B. P. Reverse-Bias Resilience of Monolithic Perovskite/Silicon Tandem Solar Cells. *Joule* **2023**, *7* (9), 1992–2002. https://doi.org/10.1016/j.joule.2023.07.017.

(184) Jiao, H.; Ni, Z.; Shi, Z.; Fei, C.; Liu, Y.; Dai, X.; Huang, J. Perovskite Grain Wrapping by Converting Interfaces and Grain Boundaries into Robust and Water-Insoluble Low-Dimensional Perovskites. *Sci. Adv.* **2022**, *8* (48), 1–10. https://doi.org/10.1126/sciadv.abq4524.

(185) Li, G.; Su, Z.; Canil, L.; Hughes, D.; Aldamasy, M. H.; Dagar, J.; Trofimov, S.; Wang, L.; Zuo, W.; Jerónimo-Rendon, J. J.; Byranvand, M. M.; Wang, C.; Zhu, R.; Zhang, Z.; Yang, F.; Nasti, G.; Naydenov, B.; Tsoi, W. C.; Li, Z.; Gao, X.; Wang, Z.; Jia, Y.; Unger, E.; Saliba, M.; Li, M.; Abate, A. Highly Efficient P-i-n Perovskite Solar Cells That Endure Temperature Variations. *Science (80-.).* **2023**, *379* (6630), 399–403. https://doi.org/10.1126/science.add7331.

List of acronyms

PV vocabulary

DH Damp heat

ETM Electron transport material

HTM Hole transport material

IEC-61265 International Electrotechnical Commission

LCOE The levelized cost of electricity

LS Light soaking

p-i-n Positive – intrinsic – negative

Pk Perovskite

PSC Perovskite solar cell

PV Photovoltaic

R.H Relative humidity

Si Silicon

TCO Transparent conductive oxide

Eff Efficiency

FF Fill Factor

J_{SC} Short-circuit current

MPPT Maximal power point tracking

Rs Series resistance

Rsh Sheet resistance

V_{OC} Open-circuit voltage

Materials and solvents

CsBr Caesium bromide

CsI Caesium iodide

FA Formamidinium

FABr Formamidinium bromide

FAI Formamidinium Iodide

MA Methylammonium

MABr Methylammonium bromide

$PbBr_2$ Lead bromide

PbI_2 Lead iodide

pFBPA pentaflourobenzylphosphonic acid

2-MP 2-methyl pyrazine

CB chlorobenzene

DMF Dimethylformamide

DMSO Dimethylsulfoxide

C_{60} Buckminsterfullerene

DPPP 1,3-bis(diphenylphosphino)propane

ITO Indium thin oxide

MeO-2PACz (2-(3,6-Dimethoxy-9H-carbazol-9-yl)ethyl)phosphonic acid

Ni_2O_3 Nickel(III) oxide

NiOOH Nickel oxide hydroxide

NiO_X Nickel oxide

np-SiO_X Silicon oxide nanoparticles

PCBM Phenyl-C61-butyric acid methyl ester

PEIE polyethylenimine ethoxylated

Poly-TPD Poly(4-butyltriphenylamine)

PTAA Poly[*bis*(4-phenyl)(2,4,6-trimethylphenyl)amine]

SAM self-assembling monolayers

SnO_X Tin oxide

Characterization
AFM Atomic force microscopy
EDX Energy-dispersive X-ray spectroscopy
EIS Electrochemical impedance spectroscopy
EQE External quantum efficiency
GI-XRD grazing incidence X-ray diffraction
J Current density
J-V Current density-voltage
PL Photoluminescence imaging
PLQY photoluminescence quantum yield
SAED selected-area electron diffraction
SEM scanning electron microscopy
STEM Scanning transmission electron microscopy
TEM Transmission electron microscopy
V Voltage
XPS X-ray photoelectron spectroscopy
XRR X-ray reflectivity

Deposition Processes
ALD Atomic layer deposition
RF Radio frequency

Contributions & CV

Publications

<u>Publication as first author</u>

1. <u>M. Dussouillez,</u> S. Moon, M. Mensi, C. M. Wolff, Y Liu, H. Yum, B. A. Kamino, A. Walter, F. Sahli, L. Lauber, G. Christmann, K. Sivula, Q. Jeangros, C. Ballif, S. Nicolay, A. Paracchino. *Understanding and Mitigating the Degradation of Perovskite Solar Cells Based on a Nickel Oxide Hole Transport Material during Damp Heat Testing*. 2022. https://doi.org/10.1021/acsami.3c02709.

2. Soon submitted
   <u>M. Dussouillez,</u> M. Mensi, S. Nicolay, C. Ballif, Q. Jeangros, A. Paracchino. *Stabilizing the chemistry of NiO$_X$ in Perovskite Solar Cells to pass the Damp Heat test*. 2024

<u>Publication as co- author</u>

1. R. A. Z. Razera, D. A. Jacobs, F. Fu, P. Fiala, <u>M. Dussouillez,</u> F. Sahli, T. C. J. Yang, L. Ding, A. Walter, A. F. Feil, H. I. Boudinov, S. Nicolay, C. Ballif, Q. Jeangros. *Instability of P-i-n Perovskite Solar Cells under Reverse Bias*. J. Mater. Chem. A 2020, 8 (1), 242–250. https://doi.org/10.1039/c9ta12032g.

Oral presentations

1. <u>M. Dussouillez,</u> A. Paracchino, L. Ding, S. Moon, B. A. Kamino, A. Walter, L. Lauber, G. Christmann, S. Rafizadeh, C. Ballif, S. Nicolay. *Improving Perovskite Solar Cell Stability Through Modification of the p-Type contact*. 37th European Photovoltaic Solar Energy Conference EU PVSEC, Lisbon (PRT), 2020.
   Abstract and Oral presentation
2. <u>M. Dussouillez,</u> S. Moon, C. M. Wolff, Y Liu, H. Yum, B. A. Kamino, A. Walter, F. Sahli, G. Christmann, K. Sivula, Q. Jeangros, C. Ballif, S. Nicolay, A. Paracchino. *Understanding and Mitigating the Degradation of Perovskite Solar Cells Based on a Nickel Oxide Hole Transport Material during Damp Heat Testing.* Tandem PV International Workshop, Freiburg (GER), 2022.
   Abstract and Oral presentation
3. Q. Jeangros, F. Sahli, P. Fiala, R. A. Z. Razera, D. A. Jacobs, F. Fu, T.C.-J. Yang, Q. Guesnay, X. Y. Chin, V. Paratte, G. Nogay, B. A. Kamino, S. Rafizadeh, A. Walter, S. Moon, A. Paracchino, <u>M. Dussouillez,</u> L. Ding, M. Boccard, S. Nicolay, A. Ingenito, and C. Ballif. *A nanometric view on performance-loss mechanisms of perovskite/c-Si multi-junction solar cells*. Asia-Pacific

International Conference on Perovskite, Organic Photovoltaics and Optoelectronics (IPEROP20), Tsukuba-shi (JAP), 2020.
Abstract and Oral presentation

Poster presentations

1. <u>M. Dussouillez,</u> S. Moon, C. M. Wolff, Y Liu, H. Yum, B. A. Kamino, A. Walter, F. Sahli, G. Christmann, K. Sivula, Q. Jeangros, C. Ballif, S. Nicolay, A. Paracchino. *Understanding and Mitigating the Degradation of Perovskite Solar Cells Based on a Nickel Oxide Hole Transport Material during Damp Heat Testing.* 8th World Conference on Photovoltaic Energy Conversion WCPEC-8, Milano (ITA), 2022.
Abstract and Poster presentation

2. <u>M. Dussouillez</u>, K. Artuk, F. Sahli, J.-D. Decoppet, Q. Jeangros, C. Ballif, A. Paracchino. *Light and Heat-Induced Degradation Pathways in Perovskite Solar Cells*. Tandem PV International Workshop, Chambéry (FRA), 2023.
Abstract and Poster presentation

3. H. Lai, F. De Giorgi, R. K. Kothandaraman, C. Chen, <u>M. Dussouillez</u>, Q. Jeangros, D. Zhao, A. N. Tiwari, F. Fu. *Thermally Evaporated p-i-n Perovskite Solar Cells with Record Certified Efficiency*. 6th International Conference on Perovskite Solar Cells and Optoelectronics (PSCO), Oxford (UK), 2023.
Abstract and Poster presentation

4. S. Rafizadeh, B. Paviet-Salomon, B. A. Kamino, A. Walter, Gabriel Christmann, V. Paratte, P. Wyss, L. Lauber, <u>M. Dussouillez</u>, A. Paracchino, S. Moon, J. J. Diaz Leon, M. Boccard, M. Despeisse, Q. Jeangros, C. Ballif, S. Nicolay. *Realization of Monolithic Both-Side Textured Perovskite-Silicon Tandem Solar Cells with >26% Efficiency on 4 cm2 Active Area over 4-inch Silicon Heterojunction Bottom Cells*. Tandem PV International Workshop, Berlin (GER), 2021.
Abstract and Poster presentation

5. R. Kothandaraman, M. Krause, H. Lai, S. Nishiwaki, S. Siegrist, M. Dussouillez, A. Walter, Q. Jeangros, R. Carron1, A. N. Tiwari and F. Fu. *Perovskite-Cu(In)GaSe2 2-terminal tandem solar cells and modules with scalable process*. 40th European Photovoltaic Solar Energy Conference EU PVSEC, Lisbon (PRT), 2023.
Abstract and Poster presentation

Marion Dussouillez

Ph.D. graduate student in perovskite solar cells

French, +33 6 86 90 19 21, +41 76 233 92 02
marion.dussouillez@gmail.com
19/07/1994 – Swiss driving license
Language: French, English

Professional experiences

Ph.D., CSEM – BU-V/ EPFL - PV-lab, Neuchâtel, Switzerland   03.2019 – 11.2023

Perovskite solar cells stability.
Study of the degradation of sputtered NiOx-based PSCs under damp heat test and light soaking at elevated temperatures.
Development of a new sputtered NiOx material to pass de IEC degradation tests.
Fabrication of perovskite solar cells from the glass/ITO substrate to the encapsulated cell.
Characterization of devices and layer materials.
Development of critical thinking about results and literature.
2 first-author research articles (https://doi.org/10.1021/acsami.3c02709, and the second soon to be submitted).
Participation in several conferences (oral and poster presentations)

Student supervisor   06.2021 – 08.2023

2 students for 3 months and a master student for 6 months

Research Internship, CSEM - PV Center, Neuchâtel, Switzerland   09.2018 – 02.2019

Continuation of the Master Thesis.

Master Thesis, EPFL - PV-lab, Neuchâtel, Switzerland   02.2018 – 07.2018

Optimization of the NiO_X hole transport layer in perovskite solar cells.
Co-sputtering of NiOx and MgOx.

Research Assistant Internship, Nanyang Technological University, Singapore   05.2017 – 09.2017

Study the interface perovskite/metal contact in situ TEM.

Course Research Program, ESILV – Leonard de Vinci Graduate School of Engineering, De Vinci   07.2016 – 08.2017

Research Center
Turbulent flow modeling and optimization in an industrial tank.

Vice-president, LeoPompom Pulv Association, Paris La Défense   06.2016 – 06.2017

Cheerleading association with more than 40 members. Triple champion of the Challenge du Monde des Grandes Ecoles.

Math private teacher (high school level)   2014 - 2015

Identify difficulties, hand down knowledge, and encourage.

Assistant – Packaging, Photoweb   07.2014 – 08.2014

Education

Higher education in engineering, ESILV Leonard de Vinci Graduate School of Engineering   2015 – 2018

Engineer's degree, New Energies

Preparatory class for national competitive exams to the "Grandes Écoles",   2012 – 2015
Vaugelas High School, Chambéry

specializing in mathematics, physics and sciences of engineering

Baccalauréat in science, Stendhal High School, Grenoble   2011 – 2012

specialty physics/chemistry, grade good enough.

Technical Competencies and Languages

Technical competencies

Experimental   Thin-film and solar cells fabrication & characterization: RF sputtering, thermal evaporation, ALD, solution-processing (e.g., spin-coating), solar cell encapsulation and lamination - IV, EQE, UV-VIS, AFM, PL, Profilometry, XPS.

Programming   SCAPS – 1D (Drift-diffusion simulation)

Languages

French   Native
English   Professional competence
Spanish   A1

Hobbies

Sport   Dance (> 15 years), hiking, running, climbing, skiing, snowboarding, sailing
Music   Transverse flute (10 years)
Trip   England, Italy, Canada, Singapore, Malaysia, Thailand, Indonesia, Vietnam, Spain, Portugal